Title

THE KINETICS OF LASER PULSE VAPORIZATION OF URANIUM CARBIDE BY MASS SPECTROMETRY

Author

Tehranian, F.

Publication Date

1983-06-01

LBL-15982

Lawrence Berkeley Laboratory
UNIVERSITY OF CALIFORNIA

Materials & Molecular Research Division

THE KINETICS OF LASER PULSE VAPORIZATION OF URANIUM CARBIDE BY MASS SPECTROMETRY

F. Tehranian
(Ph.D. Thesis)

June 1983

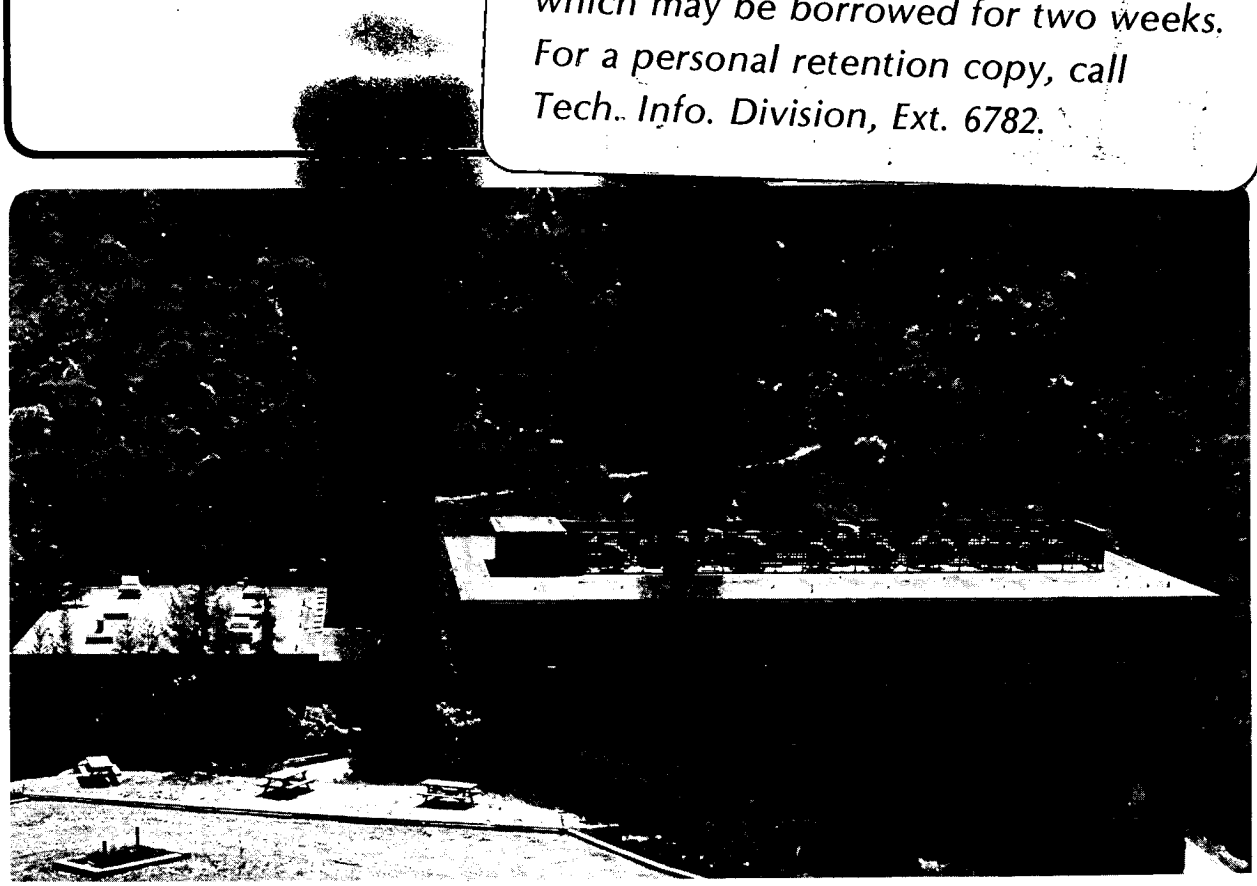

Prepared for the U.S. Department of Energy under Contract DE-AC03-76SF00098

DISCLAIMER

LBL-15982

THE KINETICS OF LASER PULSE VAPORIZATION OF URANIUM CARBIDE BY MASS SPECTROMETRY

Fatollah Tehranian

(Ph.D. Thesis)

Materials and Molecular Research Division and
Department of Nuclear Engineering
Lawrence Berkeley Laboratory
University of California
Berkeley, California 94720

This work was supported by the Director, Office of Energy Research, Office of Basic Energy Sciences, Materials Sciences Division of the U. S. Department of Energy under Contract No. DE-AC03-76SF00098.

TABLE OF CONTENTS

Page

Page

THE KINETICS OF LASER PULSE VAPORIZATION OF URANIUM CARBIDE BY MASS SPECTROMETRY

Fatollah Tehranian

(Ph. D. Thesis)

Materials and Molecular Research Division and
Department of Nuclear Engineering
Lawrence Berkeley Laboratory
University of California
Berkeley, California 94720

ABSTRACT

The kinetics of uranium carbide vaporization in the temperature range 3000 K - 5200 K was studied using a Nd-glass laser with peak power densities from 1.6×10^5 to 4.0×10^5 watts/cm^2. The vapor species U, UC_2, C_1 and C_3 were detected and analyzed by a quadrupole mass spectrometer. From the mass spectrometer signals number densities of the various species in the ionizer were obtained as functions of time. The surface of the irradiated uranium carbide was examined by scanning electron microscope and the depth profile of the crater was obtained.

In order to aid analysis of the data, the heat conduction and species diffusion equations for the solid (or liquid) were solved numerically by a computer code to obtain the temperature and composition transients during laser heating. A sensitivity analysis was used to study the effect of uncertainties in the input parameters on the computed surface temperatures. Both free-molecule and hydrodynamic flow models were considered in predicting the number density of the molecules in the ionizer using the known surface temperature transient and extrapolated partial pressures in equilibrium with the melt.

The measured temperatures were within the confidence limits of the calculations, given the uncertainties in the input data. At low laser energies the measured maximum number densities of the species in the ionizer agreed fairly well with the calculated ones. However at high laser peak power densities ($> 2 \times 10^5$ watts/cm^2) the two differed by a factor of 10 to 100. The total number of ions released from the surface during a laser pulse was measured by a Faraday cup. The total ion emission changed by a factor of 4 in the temperature range 3000 K - 4500 K. The degree of ionization (using the actual evaporation rate of the neutral species) in the same temperature range was calculated to be ~ 16%.

In the theoretical part of the investigation, low temperature partial pressure data for UC(s) were extrapolated, via the entropy and enthalpy of fusion, to calculate the partial pressures of different vapor species as functions of temperature and composition for liquid $UC_{1\pm x}$.

I. Introduction

Uranium carbide is the most promising advanced fuel for improving the performance of liquid metal fast breeder reactors. Due to higher fissile density and higher thermal conductivity than uranium dioxide, carbide fuels permit operation of fuel pins at higher linear power ratings to higher burnups and also yield a higher breeding ratio than oxide fuels.

As part of the safety analysis of the breeder reactors, the equation of state of the nuclear fuels up to ~ 6000 K is required for predicting their behavior in a hypothetical core-disruptive accident (HCDA) and to estimate the energy release during a prompt critical excursion.

Information on the properties of UC at temperatures above the melting point (2780 K) can be obtained either by extrapolating low temperature data on the solid or by direct measurement. Table I.1 summarizes the low temperature vapor pressure measurements for $UC_{1\pm x}$. Due to the rapid change of uranium and carbon activity with composition around C/U = 1 and experimental difficulties (e.g. interaction of uranium carbide with the crucible and with the oxygen in the environment), there are large discrepancies between different measurements. Because of this disagreement, extrapolation of the thermochemical properties into the liquid phase results in great uncertainties. For this reason both theoretical and experimental work is needed to provide the vapor pressure information on uranium carbide at temperatures above 3000 K.

Because of high rates of evaporation at these temperatures, conventional techniques, such as the Knudsen effusion and transpiration methods, cannot be used. Direct measurement can only be accomplished by dynamic pulse heating techniques such as the exploding wire [1-3], neutron pulse [4], electron pulse [5] and laser pulse [6-9].

Laser pulse surface heating has been used by a number of laboratories [6-9] to determine vapor pressures at very high temperature. There are at least four variants of this technique, which differ in the quantity which is measured and interpreted to give vapor pressure. The measured quantity can be the momentum of the vaporized molecules measured by the movement of a pendulum placed in front of the target [8], the rate of evaporation measured by the depth profile of the target and the time of evaporation [7], the shock wave structure (the position of the normal shock in the ambient atmosphere) by photography [10], or the number density of each molecular species at a distance from the target by a mass spectrometer [10].

Ohse et al. [11] measured the vapor pressure of uranium carbide in the temperature range 6400 to 7000 K using laser pulse heating. The Hertz-Langmuir equation [12-13] was used to calculate the vapor pressure from the rate of evaporation obtained by depth profile measurement. There was practically no variation in the measured vapor pressure in the 600 K temperature range studied. However, using the average value of the measured vapor pressure along with the literature value of the vapor pressure at the melting point, an equation for the vapor pressure as a function of temperature was derived.

Table I.1: Measure vapor pressure data over $UC_{1\pm x}$.

Measured quantity	C/U	Temperature [K] range	Log P(atm.) = A-B/T A	B	Authors	Ref.
Press. above UC	1	1948-2133	18.431	4.920×10^4	Ivanov et al.	14
U partial press	1	1910-2660	6.11	2.780×10^4	Alexander et al.	15
U partial press.	1.10	2190-2525	8.197	3.624×10^4	Vozzella et al.	16
U partial press.	1	1900-2400	7.179	2.809×10^4	Khromonozhkin et al	17
C partial press.	1	1200-2400	.360	1.324×10^4	Khromonozhkin et al	17
U partial press.	.995	2073-2373	6.775	3.121×10^4	Storms	18
UC_2 partial press.	.995	2073-2373	10.90	4.628×10^4	Storms	18
U partial press.	1.078	2073-2373	8.046	3.501×10^4	Storms	18
UC_2 partial press.	1.078	2073-2373	8.387	3.993×10^4	Storms	18
U partial press.	1.03	---	7.225	3.291×10^4	Krupka	19
U partial press.	.983	2250-2500	4.791	2.570×10^4	Anselin et al.	20
U partial press.	1.10	2250-2500	4.416	2.600×10^4	Anselin et al.	21
Pressure above UC	1.03	2150-2500	8.80	3.500×10^4	Gorbon Yu et al.	21
U partial press.	1.04	2250-2510	7.52	3.35×10^4	Pattoret et al.	22
C partial press.	1.1	2190-2525	8.347	3.608×10^4	Vozzella et al.	23
U partial press.	1.01	2173-2573	4.69	2.85×10^4	Andrievskii et al.	24
U partial press.	.97	---	5.86	2.700×10^4	Solov'ev	25

In the present study, a Nd-glass laser with a maximum energy of ~ 50 J is used to subject a small spot on the surface of near-stoichiometric uranium carbide to a submillisecond temperature transient. With laser power densities of 1.6×10^5 - 4.0×10^5 W/cm^2, surface temperatures of 3000 K to 5000 K are measured by a fast transient optical pyrometer. A quadrupole mass spectrometer identifies and analyses the various vapor species in the blowoff. The signal from the previously-calibrated mass spectrometer is used to calculate the number density of each vapor species in the ionizer. This quantity is the basis of comparison with the theoretical predictions.

In a different set of experiments, a Faraday cup near the UC target is used to collect positive ions emitted from the surface during a pulse, from which the degree of ionization of the evaporating flux is calculated.

To shed more light on the vaporization process, aluminum disks are placed in front of the target to collect any liquid droplets in the vapor. The surface of the disks are examined by scanning electron microscope and EDAX for signs of liquid droplets.

Accurate knowledge of the surface temperature is essential in this type of study. Temperature measurement by optical pyrometry relies on the single emissivity measurement by Bober et al. [26] and the high temperature calibration curve which is obtained by extrapolating the low temperature (< 3000 K) calibration with a graphite black-body cavity.

In addition to the measurement, the surface temperature is calculated by numerically solving the one-dimensional heat conduction and species diffusion equations for a moving boundary semi-infinite slab taking into account ablation and phase change but neglecting radial liquid movement. Due to incongruent vaporization of uranium carbide and subsequent diffusion of uranium and carbon in the solid (or liquid), the surface composition changes with time during a transient. These changes in C/U ratio at the surface influence the evaporation rate of all vapor species and must be considered in theoretically analyzing the processes occuring during the transient.

Due to high rate of evaporation at very high temperatures, the assumption of free-molecule flow used in low temperature evaporation studies is suspect and hydrodynamic flow may prevail. Therefore both free-molecule flow and hydrodynamic flow models are considered in the theoretical calculation of the number density of the molecules in the ionizer of the mass spectrometer. These calculations employ the surface temperature transient and estimated partial pressures of the species emitted from the target. The calculated number densities are then compared with those obtained experimentally.

II. THEORY

II.1. Extrapolation of Low Temperature Vapor Pressure Data of Uranium Carbide to the Liquid Region

II.1.1 Introduction

Knowledge of the high temperature thermodynamic properties of refractory nuclear fuels is necessary for assessing the consequences of potential accidents involving fuel melting. Methods of extrapolating the partial vapor pressures of the gaseous uranium oxides from measurements over $UO_2(s)$ through the melting point into the liquid region have been developed [27,28] but comparable treatments for uranium carbide have not been reported. In this work the model proposed by Nikol'skii [29,30] for solid UC is modified to estimate uranium pressures and carbon activities in the liquid region. The standard free energies of formation of the gaseous species are then used to calculate the partial pressures of different species as functions of temperature and the carbon-to-uranium ratio of the liquid.

II.1.2 Nikol'skii's Model for Solid $UC_{1\pm y}$

Nikol'skii's [29,30] treatment of the thermochemistry of solid nonstoichiometric uranium carbide considers the solid as a non-ideal molecular solution of U, UC and UC_2 (these are designated by subscripts 0, 1 and 2, respectively). The three constituents are assumed to be related by the equilibrium reaction:

$$UC_2 + U = 2\ UC. \qquad (2\text{-}1)$$

It is further assumed that UC_2 is responsible for the deviation from ideality, and the chemical potentials of three components are written as:

$$\mu_0 = \mu_0^o + \gamma\, x_2^2 + RT\ln x_0 \qquad (2\text{-}2)$$

$$\mu_1 = \mu_1^o + \gamma\, x_2^2 + RT\ln x_1 \qquad (2\text{-}3)$$

$$\mu_2 = \mu_2^o + \gamma\, (1-x_2)^2 + RT\ln x_2 \qquad (2\text{-}4)$$

where x_0, x_1 and x_2 are the mole fractions of U, UC and UC_2, respectively and μ_0^o, μ_1^o and μ_2^o are the standard free energies of the pure substances, γ is a nonideality parameter which is independent of composition.

The condition for equilibrium of reaction (2-1) is $\mu_2 + \mu_0 = 2\mu_1$, which yields:

$$\mu_0^o + \mu_2^o - 2\mu_1^o + \gamma(1-2x_2) + RT\ln \frac{x_0 x_2}{x_1^2} . \qquad (2\text{-}5)$$

The chemical potential of uranium is given by Equation (2-2) and that of carbon is obtained from the reaction:

$$U + C = UC \qquad (2\text{-}6)$$

which yields:

$$\mu_C = \mu_1 - \mu_0 = \mu_1^o - \mu_0^o + RT\ln \frac{x_1}{x_0} . \qquad (2\text{-}7)$$

The standard state of uranium is the monoatomic ideal gas at a pressure of 1 atm, while that of carbon is graphite. The chemical potentials of these two elements in the system are:

$$\mu_0 = RT\ln P_U \qquad (2\text{-}8)$$

$$\mu_C = RT\ln a_C . \qquad (2\text{-}9)$$

Where P_U is the partial pressure of uranium in equilibrium with the condensed phase and a_C is the carbon activity.

Combining equations (2-2) and (2-8) yields:

$$\log P_U = A_0 + Bx_2^2 + \log x_0 \qquad (2\text{-}10)$$

and, from equations (2-7) and (2-9):

$$\log a_C = A_1 + \log (x_1/x_0) \tag{2-11}$$

where:

$$A_0 = \mu_0^o/2.3026\ RT \tag{2-12}$$

$$A_1 = (\mu_1^o - \mu_0^o)/2.3026\ RT \tag{2-13}$$

$$A_2 = (\mu_0^o + \mu_2^o - 2\mu_1^o)/2.3026\ RT \tag{2-14}$$

$$B = \gamma/2.3026\ RT. \tag{2-15}$$

The mole fractions x_0, x_1 and x_2 are obtained from the solution of the following system of three equations. The carbon-to-uranium ratio of the solid (C/U) is related to the mole fractions by:

$$(C/U) - x_1 - 2x_2 = 0. \tag{2-16}$$

Equation (2-5) is written as:

$$A_2 + B(1 - 2x_2) + \log(x_0 x_2/x_1^2) = 0 \tag{2-17}$$

and the mole fractions sum to unity.

$$x_0 + x_1 + x_2 = 1. \tag{2-18}$$

To determine the parameters A_0, A_1, A_2 and B, Nikol'skii used the uranium pressure and carbon activity measured by Storms [31] for different compositions (i.e. C/U). By repeating the calculations for different temperatures he obtained the following temperature dependences:

$$A_0 = 4.8283 - (22243/T) \tag{2-19}$$

$$A_1 = 1.3304 - (9643/T) \tag{2.20}$$

$$A_2 = -2.7611 + (12379/T) \tag{2.21}$$

$$B = 0.0041 + (2089/T). \tag{2.22}$$

II.1.3 Extrapolation to the Liquid Region

To estimate the thermochemical properties of the uranium-carbon system at temperatures above the melting point of UC, Nikol'skii's model for the solid phase is assumed to apply to the liquid phase as well. That is, liquid uranium carbide ($UC_{1\pm y}$) is considered as a mixture of U, UC and UC_2, in which the last is responsible for deviation from ideal solution behavior. Following the same steps which were taken for the solid phase, we obtain for the liquid phase equations identical in form to equations (2-10) - (2-18). The constants A_0, A_1, A_2 and B, however, are different when the condensed phase is liquid.

Since there are no uranium pressure or carbon activity data for the liquid region, we cannot determine the parameters as in the solid case. Instead, we relate liquid and solid properties through enthalpy and entropy of fusion. For the solid, temperature dependence of μ_i^o (i = 0,1,2) is of the general form:

$$\mu_i^o = -a_i T + b_i . \qquad (2\text{-}23)$$

If we assume that the corresponding liquid properties (denoted by primes), have similar temperature dependences,

$$\mu_i'^o = -a_i' T + b_i' . \qquad (2\text{-}24)$$

Then we can conclude that

$$a_i' = a_i + \Delta S_{mi} \qquad (i=0,1,2) \qquad (2\text{-}25)$$

$$b_i' = b_i + \Delta H_{mi} = b_i + T_{mi}\,\Delta S_{mi} \qquad (i=0,1,2) \qquad (2\text{-}26)$$

where ΔS_{mi} and ΔH_{mi} are the entropy and enthalpy of fusion of the pure components and the T_{mi} are their melting points. Estimates of these properties are given in Table (2.1).

Table 2.1. Entropies of fusion.

	T_{mi}, K	ΔS_{mi} cal/mole-K
U	1408	1.55
UC	2780	4.0
UC_2	2500	4.0, 6.0

The values of ΔS_m for U and UC are taken from the literature [32], [33]. For UC_2 we used either the same value for UC or R per atom (6 cal/mole K) suggested by Leibowitz [34]. Using the values in Table 2.1 in Eqs. (2-24) - (2-26) fixes the $\mu_i'^o$ which, when inserted into the liquid phase analogs of Eqs. (2-12) - (2.14) yield:

$$A_0' = 4.4883 - 2.1763 \times 10^4/T \quad (2\text{-}27)$$

$$A_1' = 0.8018 - 7.7069 \times 10^3/T \quad (2\text{-}28)$$

$$A_2' = -2.2325 + 1.0389 \times 10^4/T \text{ for } \Delta S_{m2} = 4.0 \text{ cal/mole-K}$$

or

$$A_2' = -2.6799 + 1.1607 \times 10^4/T \text{ for } \Delta S_{m2} = 6.0 \text{ cal/mole-K}. \quad (2\text{-}29)$$

To find B' we used the carbon activity at the melting point of UC [31]. This was obtained by extrapolating the data in the solid phase to the melting point and solving equations (2-11), (2-16), (2-17) and (2-18) at T = 2780 K, C/U = 1 and with the constants A_0, ..B replaced by A_0' .... B'. Because the liquid and solid phases are in equilibrium at the melting point, the carbon activity of the liquid is equal to that in the solid, obtained by extrapolation. Since this procedure gives only one value of B' in the liquid region (i.e. at melting point), we cannot find B' for different temperatures. As a result

we assumed that γ' is constant and so $B' = \frac{\text{constant}}{T}$, which is approximately the behavior for B for the solid (see Eq. (2-22). Using the value of B' at the melting point, we find:

$$B' = \frac{1722.6}{T} \text{ for } \Delta S_{m2} = 4.0 \text{ cal/mole-K}$$

or

$$B' = 1753.0/T \text{ for } \Delta S_{m2} = 6.0 \text{ cal/mole-K} \qquad (2\text{-}30)$$

Even though the uranium pressure in equilibrium with UC(l) and UC(s) at the melting point is available by extrapolation of Storms' data [31], this information is not useful in fixing A_2' or B'. The reason is that the equation in which this datum appears (Eq. (2-10) does not contain A_2' and at the melting point of UC the term containing B' is very much smaller than the other terms. Therefore, Eq. (2-10) serves primarily as a check on the value of A_0' and A_1' and the carbon activity at the melting point. The uranium pressure determined in this manner is 3.76×10^{-5} atm which compares well with the extrapolated experimental value of 3.95×10^{-5} atm.

Use of the parameters A_0', A_1, A_2' and B' in the calculational method previously developed for the solid gives the uranium partial pressure and the carbon activity as functions of composition and temperature in the liquid region.

II.1.4 Partial Pressure of Other Vapor Species

The partial pressure of C(g) is obtained by using the calculated carbon activity from Eq. (2-11) and the known partial pressure of C(g) over graphite. Equation (2-10) gives the uranium pressure. The partial pressure of other vapor species calculated by use of the gaseous equilibria:

$$U(g) + 2C(g) = UC_2(g) \tag{2-31}$$

$$2C(g) = C_2(g) \tag{2-32}$$

$$3C(g) = C_3(g). \tag{2-33}$$

From which p_{UC_2}, p_{C_2} and p_{C_3} are determined by:

$$p_{UC_2} = p_U\, p_C^2 \exp[\Delta G_U^o + 2\Delta G_C^o - \Delta G_{UC_2}^o]/RT \tag{2-34}$$

$$p_{C_2} = p_C^2 \exp[2\Delta G_C^o - \Delta G_{C_2}^o]/RT \tag{2-35}$$

$$p_{C_3} = p_C^3 \exp[3\Delta G_C^o - \Delta G_{C_3}^o]/RT\ . \tag{2-36}$$

The free energies of formation of the gaseous molecules are given in Ref. [31].

Figures (2-1) and (2-2) show the calculated partial pressures of different species and the total vapor pressure of $UC_{1\pm y}$ as a function of composition at 4000 K. Figure (2-3) shows the temperature dependence of the total pressure calculated for $UC_{1.0}$ and compared with the result of calculations by Finn et al. [33] for stoichiometric material. The two computations differ by a factor of less than ~ 2. The choice of entropy of fusion of UC_2 (Table 2-1) affects primarily the partial pressure of this species. Partial pressure of different vapor species, total pressure and carbon-to-uranium ratio in the vapor as functions of composition and temperature are given in Table (2-2).

Table 2-2. Partial Pressures of Different Vapor Species, Total Vapor Pressure and Carbon to Uranium Ratio of the Gas as a Function of Temperature and Composition over Uranium Carbide.

$(C/U)_s$	T	P_u	P_C	P_{C_2}	P_{C_3}	P_{UC_2}	P_T	$(C/U)_g$
1.80	2000.00	.1534E-04	.2657E-05	.3529E-06	.1719E-05	.1423E-05	.2143E-04	1.7936
1.80	3000.00	.8874E-04	.2053E-04	.3721E-05	.1559E-04	.1263E-04	.1412E-03	2.5708
1.80	3200.00	.4073E-03	.1234E-03	.2044E-04	.1084E-03	.8564E-04	.7542E-03	3.5468
1.80	3400.00	.1540E-02	.5041E-03	.1046E-03	.6077E-03	.4640E-03	.3401E-02	4.7524
1.80	3600.00	.4936E-02	.2498E-02	.9575E-03	.2863E-02	.2095E-02	.1335E-01	6.2339
1.80	3800.00	.1375E-01	.8963E-02	.4239E-02	.1168E-01	.8065E-02	.4670E-01	8.0243
1.80	4000.00	.3397E-01	.2852E-01	.1642E-01	.4219E-01	.2713E-01	.1482E+00	10.1515
1.80	4200.00	.7557E-01	.8196E-01	.5678E-01	.1378E+00	.8136E-01	.4336E+00	12.6615
1.80	4400.00	.1545E+00	.2153E+00	.1775E+00	.4105E+00	.2205E+00	.1178E+01	15.5286
1.80	4600.00	.2922E+00	.5234E+00	.5093E+00	.1131E+01	.5476E+00	.3004E+01	18.7976
1.80	4800.00	.5183E+00	.1187E+01	.1351E+01	.2900E+01	.1250E+01	.7215E+01	22.4391
1.80	5000.00	.8697E+00	.2532E+01	.3341E+01	.6968E+01	.2702E+01	.1641E+02	26.4627
1.70	2800.00	.1590E-04	.2606E-05	.3396E-06	.1615E-05	.1420E-05	.2168E-04	1.6746
1.70	3000.00	.9800E-04	.1942E-04	.3329E-05	.1319E-04	.1248E-04	.1464E-03	2.1190
1.70	3200.00	.4753E-03	.1130E-03	.2471E-04	.8239E-04	.8368E-04	.7803E-03	2.6326
1.70	3400.00	.1882E-02	.5390E-03	.1470E-03	.4317E-03	.4523E-03	.3452E-02	3.2492
1.70	3600.00	.6272E-02	.2179E-02	.7289E-03	.1903E-02	.2027E-02	.1311E-01	4.0000
1.70	3800.00	.1803E-01	.7660E-02	.3113E-02	.7349E-02	.7766E-02	.4394E-01	4.9250
1.70	4000.00	.4564E-01	.2411E-01	.1173E-01	.2550E-01	.2605E-01	.1330E+00	6.0661
1.70	4200.00	.1037E+00	.6850E-01	.3966E-01	.8045E-01	.7786E-01	.3702E+00	7.4400
1.70	4400.00	.2140E+00	.1765E+00	.1221E+00	.2340E+00	.2106E+00	.9539E+00	9.0750
1.70	4600.00	.4105E+00	.4312E+00	.3457E+00	.6326E+00	.5222E+00	.2342E+01	10.9756
1.70	4800.00	.7342E+00	.9735E+00	.9085E+00	.1599E+01	.1199E+01	.5415E+01	13.1431
1.70	5000.00	.1240E+01	.2069E+01	.2230E+01	.3799E+01	.2573E+01	.1191E+02	15.5649
1.60	2900.00	.1405E-04	.2810E-05	.3947E-06	.2023E-05	.1457E-05	.2073E-04	2.1623
1.60	3000.00	.9108E-04	.2019E-04	.3599E-05	.1483E-04	.1265E-04	.1431E-03	2.4150
1.60	3200.00	.4693E-03	.1140E-03	.2511E-04	.8541E-04	.8416E-04	.7779E-03	2.7012
1.60	3400.00	.1946E-02	.5283E-03	.1412E-03	.4066E-03	.4493E-03	.3471E-02	3.0462
1.60	3600.00	.6747E-02	.2065E-02	.6670E-03	.1667E-02	.1997E-02	.1316E-01	3.4050
1.60	3800.00	.2084E-01	.7205E-02	.2740E-02	.6060E-02	.7598E-02	.4366E-01	4.0532
1.60	4000.00	.5213E-01	.2225E-01	.9990E-02	.2083E-01	.2534E-01	.1297E+00	4.7814
1.60	4200.00	.1209E+00	.6242E-01	.3234E-01	.6088E-01	.7541E-01	.3526E+00	5.6978
1.60	4400.00	.2545E+00	.1610E+00	.9933E-01	.1718E+00	.2033E+00	.8899E+00	6.8131
1.60	4600.00	.4933E+00	.3858E+00	.2769E+00	.4533E+00	.5026E+00	.2112E+01	8.1390
1.60	4800.00	.8914E+00	.8657E+00	.7184E+00	.1125E+01	.1151E+01	.4751E+01	9.6757
1.60	5000.00	.1518E+01	.1831E+01	.1746E+01	.2673E+01	.2465E+01	.1019E+02	11.4162
1.50	2600.00	.1178E-04	.3149E-05	.4958E-06	.2848E-05	.1534E-05	.1980E-04	3.1744
1.50	3000.00	.8146E-04	.2163E-04	.4205E-05	.1873E-04	.1310E-04	.1393E-03	3.1188
1.50	3200.00	.4368E-03	.1194E-03	.2756E-04	.9024E-04	.8599E-04	.7660E-03	3.1354
1.50	3400.00	.1892E-02	.5381E-03	.1465E-03	.4297E-03	.4531E-03	.3459E-02	3.2255
1.50	3600.00	.6604E-02	.2074E-02	.6606E-03	.1641E-02	.1992E-02	.1317E-01	3.4299

Table 2-2 Continued

$(C/U)_s$	T	P_u	P_C	P_{C_2}	P_{C_3}	P_{UC_2}	P_T	$(C/U)_g$
1.50	3800.00	.2095E-01	.7026E-02	.7605E-02	.5527E-02	.7514E-02	.4362E-01	3.7629
1.50	4000.00	.5555E-01	.2135E-01	.9126E-02	.1769E-01	.2487E-01	.1087E+00	4.2467
1.50	4200.00	.1316E+00	.5911E-01	.2954E-01	.5170E-01	.7359E-01	.3455E+00	4.6981
1.50	4400.00	.2814E+00	.1510E+00	.8730E-01	.1415E+00	.1975E+00	.8587E+00	5.7268
1.50	4600.00	.5527E+00	.3568E+00	.2394E+00	.3646E+00	.4865E+00	.2003E+01	6.7360
1.50	4800.00	.1004E+01	.7999E+00	.6134E+00	.8870E+00	.1111E+01	.4412E+01	7.9241
1.50	5000.00	.1730E+01	.1663E+01	.1476E+01	.2043E+01	.2374E+01	.9306E+01	9.2862
1.40	2600.00	.3978E-05	.3529E-05	.6225E-06	.4007E-05	.1633E-05	.1977E-04	4.6507
1.40	3000.00	.2753E-04	.2395E-04	.4956E-05	.2581E-04	.1369E-04	.1386E-03	4.0442
1.40	3200.00	.4064E-03	.1555E-03	.3043E-04	.1130E-03	.8833E-04	.7646E-03	3.6634
1.40	3400.00	.1826E-02	.5515E-03	.1538E-03	.4624E-03	.4593E-03	.3453E-02	3.4746
1.40	3600.00	.6774E-02	.2051E-02	.6647E-03	.1656E-02	.1996E-02	.1317E-01	3.4603
1.40	3800.00	.2129E-01	.6925E-02	.2531E-02	.5388E-02	.7455E-02	.4359E-01	3.6189
1.40	4000.00	.5793E-01	.2075E-01	.8630E-02	.1675E-01	.2449E-01	.1281E+00	3.9261
1.40	4200.00	.1393E+00	.5682E-01	.2729E-01	.4592E-01	.7201E-01	.3414E+00	4.4048
1.40	4400.00	.3018E+00	.1438E+00	.7926E-01	.1224E+00	.1923E+00	.8397E+00	5.0503
1.40	4600.00	.5983E+00	.3395E+00	.2144E+00	.3089E+00	.4720E+00	.1933E+01	5.8604
1.40	4800.00	.1101E+01	.7520E+00	.5429E+00	.7307E+00	.1075E+01	.4210E+01	6.8285
1.40	5000.00	.1902E+01	.1576E+01	.1295E+01	.1680E+01	.2290E+01	.8743E+01	7.9539
1.30	2800.00	.8939E-05	.3827E-05	.7324E-06	.5114E-05	.1721E-05	.2033E-04	6.0335
1.30	3000.00	.6795E-04	.2481E-04	.5432E-05	.2749E-04	.1412E-04	.1393E-03	4.7116
1.30	3200.00	.3944E-03	.1282E-03	.3160E-04	.1217E-03	.8958E-04	.7658E-03	3.9190
1.30	3400.00	.1823E-02	.5518E-03	.1541E-03	.4634E-03	.4593E-03	.3452E-02	3.4830
1.30	3600.00	.6909E-02	.2050E-02	.6652E-03	.1584E-02	.1976E-02	.1316E-01	3.3172
1.30	3800.00	.2205E-01	.6745E-02	.2401E-02	.4978E-02	.7326E-02	.4350E-01	3.3577
1.30	4000.00	.6072E-01	.2034E-01	.8102E-02	.1463E-01	.2393E-01	.1274E+00	3.5751
1.30	4200.00	.1474E+00	.5451E-01	.2511E-01	.4054E-01	.7009E-01	.3376E+00	3.9544
1.30	4400.00	.3215E+00	.1373E+00	.7217E-01	.1064E+00	.1865E+00	.8238E+00	4.4883
1.30	4600.00	.6412E+00	.3226E+00	.1935E+00	.2649E+00	.4565E+00	.1879E+01	5.1721
1.30	4800.00	.1196E+01	.7124E+00	.4965E+00	.6267E+00	.1037E+01	.4048E+01	5.9993
1.30	5000.00	.2057E+01	.1487E+01	.1153E+01	.1412E+01	.2205E+01	.8314E+01	6.9647
1.20	2800.00	.9065E-05	.3781E-05	.7147E-06	.4930E-05	.1703E-05	.2013E-04	5.8562
1.20	3000.00	.7121E-04	.2387E-04	.5030E-05	.2450E-04	.1370E-04	.1303E-03	4.1890
1.20	3200.00	.4225E-03	.1213E-03	.2844E-04	.1030E-03	.8581E-04	.7610E-03	3.3243
1.20	3400.00	.1972E-02	.5190E-03	.1357E-03	.3032E-03	.4377E-03	.3446E-02	2.9892
1.20	3600.00	.7403E-02	.1921E-02	.5666E-03	.1303E-02	.1881E-02	.1316E-01	2.7745
1.20	3800.00	.2386E-01	.6332E-02	.2116E-02	.4118E-02	.6984E-02	.4341E-01	2.8369
1.20	4000.00	.6551E-01	.1805E-01	.7171E-02	.1218E-01	.2286E-01	.1266E+00	3.0538
1.20	4200.00	.1586E+00	.5138E-01	.2231E-01	.3395E-01	.6703E-01	.3337E+00	3.4095
1.20	4400.00	.3457E+00	.1235E+00	.6424E-01	.8934E-01	.1786E+00	.8073E+00	3.8965
1.20	4600.00	.6893E+00	.3044E+00	.1723E+00	.2225E+00	.4370E+00	.1826E+01	4.5110
1.20	4800.00	.1275E+01	.6726E+00	.4329E+00	.5261E+00	.9926E+00	.3899E+01	5.2516
1.20	5000.00	.2215E+01	.1402E+01	.1024E+01	.1182E+01	.2110E+01	.7913E+01	6.1122
1.10	2800.00	.1210E-04	.2933E-05	.4301E-06	.2301E-05	.1368E-05	.1913E-04	2.6941
1.10	3000.00	.9493E-04	.1055E-04	.3037E-05	.1149E-04	.1103E-04	.1390E-03	2.0042
1.10	3200.00	.5492E-03	.9636E-04	.1796E-04	.5165E-04	.7043E-04	.7856E-03	1.7435
1.10	3400.00	.2463E-02	.4259E-03	.9164E-04	.2126E-03	.3694E-03	.3568E-02	1.7074
1.10	3600.00	.9011E-02	.1634E-02	.4100E-03	.8021E-03	.1637E-02	.1340E-01	1.8127
1.10	3800.00	.2775E-01	.5549E-02	.1625E-02	.2771E-02	.6233E-02	.4393E-01	2.0236
1.10	4000.00	.7423E-01	.1690E-01	.5766E-02	.8703E-02	.2082E-01	.1265E+00	2.3276
1.10	4200.00	.1765E+00	.4603E-01	.1853E-01	.2570E-01	.6193E-01	.3294E+00	2.7235
1.10	4400.00	.3797E+00	.1193E+00	.5455E-01	.6900E-01	.1665E+00	.7900E+00	3.2143
1.10	4600.00	.7510E+00	.2825E+00	.1484E+00	.1779E+00	.4101E+00	.1770E+01	3.8054

Table 2-2 Continued

$(C/U)_s$	T	P_u	P_C	P_{C_2}	P_{C_3}	P_{UC_2}	PT	$(C/U)_g$
1.10	4800.00	.1382E+01	.6265E+00	.3763E+00	.4263E+00	.9351E+00	.3746E+01	4.4988
1.10	5000.00	.2393E+01	.1311E+01	.8951E+00	.9660E+00	.1992E+01	.7557E+01	5.2933
1.00	2800.00	.4851E-04	.9160E-06	.4135E-07	.7011E-07	.4467E-06	.4139E-04	.1401
1.00	3000.00	.2275E-03	.8014E-05	.5669E-06	.9270E-06	.4933E-05	.2419E-03	.2493
1.00	3200.00	.1027E-02	.5290E-04	.5411E-05	.0544E-05	.3069E-04	.1134E-02	.3861
1.00	3400.00	.3600E-02	.2768E-03	.3876E-04	.5849E-04	.2452E-03	.4487E-02	.5838
1.00	3600.00	.1250E-01	.1135E-02	.2193E-03	.3138E-03	.1215E-02	.1544E-01	.8376
1.00	3800.00	.3540E-01	.4387E-02	.1020E-02	.1379E-02	.4996E-02	.4719E-01	1.1421
1.00	4000.00	.8947E-01	.1414E-01	.4035E-02	.5142E-02	.1756E-01	.1304E+00	1.5204
1.00	4200.00	.2047E+00	.4063E-01	.1396E-01	.1679E-01	.5469E-01	.3302E+00	1.9564
1.00	4400.00	.4293E+00	.1061E+00	.4314E-01	.4917E-01	.1489E+00	.7767E+00	2.4631
1.00	4600.00	.8346E+00	.2554E+00	.1213E+00	.1315E+00	.3726E+00	.1715E+01	3.0472
1.00	4800.00	.1518E+01	.5726E+00	.3145E+00	.3257E+00	.8585E+00	.3590E+01	3.7136
1.00	5000.00	.2609E+01	.1207E+01	.7592E+00	.7546E+00	.1842E+01	.7172E+01	4.4645
.90	2800.00	.1812E-03	.1913E-06	.1830E-08	.6386E-09	.8714E-07	.1815E-03	.0057
.90	3000.00	.6890E-03	.2505E-05	.5540E-07	.2832E-07	.1460E-05	.6930E-03	.0218
.90	3200.00	.2302E-02	.2263E-04	.9899E-06	.6667E-06	.1628E-04	.2343E-02	.0618
.90	3400.00	.6947E-02	.1494E-03	.1129E-04	.9192E-05	.1282E-03	.7245E-02	.1497
.90	3600.00	.1917E-01	.7613E-03	.8896E-04	.8108E-04	.7559E-03	.2086E-01	.3024
.90	3800.00	.4864E-01	.3144E-02	.5217E-03	.5042E-03	.3511E-02	.5632E-01	.5359
.90	4000.00	.1139E+00	.1096E-01	.2423E-02	.2393E-02	.1343E-01	.1431E+00	.8529
.90	4200.00	.2473E+00	.3328E-01	.9363E-02	.9228E-02	.4385E-01	.3430E+00	1.2516
.90	4400.00	.5002E+00	.9032E-01	.3125E-01	.3031E-01	.1257E+00	.7778E+00	1.7291
.90	4600.00	.9483E+00	.2232E+00	.9265E-01	.8776E-01	.3233E+00	.1675E+01	2.2841
.90	4800.00	.1696E+01	.5098E+00	.2491E+00	.2296E+00	.7595E+00	.3444E+01	2.9162
.90	5000.00	.2876E+01	.1086E+01	.6171E+00	.5529E+00	.1652E+01	.6788E+01	3.6254
.80	2800.00	.3510E-03	.8622E-07	.3691E-09	.6263E-10	.3590E-07	.3511E-03	.0013
.80	3000.00	.1284E-02	.1208E-05	.1288E-07	.3173E-08	.6325E-06	.1286E-02	.0052
.80	3200.00	.4042E-02	.1169E-04	.2644E-06	.9232E-07	.7634E-05	.4062E-02	.0170
.80	3400.00	.1130E-01	.8439E-04	.3603E-05	.1657E-05	.6656E-04	.1145E-01	.0474
.80	3600.00	.2873E-01	.4730E-03	.3435E-04	.1945E-04	.4374E-03	.2970E-01	.1134
.80	3800.00	.6756E-01	.2135E-02	.2406E-03	.1579E-03	.2249E-02	.7236E-01	.2370
.80	4000.00	.1485E+00	.8022E-02	.1299E-02	.9389E-03	.9380E-02	.1681E+00	.4385
.80	4200.00	.3063E+00	.2586E-01	.5653E-02	.4330E-02	.3279E-01	.3750E+00	.7305
.80	4400.00	.5962E+00	.7343E-01	.2065E-01	.1629E-01	.9901E-01	.8056E+00	1.1167
.80	4600.00	.1099E+01	.1877E+00	.6549E-01	.5216E-01	.2647E+00	.1669E+01	1.5950
.80	4800.00	.1924E+01	.4393E+00	.1850E+00	.1470E+00	.6399E+00	.3335E+01	2.1603
.80	5000.00	.3210E+01	.9556E+00	.4751E+00	.3736E+00	.1421E+01	.6440E+01	2.8078
.70	2800.00	.5236E-03	.5184E-07	.1343E-09	.1270E-10	.1849E-07	.5237E-03	.0005
.70	3000.00	.1902E-02	.7165E-06	.4532E-08	.6627E-09	.3297E-06	.1903E-02	.0020
.70	3200.00	.5905E-02	.7064E-05	.3643E-07	.2034E-07	.4069E-05	.5916E-02	.0058
.70	3400.00	.1615E-01	.5246E-04	.1332E-05	.3980E-06	.3676E-04	.1624E-01	.0195
.70	3600.00	.3985E-01	.3060E-03	.1437E-04	.5264E-05	.2536E-03	.4043E-01	.0493
.70	3800.00	.9041E-01	.1443E-02	.1107E-03	.4930E-04	.1385E-02	.9341E-01	.1108
.70	4000.00	.1912E+00	.5725E-02	.6613E-03	.3411E-03	.6151E-02	.2041E+00	.2233
.70	4200.00	.3805E+00	.1936E-01	.3169E-02	.1817E-02	.2283E-01	.4277E+00	.4069
.70	4400.00	.7175E+00	.5735E-01	.1260E-01	.7759E-02	.7267E-01	.8678E+00	.6774
.70	4600.00	.1268E+01	.1516E+00	.4284E-01	.2760E-01	.2030E+00	.1713E+01	1.0433
.70	4800.00	.2208E+01	.3654E+00	.1200E+00	.8456E-01	.5081E+00	.3294E+01	1.5052
.70	5000.00	.3631E+01	.8117E+00	.3432E+00	.2294E+00	.1159E+01	.6175E+01	2.0591
.60	2800.00	.6970E-03	.3341E-07	.5580E-10	.3401E-11	.1022E-07	.6970E-03	.0002
.60	3000.00	.2526E-02	.4634E-06	.1896E-08	.1793E-09	.1832E-06	.2527E-02	.0010
.60	3200.00	.7807E-02	.4599E-05	.4098E-07	.5616E-08	.2281E-05	.7814E-02	.0032

Table 2-2 Continued

$(C/U)_s$	T	P_u	P_C	P_{C_2}	P_{C_3}	P_{UC_2}	P_T	$(C/U)_g$
.60	3400.00	.2119E-01	.3455E-04	.6040E-06	.1137E-06	.2033E-04	.2125E-01	.0094
.60	3600.00	.5169E-01	.2051E-03	.6459E-05	.1586E-05	.1480E-03	.5205E-01	.0241
.60	3800.00	.1154E+00	.9951E-03	.5226E-04	.1598E-04	.8344E-03	.1173E+00	.0557
.60	4000.00	.2393E+00	.4051E-02	.3312E-03	.1209E-03	.3857E-02	.2477E+00	.1169
.60	4200.00	.4662E+00	.1416E-01	.1695E-02	.7110E-03	.1497E-01	.4978E+00	.2242
.60	4400.00	.8602E+00	.4336E-01	.7203E-02	.3354E-02	.4981E-01	.9640E+00	.3957
.60	4600.00	.1513E+01	.1184E+00	.2606E-01	.1309E-01	.1451E+00	.1816E+01	.6471
.60	4800.00	.2543E+01	.2929E+00	.8221E-01	.4353E-01	.3768E+00	.3344E+01	.9666
.60	5000.00	.4130E+01	.6657E+00	.2309E+00	.1266E+00	.8867E+00	.6039E+01	1.4239
.50	2800.00	.8707E-03	.2230E-07	.2486E-10	.1011E-11	.5688E-08	.8707E-03	.0001
.50	3000.00	.3152E-02	.3098E-06	.6473E-09	.5357E-10	.1022E-06	.3153E-02	.0005
.50	3200.00	.9728E-02	.3065E-05	.1840E-07	.1694E-08	.1278E-05	.9731E-02	.0017
.50	3400.00	.2632E-01	.2331E-04	.2748E-06	.3490E-07	.1162E-04	.2635E-01	.0049
.50	3600.00	.6388E-01	.1396E-03	.2992E-05	.5000E-06	.8470E-04	.6410E-01	.0126
.50	3800.00	.1416E+00	.6861E-03	.2485E-04	.5240E-05	.4867E-03	.1426E+00	.0294
.50	4000.00	.2906E+00	.2843E-02	.1631E-03	.4179E-04	.2306E-02	.2962E+00	.0628
.50	4200.00	.5598E+00	.1015E-01	.8710E-03	.2618E-03	.9233E-02	.5803E+00	.1236
.50	4400.00	.1019E+01	.3183E-01	.3881E-02	.1326E-02	.3181E-01	.1088E+01	.2257
.50	4600.00	.1769E+01	.8906E-01	.1475E-01	.5575E-02	.9601E-01	.1974E+01	.3845
.50	4800.00	.2941E+01	.2257E+00	.4882E-01	.1992E-01	.2581E+00	.3493E+01	.6143
.50	5000.00	.4707E+01	.5245E+00	.1433E+00	.6188E-01	.6272E+00	.6064E+01	.9255

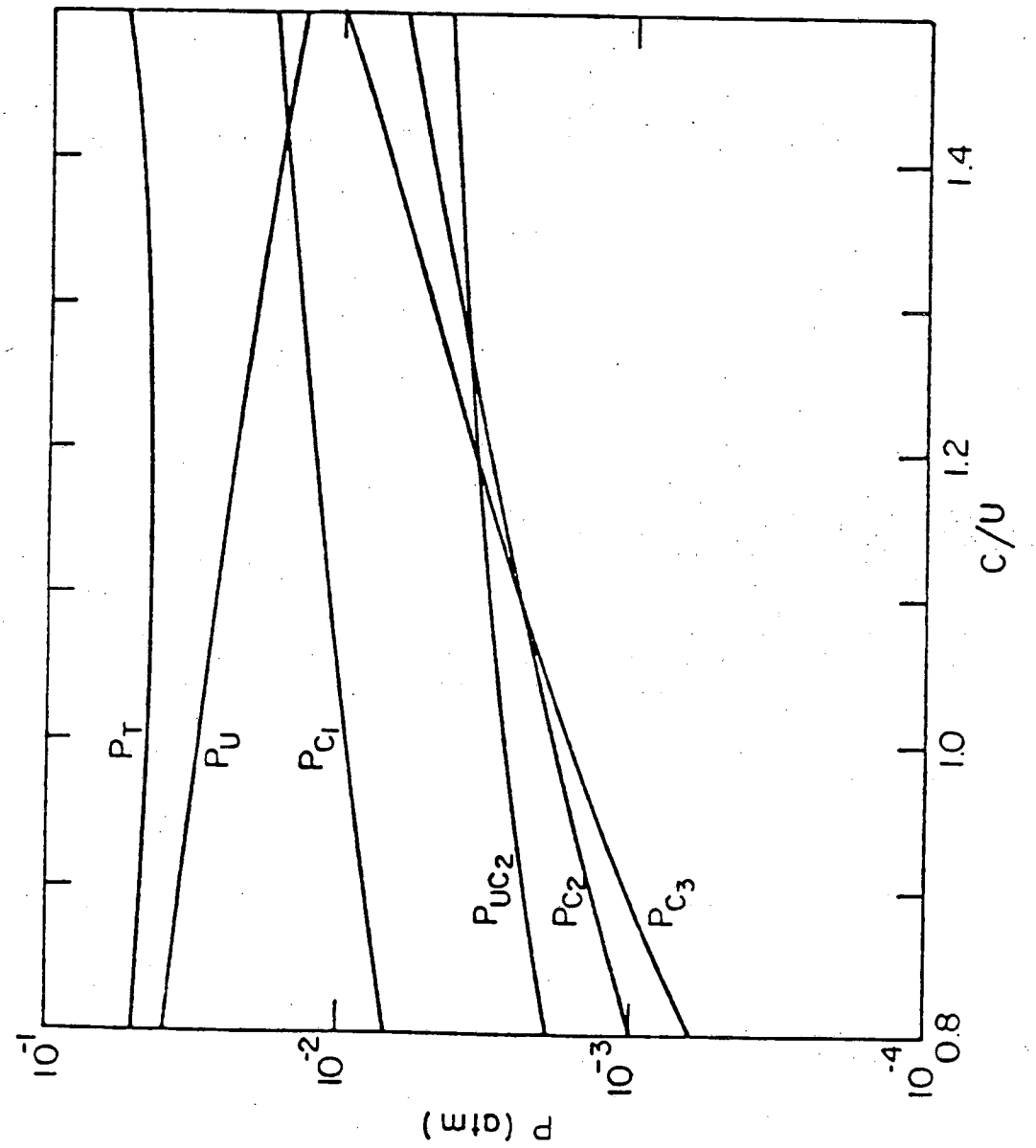

Fig. 2-1. Partial pressures of different species as a function of composition at 4000 K. ΔS_m (UC_2) = 4.0 cal/mole-K.

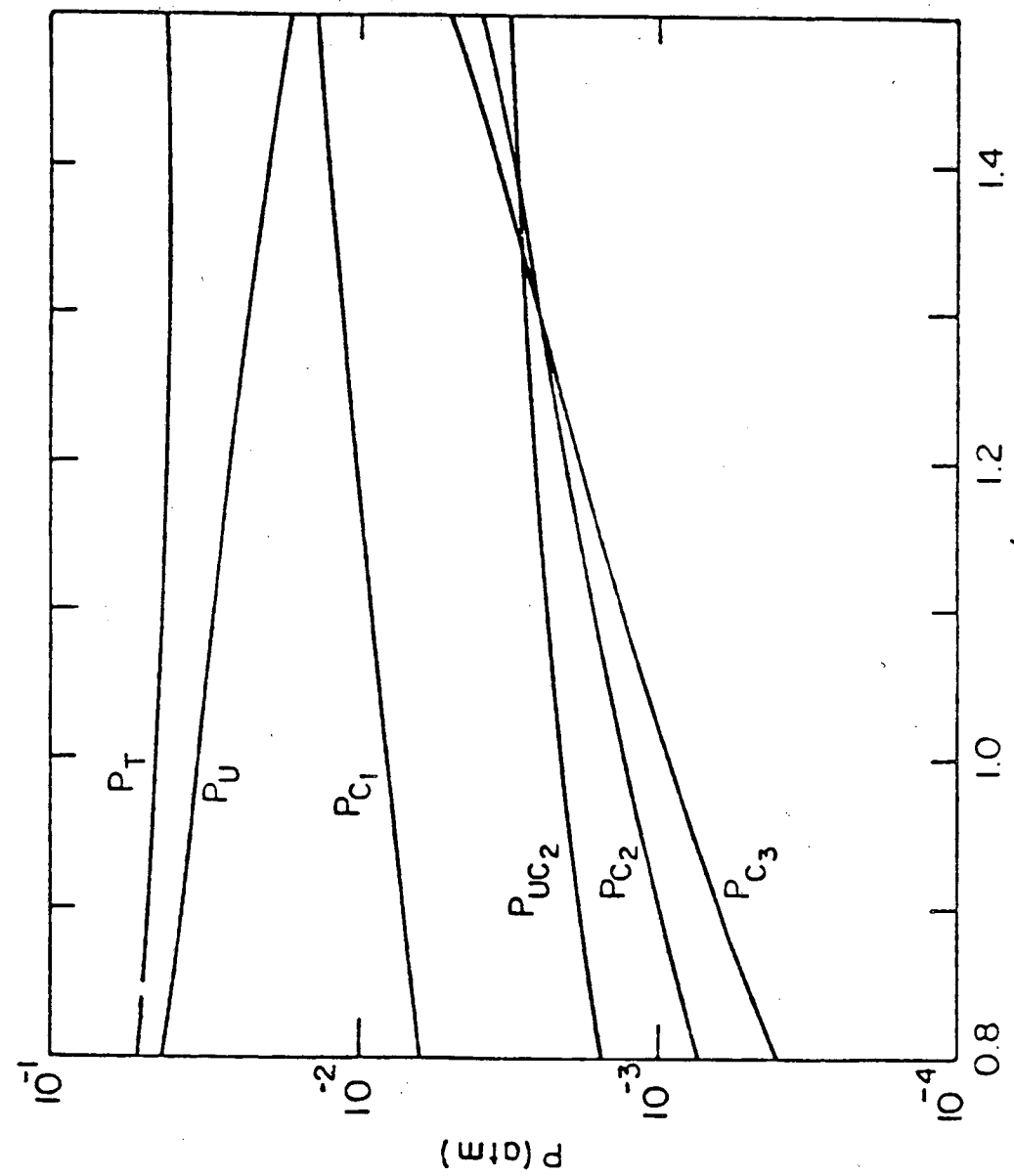

Fig. 2-2. Partial pressures of different species as a function of composition at 4000 K ΔS_m (UC_2) = 6.0 cal/mole-K.

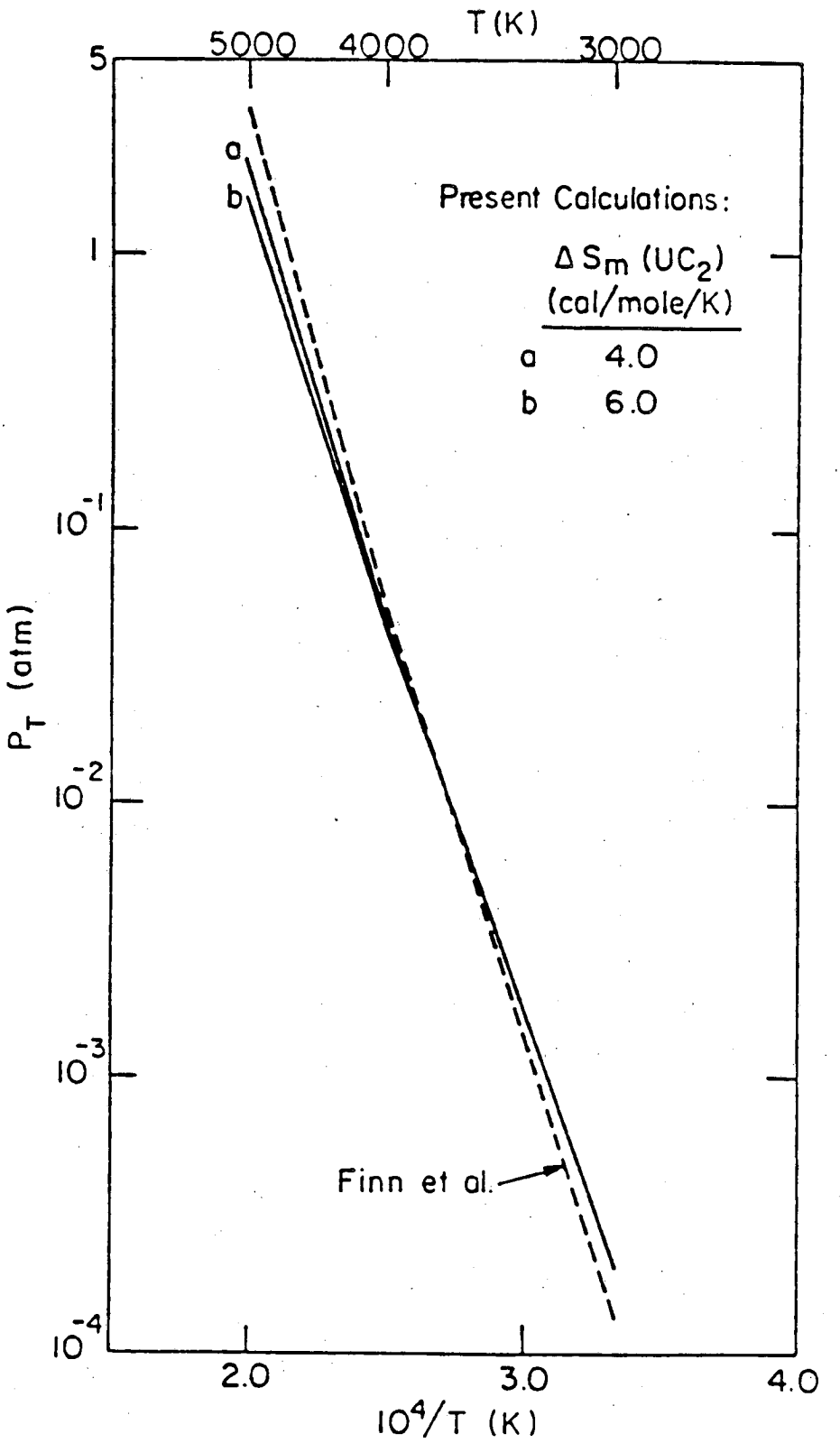

XBL819-6545

Fig. 2-3. Total vapor pressure over liquid $UC_{1.0}$ as a function of temperature.

II.2. Temperature Calculations

The surface temperature of the target subjected to a laser pulse is calculated by simultaneously solving the heat conduction and carbon diffusion equations. The target is considered as a semi-infinite slab which is irradiated by a laser pulse. For pulsed laser heating the depth of the material heated is much less than the dimensions of the surface area heated. Consequently one dimensional heat conduction, one dimensional ablation (no radial liquid movement) with phase change and one dimensional carbon diffusion are assumed.

II.2.1 Carbon Diffusion Equation

At the beginning of the laser heating (while the sample is still solid) carbon mobility is much greater than uranium mobility and so carbon atoms diffuse through fixed uranium atom Lattice. But after the sample surface melts, carbon and uranium move in opposite direction with equal diffusion coefficients (binary diffusion coefficients in liquid UC). Most of the time during laser heating the sample is in liquid phase.

The equation for conservation of carbon is:

$$\frac{\partial C_c}{\partial t} = - \frac{\partial}{\partial z} J_c \qquad (2\text{-}37)$$

where

C_c = mass concentration of carbon atoms in the sample, g/cm^3

J_c = carbon diffusive flux in the sample, g/cm^2-sec.

To account for the possibility of significant ablation from the surface, the semi-infinite solid ($z > 0$) can be considered to be moving in the negative z-direction at speed v relative to the surface. So we

can make the following coordinate transformation:

$$x = z - vt \tag{2-38}$$

where z is the coordinate from the original surface.

After the coordinate transformation, the carbon conservation equation becomes:

$$\frac{\partial C_c}{\partial t} = - \frac{\partial}{\partial x} J_c + v \frac{\partial C_c}{\partial x} . \tag{2-39}$$

II.2.2 Energy Equation

The general energy equation is

$$\rho C_p \frac{\partial T}{\partial t} - \rho C_p v \frac{\partial T}{\partial x} = - \frac{\partial q}{\partial x} + Q_v \tag{2-40}$$

where ρ = mass density, g/cm^3

T = temperature, Kelvin

q = heat flux, W/cm^2

Q_v = volumetric heat source, W/cm^3.

II.2.3 Carbon Diffusive Flux and Heat Flux

Carbon diffusion equation (2-39) and energy equation (2-40) are interrelated through the two fluxes J_c and q. Neglecting the Soret and Dufour effects, the two fluxes are given by:

$$J_c = - D_c \frac{\partial C_c}{\partial x} \tag{2-41}$$

$$q = - k \frac{\partial T}{\partial x} \tag{2-42}$$

where D_c = diffusion coefficient of carbon in uranium carbide, cm^2/sec

k = thermal conductivity of uranium carbide, W/cm-K.

II.2.4 Initial and Boundary Conditions

Two initial conditions and four boundary conditions are needed in order to solve the two partial differential equations. The initial conditions are:

$$\text{at} \quad t = 0 \qquad T(x,0) = T_0 \text{ and } C_c(x,0) = C_c^\circ \tag{2-43}$$

where T_0 is the target temperature before laser impingement and C_c° is the initial mass concentration of carbon.

The boundary conditions are:

(i) At the moving interphase bounary, x = 0:

As a result of incongruent evaporation, the composition of the material at the surface changes and a concentration gradient is formed inside the uranium carbide sample which causes the transfer of carbon between the bulk and the surface.

The mass balance for carbon at the interphase boundary gives:

$$J_c^d = J_c^g + vC_c^s \quad \text{at } x = 0 \tag{2-44}$$

where J_c^d is the flux of carbon at the surface due to diffusion from the bulk, C_c^s is the concentration of carbon in the solid (liquid) at the surface, J_c^g is the total mass flux of carbon into the gas phase,

$$J_c^g = -(\phi_C + 2\,\phi_{C_2} + 3\,\phi_{C_3} + 2\,\phi_{UC_2})\,M_C \tag{2-45}$$

and v is the surface recession velocity, which is the ratio of the evaporation mass flux of uranium-bearing species J_U^g and the mass concentration of uranium atom in the solid C_U.

$$v = -J_U^g / C_U = (\phi_U + \phi_{UC_2})\,M_U/C_U \tag{2-46}$$

The sign convention is that a flux (mass or heat) is positive if it is in the positive x direction.

The rate of evaporation of species i, ϕ_i is given by Langmuir equation as

$$\phi_i = \frac{(1-\beta)\alpha P_i}{\sqrt{2\pi m_i K T_s}} \tag{2-47}$$

where T_s is the surface temperature, P_i is the equilibrium pressure of species i at the surface composition and temperature and α is the evaporation coefficient. β is the fraction of the molecules back-scattered to the surface in a collision-dominated flow. It has been shown [35-37] that in this type of flow the net rate of evaporation is 82% of the value given by Langmuir equation (i.e. $\beta = 0.18$).

Combining eqs. (2-41) and (2-44), we have:

$$- D_c \left(\frac{\partial C_c}{\partial x}\right)_{x=0} = J_c^g + v\, C_c^s \,. \tag{2-48}$$

The heat flux in the solid at the interphase boundary is balanced by the heat loss carried by evaporation, the radiation heat loss and the heat flux input from the laser (for surface absorption only), i.e.,

$$(q)_{x=0} = - \sum_i M_i \phi_i \Delta H_i^v - \epsilon_t \sigma (T_s^4 - T_b^4) + Q_s \tag{2-49}$$

where ΔH_i^v = heat of vaporization of species i, J/g

T_b = the ambient temperature (usually room temperature), K

ϵ_t = total hemispherical optical emissivity

σ = Stefan-Boltzmann constant

and Q_s = surface heat source, W/cm^2.

Combining eqs. (2-43) and (2-50), we have:

$$-k\left(\frac{\partial T}{\partial x}\right)_{x=0} = -\sum_i M_i\phi_i\Delta H_i^v - \varepsilon_t\sigma(T_s^4 - T_b^4) + Q_s \qquad (2\text{-}50)$$

(ii) Far from the surface, $x = \infty$

$$T(\infty,t) = T_0 \text{ and } C_c(\infty,t) = C_c^\circ \qquad (2\text{-}51)$$

II.2.5 Carbon Diffusion and Heat Conduction Equation

Substituting the fluxes, eqs. (2-41) and (2-42), into the partial differential equations (2-39) and (2-40), we obtain the two boundary value problems to be solved for T and C_c:

$$\frac{\partial C_c}{\partial t} = \frac{\partial}{\partial x}\left(D_c\frac{\partial C_c}{\partial x}\right) + v\frac{\partial C_c}{\partial x} \qquad (2\text{-}52)$$

$$\frac{\partial T}{\partial t} = \frac{1}{\rho C_p}\frac{\partial}{\partial x}\left(k\frac{\partial T}{\partial x}\right) + v\frac{\partial T}{\partial x} + \frac{Q_v}{\rho C_p} \qquad (2\text{-}53)$$

I.C.: $T(x,0) = T_0$ and $C_c(x,0) = C_c^\circ$ at $t = 0$ (2-54)

B.C.: $$k\left(\frac{\partial T}{\partial x}\right)_{x=0} = \sum_i M_i\phi_i\Delta H_i^v + \varepsilon_t\sigma\left(T_s^4 - T_b^4\right) - Q_s \qquad (2\text{-}55)$$

$$D_c\left(\frac{\partial C_c}{\partial x}\right)_{x=0} = -\left(J_c^g + vC_c^s\right) \qquad (2\text{-}56)$$

$$T(\infty,t) = T_0 \text{ and } C_c(\infty,t) = C_c^\circ \qquad (2\text{-}57)$$

Physical properties of the solid and liquid are taken to be independent of carbon concentration. The ablation heat term $\sum_i M_i\phi_i\Delta H_i^v$ is approximated by $J_{tot}\Delta H_{vap}$, where ΔH_{vap} is the heat of vaporization of UC and J_{tot} is the sum of $M_i\phi_i$ for all vapor species.

Since we are interested in the carbon-to-uranium ratio, C/U, rather than the carbon concentration, C_c, we define the former by:

$$r = \frac{C_c/M_c}{C_U/M_U} \qquad (2\text{-}58)$$

We also assume that all the laser energy is absorbed at the surface

(i.e. $Q_v = 0$). The surface heat source, Q_s, used in the boundary condition is expressed as $(1-R)Q_i(t)$, where R is the reflectivity of the surface to the laser light and $Q_i(t)$ is the laser power density incident on the surface at time t.

With the above simplifications and variable change, Eqs. (2-52) to (2-57) can be written as:

$$\frac{\partial r}{\partial t} = \frac{\partial}{\partial x}\left(D_c \frac{\partial r}{\partial x}\right) + v \frac{\partial r}{\partial x} \tag{2-59}$$

$$\frac{\partial T}{\partial t} = \frac{1}{\rho C_p} \frac{\partial}{\partial x}\left(k \frac{\partial T}{\partial x}\right) + v \frac{\partial T}{\partial x} \tag{2-60}$$

I.C.: $T(x,0) = T_0$ and $r(x,0) = r_0$ (2-61)

B.C.: $$\left(\frac{\partial T}{\partial x}\right)_{x=0} = \frac{\Delta H_{vap}}{k_s} \sum_i M_i \phi_i + \varepsilon_t \sigma (T_s^4 - T_b^4) - (1-R)Q_i(t) \tag{2-62}$$

$$\left(\frac{\partial r}{\partial x}\right)_{x=0} = -\frac{1}{D_c} \frac{M_U}{C_U} \left[\left(\phi_C + \phi_{C_2} + \phi_{C_3} + 2\phi_{UC_2}\right) + \left(\phi_U + \phi_{UC_2}\right) r_s\right] \tag{2-63}$$

$$T(\infty,t) = T_0 \text{ and } r(\infty,0) = r_0. \tag{2-64}$$

Due to nonlinearities resulting from the temperature-dependent thermal properties, the connective-like term appearing from coordinate transformation and the nonlinear boundary conditions containing temperature dependent ablative and radiation heat loss terms, analytical solution is not possible. This problem has been dealt with for ZrH by Olstad [38,39] and for UQ_2 by Tsai [10]. In both cases finite difference methods [40-40] have been used to numerically solve the problem. Tsai [10] has developed a program called STAR which solves one dimensional time-dependent heat conduction and diffusion equations considering melting, moving boundary, ablation, and radiation heat

losses. This program is used to solve Eqs. (2-59) and (2-60) along with Eqs. (2-61) to (2-64) as initial and boundary conditions.

II.2.6 Sample Calculations for UC

The thermal properties of the material along with the laser pulse characteristics (energy, power shape, effective area) described in Section III.2.1 are used as input to the program. The output consists of the surface temperature and composition as a function of time and temperature and composition profile in the sample at maximum surface temperature.

The thermal properties of UC in the solid phase are very well established. In the liquid phase, however, information on these properties is rare. The vapor pressure as functions of temperature and composition in the liquid phase was calculated in Section II.1. For other properties like thermal conductivity and emissivity the best recommended values were used. Table 2-3 shows the values of the thermodynamic properties for solid and liquid uranium carbide which were used in the computer program.

Figure 2-4 shows the normalized laser power shape, which is independent of laser pulse energy. The effective width of this pulse, defined in Section III.2.1.1, is calculated to be 0.18 msec. The calculations are for a 12J laser pulse. Using the effective pulse width given above in Eq. (3-5) along with an effective area of 0.2 cm^2 obtained in Section III.2.1.2 results in a peak power density Q_i^{max} of 3.3×10^5 W/cm^2. The initial C/U ratio and temperature of the sample are taken as 1.05 and 1800 K respectively.

Table 2-3. Material properties used in computer code (STAR)

Material Properties	Value used*	temp. range, K
Melting point, T_m (K)	2780	
Density, ρ (g/cm^3)	$\rho = 13.5[1-3.9\times10^{-5}(T-300)]$	$T<T_m$
	$\rho = 12.57/(1+9.98\times10^{-5}T)$	$T>T_m$
Thermal conductivity, k (W/cm-K)	$k = 0.2169-3.0372\times10^{-5}(T-273) + 3.6065\times10^{8}(T-273)^2$	$323<T<973$
	$k = 0.2019+1.4785\times10^{-5}(T-273)$	$973<T<2780$
	$k = 0.2048$	$T>2507$
Specific heat, C_p (W/mole-K)	$C_p = 61.5589-2.2349\times10^{-3}T+4.1763\times10^{-6}T^2 -9.9471\times10^{5}/T^2$	$300<T<2780$
	$C_p = 49.839+7.7869\times10^{-3}T$	$T>2780$
Heat of sublimation, ΔH_s (J/g)	2090	
Heat of Fusion, ΔH_f (J/g)	195	
Diffusion coefficient, D_c (cm^2/sec)	$D_c = 0.02\ \exp(-25252./T)$	$T<2780$
	$D_c = 0.114\ \exp(-2.33\times10^{4}/T)$	$T>2780$
Total emissivity, ϵ_t	0.5	
Reflectivity, R	0.5	
Partial pressures of Different species (atm)	Equations derived in Section II.1	
Evaporation coefficient, α	Assumed to be unity	

*All values except for the partial vapor pressures are taken from Appendix A.

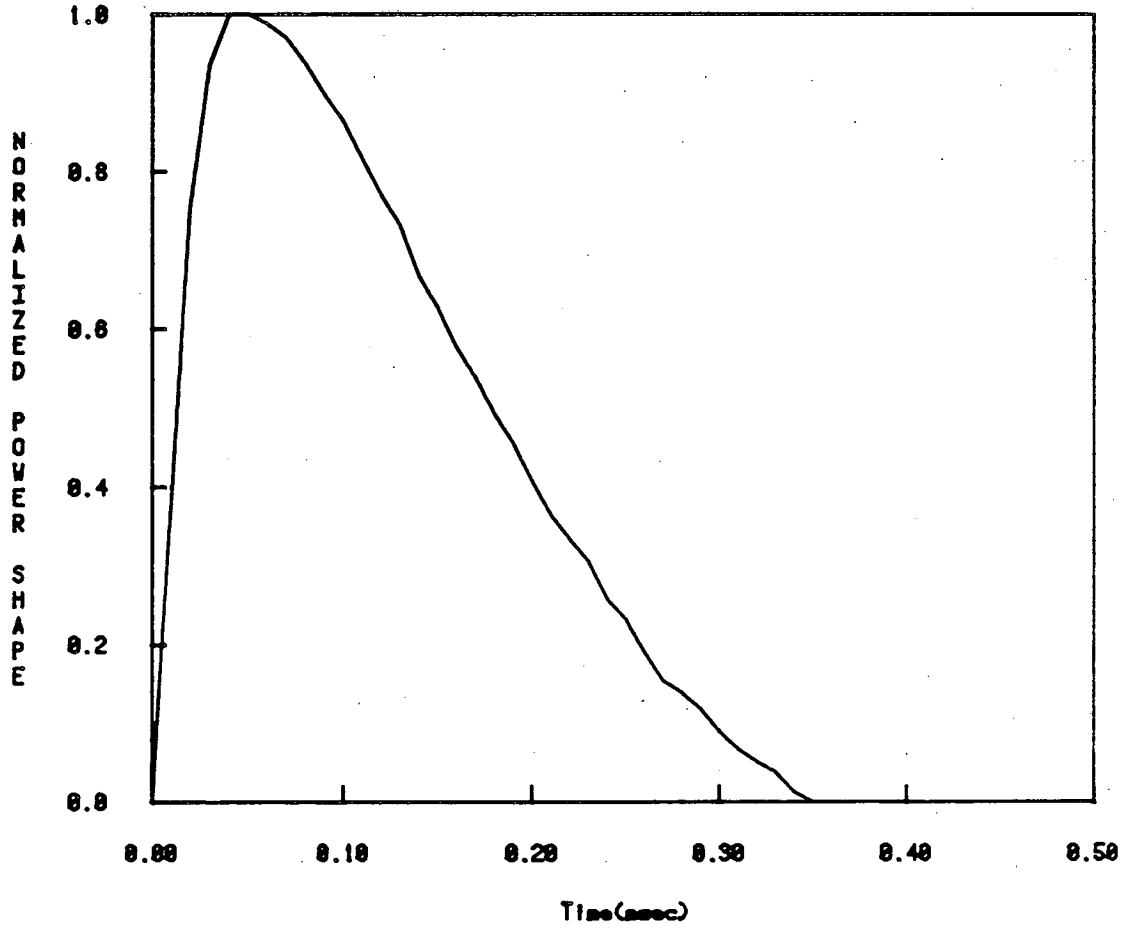

Fig. 2-4: Normalized Laser Power Shape

Figure (2-5) and (2-6) show the surface temperature and C/U ratio at the surface, respectively. The surface temperature starts increasing at the beginning of the laser pulse and goes through a maximum at about .15 msec. Cooling of the surface to the initial temperature occurs in few milliseconds. As Fig. (2-6) shows, due to preferential vaporization of uranium at low temperatures, the C/U ratio first increases. At higher temperatures however, due to the shift in the congruently vaporizing composition to lower C/U ratios, the surface becomes uranium-rich. Because of diffusion of carbon from the bulk to the surface, the composition returns to its initial composition. Figures (2-7) and (2-8) show the temperature profile and composition profile respectively at the time of maximum surface temperature.

II.2.7 Sensitivity Analysis

Because of uncertainty in the material properties in the liquid phase, a sensitivity analysis is used to study the effect of some of these uncertainties on the temperature calculation described in the previous section. This analysis is based on the Response Surface Method (RMS) [45,46]. This method utilizes a systematic sampling of the true surface response (outputs of the code) which is approximated by a polynomial equation in the input variables. The coefficients of the polynomial are calculated using the computer outputs. Then the mean and variance are calculated from the coefficients of the polynomial. The details of the RSM are presented in appendix B, so only a brief description of the procedure will be given here.

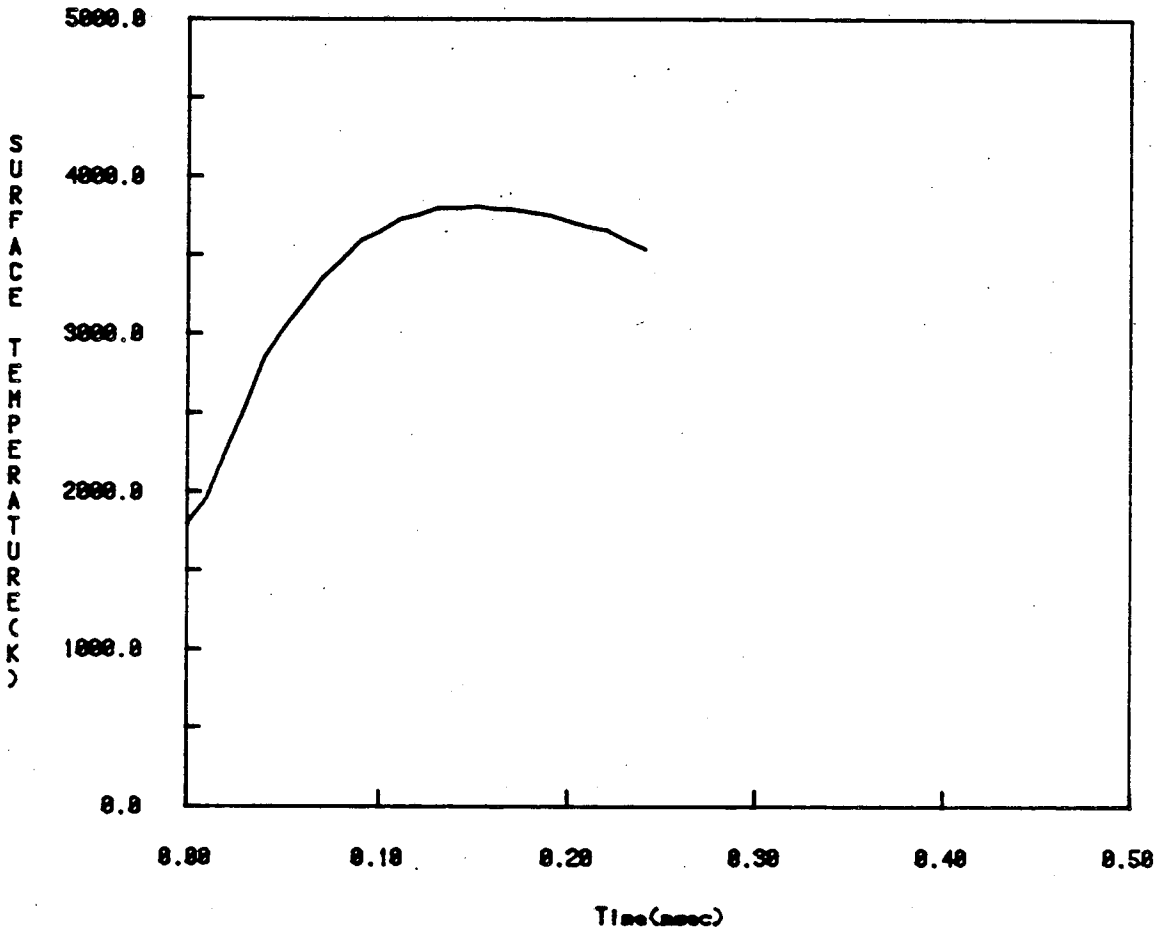

Fig. 2-5: Surface Temperature Transient For E=12. Joules

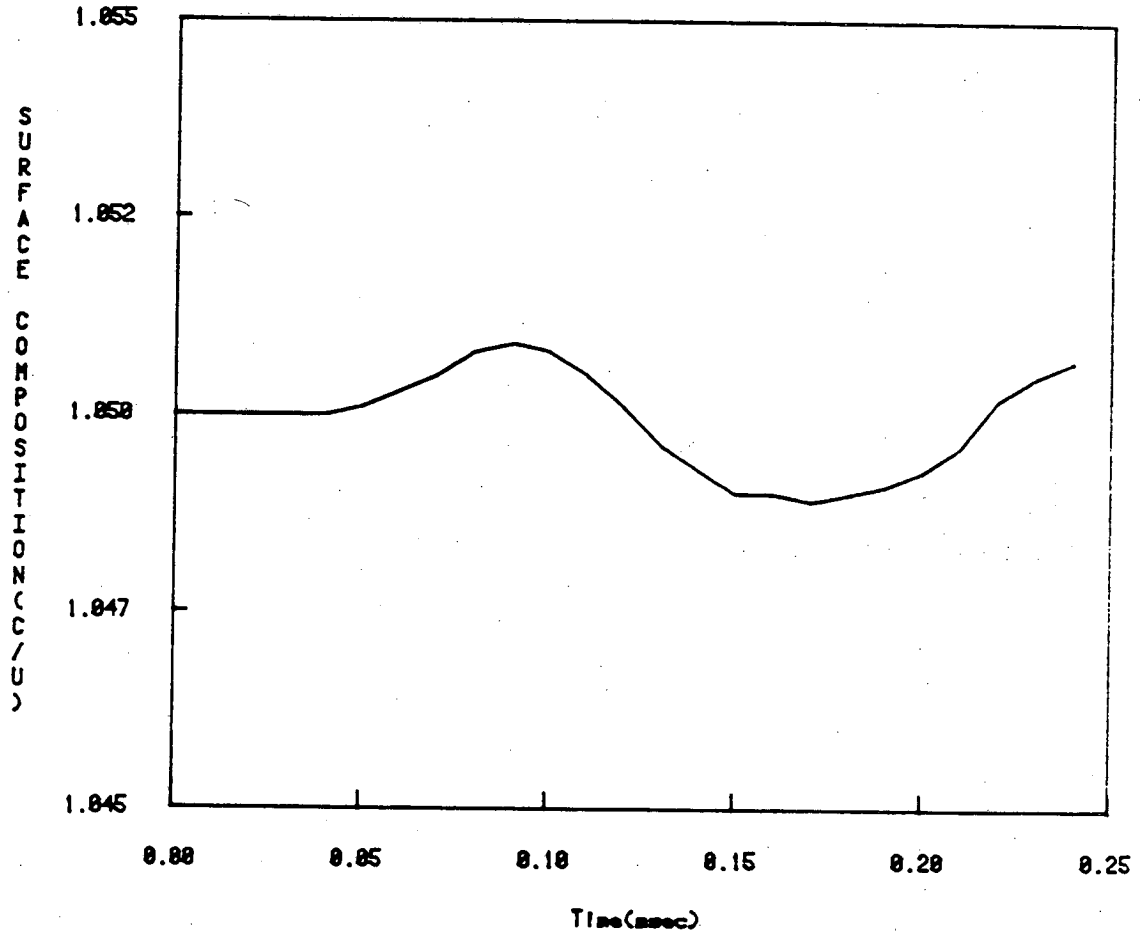

Fig. 2-6: Surface Composition Transient For E=12. Joules

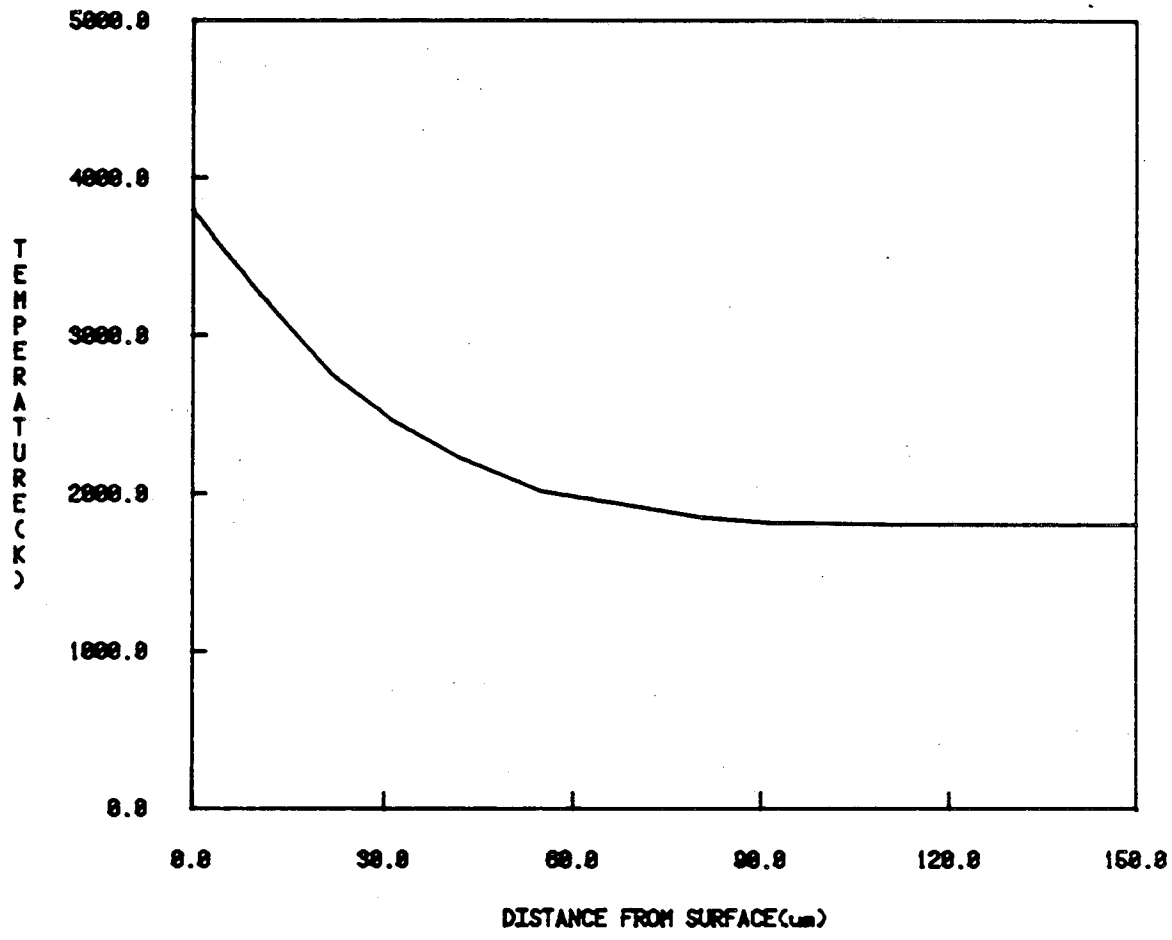

Fig. 2-7: Temperature Profile In The Sample at Maximum Surface Temperature For E=12. Joules.

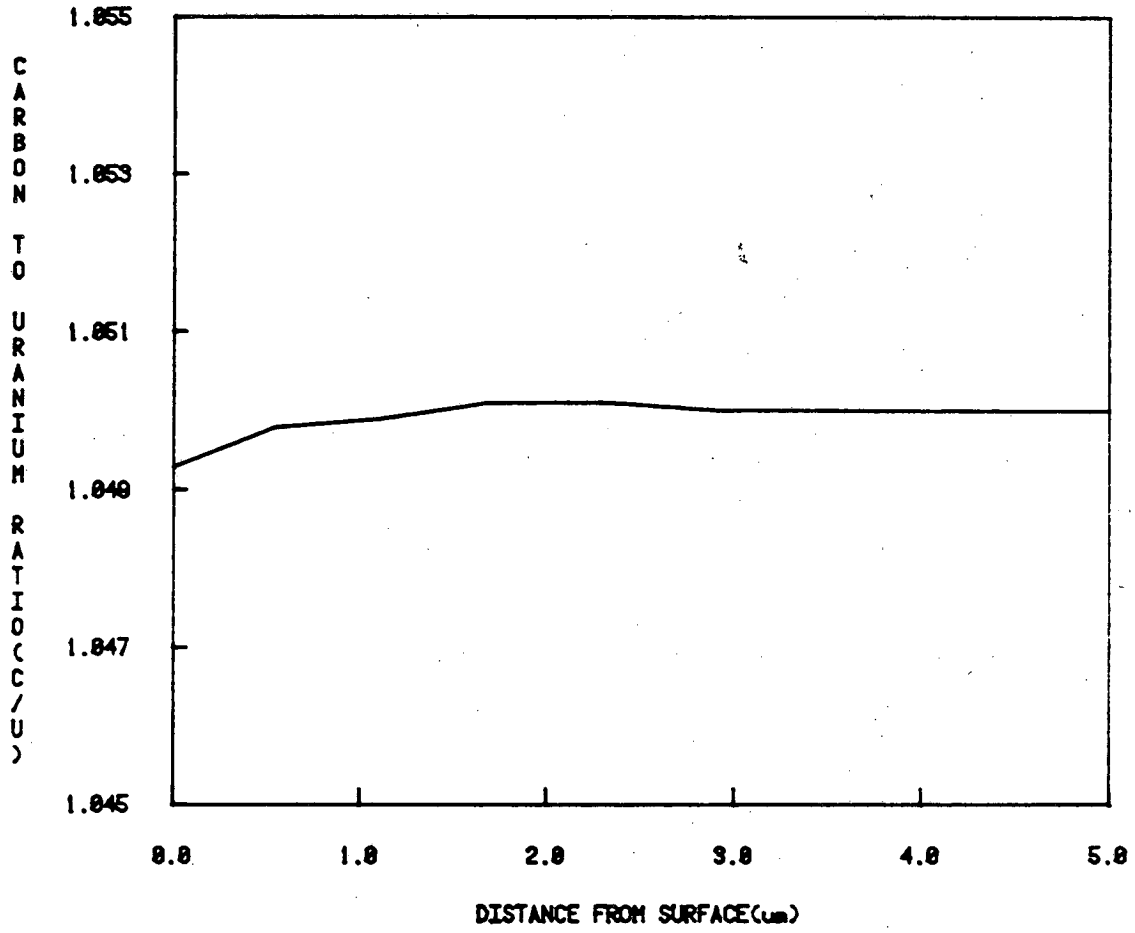

Fig. 2-8: Carbon-to-Uranium Ratio Profile at Maximum Surface Temperature For E=12. Joules

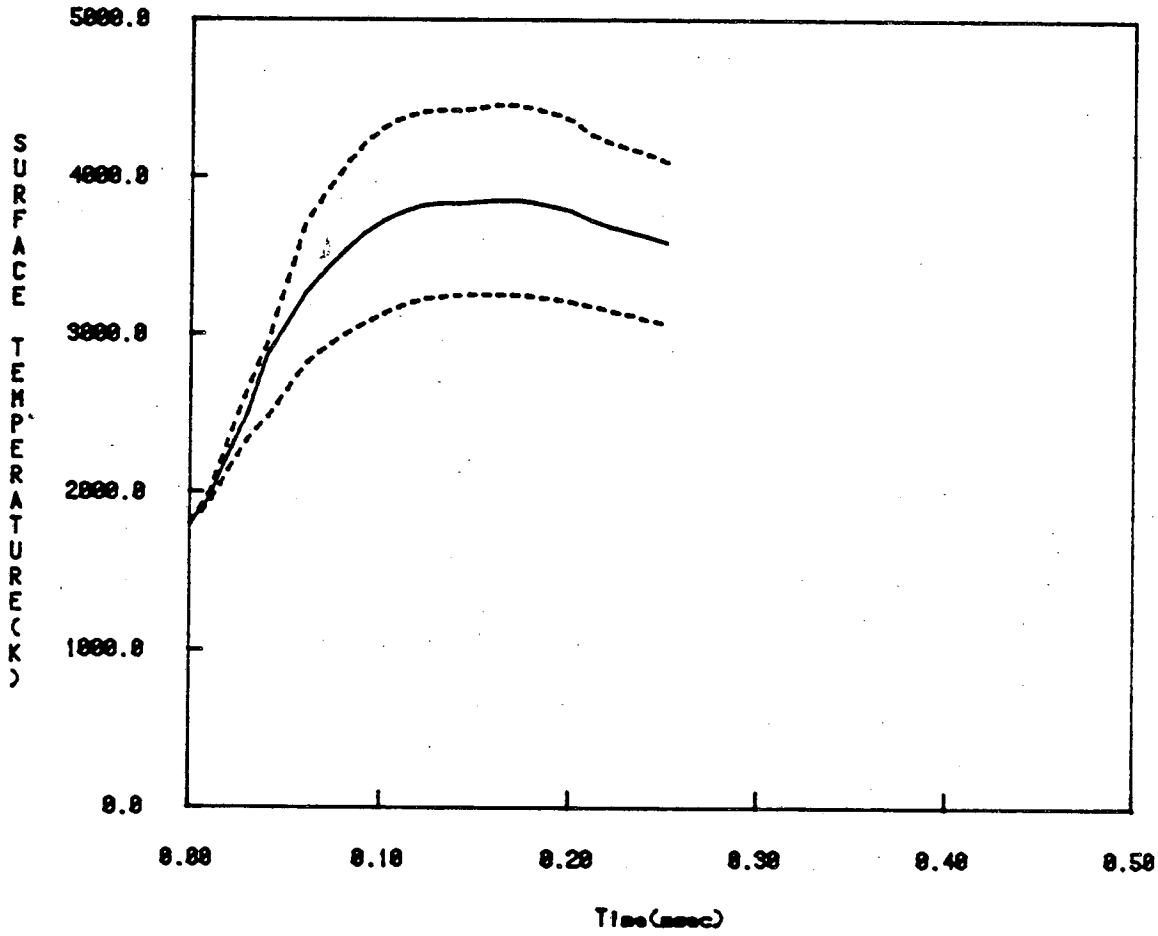

Fig. 2-9. Mean and variance of surface temperature transient for E = 12.0 J from sensitivity analysis.

——— mean value
---------- lower limit and upper limit

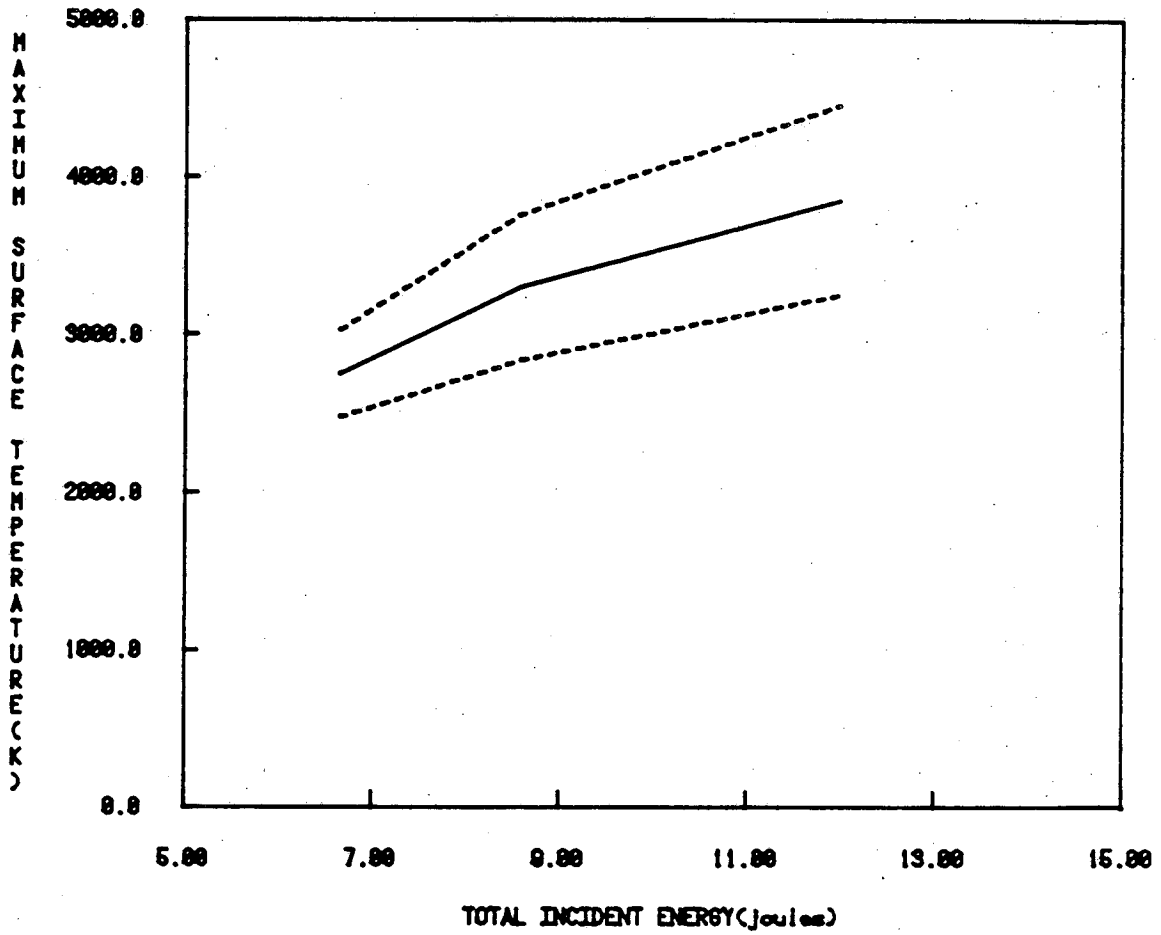

Fig. 2-10. Mean and variance of the max. surface temperature vs. incident laser energy.

The three input variables which are deemed uncertain in the analysis are the thermal conductivity (k), the reflectivity (R) and the effective area (A_{eff}) defined in Section III.2. Table (2-4) shows all of the combinations of these three input variables as well as the laser energies used in different computer runs. The surface temperatures obtained in different runs are used in eq. (B-8) of Appendix B to calculate the coefficients C_1, C_2, C_3, C_{12}, C_{13} and C_{23}. The mean, variance and fractional contributions of each of the three input variables to the response variance are then calculated using these coefficients in eqs. (B-9) - (B-11). For each of the three input laser energy values, Table (2-5) shows the mean and variance of the maximum surface temperature along with the fractional contributions of the three input variables, k, R and A_{eff}. Note that the reflectivity, R is the major contributer to the variance. The contribution of the effective area, A_{eff} is important at low energy values and decreases as energy increases, whereas the thermal conductivity, k has the opposite effect. The table also shows that there is 10-15% uncertainty in the temperature calculations with the recommended values of the input parameters (Table 2.3). Figure (2-9) shows the mean and variance of the surface temperature transient for a 12J laser pulse. The mean and variance of the maximum surface temperature as a function of laser energy are shown in Fig. (2-10).

II.3 Calculated Number Density of Molecules at the Ionizer

The molecular density along the centerline of the expansion depends upon the rate of vaporization, the angular distribution and the speed distribution of the molecules. The net rate of evaporation and

Table 2-4. Input variables of sensitivity study for UC vaporation.

Run No.	E_i (J)	Input Variables x_1 (a)	x_2 (b)	x_3 (c)
I-1		+1	+1	+1
I-2		-1	+1	-1
I-3		+1	-1	+1
I-4	6.7	-1	+1	+1
I-5		-1	-1	-1
I-6		-1	-1	+1
I-7		+1	+1	-1
I-1		+1	+1	+1
I-2		-1	+1	-1
I-3		+1	-1	+1
I-4	8.6	-1	+1	+1
I-5		-1	-1	-1
I-6		-1	-1	+1
I-7		+1	+1	-1
I-1		+1	+1	+1
I-2		-1	+1	-1
I-3		+1	-1	+1
I-4	12.0	-1	+1	+1
I-5		-1	-1	-1
I-6		-1	-1	+1
I-7		+1	+1	-1

(a) $x_1 = +1$: $k = 0.246$ W/cm-K; $x_1 = -1$: $k = 0.164$ W/cm-K

(b) $x_2 = +1$: $R = 0.60$; $x_2 = -1$: $R = 0.40$

(c) $x_3 = +1$: $A_{eff} = 0.22$ cm^2; $x_3 = -1$: $A_{eff} = 0.18$ cm^2

Table 2-5. Measured variance of the response from the STAR code.

Energy (J)	Maximum Surface Temp(K)		Contribution(%)		
	Mean	Variance	k	R	A_{eff}
6.66	2755	281	1	63	36
8.58	3299	462	27	62	11
12.00	3852	586	31	57	12

the features of the expansion depend upon whether the vapor leaves the surface in free-molecule flow or as a collision-dominated flow.

II.3.1 Free Molecule Flow

In a free molecule flow, the angular distribution varies as cosθ, where θ is the angle from the surface normal and the speed distribution is that of a Maxwell-Boltzmann gas at the instantaneous temperature of the surface. The molecular density at the ionizer of the mass spectrometer in a transient evaporation of a target with surface temperature of $T_s(t)$ located at a distance ℓ from the ionizer has been derived by Olstad [38,39]:

$$n(t) = \frac{\alpha A_s}{K} \left(\frac{m}{2\pi K}\right)^{3/2} \int_0^t \frac{P(T_s)}{T_s^{3/2}(t-\tau)^4} \exp\left[\frac{-m\ell^2}{2KT_s(t-\tau)^2}\right] d\tau \quad (2\text{-}73)$$

where α = condensation coefficient (assumed = 1)

ℓ = distance from source to the ionizer (40 cm)

A_s = surface area viewed by mass spectrometer (= 7.9×10^{-3} cm^2).

K = Boltzmann constant

m = molecular mass

P = partial pressure at temperature T_s and surface C/U* ratio

T_s = surface temperature

τ = time of emission of the molecule from the surface

t = time of arrival of the molecule at the ionizer.

---

*The calculations of Section II.2 showed that the changes in surface composition for temperatures up to 4500K are small. So the partial pressures of the species are basically a function of surface temperature only.

The following assumptions have been made in deriving the above equation.

1) The vapor is in thermal equilibrium with the surface.

2) The vaporation is Hertz-Langmiur i.e., the rate of vaporization is given by:

$$\phi = \frac{\alpha P(T_s)}{\sqrt{2\pi m K T_s}} \text{ molecules/cm}^2\text{-sec} \qquad (2\text{-}74)$$

3) The velocity distribution of the vaporizing molecules is Maxwellian.

4) The angular distribution is cosine.

5) The expansion of the flow from the source to the ionizer is collision free.

For a steady state condition such as that used in mass spectrometer calibration, the number density is given by:

$$n = \frac{\alpha A_s P(T)}{4\pi \ell^2 kT} \qquad (2\text{-}75)$$

II.3.2 Collision-Dominated Flow

In the gas dynamic model, the flux from the vaporized solid is divided into three regions (Fig. 2-11). The properties in each are governed by equations characteristic of the type of flow in that region. The regions are related by matching conditions at their boundaries.

Region 1, which is called the Knudsen Layer, has a thickness of the order of a few mean free paths. The molecules leaving the surface possess a Maxwellian velocity distribution in the forward hemisphere at a temperature equal to surface temperature (just as in Langmuir vaporization). However, the distribution of molecules at the outer

boundary of the Knudsen layer differs from Maxwellian due to intermolecular collisions which result in re-establishment of equilibrium at a distance of a few mean free paths from the surface (plane 1 in Fig. 2-11). It has been shown that the limiting hydrodynamic velocity of the vapor in the Knudsen layer is the sonic velocity, which occurs at high surface heat fluxes and in high vacuum.

The second region is the Hydrodynamic Region which starts at the sonic plane. The flow of the vapor in this region resembles that of a supersonic free expansion of a gas from a sonic orifice into a vacuum. Section C.3.2 gives the solution of the hydrodynamic equations along with appropriate boundary conditions determined from the Knudsen layer analysis.

As the vapor moves away from the surface, its density decreases because of expansion. Finally a point is reached beyond which there are no more collisions between molecules. This freezing plane in Fig. 2-11 is discussed in Section C.3.3.

In this type of collision-dominated flow the net rate of evaporation from an area of $A_s cm^2$ is given by:

$$\Phi = \alpha \frac{(1-\beta)P(T_s)A_s}{\sqrt{2\pi mKT_s}} \qquad (2-76)$$

where the backscattering factor β has been calculated to be 0.18 [35,37]. The angular distribution in this type of flow varies as $\cos^2\theta$ and unlike free molecule flow, the molecules vaporized at a particular target temperature will travel with the same speed beyond the freezing plane.

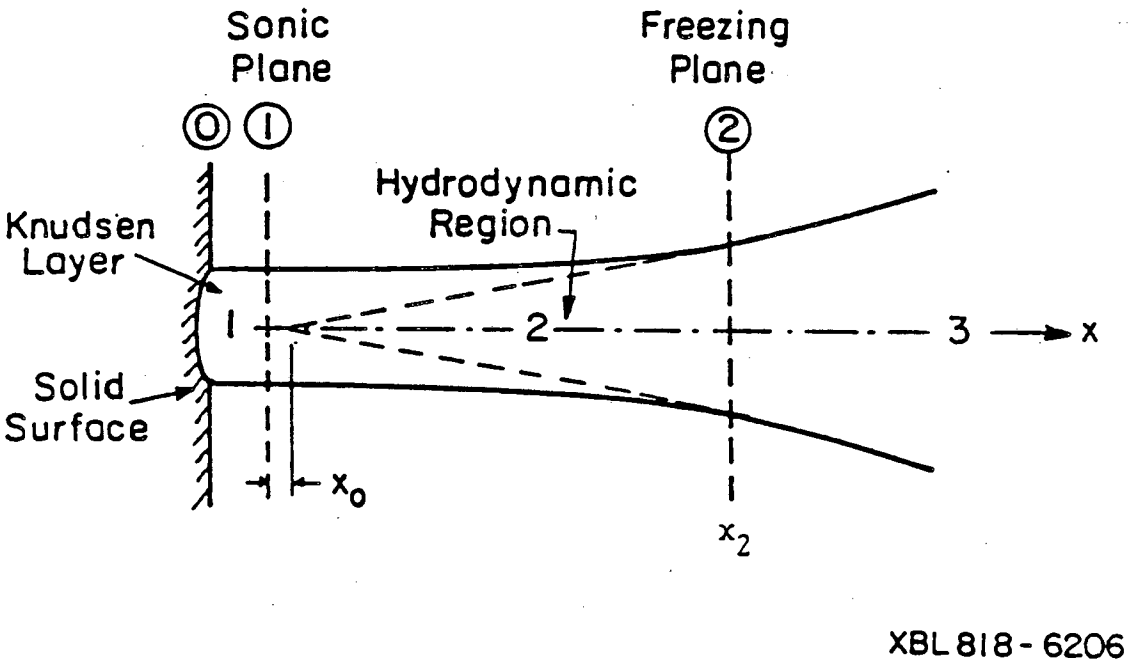

Fig. 2-11: Flow Regions and the Enlarged Knudsen Layer

The number density of the molecules at time t in the ionizer of the mass spectrometer following transient evaporation from a target with surface temperature $T_s(t)$ located at a distance of ℓ from the ionizer is the sum of contributions from all molecules whose transit times satisfy the relation:

$$t_{tr}\,[T_s(\tau)] = t - \tau \tag{2-77}$$

where τ is the time at which molecules depart from the surface. The transit time is equal to ℓ/u_T, where u_T is the terminal velocity of the molecules emitted at surface temperature T_s. The number density is then given as:

$$n(t) = \frac{1}{\ell^2 F}\left\{\frac{\Phi(\tau_1)}{u_T(\tau_1)} + \frac{\Phi(\tau_2)}{u_T(\tau_2)} + \ldots\right\} \tag{2-78}$$

where $\tau_1, \tau_2, \ldots$ are the roots of eq. (2-77) for time t.

$F = 2\pi \int_0^{\pi/2} f(\theta)\,d(\cos\theta)$, $f(\theta)$ being the angular distribution.

The details of the derivation of eq. (2-78) are given in appendix B.

III. EXPERIMENTAL

III.1 Apparatus

III.1.1 Introduction

The experimental apparatus shown in Figs. (3.1) and (3.2) consists of five main components: The laser and equipment for measurement of its power and energy, the target vacuum chamber, the detector vacuum chamber, the optical pyrometer for surface temperature measurement and the transient data recording system.

The entire system was aligned before each experimental run by three He-Ne CW gas lasers as follows.

(i) The position of the electron bombardment heater holding the sample is adjusted so that the beam coming from laser No. 1 through the ionizer of the mass spectrometer and the two collimating apertures hits the center of the target.

(ii) The alignment of the Nd-glass laser with the center of the target surface as well as the alignment of the 100% rear mirror reflector and the 8% plane output reflector in the Nd-glass laser cavity is accomplished by gas lasers No. 2 and No. 3 (the complete alignment procedure is given in Ref. [40]).

(III) The transient optical pyrometer is aligned by focusing through the glass window of the target chamber on the center of the target which is illuminated by gas lasers No. 1 and No. 3.

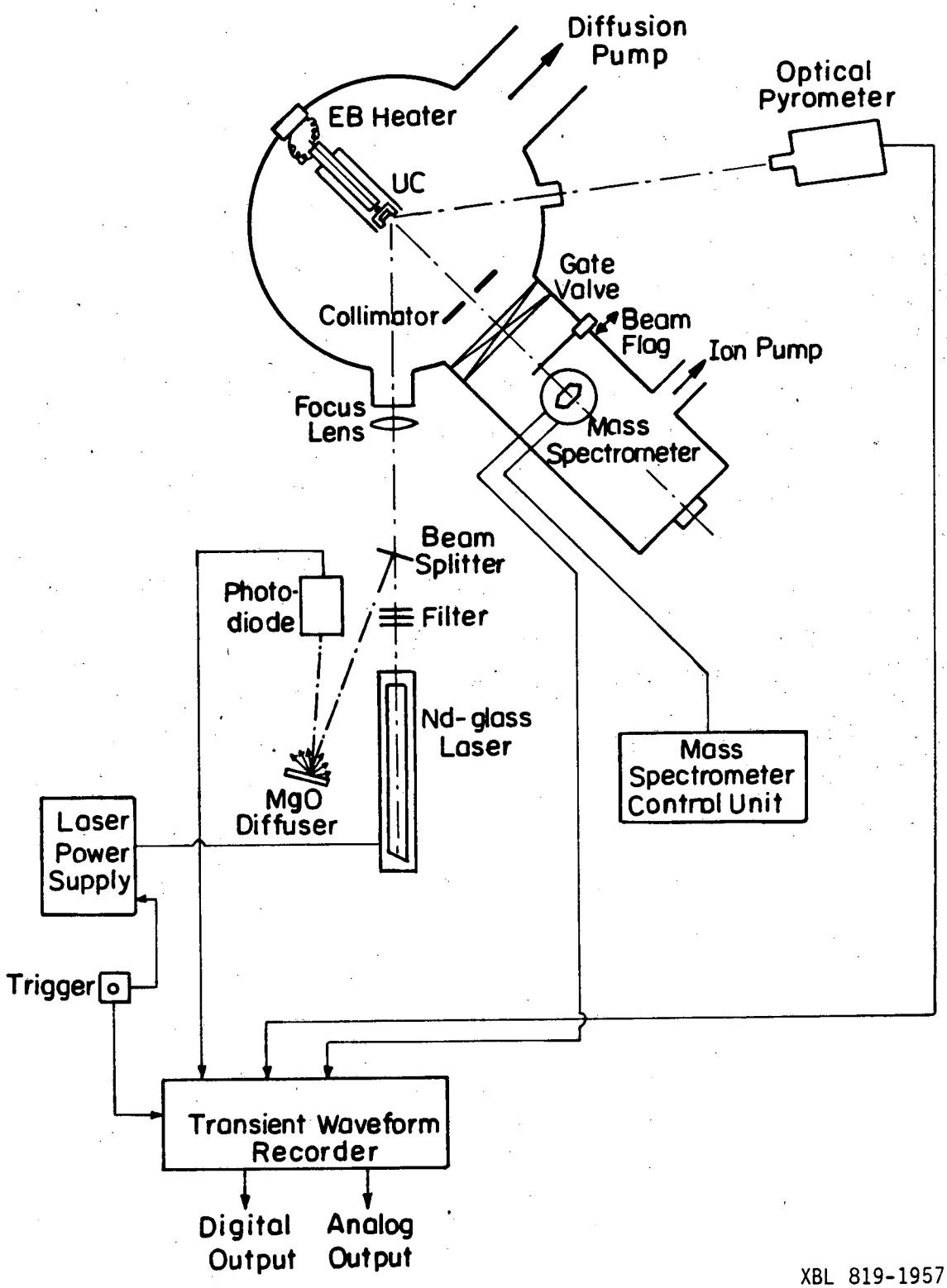

Fig. 3.1. The apparatus setup of the laser-induced vaporization study by mass spectrometry.

CBB 818-7828

Fig. 3-2.

Although the alignment procedure is very difficult and time consuming it can be done quite accurately by using very stable and adjustable Hercules tripods for the gas lasers and the optical pyrometer.

III.1.2 Laser System

The laser used for heating the UC samples is an American Optical 1.06 μm Nd-glass laser with an Owens-Illinois ED-2-3 silicate glass replacement rod doped with 3% Nd^{+3} ions (concentration of $0.91 \times 10^{20}/cm^3$). The rod has a diameter of 1.27 cm and is 50 cm long. The rod length-to-diameter ratio is optimized at 40 for maximum efficiency [40,41]. The rod is cooled on the outside and ends by distilled water. The laser is optically pumped by two linear xenon flashtubes closely coupled to the laser rod with a highly reflective silver reflector. The "conventional" mode is used in the experiment, which means that the laser pulse duration is governed by the flash discharge duration (~ 200 μsec). The laser output energy used is about 15 J and the energy deposited on the target is varied by a set of neutral density filters placed immediately after the output reflector. The measured beam divergence is about 12 milliradians and the spot size on the target, after passing through a 100 cm beam correcting lens and a 20 cm focusing lens, is an ellipse with minor and major diameters of ~ 2 mm and 2.5 mm, respectively. The laser beam is partially split to a MgO diffuser and detected by a calibrated Korad KD-1 photodiode whose signal is recorded by the Biomation 1015 transient recorder (to be described later). This gives the laser energy and power as a function of time.

III.1.3 Target Chamber

The target chamber is pumped to 10^{-7} Torr by a 500 liters/sec, 6 inch NRC vacuum diffusion pump with a Granville-Phillips liquid nitrogen cold trap. The uranium carbide target is held on a tungsten cap on the head of an electron bombardment heater. The electron bombardment heater shown in Fig. (3-3) is mounted on a rotary feedthrough fixed on the vacuum flange so that the target can be rotated after each shot to provide fresh area for subsequent laser pulses. Each sample is heated by electron bombardment to 1800 K (uranium carbide is plastic at this temperature [42]) in order to avoid cracking resulting from the large thermal stress induced by laser heating.

Two collimating apertures, one 1 mm diameter located at 10 cm from the target and the other 3.2 mm diameter 20 cm from the target, are positioned along the molecular beam axis to ensure that only the center part of the beam reaches the ionizer of the mass spectrometer in the detection chamber.

A Farady-cup ion detector consisting of a copper cup, a 90 volt battery and a 10 MΩ resistor in parallel with a 20 μf capacitor and a 5Ω resistor is used to detect the ion signals from the partially ionized gas ejected from the laser-heated target. A stainless steel grid with an adjustable positive voltage is used to separate the thermal electrons emitted from the target from the positive ions. Two metal plates are mounted on feedthroughs on each side of the chamber to protect the glass windows for laser beam entry and for temperature measurement from being coated during steady state heating of the sample. They are removed by feedthroughs prior to laser pulsing.

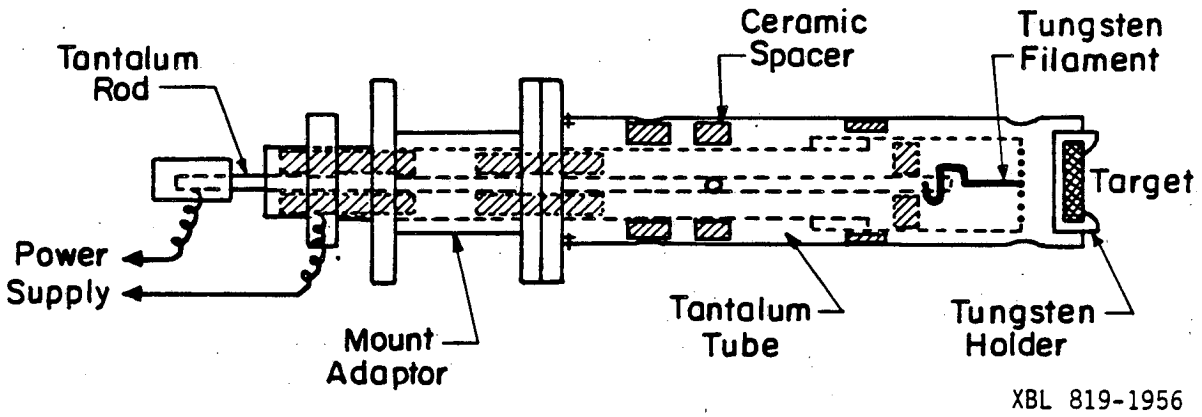

Fig. 3.3 Electron beam bombardment heater.

III.1.4 Detector Chamber

The detector chamber is pumped by a 200 liter/sec ULTEK ion pump and a Varian titanium sublimation pump. With the gate valve closed, the detector chamber is kept under a vacuum of ~ 10^{-10} Torr. During experimental runs with the gate valve open, the pressure increases to 10^{-8} torr range. The mass spectrometer ionizer is located 40 cm from the target. A beam flag mounted on a linear feedthrough is positioned between the collimating aperture and the ionizer. The beam flag is used for blocking molecules emitted from the target or the Knudsen cell to measure the background signal when calibrating the mass spectrometer by steady state vaporization of UC.

The detector is an EAI Quad 250 quadrupole mass spectrometer with its axis perpendicular to the molecular beam path (i.e. perpendicular to the normal to the target surface). The detector is molecular density sensitive. A small percentage (< 0.01%) of the molecular beam passing through the ionizer is ionized by the electrons emitted from one of the two tungsten filaments. Some of the ions are then accelerated by the ion potential at the entry of the quadrupole structure and focused by an electrostatic lens into the quadrupole section. The quadrupole as a mass filter applies R. F. and D. C. fields which allows only ions within a specific range of charge-to-mass ratio to achieve stable orbits and thereby reach the end of the structure and be detected by a Bendix electron multiplier. The current signal produced at the electron multiplier output is recorded in one of the channels of the transient waveform recorder.

III.1.5 Optical Pyrometer

The target surface temperature is measured by a PYRO "photomatic I" automatic optical pyrometer manufactured by Pyrometer Instrument Company, Inc. The instrument consists of two parts: (1) The optical unit which consists of a high sensitivity photomultiplier tube, an interference filter for wavelength of 6500 ± 100 Å, a high voltage power supply and preamplifier, a set of three range filters, an objective lens, a reference standard lamp and a modulating oscillator, (2) The electronic unit which consists of a temperature indicating meter, scale range selector and indicator lights, function switch knob, a null balance control, a recorder jack and a controller jack [43]. The two units are connected by a cable.

The pyrometer has two modes of operation; automatic and transient. The automatic mode was used for preheating when steady state temperatures were measured. In this mode, it operates on the same principle as the disappearing filament pyrometer except that an auto-adjusting feedback electronic null-balance system replaces the human eye in comparing the target source radiation with the internal reference.

The transient mode bypasses the internal lamp and operates as an optical system coupled directly to a photomultiplier. Since the power supply in the as-received optical unit was not regulated, an external regulated, high stability FLUKE power supply was used in the transient mode operation. In this mode, the unit has a response on the order of nanoseconds, thus easily allowing measurements of temperature transients in the range of milliseconds. The target focusing is adjustable

from 20 cm to infinity. The target diameter was about 1.22 mm. After taking into account the 45° incidence, the major axis of the pyrometric viewing spot was about 1.73 mm. The pyrometer output is recorded by one of the channels of the transient waveform recorder.

III.1.6 Transient Data Recording

A 4-channel transient waveform recorder manufactured by Gould Inc., The Biomation Model 1015, was used to record the signals from the laser power photodiode, the optical pyrometer, the mass spectrometer and the ion detector. It has four input channels each with 1014 words memory capacity so that it can record four different signals simultaneously. The fastest sampling rate of this device is 10 μs/sample (or 100 KHZ). The recorder is started by the same signal which triggers the laser flashtubes. It then samples and digitizes the input signals by A/D converters, and stores the counts in the memory. The signals are then retrieved later through built-in D/A converters by an x-y plotter at a slower rate. A unique capability of this device is its ability to record the signals preceding the trigger time. This "pretrigger recording" feature ensures recording of the leading baseline and the rise of the signal. This device greatly reduces the error inherent in analyzing the photographed signals monitored by an oscilloscope [44].

III.1.7 Specimens

The uranium carbide specimens were provided by Materials Science Division of Argonne National Laboratory. According to ANL, the specimens have a density of 99% of theoretical density and a carbon-to-uranium ratio of ~1.05. The nitrogen and oxygen impurities are

less than 1500 pm. The specimens were kept in a glovebox under argon atmosphere to avoid oxidation. Immediately before the laser experiment, wafers with a diameter of 0.6 cm and thickness of 1.2 mm were cut and polished by silicon carbide abrasives and diamond paste to ~ 6 μm roughness using Hyprez oil as lubricant.

III.2 System Calibration

III.2.1 Laser Parameters

Each laser shot is characterized by i) temporal power shape (ii) radial power distribution and iii) pulse energy. These parameters, which are used as input to the computer code for the calculation of temperatures and compositions in the sample, should be known in each experiment.

III.2.2.2 Temporal laser power shape. The variation of laser power with time is measured by a Korad KD-1 photodiode. This photodiode is calibrated by a Korad K-J2 calorimeter which is precalibrated by the manufacturer. The output of the photodiode is a voltage signal V(+) from which the laser power as a function of time can be obtained in the following way:

The effective pulse width t_{pul} can be written as:

$$t_{pul} = \frac{E}{P_{max}} = \int \frac{P(t)}{P_{max}} dt = \int \frac{V(t)}{V_{max}} dt \qquad (3-1)$$

where E = incident total energy of the pulse in Joules,

$P(t)$ = incident power at time t in watts,

P_{max} = incident maximum power in watts,

$V(t)$ = voltage output of the photodiode at time t,

and V_{max} = maximum output voltage of the photodiode.

The above relation is valid as long as the response of the photodiode is linear. Using the normalized power shape of Fig. (2-4) which is the same for all energies in Eq. (3-1), an effective pulse time (t_{pul}) of 0.18 msec is obtained. The total incident laser energy (E) is obtained from the output signal of the calorimeter. Then Eq. (3-1) yields P_{max}. The incident power at any time t can be obtained from the proportionality of P to V:

$$P(t) = V(t) \frac{P_{max}}{V_{max}} \tag{3-2}$$

III.2.1.2 Radial laser power distribution. The radial power distribution of the laser pulse is needed to determine the peak power density at the center of the beam spot where the surface temperature is measured and from which the mass spectrometer signal arises. The peak power density is also used in the calculation of the temperature profile. The knife-edge technique [10,47,48] is used for this measurement. A sharp-edge razor blade is moved across the focal plane by a micrometer at an angle of 45 degrees and the transmitted energy as a function of blade-edge position is measured with the calorimeter (Fig. 3-4). The transmitted energy curve is then differentiated and fitted to a parabolic distribution, assuming axial symmetry. Figure 3.5 shows the computer fit of the normalized intensity profile $I(r)/I_p$, where I(r) is the energy density at radius r and I_p is the energy density at the center r = 0, $I_p = \int Q_i(t)dt$, $Q_i(t)$ being the central power density at time t.

Since E = total energy of the laser pulse = $\int_0^\infty I(r)2\pi r dr$,

$$\frac{E}{I_p} = \int_0^\infty \frac{I(r)}{I_p} 2\pi r dr = A_{eff} \tag{3-3}$$

where A_{eff}, the effective area defined above is obtained by integrating the normalized intensity profile. For the focused laser spot shown in Fig. 3.5 in which the 45° angle of incidence is already taken into account, A_{eff} is equal to 0.20 cm^2. This is the area which would be illuminated by a spatially uniform laser pulse of power density $Q_i(t)$ and give the total energy in the actual pulse. The mass spectrometer and optical pyrometer viewing spots are also shown in Fig. 3.5. The latter defines the area A_s in Section. II.3.

The central energy density is equal to the ratio of total energy to the effective area, or E/A_{eff}. Since $I_p = \int Q_i(t)dt$,

$$\frac{I_p}{Q_i^{max}} = \int \frac{Q_i(t)}{Q_i^{max}} dt = \int \frac{P(t)}{P_{max}} dt = t_{pul} \tag{3-4}$$

where Q_i^{max} is the maximum (in time) central power density in W/cm^2. Combining Eqs. (3-3) and (3-4) the central maximum power density is

$$Q_i^{max} = \frac{E}{A_{eff}\ t_{pul}} \tag{3-5}$$

This quantity along with the normalized laser power pulse shape (Fig. 2-4) give the power density source $Q_i(t)$ needed in eq. (2.62) for the theoretical calculations.

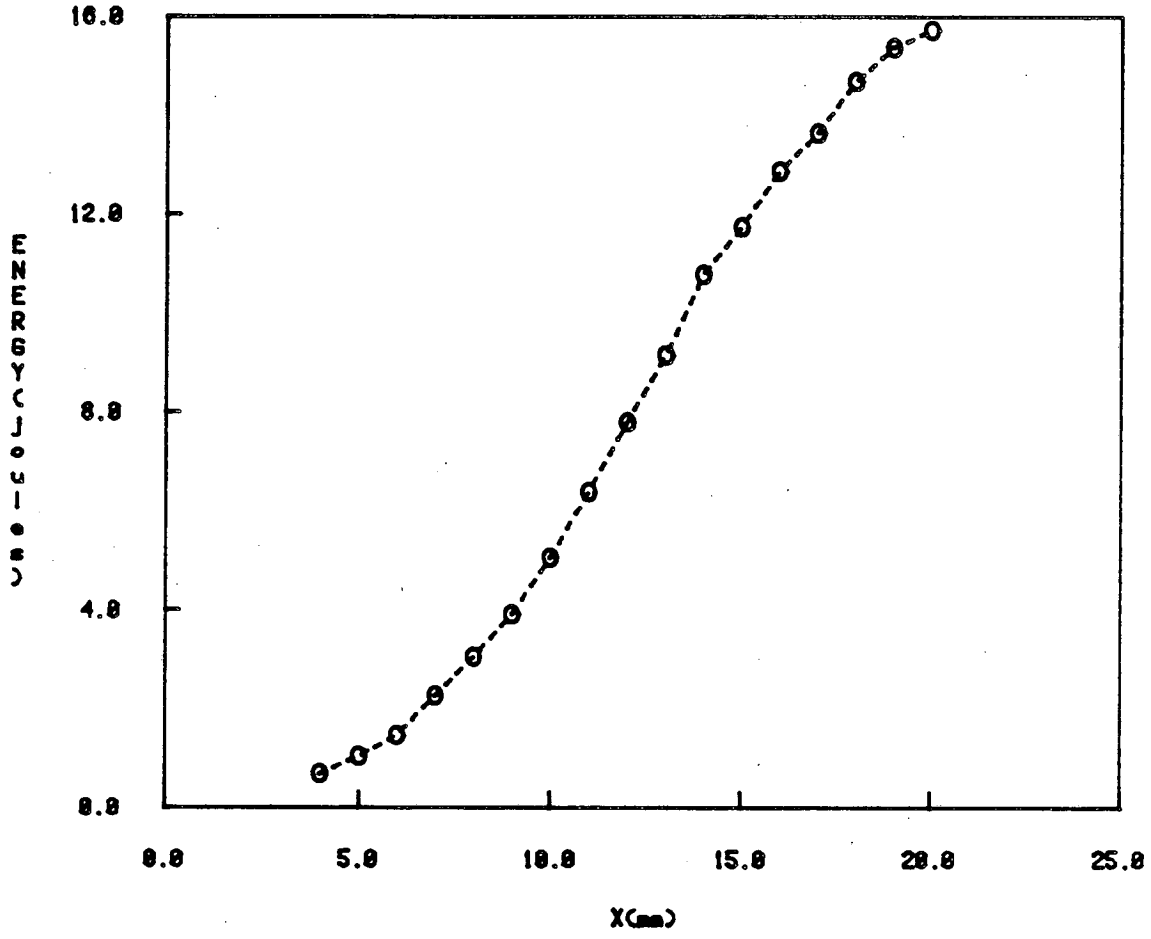

Fig. 3-4. Transmitted energy vs. knife-edge position in laser radial power distribution measurement (x is the knife-edge position in the direction of micrometer motion at 45° to the laser beam path).

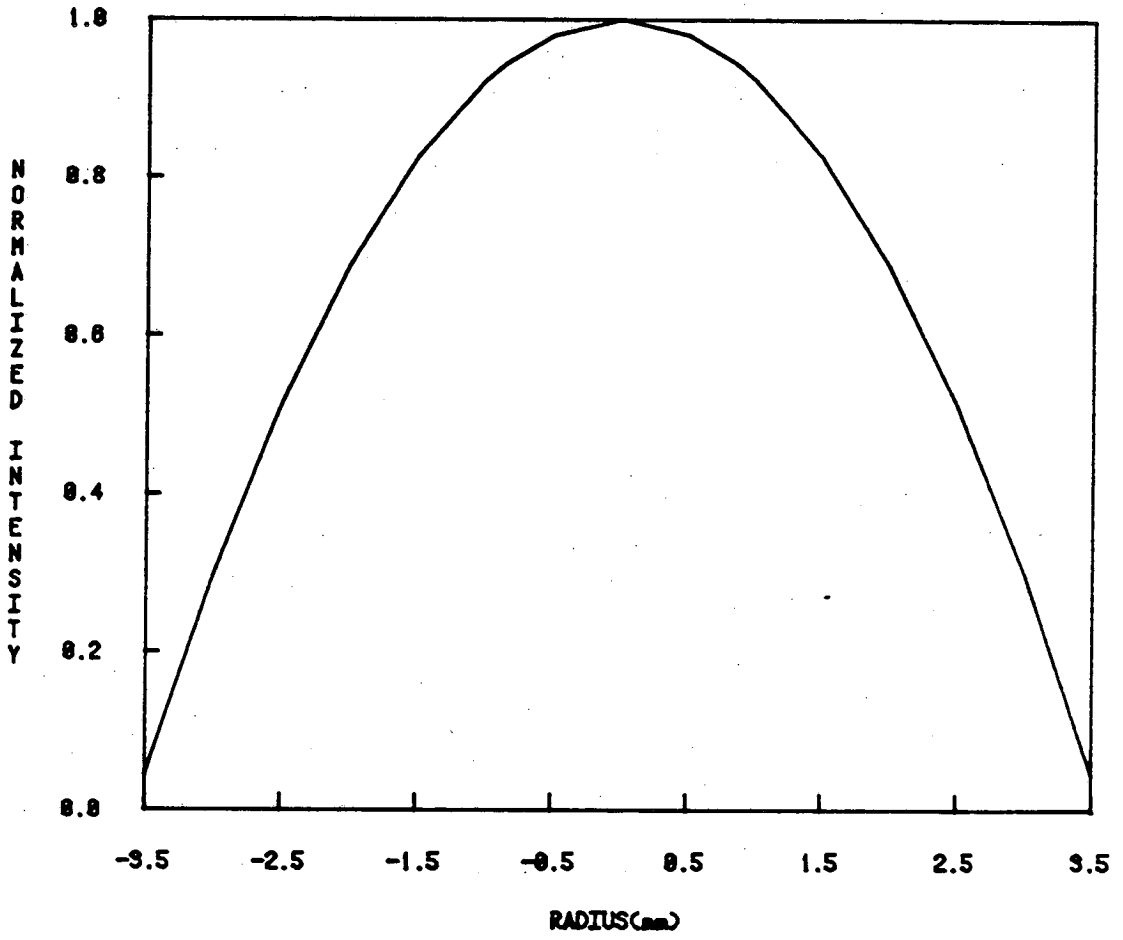

Fig. 3-5. Normalized laser radial power intensity distribution from knife-edge measurement (along major axis).
a: mass spectrometer viewing spot(~1 mm diameter)
b: optical pyrometer viewing spot(~1.73 mm diameter)

III.2.1.3 Incident laser energy. The laser energy before passing through the focusing lens and the target chamber glass window is determined by the measured photodiode signal and the photodiode calibration curve (Fig. 3.6). To obtain the incident laser energy on the target, the measured value should be corrected for absorption by the lens and glass window. The neutral density filters used for varying the pulse energy are placed between the laser front reflector mirror and the beam splitter so that the energy measured from the photodiode output has already accounted for this attenuation factor. So, if E is the energy obtained from the photodiode signal and the calibration curve and τ_{lens} and τ_{window} are the transmissivities of the lens and the glass window, then the incident energy on the target will be

$$E_i = E\tau_{lens}\tau_{window} \tag{3-6}$$

I.2.2 Optical Pyrometer Calibration

The automatic optical pyrometer used for surface temperature measurement was calibrated at NASA-AMES Research Center using a THERMOGAGE and pyrolytic graphite cavity. A manual optical pyrometer calibrated by National Bureau of Standards was used for reading the "true" temperature of the cavity. The output voltage signal from the automatic pyrometer in the transient mode was measured for the second and third scales (two different filters) by a calibrated digital voltmeter for each cavity temperature measured by the standard pyrometer.

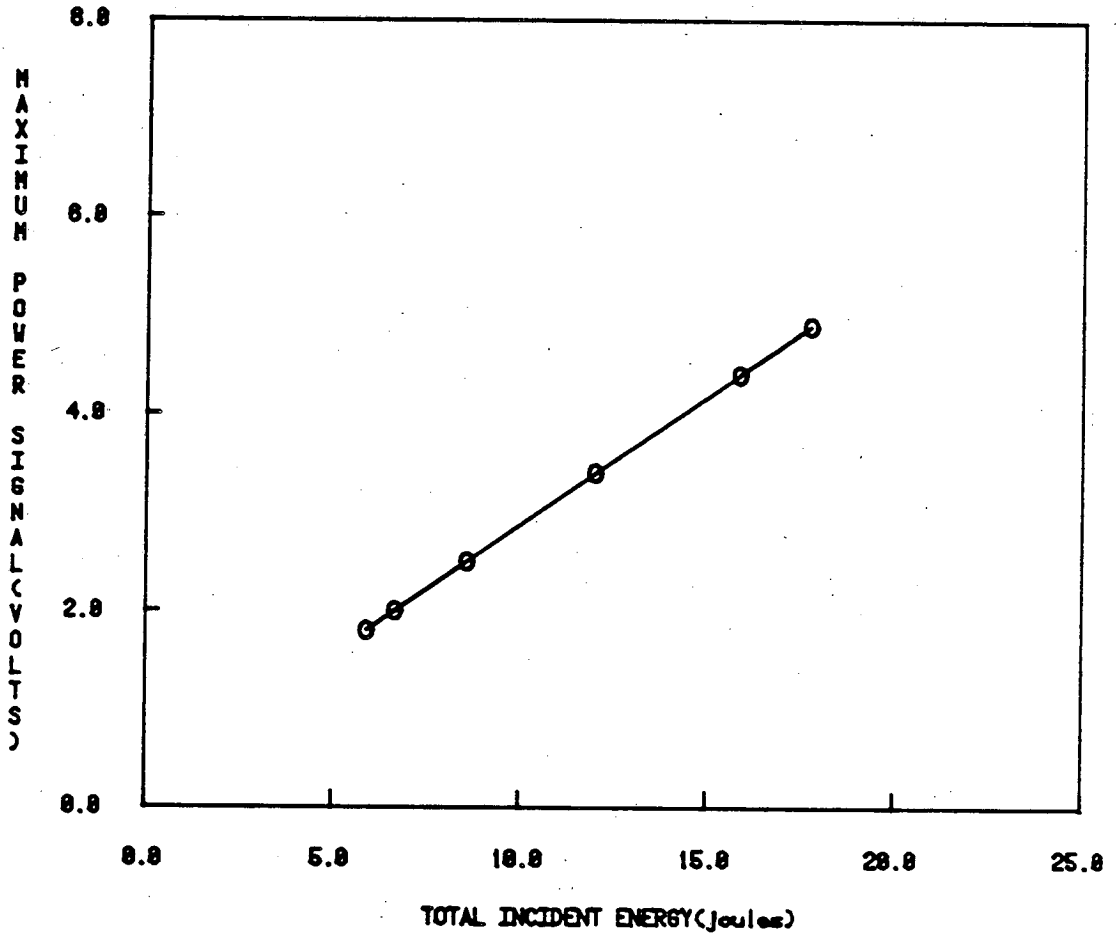

Fig. 3-6: Photodiode Calibration Curve

The maximum temperature used for calibration was ~ 3000 K to avoid damage to the cavity due to graphite ablation. Calibration for higher temperatures was done by extrapolating the low temperature data using the absorbing glass formula; if T_2 and T_3 are the temperatures measured by the standard pyrometer for the same output signal (V(volt) or T(K)) of the automatic pyrometer in the second and third range, we can write:

$$A_2 = \frac{1}{T_2} - \frac{1}{T} \tag{3-7}$$

$$A_3 = \frac{1}{T_3} - \frac{1}{T} \tag{3-8}$$

where A_2 and A_3 are two constants whose values depend on the two filters used for the second and third scale.

Combining equations (3-7) and (3-8) results in:

$$A_{23} = \frac{1}{T_2} - \frac{1}{T_3} \tag{3-9}$$

where $A_{23} = A_2 - A_3$ is a new constant.

A value of 2.3×10^{-4} was obtained for A_{23} by using the calibration data in the range where the output signal of the auto-pyrometer for second and third scales overlapped. This value of A_{23} along with the measured temperatures in the second scale (T_2) were then used in equation (3-9) to extrapolate the third scale temperature measurement, T_3. Figure 3-7 shows the result of the calibration.

The calibration data along with the extrapolated values were fitted to the following equation

$$\log V = \log \frac{C}{e^{B/T} - 1} = A - \log(e^{B/T} - 1) \tag{3-10}$$

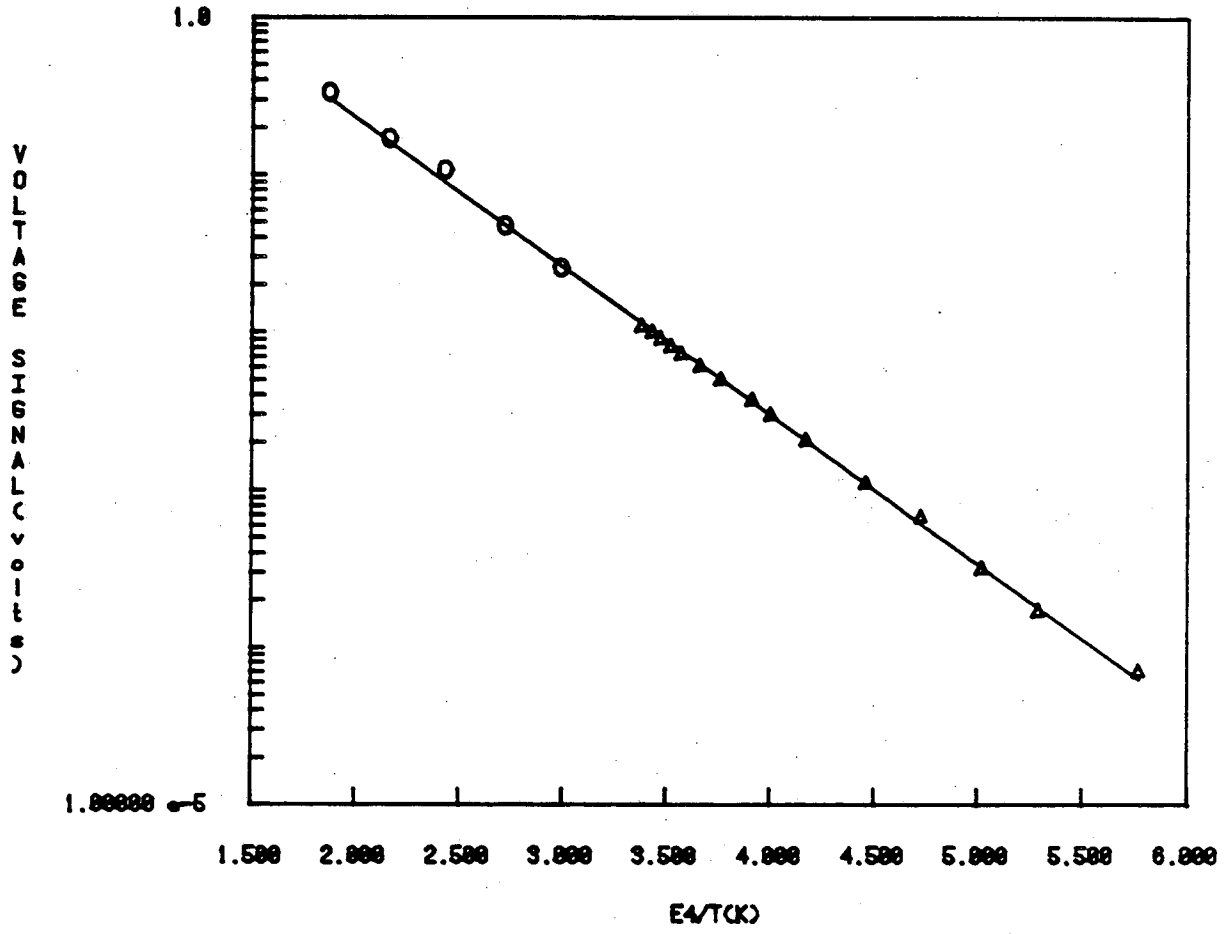

Fig. 3-7. Transient pyrometer calibration curve.

▲ calibration data

O extrapolation

——— equation 3-18

which is direct result of Plank's radiation law. The values of A and B are 1.2496 and -21713 K, respectively.

The temperature obtained by using either the calibration curve of Fig. 3-7 or the calibration equation (3-10) is corrected for the non-unity surface emissivity of the target and also for the vacuum chamber glass window through which temperature is measured. The correction for the emissivity is made by equation:

$$\frac{1}{T_t'} = \frac{1}{T_b} + (\lambda/C_2) \ln \epsilon_\lambda \qquad (3\text{-}11)$$

where T_t' is the true temperature before the glass window correction, T_b is the "brightness" temperature, λ is the wavelength at which thermal radiation is detected (6500°A), C_2 is a constant (1.438 cm-K) and ϵ_λ is the optical emissivity at a wavelength of λ (see Appendix A).

The correction for the glass window is made by:

$$\frac{1}{T_t} = \frac{1}{T_t'} + A \qquad (3\text{-}12)$$

where T_t is the true temperature of the surface and A is the glass window absorption constant. The value of A is obtained by measuring the temperature of a tungsten strip lamp with and without the glass window and using an equation similar to Eq. (3-12). The glass window used in our experiment has an A-value of 3.63×10^{-6}.

Combining equations (3-11) and (3-12) results in a relation between the "brightness" temperature obtained by the optical pyrometer signal through the calibration curve and the true surface temperature as:

$$\frac{1}{T_t} = \frac{1}{T_b} + (\lambda/C_2) \ln \varepsilon_\lambda + A \qquad (3\text{-}13)$$

III.2.3 Mass Spectrometer Calibration

The quadrupole mass spectrometer used to detect the vapor species was calibrated for U, UC_2, C_3 and C signals using a tantalum tube with a 1 mm aperture as a Knudsen cell. A diagram of the device is shown in Fig. 3-8. The cell was filled with UC_2 and excess graphite. Because of the low vapor pressure of this material as well as the low sensitivity of the mass spectrometer, the Knudsen cell was placed in the detector chamber 6 cm from the ionizer. The temperature was measured by focusing a manual optical pyrometer on a 1 mm black body hole in the tube wall opposite to the aperture facing the mass spectrometer.

A.C. currents up to 200A were used in the heating of the tube. Uranium molecules could be detected above background at temperatures > 2220 K. No UC_2 molecules were detected below 2300 K. C and C_3 signals appeared at a temperature of 2210 K. The temperature range of calibration for U and UC_2 was from 2210 K to 2600 K. For C and C_3 the temperature range was from 2210 K to 2420 K.

The mass spectrometer signal during calibration was measured by a Keithly nanometer. For each data point, the background was first measured by moving the beam flag in front of the ionizer. The molecular beam from the tantalum oven was then measured by removing the flag. The true signal is the difference between the measured signal and the background.

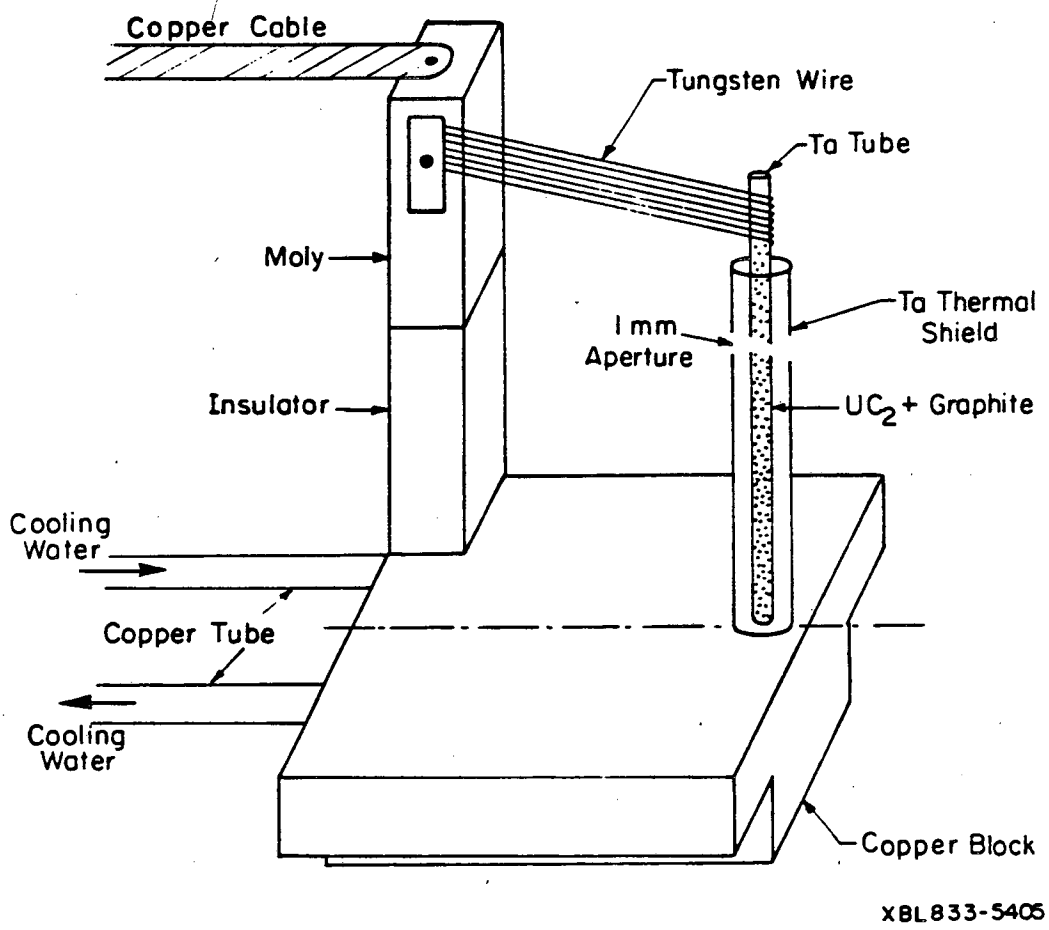

Fig. 3-8. A schematic view of the Knudsen cell used for calibration of the mass spectrometer for U, UC_2, C, and C_3.

High mass range was used when measuring U and UC_2 signal and the low mass range when measuring C and C_3. The other mass spectrometer settings used in both the calibration and the laser experiments are:

H.V. = - 3000V

$V_{electron}$ = 36V

V_{ion} = 15V

V_{focus} = 0

$V_{extractor}$ = 10V

$I_{extractor}$ = 2 mA

Width = 1.23 for high mass range

= 1.64 for low mass range

Resolution setting = 6.41

The resolution was adjusted so that the valley between adjacent mass peaks 238(U^+) and 262(UC_2^+) just touched the base line. The ion voltage was adjusted to avoid mass peak splitting. The rest of the settings were chosen to obtain the largest possible signal. Figure 3-9 shows the result of calibration for U and UC_2 as log(IT) versus $\frac{1}{T}$. The calibration curves for C and C_3 are given in Fig. 3-10. From the slopes of the curves in these figures, the heats of sublimation for U, UC_2, C and C_3 are found to be -146, -190, -147 and -198 kcal/mole respectively. The corresponding literature values are: ____, ____, ____, and ____.

For a steady state source and free molecular flow, the average molecular density of the molecules reaching the ionizer (n), assuming unit evaporation coefficient, is given by:

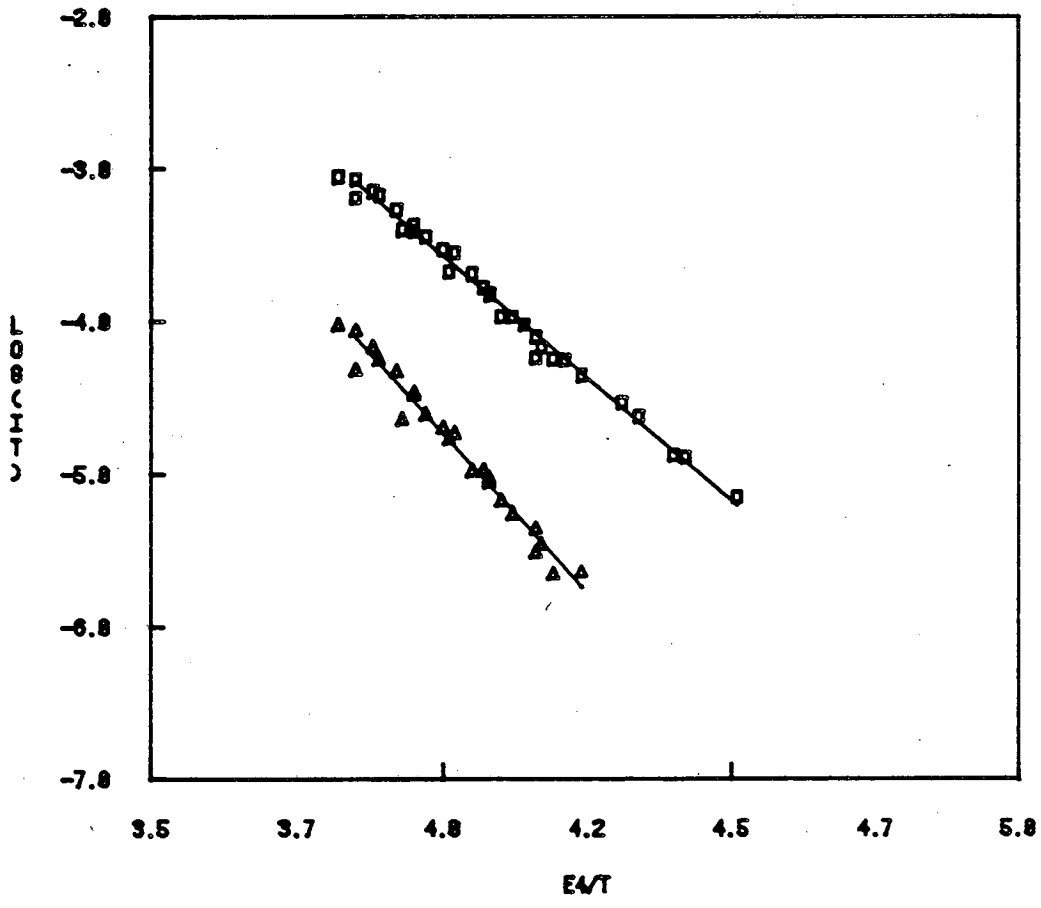

Fig. 3-9. Calibration curves for U and UC_2.

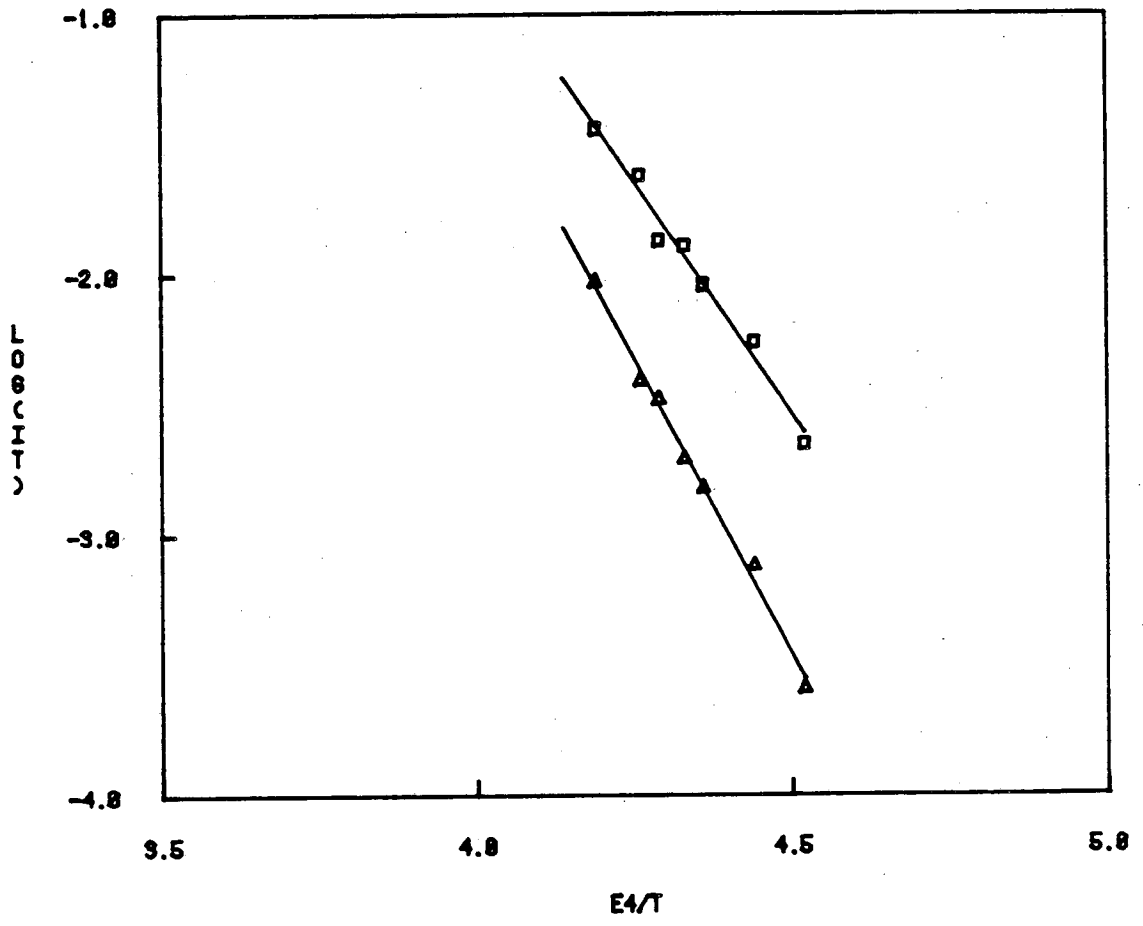

Fig. 3-10. Calibration curves for C and C_3.

$$n = \frac{A_{cell}\ P(T)}{4\pi S^2 KT} \tag{3-14}$$

where A_{cell} = The area of the 1 mm aperture in the Knudsen cell wall

P = equilibrium partial pressure of a particular species

S = distance between the aperture and the mass spectrometer ionizer.

K = Boltzmann constant

T = Temperature.

Equation (3-14) can be written as:

$$n = K_g\ K_U \frac{P}{T} \tag{3-15}$$

where K_U = unit conversion factor (from atm/K to molecules/cm^3)

and K_g = geometric constant $\frac{A_{cell}}{4\pi S^2}$.

The value of K_U is 7.32×10^{21} molecules/cm^3-K atm and that of K_g is 2.42×10^{-5} for a 1 mm aperture and a distance of 6 cm.

The current signal of each species measured is proportional to the number density of ions of that species produced from all neutral molecules by electron impact in the ionizer. As shown by Tsai [10], the current of the ion designed by i is

$$I_i = K_{MS}\ K_g\ K_U \left[\frac{P_i}{T} \sigma_i \beta_i F_{ii}^{+} \sum_{j \pm i} \frac{P_j}{T} \sigma_j \beta_i F_{ji} \right] \tag{3-16}$$

where K_{MS} consists of the characteristic parameters of the mass spectrometer and

σ_i = ionization cross section of species i (cm^2)

F_{ii} = Fraction of i neutrals which produce i^+ ions

F_{ji} = Fraction of j neutrals which produce i^+ ions

β_i = number of secondary electrons produced at the first dynode per incident ion.

In the uranium carbide system U, UC_2, C and C_3 are the major vapor species. The partial pressures of C_2 and heavier molecules are orders of magnitude smaller than the above four. Uranium ions (U^+) in the ionizer are produced either from ionization of U neutrals ($U + e \rightarrow U^+ + 2e$) or by fragmentation of UC_2 molecules ($UC_2 + e \rightarrow U^+ + C_2 + 2e$). UC_2 ions (UC_2^+) can only be produced by the ionization of UC_2 molecules. C^+ ions are either produced by ionization of C neutrals ($C + e \rightarrow C^+ + 2e$), or by fragmentation of C_3 neutrals ($C_3 + e \rightarrow C^+ + C_2 + 2e$). Denoting U, C, UC_2, and C_3 by 0, 1, 2 and 3 respectively we can write equation (3-16) for U^+, C^+, UC_2^+ and C_3^+ current signals as:

$$I_0 = K_{MS}\, K_g\, K_U \left[\frac{P_0}{T} \sigma_0 \beta_0 + \frac{P_2}{T} \sigma_2 \beta_0 F_{20} \right] \qquad (3\text{-}17)$$

$$I_1 = K_{MS}\, K_g\, K_U \left[\frac{P_1}{T} \sigma_1 \beta_1 + \frac{P_3}{T} \sigma_3 \beta_1 F_{31} \right] \qquad (3\text{-}18)$$

$$I_2 = K_{MS}\, K_g\, K_U \left[\frac{P_2}{T} \sigma_2 \beta_2 F_{22} \right] \qquad (3\text{-}19)$$

$$I_3 = K_{MS}\, K_g\, K_U \left[\frac{P_3}{T} \sigma_2 \beta_3 F_{33} \right] \qquad (3\text{-}20)$$

Since the partial pressures of UC_2 is at least one order of magnitude smaller than that of uranium in the temperature range of calibration, the second term on the right hand side of equation (3-17) can be neglected and Eqs. (3-17) - (3.-20) written as:

$$I_0 = K_0 K_g K_U \frac{P_0}{T} \tag{3-21}$$

$$I_1 = K_1 K_g K_U \left[\frac{P_1}{T} + \frac{P_3}{T}\frac{\sigma_3}{\sigma_1} F_{31}\right] \tag{3-22}$$

$$I_2 = K_2 K_g K_U \frac{P_2}{T} \tag{3-23}$$

$$I_3 = K_3 K_g K_U \frac{P_3}{T} \tag{3-24}$$

where $K_0 = K_{MS}\sigma_0\beta_0$

$K_1 = K_{MS}\sigma_1\beta_1$

$K_2 = K_{MS}\sigma_2\beta_2 F_{22}$

and $K_3 = K_{MS}\sigma_3\beta_3 F_{33}$.

Using the results of calibration for U, UC_2 and C_3 (Figs. 3-9 and 3-10) along with the literature values for P_U, P_{UC_2} and P_{C_3} [31] in Eqs. (3-21), (3-23) and (3-24), the calibration constants K_0, K_2 and K_3 are calculated in amp cm^3/molecule as: 2.07×10^{-14}, 8.83×10^{-15} and 8.55×10^{-13}, respectively. The calibration curve for monatomic carbon of Fig. 3-10 is used to obtain K_1 and F_{31} by fitting the data to Eq. (3-22). Literature values for P_C and P_{C_3} [31] and $\sigma_3/\sigma_1 \simeq 2.25$ were used in this calculation. The calculated values of K_1 and F_{31} are 2.60×10^{-12} and 0.65, respectively.

III.3 Laser Experiment

III.3.1 Experimental Procedure

The following steps are taken before each experimental run:

1) The UC sample, prepared as described in Section III.1.7, is mounted on the electron bombardment heater and installed in the target chamber.

2) The target chamber is evacuated by the mechanical and diffusion pumps to ~ 10^{-8} torr pressure.
3) The gate valve between the target chamber and the detector chamber is opened. The detector chamber is always kept under vacuum.
4) The system and the Nd-glass laser are aligned as described in Section II-A-1.
5) The Nd-glass laser power supply is turned on and the voltage is set.
6) The fine alignment of the Nd-glass laser is done by shooting the laser through an aperture on to a polaroid film. The optical components are adjusted until the burnt spot on the polaroid is exactly on the spot illuminated by gas laser No. 3.
7) The optical pyrometer is aligned and focused on the spot where the gas laser No. 3 hits the target.
8) The target is preheated by the E. B. heater to a steady temperature of 1800 K. The temperature is measured by the optical pyrometer in the automatic mode.
9) The photodiode, optical pyrometer and the mass spectrometer are connected to the transient wave recorder.
10) The optical pyrometer is set at transient operate mode.
11) The mass spectrometer is tuned to the mass of the species to be measured.
12) Depending on the laser energy desired, up to seven neutral density filters are placed between the Nd-glass laser and the beam splitter.

13) The full scale of each channel of the transient recorder is chosen, based on the estimated voltage signal, to attain the highest sensitivity.

14) Set the transient recorder at the "Ready" mode for data recording by pushing the "Arm" button.

15) Trigger the Nd-glass laser.

16) Three signals are recorded by the transient recorder. The recording stops automatically after a pre-set delayed triggering signal is received by the recorder.

17) The digitized signals are transferred to an oscilloscope for picture taking and to the x-y recorder for later analysis.

18) The mass spectrometer is set for another species.

19) Steps (13) to (17) are repeated for all vapor species of interest using the same target and so completing one run for one laser energy.

20) Different numbers of filter are used for different energies and steps (12) to (18) are repeated.

III.3.2 Interpretation of the Signals

Figure 3-13 shows a typical mass spectrometer signal recorded by the transient recorder. At each laser energy four such signals are recorded for U^+, C^+, UC_2^+ and C_3^+. To obtain the number density of neutral molecules of each species in the ionizer the following steps are taken:

1) Correction for the RC time constant of the external circuit:

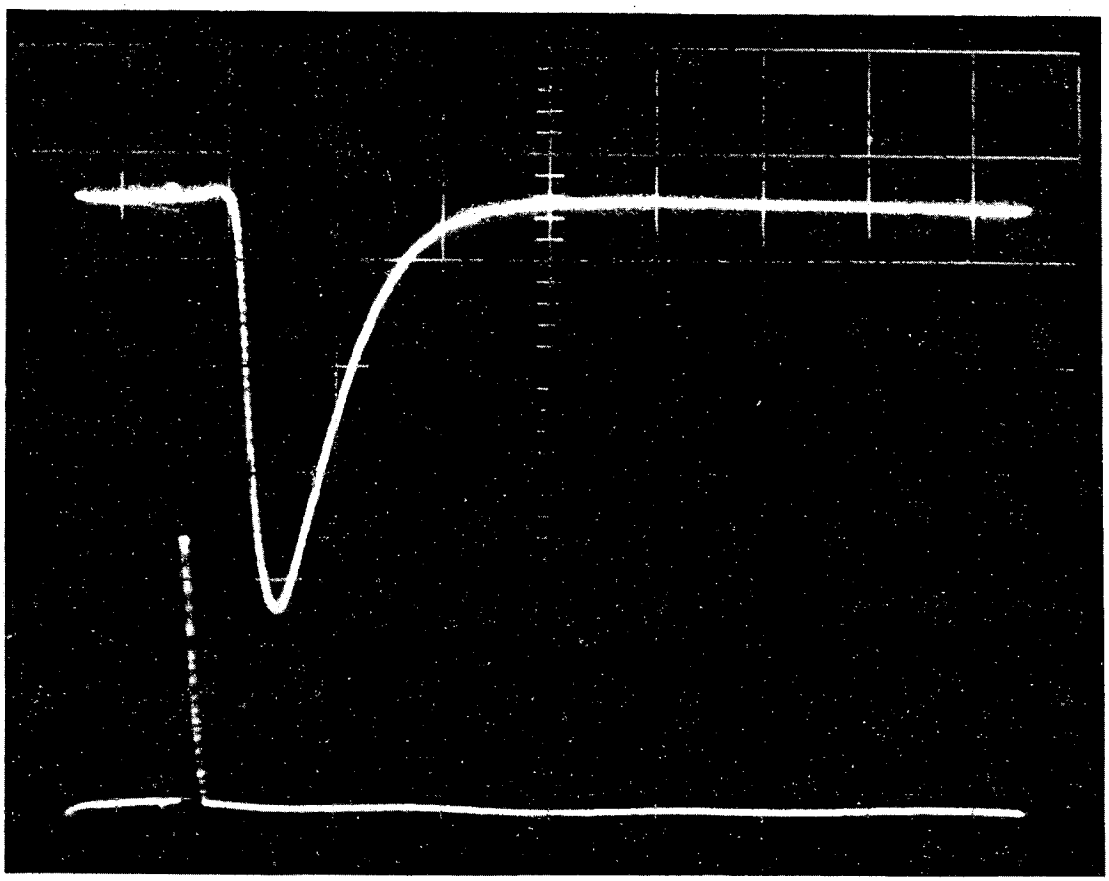

XBB 834-3298

Fig. 3-10. A typical mass spectrometer signal.

The output voltage signal of the mass spectrometer for each species (V) is corrected for the RC time constant of the external circuit to obtain the output current of the electron multiplier (I_{em}).

$$I_{em}(t) = (C + C_b) \frac{dV(t)}{dt} + \frac{V(t)}{R_b} \qquad (3\text{-}25)$$

where C = The cable line capacitance.

C_b = The transient recorder (Biomation 1015) input capacitance

R_b = The input resistance of the transient recorder.

2) Correction for the electron multiplier efficiency:

The ion current at the first dynode of the electron multiplier (I_{fd}) is given by:

$$I_{fd}(t) = \frac{I_{em}(t)}{G\beta} \qquad (3\text{-}26)$$

where G = electron multiplier gain.

β = number of the secondary electrons emitted at the first dynode (may differ for each ion collected).

3) Correction for the drift time and efficiency of the quadrupole structure:

The ion current in the ionizer (I) is related to the ion current at the first dynode by:

$$I(t) = \frac{I_{fd}(t+t_d)}{\gamma} \qquad (3\text{-}27)$$

where t_d = drift time of ions from the ionizer through quadrupole (acceleration time before quadrupole is neglected

γ = the fraction of the ions produced in the ionizer which reach the electron multiplier.

The drift time can be calculated from the ion kinetic energy at the quadrupole entrance, eV_{ion}:

$$eV_{ion} = \frac{1}{2} m \left(\frac{L_q}{t_d} \right)^2 \tag{3-28}$$

where V_{ion} = ion potential relative to the ionizer.

e = ion charge.

m = ion mass.

L_q = length of the quadrupole structure (14 cm).

Solving for t_d gives

$$t_d = L_q \left(\frac{m}{2eV_{ion}} \right)^{1/2} \tag{3-29}$$

$$t_d = 1.01 \times 10^{-5} \left(\frac{M}{15} \right)^{1/2} \tag{3-30}$$

in which t_d is in seconds and M is the molecular weight in g/mole. Equation (3-30) results in

t_d = 0.0402 msec for U^+ (mass 238)

= 0.0422 msec for UC_2^+ (mass 262)

= 0.0090 msec for C^+ (mass 12)

= 0.0156 msec for C_3^+ (mass 36).

4) Correction for the ionization cross section and the fragmentation pattern:

Following the same steps taken in Section III.2.3 for steady steate calibration of the mass spectrometer, the i^+ ion current in the ionizer is derived as:

$$I_i(t) = [\sigma_i n_i(t) F_{ii} + \sum_{j \neq i} \sigma_j n_j(t) F_{ji}] \, I_e L \tag{3-31}$$

where $\sigma_i(\sigma_j)$ = total ionization cross section of i(j) neutral.

F_{ii} = fraction of i neutral which becomes i^+ ions.

F_{ji} = fraction of j neutral ($m_j > m_i$) which produces i^+.

$n_i(n_j)$ = molecular density of i(j) neutral in the ionizer.

I_e = emission electron current of the ionizer filament.

L = length of the electron sheet.

Combining steps (1) to (4) yields:

$$\frac{1}{G\beta_i\gamma}\ (C + C_b)\ \frac{dV_i(t+t_d)}{dt} + \frac{V_i(t+t_d)}{R_b} = \left[\ \sigma_i n_i(t)F_{ii} + \sum_{j\neq i} \sigma_j F_{ji} n_j(t)\ \right] I_e L.$$

Rearranging this equation gives for each species i:

$$V_i'(t) = \tau_{RC}\ \frac{dV_i(t+t_{d_i})}{dt} + V_i(t+t_{d_i}) = K_{MS}\beta_i R_b[\sigma_i n_i(t)F_{ii} + \sum_{j\neq i} \sigma_j n_j(t)F_{ji}] \qquad (3\text{-}32)$$

where the left side of the equation (V_i') is the output signal of the mass spectrometer after being corrected for the external circuit time constant and

$$\tau_{RC} = R_b\ (C\ + C_b)$$
$$K_{MS} = I_e L G \gamma. \qquad (3\text{-}33)$$

The transient recorder input resistance (R_b) of 1MΩ, the transient recorder input capacitance (C_b) of 25 pf and the line capacitance (C) of about 175 pf result in an RC time constant (τ_{RC}) of 0.2 msec.

It is shown by Tsai [10] that K_{MS} defined by Eq. (3-33) is the same as that in Eq. (3-16).

Using 0,1,2 and 3 for U, C, UC_2 and C_3 as before and the same approximations used in the calibration, Eq. (3-32) can be written for different species as:

$$V_0'(t) = \tau_{RC} \frac{dV_0(t+t_{d_0})}{dt} + V_0(t+t_{d_0}) = K_{MS}\beta_0 R_b \sigma_0 n_0(t) = K_0 R_b n_0(t) \quad (3\text{-}34)$$

$$V_1'(t) = \tau_{RC} \frac{dV_1(t+t_{d_1})}{dt} + V_1(t+t_{d_1}) = K_{MS}\beta_1 R_b[\sigma_1 n_1(t) + \sigma_3 n_3(t) F_{31}]$$

$$= K_1 R_b[n_1(t) + \frac{\sigma_3}{\sigma_1} n_3(t) F_{31}] \quad (3\text{-}35)$$

$$V_2'(t) = \tau_{RC} \frac{dV_2(t+t_{d_1})}{dt} + V_1(t+t_{d_1}) = K_{MS}\beta_2 R_b \sigma_2 n_2(t) F_{22}$$

$$= K_2 R_b n_2(t) \quad (3\text{-}36)$$

$$V_3'(t) = \tau_{RC} \frac{dV_3(t+t_{d_3})}{dt} + V_3(t+t_{d_1}) = K_{MS}\beta_3 R_b \sigma_3 n_3(t) F_{33}$$

$$= K_3 R_b n_3(t). \quad (3\text{-}37)$$

K_0, K_1, K_2, K_3 and F_{31} are the calibration constants and fraction of C_3 fragmented to C obtained in Section III.2.3. The four equations (3-34) - (3-37) are solved for the four unknowns $n_1(t)$, $n_2(t)$, $n_3(t)$ and $n_4(t)$.

III.3.3 Surface Temperature Measurement

The target surface temperature in each laser shot is measured by the transient optical pyrometer, whose calibration was described in Section III.2.2. The time response of the pyrometer is in the nano-second range, which is orders of magnitude smaller than the half-width of the surface temperature signal. To minimize the effect of the RC time constant of the external circuit on the pyrometer signal, a 20 KΩ

resistance is connected parallel to the transient recorder input resistance. As a result there is no need for RC correction of the temperature signal. The pyrometer output signal along with the calibration curve of Fig. 3-7 is used to characterize the temperature transient.

IV. RESULTS AND DISCUSSION

A total of eight experimental runs were carried out. In each run the signals for the four major species U, UC_2, C and C_3 along with the surface temperature and laser power were measured. The surfaces of the laser-irradiated samples were examined by scanning electron microscope and the depth of the crater produced was measured by an inductive sensor tip scanning across the crater profile. The total number of ions emitted from the surface was measured in separate tests for four different laser energies. The range of the laser energies used in the experiment was from 5.9 to 14.5 J, which is equivalent to peak power densities of 1.6×10^5 to 4.0×10^5 watts/cm^2. The peak power densities obtained along with the normalized power trace are used in the STAR code for temperature calculations.

IV.1 Surface Temperature

The points in Fig. 4-1 show the measured surface temperature of the target as a function of time. The three lines show the lower limit, the upper limit and the mean value of the surface temperature obtained by the sensitivity analysis (Appendix B) for a laser energy of 12 J. The values of the material properties given in Table 2.3 were used in the calculations. The initial C/U ratio and temperature of the sample were taken as 1.05 and 1800 K respectively. Figure 4-1 shows that there is good agreement between the times of the calculated and measured temperature maxima. The measured maximum surface temperatures as a function of incident laser energy are shown in Fig. 4-2.

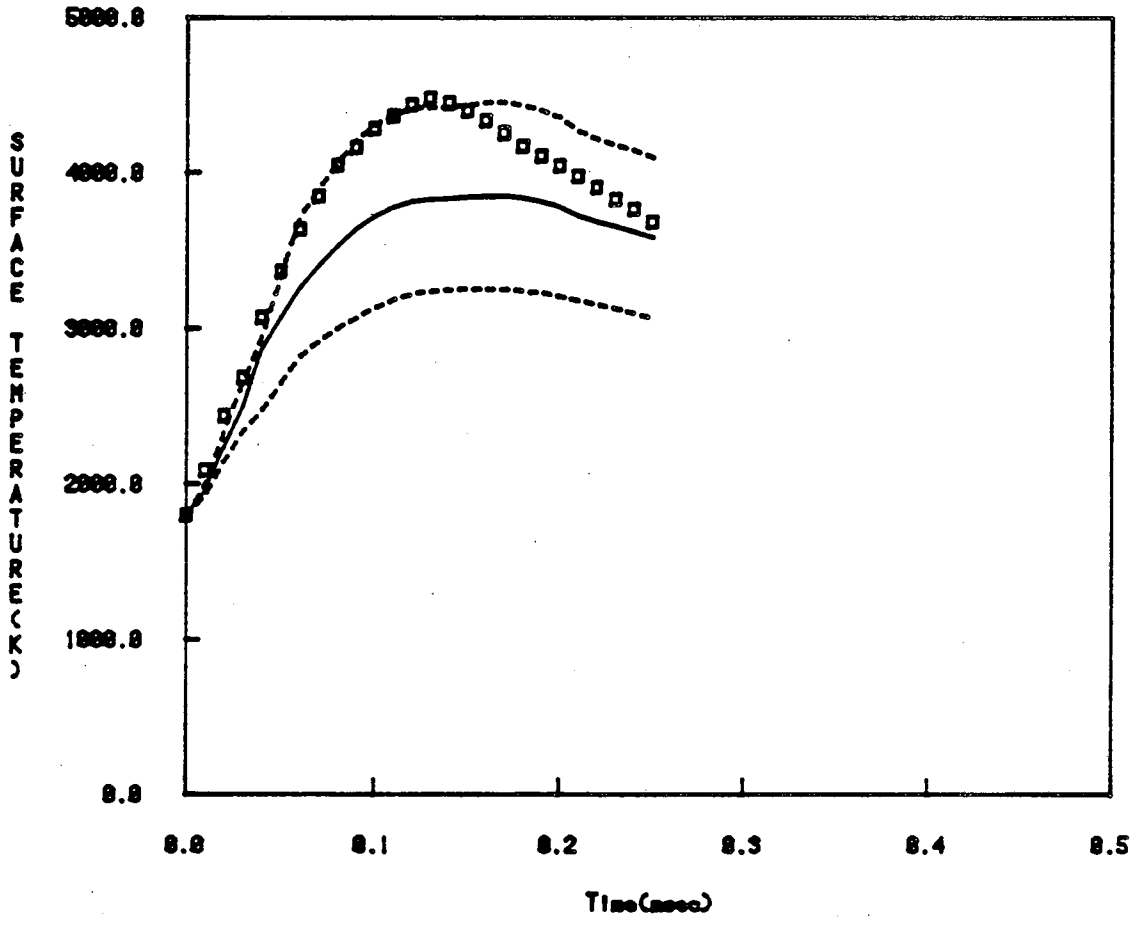

Fig. 4-1. Measured and calculated surface temperature profile for E = 12 J.

——— mean value □ Experimental values

---------- lower limit and upper limit

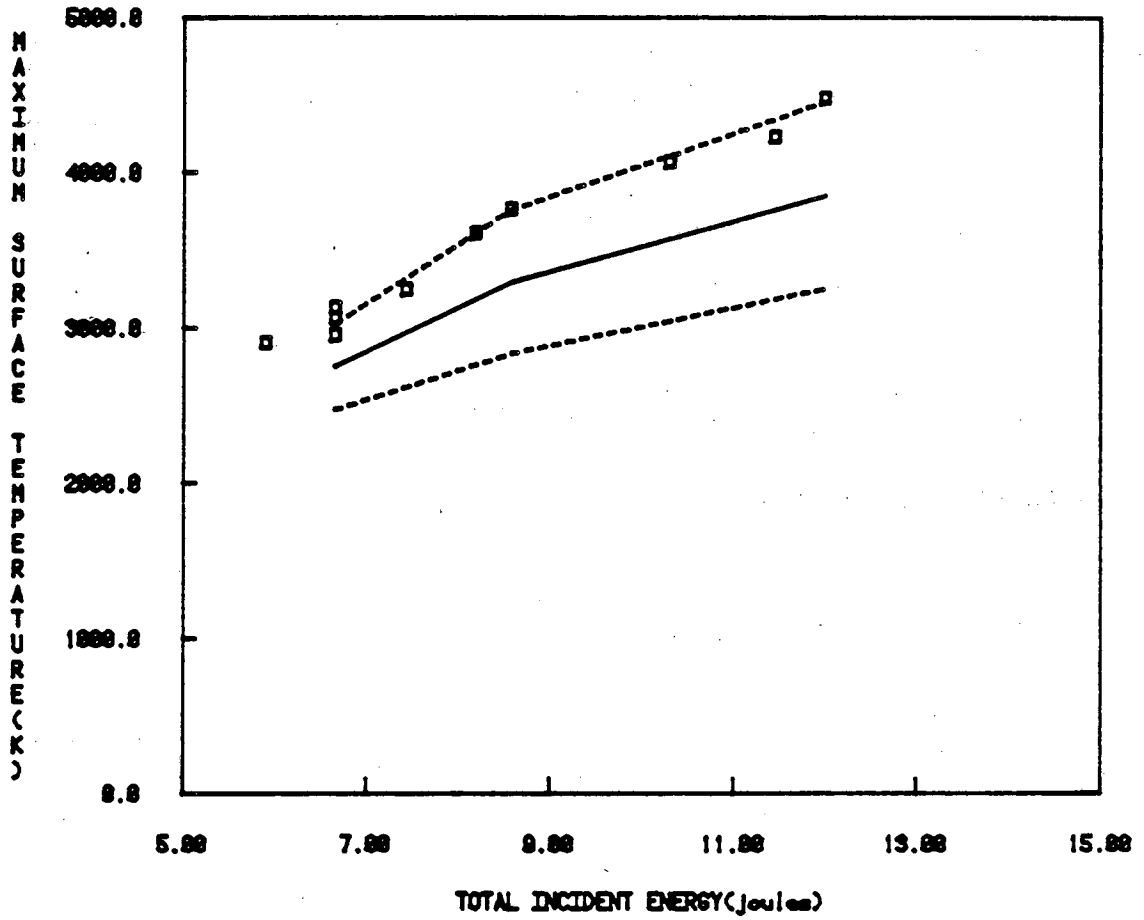

Fig. 4-2. Measured and calculated maximum surface temperature vs. total incident energy.

Again the lines show the result of calculation along with the sensitivity analysis. Although the measured temperature is within the confidence limits of the calculated results, there is substantial difference between the measured and the mean calculated values. The main source of this discrepancy is considered to be due to too large a reflectivity (R) of liquid uranium carbide, obtained from the emissivity ($R = 1 - \varepsilon$) measured by Bober [26]. A low value of emissivity results in a high measured temperature through eq. (3-14), while a high reflectivity results in lower energy deposited on the surface (eq. (2-62)) and therefore lower calculated temperatures. The best agreement between measured temperature and the calculated one is when the emissivity is taken to be about 0.8 for the pyrometer correction and the reflectivity of 0.2 used for the absorbed energy calculation. Measurements of the reflectivity of metallic surfaces irradiated by a normal pulse Nd-glass laser have shown that the reflectivity drops to a low value in the first 50 μsec of the pulse, so that most of the pulse energy is absorbed despite the initial high reflectivity of the target [49]. This may explain the higher measured temperatures compared to the calculated (mean) values when $\varepsilon=R=0.5$ is assumed.

IV.2 Number Densities of Vaporized Species

Figure (4-3) and (4-4) show typical mass spectrometer signals for different major vapor species recorded by the transient recorder. Each signal consists of only one peak due to the thermal neutrals. The extra peak due to fast ions observed by Tsai [10] in laser evaporation of UO_2 is absent. The signals are corrected for the RC time constant of the circuit and the drift time in the quadrupole structure

of the mass spectrometer (Section III.3.2). Figures (4-5) - (4-8) show the raw mass spectrometer output, V(t) along with the corrected signal, V'(t), for all the vapor species for one run. The origin of the coordinate system is the beginning of the laser pulse. Similar results for other runs are given in Appendix D.

Equations (3-34) - (3-37) are used to calculate the transient number density of neutral molecules in the ionizer of the mass spectrometer. The value of the calibration constants used in these equations are given in Section III.2.3. Figure (4-9) shows a typical measured normalized number density of uranium as a function of time compared with the results of calculations based on the free molecule flow and the gasdynamic models. The free molecule flow model is closer to the experimental result than the hydrodynamic flow model. The latter results in a theoretical response which has a narrower width and quicker time-of-arrival than the measured signal.

Figures (4-10) - (4-13) show the measured maximum number densities of the neutral molecules, n_U^{max}, $n_{UC_2}^{max}$, n_C^{max} and $n_{C_3}^{max}$, in the ionizer as a function of incident laser energy. The results of calculations based on measured temperatures and using the "mean" calculated temperatures are also shown. Had the surface reflectivity been chosen as 0.2 instead of 0.5, the calculated curves would have been much closer to the measured curves. The calculated maximum number densities increase as energy increases, following the analogous tendency of the estimate equilibrium pressures (Table 2-2). The measured number densities are in relatively good agreement with the theoretical results

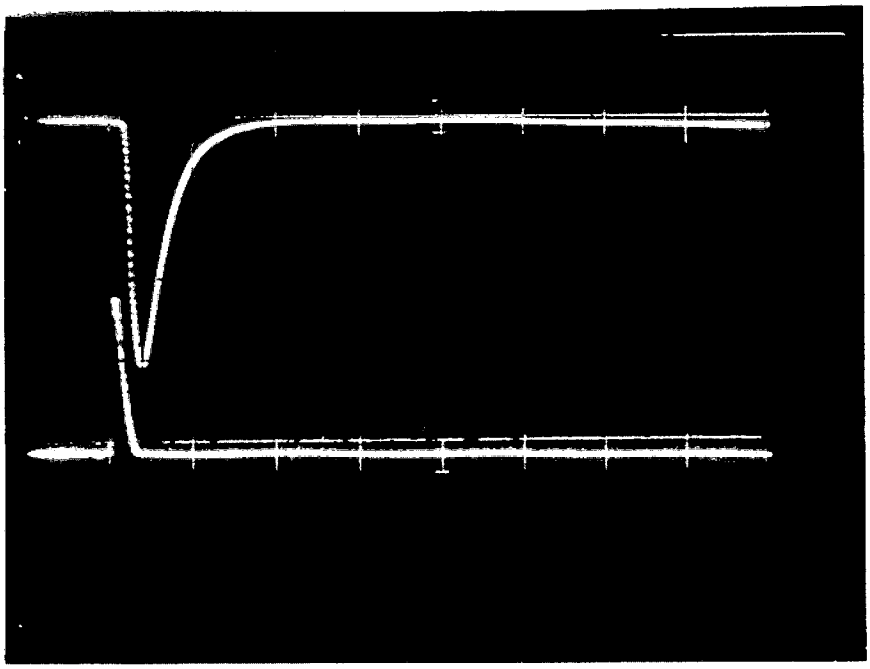

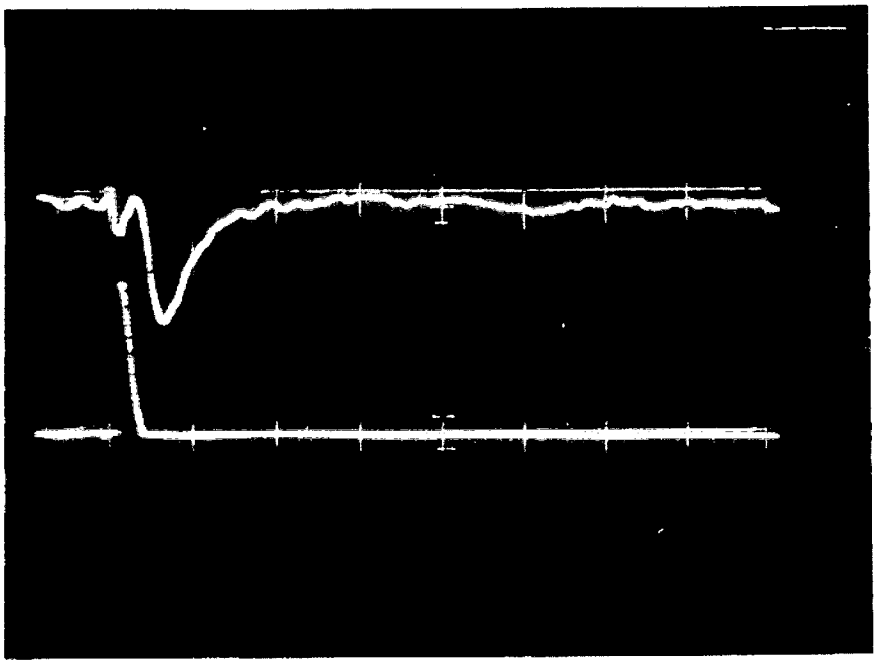

XBB 834-3300

(b)

Fig. 4-2. Mass spectrometer signal (top trace) and laser power profile (bottom trace) for Run #5 (a) U^+ (b) UC_2^+.

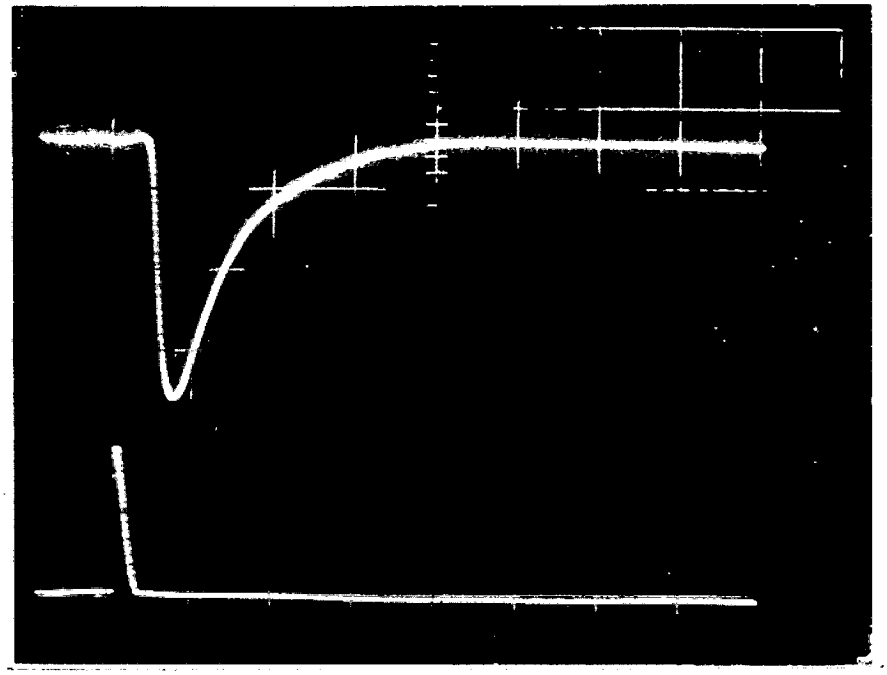

(a)

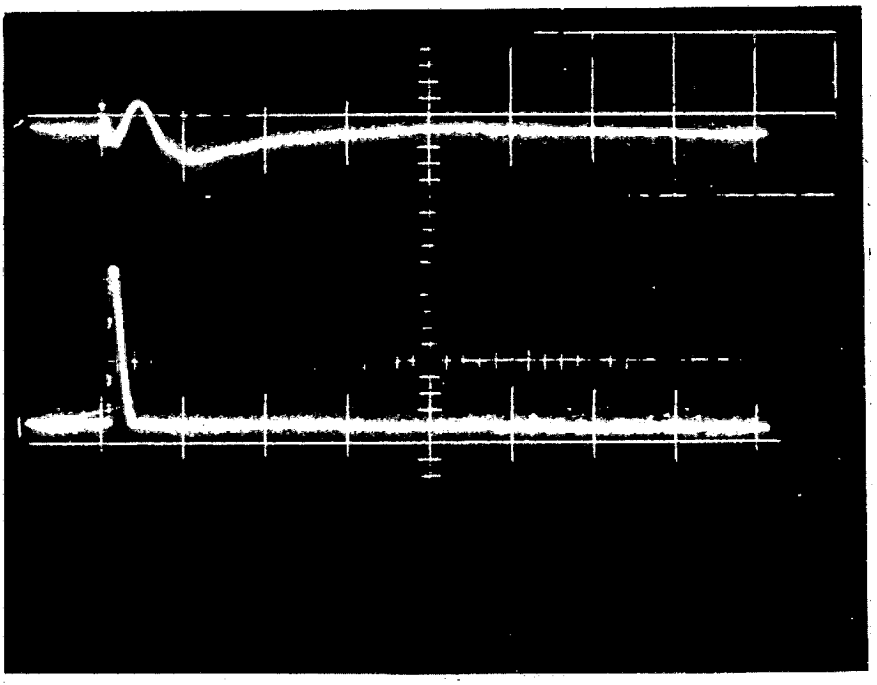

XBB 834-3299

(b)

Fig. 4-4. Mass spectrometer signal (top trace) and laser power profile (bottom trace) for Run #5 (a) C_1^+ (b) C_3^+.

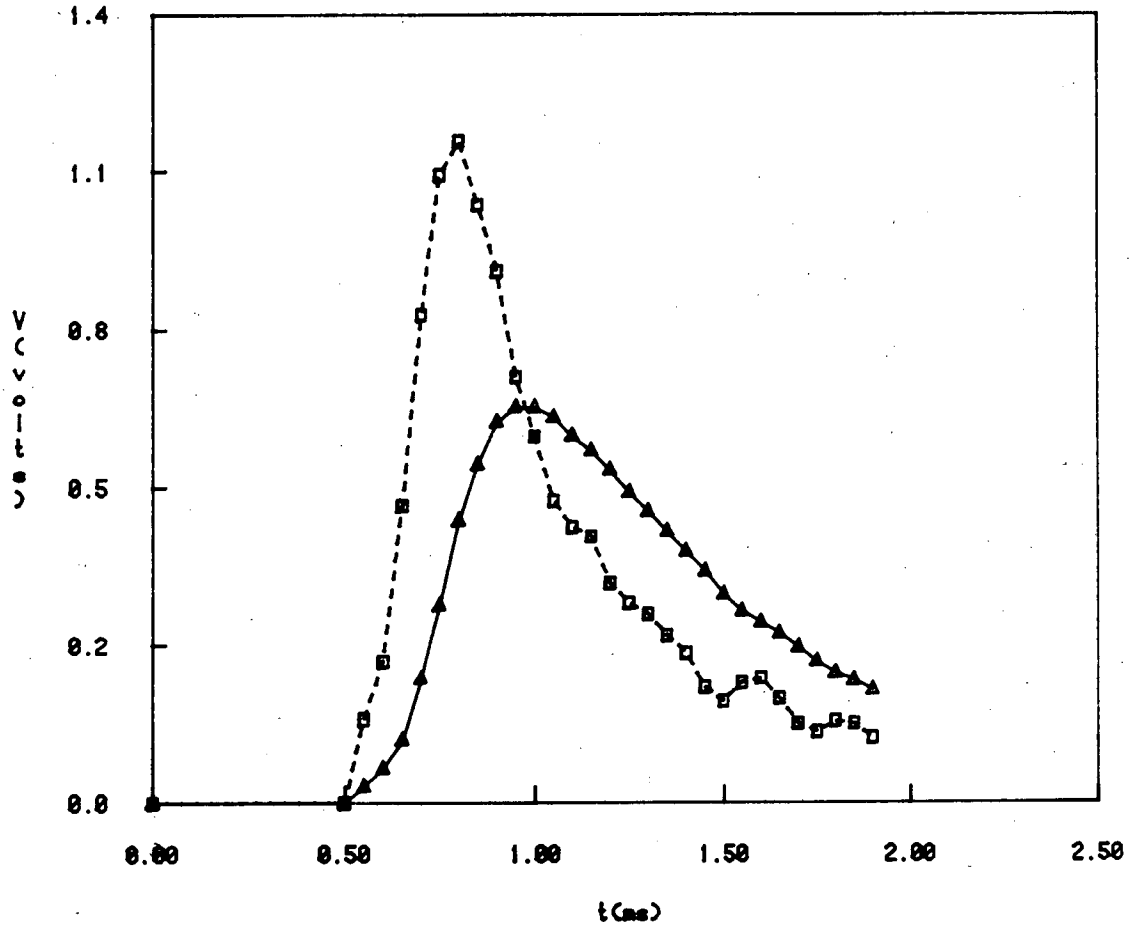

Triangle-Measured data Square-Corrected data
Fig. 4-5:U Signal(Run8);E=14.5 joules

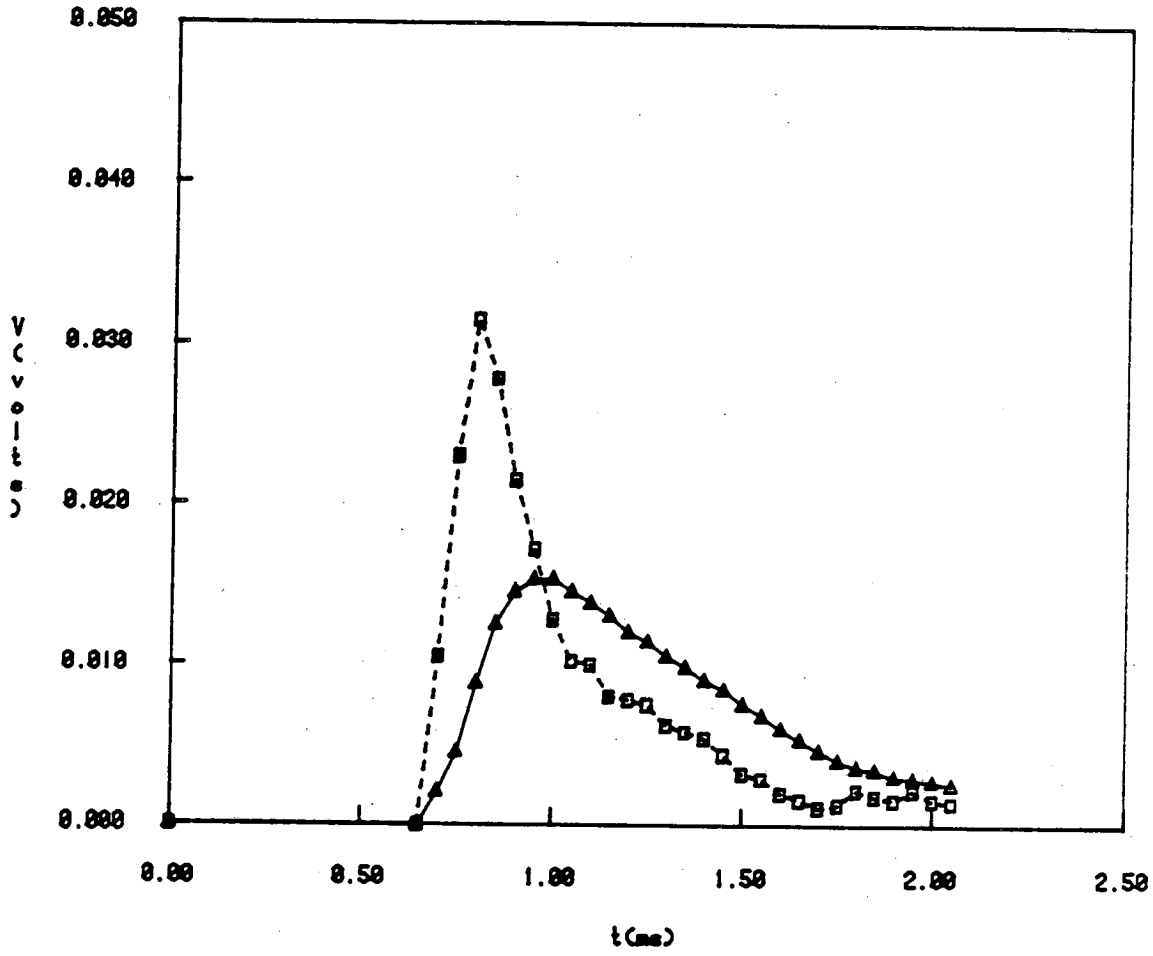

Triangle- Measured data Square-Corrected data
Fig. 4-6:UC2 Signal(Run8);E=14.5 joules

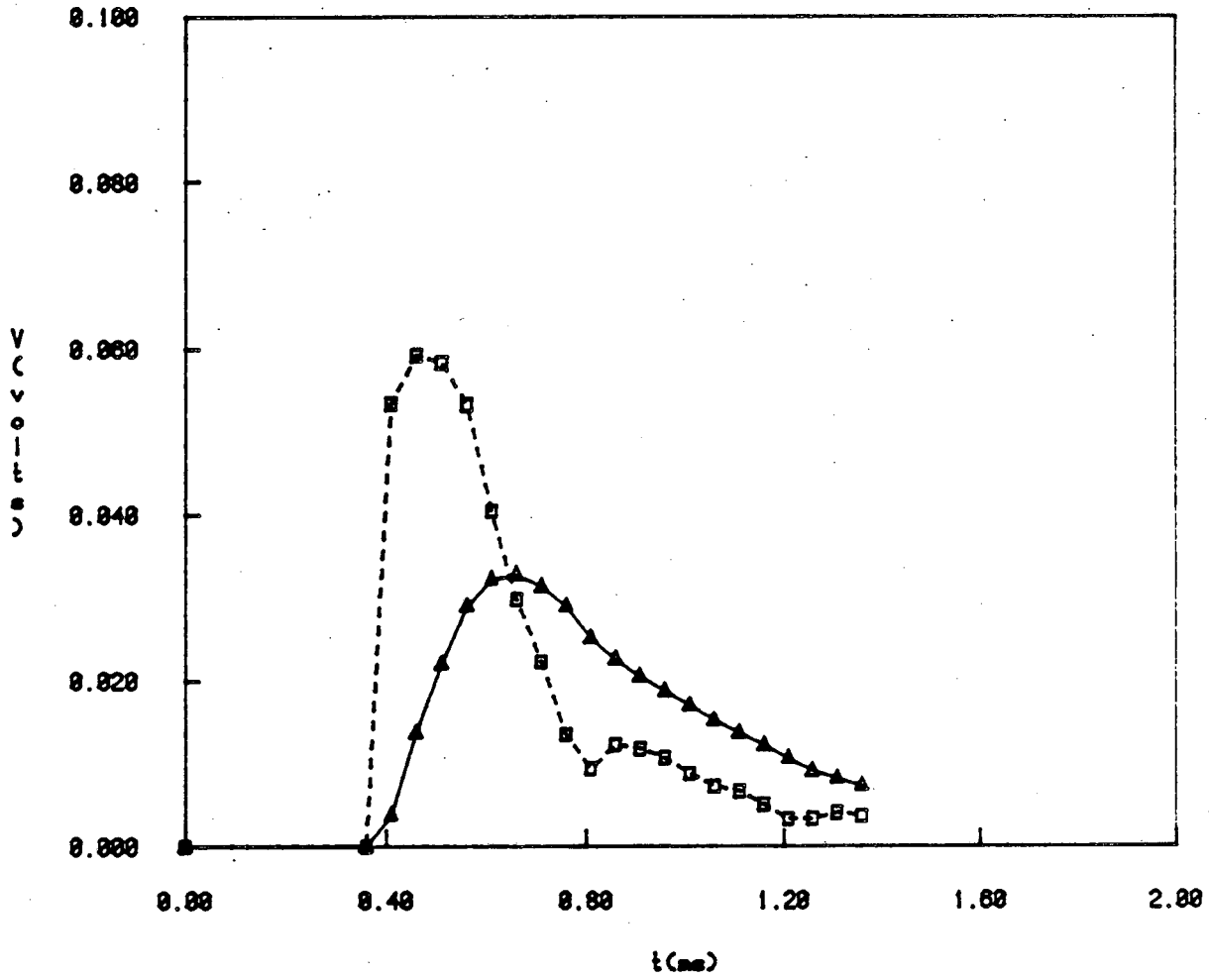

Triangle-Measured data Square-Corrected data
Fig. 4-7:C3 Signal(Run8);E=14.5 joules

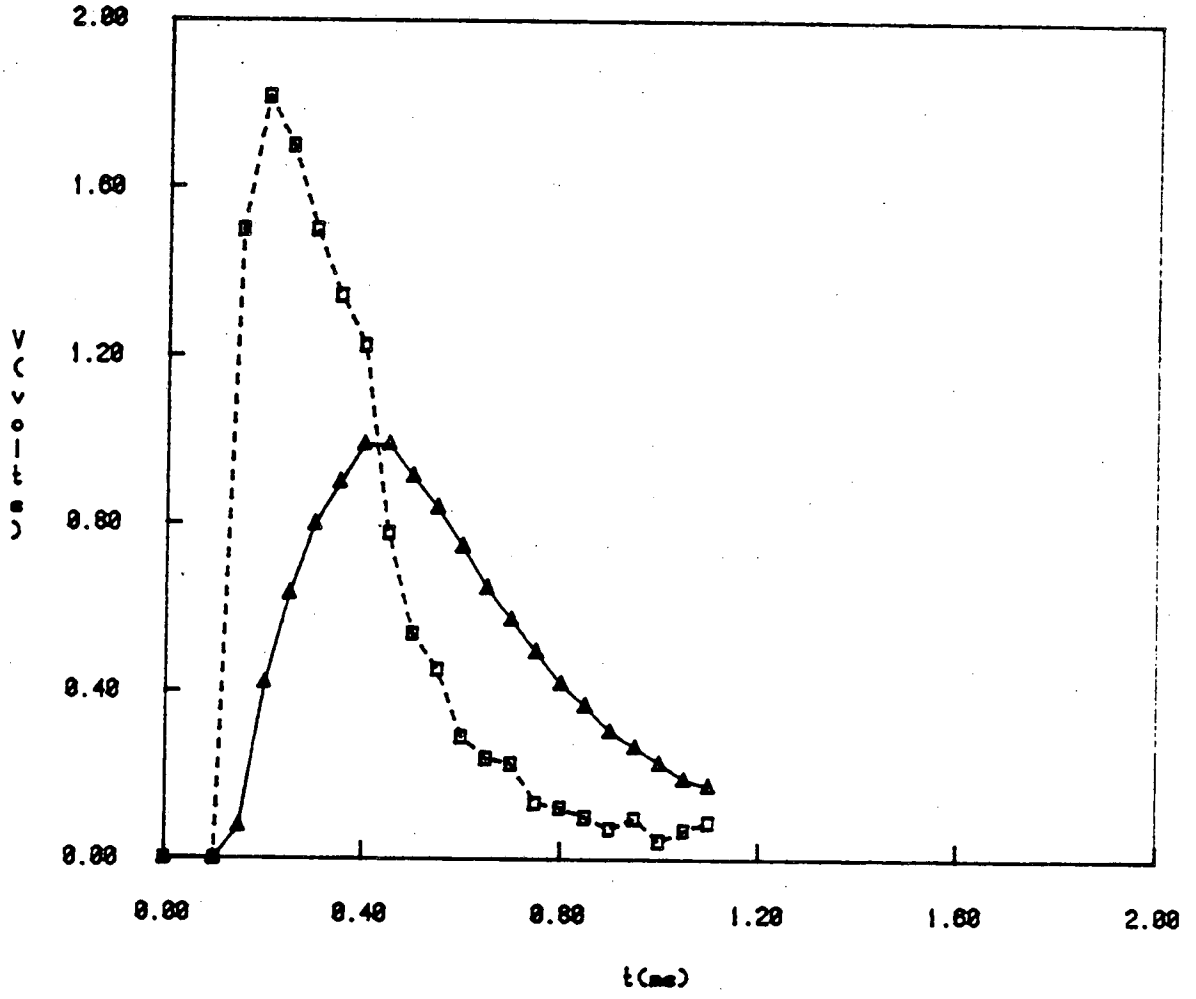

Triangle- Measured data Square- Corrected data
Fig. 4-8:Cl Signal(Run8);E=14.5 joules

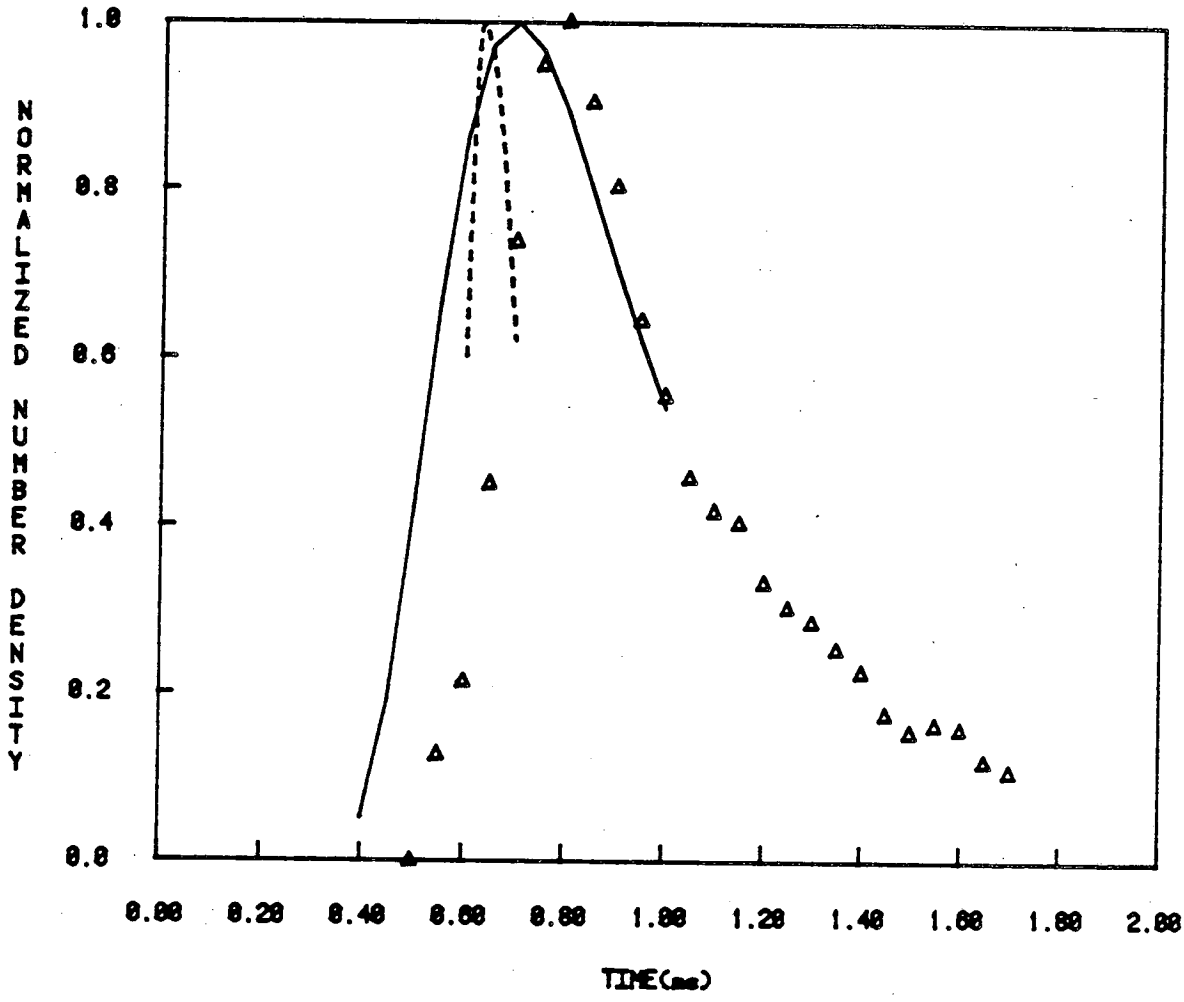

Fig. 4-9. Normalized mass spectrometer signals for U^+ at E = 12 J.

NCal(Molecular Flow Model) Triangles-Nexp
Ncal(Gas Dynamics Flow Model)

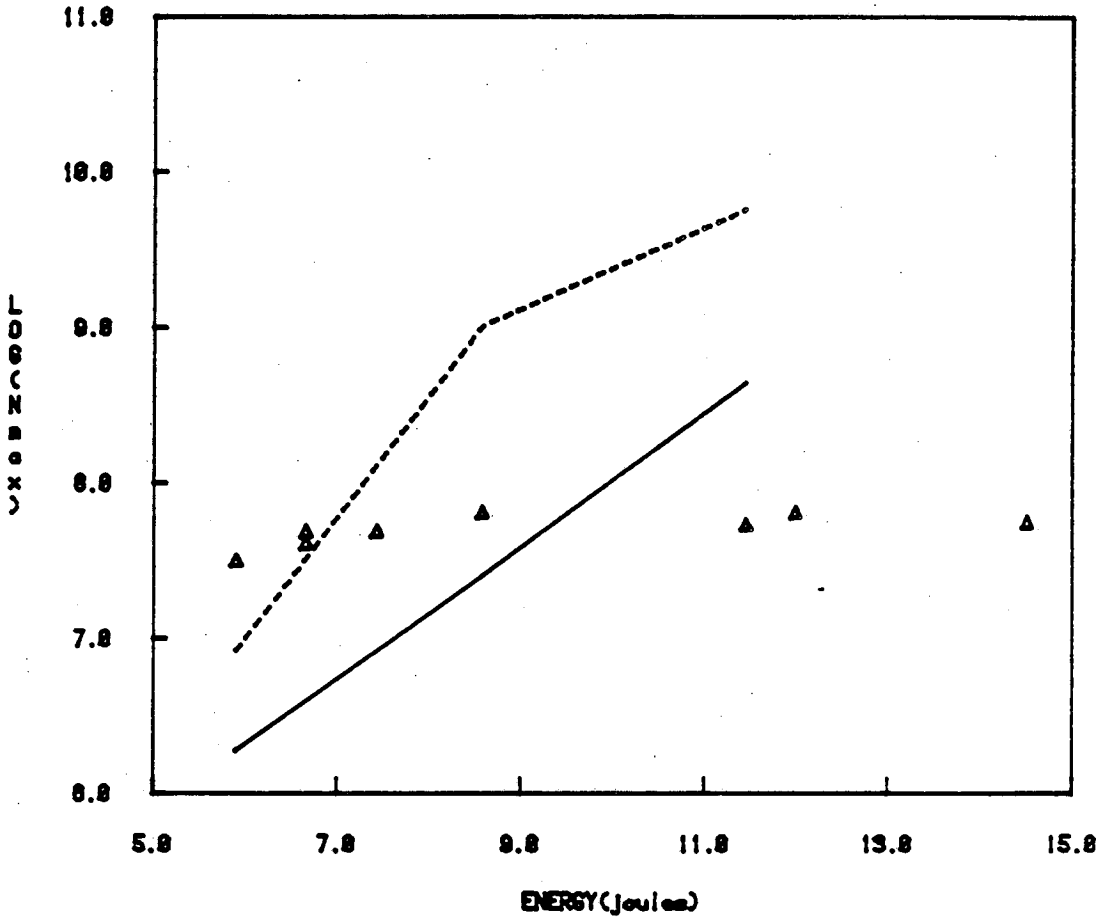

Fig. 4-10. Maximum number density of U vs energy.

▲ Nmax(exp) ---------- Nmax based on Texp

———— Nmax based on Tcal

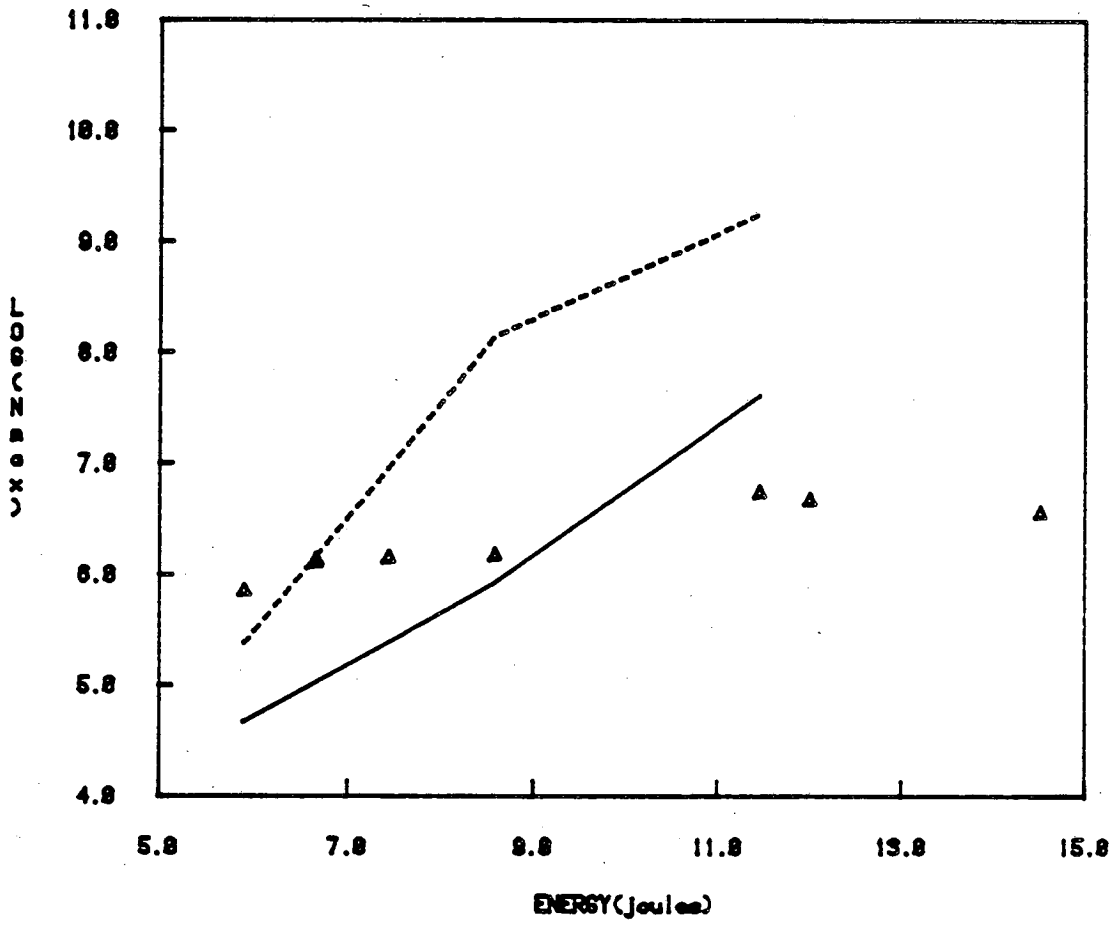

Fig. 4-11. Maximum number density of UC_2 vs energy.

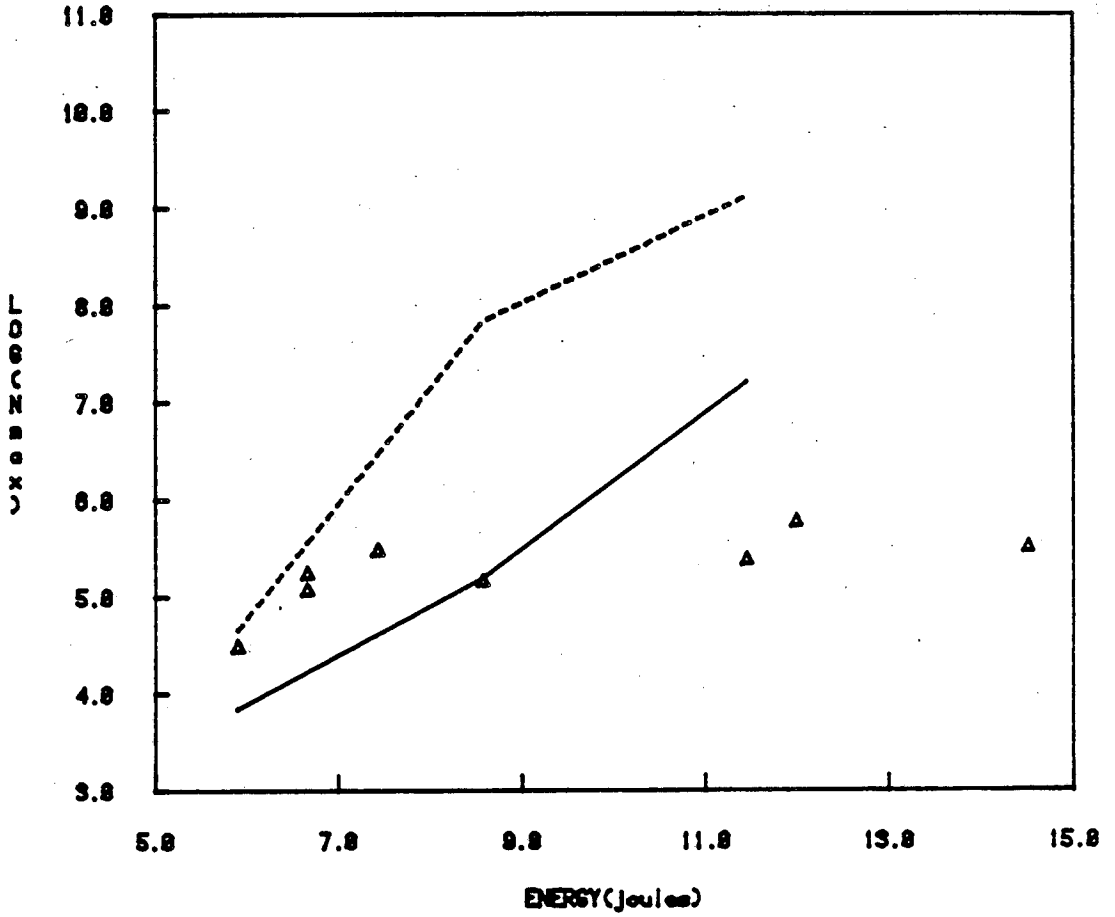

Fig. 4-12. Maximum number density of C_3 vs energy.

▲ Nmax(exp) ---------- Nmax based on Texp

———— Nmax based on Tcal

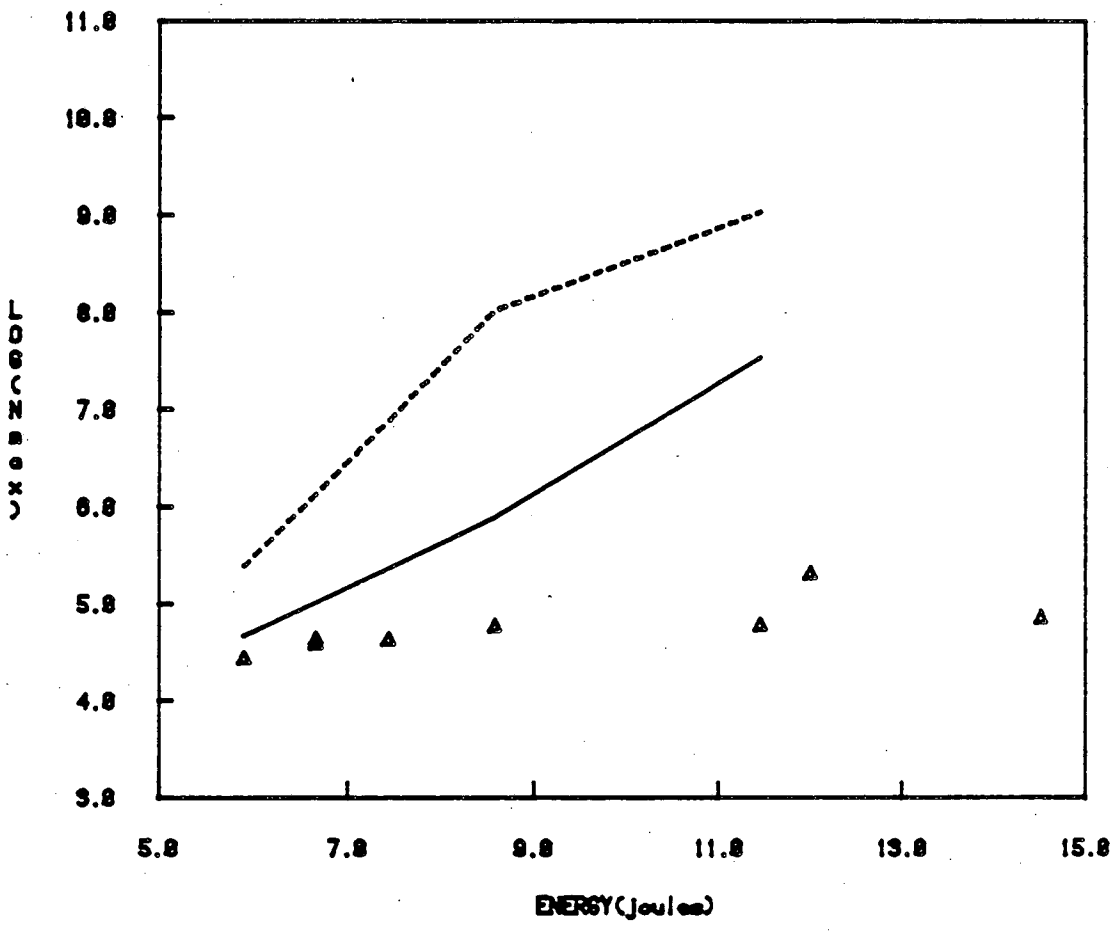

Fig. 4-13. Maximum number density of C_3 vs energy.

at low energies (< 7 J). However, they basically remain constant at higher energies and even decrease at the highest incident energy.

There are several possible explanations for the discrepancy between the measured and calculated maximum number densities,

(a) lack of laser heating of the surface

(b) cluster formation and liquid droplets in the vapor

(c) an abnormal angular distribution of the evaporated species

(d) depletion of one of the species (U or C) at the surface

(e) backscattering of the molecules due to collisions in the vapor

(f) thermal ionization of the vapor molecules

(g) actual partial pressures lower than theoretical estimation

(h) non-unity evaporation coefficient.

In the following paragraphs each possibility is considered.

(a) The temperature measurements for different incident laser energies (given in Appendix D) and the scanning electron micrographs of laser irradiated targets for incident laser energies of 12J and 8J (shown in Fig. 4-15) strongly support that the laser energy reaches the target surface and that the surface temperature and radial extent of melting go up consistently as the laser energy increases. There is no evidence of shielding of the surface from laser irradiation at any laser pulse energy.

(b) The absence of uranium dimers (U_2^+) and also low (C_3^+) signal suggests that cluster formation or gross condensation due to collisions is negligible. The absence of liquid droplets on the aluminum disk placed in front of the target during a laser pulse experiment (Section IV.6) also shows that the blowoff consisted solely of vapor molecules.

(c) In a similar study, the angular distribution of the vapor measured by Tsai [10] showed a $\cos^n\theta$ distribution, n being between 1 and 2. Therefore, the angular distribution is not too far from the $\cos\theta$ distribution and its effect on the number densities is very small.

(d) The maximum number densities of all species behave similarly with increasing laser pulse energy which means that improper theoretical treatment (Section II.2) of depletion of one element due to the effect of incongruent vaporization and diffusion-limited replenishment of the surface on the rate of vaporization cannot be the reason for low values of the number densities.

(e) The reduction in the net rate of evaporation due to the backscattering of the molecules in a collision dominated flow, which is at most 18% [35], cannot be responsible for a factor of 100 difference between measured and calculated number densities at high laser energies.

(f) The results of the ion collection experiments given in Section IV.4 shows that about 16% of the molecules are thermally ionized, so the possibility of low neutral molecule number densities due to ionization is eliminated.

(g) The only total vapor pressure measurement on uranium carbide has been reported by Ohse et al. [11] who used a laser heating technique to obtain vapor pressure data in the temperature range 6400K to 7000K. However, in this 600K temperature range there was practically no variation in the measured vapor pressure. This behavior is remarkably similar to that seen in Figs. (4-10) - (4-13) although Ohse's data represent higher temperatures and larger evaporation rates.

(h) The evaporation coefficient, whose value is between zero and one, is as important in vapor pressure measurements as the surface emissivity is in the surface temperature measurements. Unfortunately the measurement of evaporation coefficients is very difficult and experimental data in the literature are nonexistent. For UO_2, vaporization of UO_2 is predicted theoretically to proceed at the equilibrium rate [69].

In Table 4-1 the measured ratios of maximum number densities of UC_2 to U and C_3 to C are given. Also shown in this table are the results of calculations based on calculated temperatures and measured temperatures. The measured results for $n_{UC_2}^{max} / n_U^{max}$ agree fairly well with the results of two calculations, falling in the middle of the predictions. The theoretical predictions of the prepondance of atomic uranium over UC_2 and the total absence of UC appear to be valid at very high temperatures. For $n_{C_3}^{max} / n_C^{max}$, however, the measured values are as much as order of magnitude lower than the calculated ones.

Table 4.2 shows the calculated and measured times of the maxima of U^+ and UC_2^+ signals for each laser energy. The ratios of the times of maxima are also given. Although the predicted arrival times decrease as the laser energy increase (because of the higher surface temperatures achieved), the experimental values show the opposite tendency. The region of "sluggish" U and UC_2 (i.e. for E > ~9J) roughly corresponds to the regime in which the magnitude of the signals are far below predictions based on extrapolated pressures and an equilibrium vaporization model. The experimental arrival time ratios shown in

TABLE 4.1.
The ratios of maximum densities of UC_2 to U and C_3 to C.

Run No.	E (J)	$n_{UC_2}^{max} / n_U^{max}$			$n_{C_3}^{max} / n_C^{max}$		
		Theory*	Theory**	Exp	Theory*	Theory**	Exp
I	5.9	.020	.029	.022	6.71	5.41	.89
II	6.7	.026	.044	.033	6.79	3.74	.33
III	6.7	.026	.031	.026	6.79	5.26	.25
IV	7.4	.030	.163	.032	5.50	1.39	.14
V	8.6	.034	.136	.023	4.89	1.53	.40
VI	11.5	.094	.311	.101	2.09	.83	.25
VII	12.0	.130	.437	.074	1.67	.64	.34
VIII	14.5	.200	1.37	.64	.65	.28	.22

* Based on calculated temperatures.
** Based on measured temperatures.

TABLE 4.2.
Time of Maximum of U and UC_2 Signals

Run No.	E (J)	Time of max of U Signal (msec) Theory (a)	Theory (b)	Exp	Time of max of UC_2 Signal (msec) Theory (a)	Theory (b)	Exp	Ratio of Times of Max Theory (a)	Theory (b)	Exp
I	5.9	.82	.84	.65	.85	.87	.80	1.01	1.04	1.23
II	6.7	.79	.84	.68	.82	.87	.85	1.03	1.04	1.25
III	6.7	.83	.84	.70	.86	.87	.70	1.04	1.04	1.00
IV	7.4	.75	.83	.68	.76	.85	.68	1.01	1.02	1.00
V	8.6	.73	.82	.73	.75	.85	.80	1.03	1.04	1.10
VI	11.5	.67	.76	.84	.69	.78	.95	1.03	1.03	1.13
VII	12.0	.67	.73	.83	.68	.76	.90	1.01	1.04	1.08
VIII	14.5	.62	.71	.81	.64	.72	.87	1.03	1.01	1.07

a: Based on measured temperature.
b: Based on calculated temperature (mean values).

the last column are in good agreement with the calculated values and are consistent with the relative masses of U and UC_2.

Table 4.3 shows the corresponding times of the maxima for the C^+ and C_3^+ signals. The ratios of the two are also given. The experimental results are in generally good agreement with the calculated ones. The atomic carbon results are particularly in good agreement with predictions, both with respect to the magnitude of time of arrival and the variation with laser energy. The experimental trimer times-of-arrival, on the other hand, are all larger than the expected thermal equilibrium values and do not vary appreciably with laser energy. The ratios of the arrival times of C_3 and C shown in Table 4.3 are somewhat larger than expected from the theoretical calculation; the former are closer to the simplistic square-root-of-mass-ratios rule of thumb, however.

IV.3 Gas Phase Composition

To estimate the vapor composition from the experiment, it is assumed that the vapor composition at the target surface can be approximated by that in the ionizer. Using number densities instead of partial pressures we can write:

$$(C/U)_{gas} = \frac{P_C + 3\,P_{C_3} + P_{UC_2}}{P_U + P_{UC_2}} = \frac{n_C^{max} + 3\,n_{C_3}^{max} + 2\,n_{UC_2}^{max}}{n_U^{max} + n_{UC_2}^{max}} \quad . \tag{4.1}$$

The experimental results as well as the theoretical ones are shown in Table 4.4. Except for the highest energy laser pulse, the C/U ratios of the gas agree tolerably with predicted values, including carbon enrichment of the gas at high temperature. The vapor is leaner in carbon than the solid ($(C/U)_{initial} = 1.05$), so the vaporization

TABLE 4.3.
Time of Maximum of C and C_3 Signals

Run No.	E (J)	Time of max of C			Time of max of C_3			Ratio of Times of Max		
		Theory		Exp	Theory		Exp	Theory		Exp
		(a)	(b)		(a)	(b)		(a)	(b)	
I	5.9	.32	.35	.35	.43	.45	.50	1.34	1.29	1.7
II	6.7	.31	.35	.30	.42	.45	.48	1.35	1.29	1.6
III	6.7	.34	.35	.27	.45	.45	.37	1.32	1.29	1.4
IV	7.4	.31	.32	.25	.40	.44	.54	1.29	1.38	2.1
V	8.6	.29	.32	.25	.31	.43	.40	1.31	1.34	1.6
VI	11.5	.25	.30	.27	.34	.40	.47	1.36	1.33	1.9
VII	12.0	.26	.29	.20	.35	.39	.47	1.35	1.34	1.6
VIII	14.5	.25	.28	.20	.33	.38	.46	1.32	1.36	2.3

a: Based on measured temperature.
b: Based on calculated temperature.

TABLE 4.4.
Carbon-to-Uranium Ratio in the Gas Phase.

Run No.	E_i (J)	T_s^{max}(K) Calc(a)	T_s^{max}(K) Meas(b)	THEORY $(C/U)_{gas}$ (a)	THEORY $(C/U)_{gas}$ (b)	EXPERIMENT $(C/U)_{gas}$
I	5.9	2701	2910	.15	.13	.17
II	6.7	2819	3136	.22	.13	.26
III	6.7	2819	2959	.15	.13	.21
IV	7.4	2945	3250	.64	.15	.24
V	8.6	3001	3765	.57	.16	.19
VI	11.5	3535	4230	1.08	.41	.70
VII	12.0	3719	4479	1.37	.53	.57
VIII	14.5	4205	5290	2.65	2.55	.47

(a): Based on calculated temperatures (mean property value).

(b): Based on measured temperatures.

process enriches the surface in this element. The reduction of the (C/U) of the solid surface is recognized in the theory of Section II.2 which is used to calculate $T_s(t)$ and in Section II.3 when n(t) is calculated.

IV.4 Ion Collection

As part of the mass spectrometric measurements described in previous sections, the ionizer emission current was set to zero in order to detect the fast thermal ions without detecting neutrals. Even at the highest laser energy, no ion signal was detected. No ions were observed even when the "ion potential" setting of the mass spectrometer was set equal to zero, which removed the +15V bias of the ionizer cage. This means that either the low energy ions could not reach the ionizer of the mass spectrometer or there were no ions.

In a different set of experiments, a Faraday-cup was used to collect all the ions emitted by the surface (Section III.1.3). Figure 4.14 shows a typical ion signal recorded by the transient recorder along with the usual laser power trace. The total charge collected in each shot was calculated by integrating the ion signal: $Q = \int_0^t \frac{V(t)}{R}\,dt$, R being the resistance of the external circuit. Since the majority of the ions are expected to be singly charged, the total number of ions is obtained by dividing the total charge collected by the electronic charge. Table 4.5 shows the number of ions collected versus incident laser energy. Since the percentage of the molecules which are thermally ionized increases with temperature [68], the number of ions collected should have sharply increased. But as Table 4.5 shows the number of ions increases only by a factor of 4 for a temperature range 3000K to 4500K.

The degree of ionization for each laser shot is obtained by dividing the total number of ions by the actual number of molecules evaporated. The latter is obtained in the following way:
The equilibrium rate of evaporation of species i is given by the Hertz-Langmuir equation as:

$$R_i = \frac{\alpha_i P_i(T_s, X_s) A_s}{\sqrt{2\pi m_i k T_s}} \tag{4.2}$$

where

R_i = evaporation rate of species i (i = U, UC_2, C, C_3), molecules/C_m^2-sec

P_i = partial pressure of species i, dyne/C_m^2

α_i = evaporation coefficient of species i (assumed unity)

T_s = measured surface temperature, K

X_s = surface composition

A_s = effective laser spot area

m_i = molecular mass of species i, grams

k = Boltzman constant, ergs/K.

The theoretical total number of molecules of species i evaporated in one laser shot is obtained by integrating equation (4-2) over the laser pulse time.

$$(Q_i)_{theory} = \int_0^\infty R_i(t)dt \tag{4-3}$$

where $(Q_i)_{theory}$ calculated number of molecules of species i evaporated in one laser shot. Let's define f_i as

$$f_i = \frac{(n_i^{max})_{exp}}{(n_i^{max})_{theory}}$$

where $(n_i^{max})_{exp}$ = The measured maximum number density of species i in the ionizer.

$(n_i^{max})_{theory}$ = The calculated maximum number density of species i in the ionizer.

The values of f_i as a function of incident laser energy are obtained from Figs. (4-10) - (4-13).

The actual number of molecules of species i evaporated in one laser shot can be obtained as:

$$(Q_i)_{actual} = f_i(Q_i)_{theory}. \qquad (4-4)$$

The total number of vapor molecules evaporated in one laser shot, $(Q)_{actual}$ is obtained by summing over the contribution of all vapor species as:

$$(Q)_{actual} = \sum_{\substack{i=U,UC_2,\\ C,C_3}} f_i(Q_i)_{theory}. \qquad (4-5)$$

The values of $(Q)_{actual}$ and the degree of ionization for different laser energies are given in Table 4.5.

IV.5 Surface Morphology

Figure 4.15.1 and 4.15.2 show the scanning electron micrographs of UC samples irradiated by (1) five 12-J energy laser pulses and (2) five 8-J energy laser pulses respectively. The liquid movement away from the center of the laser spot due to the recoil forces of the evaporating material [50] is very well displayed in these pictures. The

TABLE 4.5
The Total Number of Ions Collected
and Degree of Ionization of the Vapor

E_i(j)	Measured max T_s (K)	No. of Ions Collected	Total No.* of Vapor Molecules	Percent Ionization
6.4	3000	2.5×10^{13}	1.6×10^{14}	16
8.1	3560	4.0×10^{13}	3.9×10^{14}	10
10.1	4050	6.0×10^{13}	3.6×10^{14}	17
12.8	4600	1.4×10^{14}	8.1×10^{14}	17

*See text

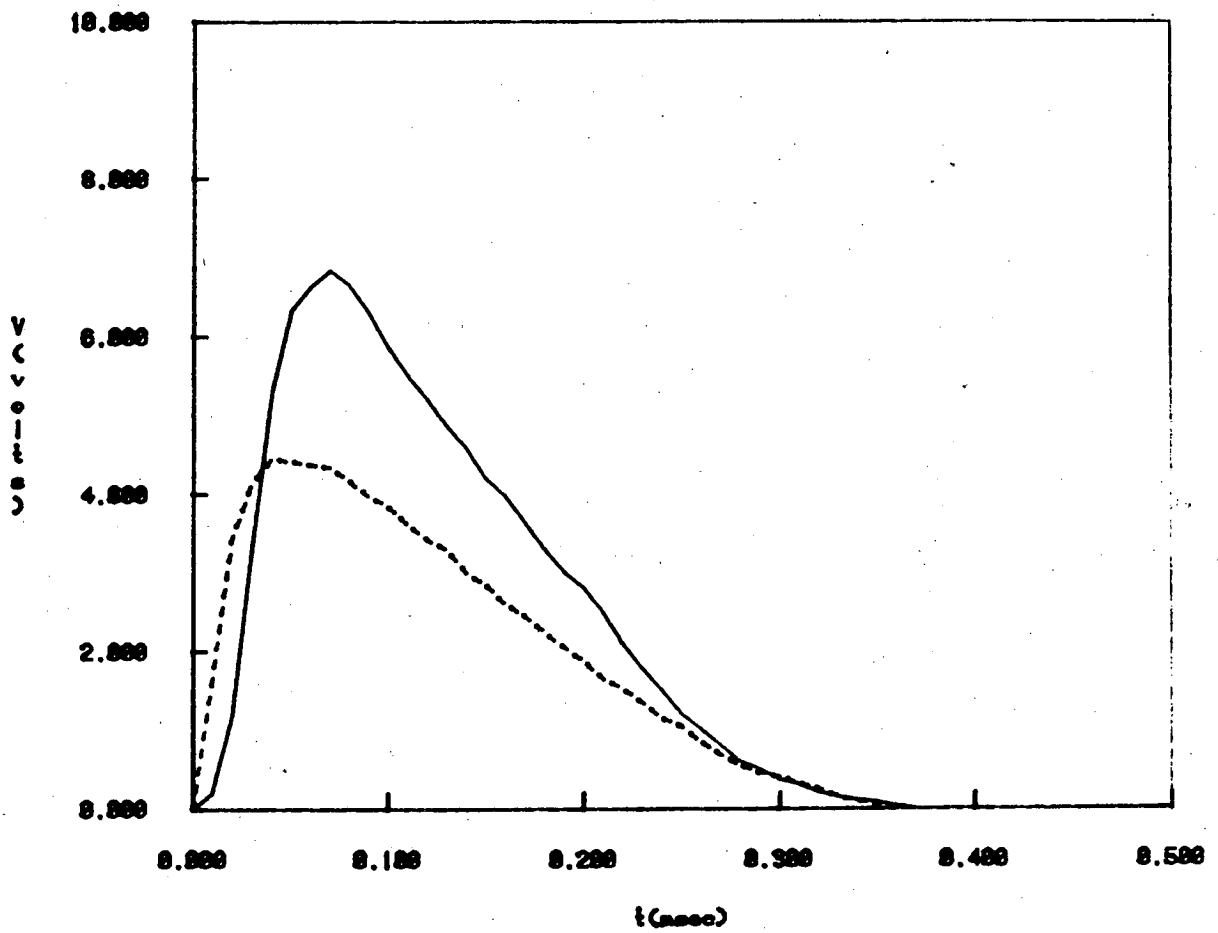

Fig. 4-14. In signal and laser power shape.

solid line-ion signal
dotted line-power signal

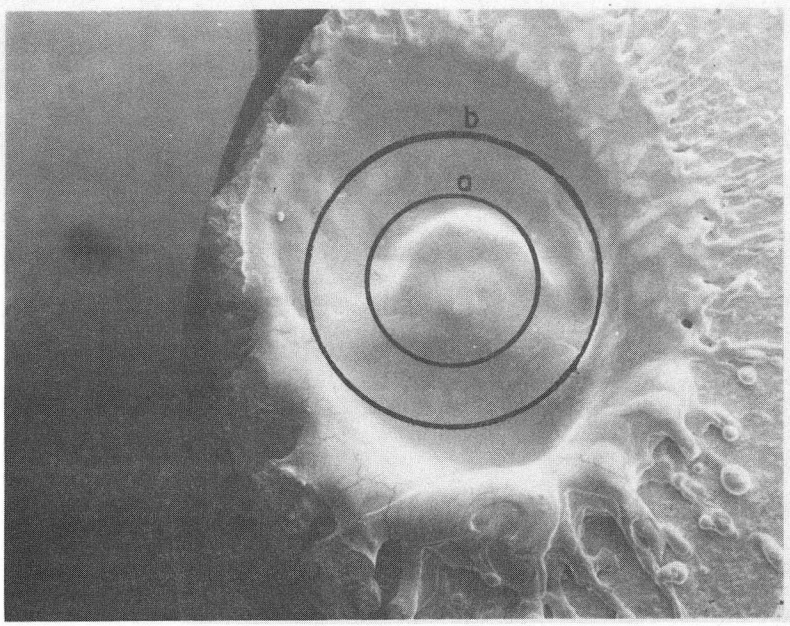

(1)

1mm

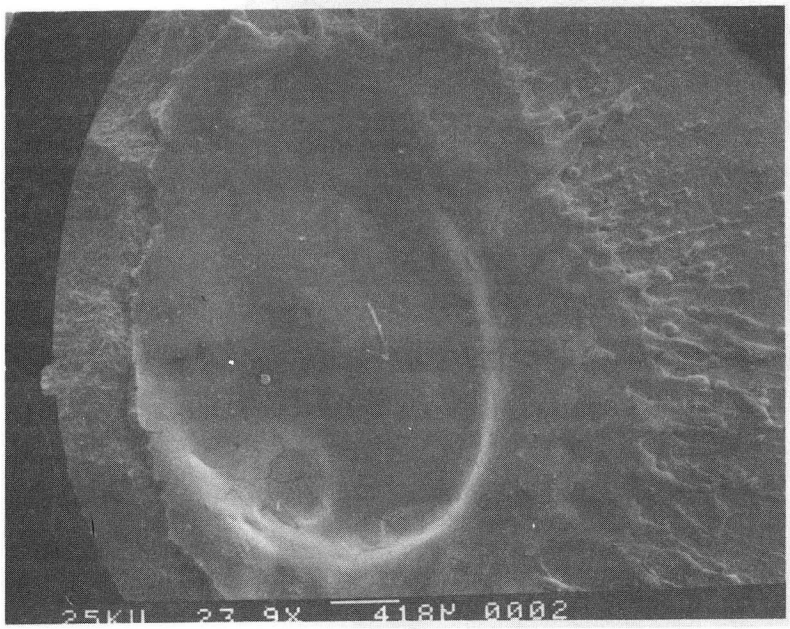

(2)

XBB 833-2071

Fig. 4-15. Scanning electron micrographs of laser irradiated target signal (1) five 12-J pulses, (2) five 8-J pulses. (1) Optical pyrometer viewing spot (~ 1.7mm in diameter). (2) Mass spectrometer viewing spot (~ 1mm in diameter).

melted zone is an ellipse with major and minor diameters of ~ 2.5 mm and 2.0 mm, respectively.

Figure 4.16.a and 4.16.b show high-magnification scanning electron micrographs of the target surface before and after a laser shot. The UC surface before irradiation (Fig. 4.16.b) shows distinct grain structure, whereas the same surface after being irradiated, (Fig. 4.16.a) contrary to UO_2 which maintains the grain structure [10], has completely different structure.

Due to the high rate of evaporation of the laser irradiated material a crater is produced at the focal spot as shown in Fig. 4.15. Ready [51] has experimentally determined the relation between the depth of a crater produced by a laser shot and the surface temperature. Ohse [52] and Tsai [10] measured the depth of the crater create in UO_2 samples by an inductive sensor tip scanning across the creater profile. The same method is used in this study to measure the crater depth in UC samples. Figure 4.17.a and 4.17.b show the crater depth profile along the major and minor axis respectively. Due to the contribution of the liquid movement to the depth of the crater, any estimation of the vaporized material from the depth profile of the crater [10] results in large errors.

IV.6 Liquid Droplets in the Vapor

To determine if the blowoff consisted solely of vapor molecules or also contained liquid droplets, an aluminum disk was placed in front of the target during one experiment. The surface of the disk was then examined by the Scanning Electron Microscope and EDAX (for elemental analysis). Figure 4.18.a is the scanning electron micrograph of the

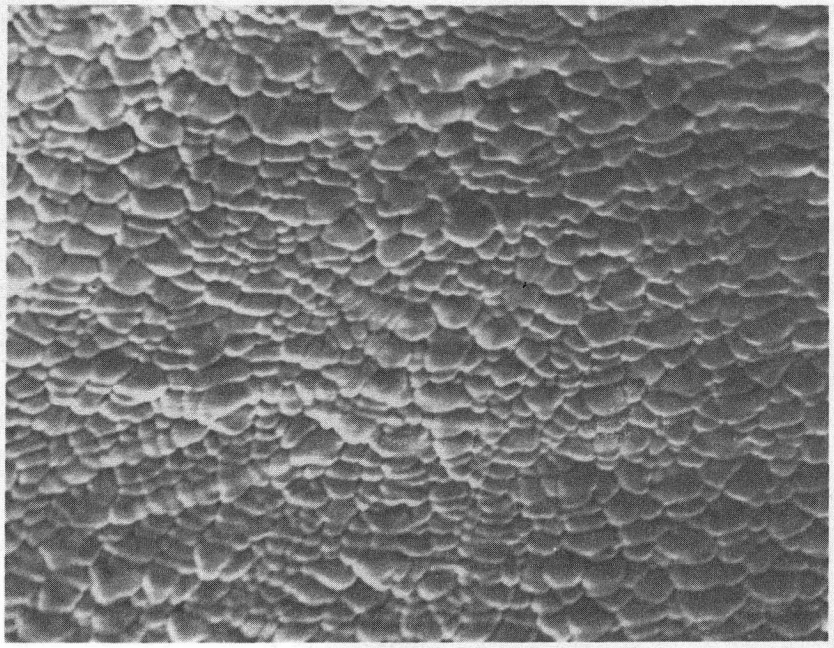

(a)

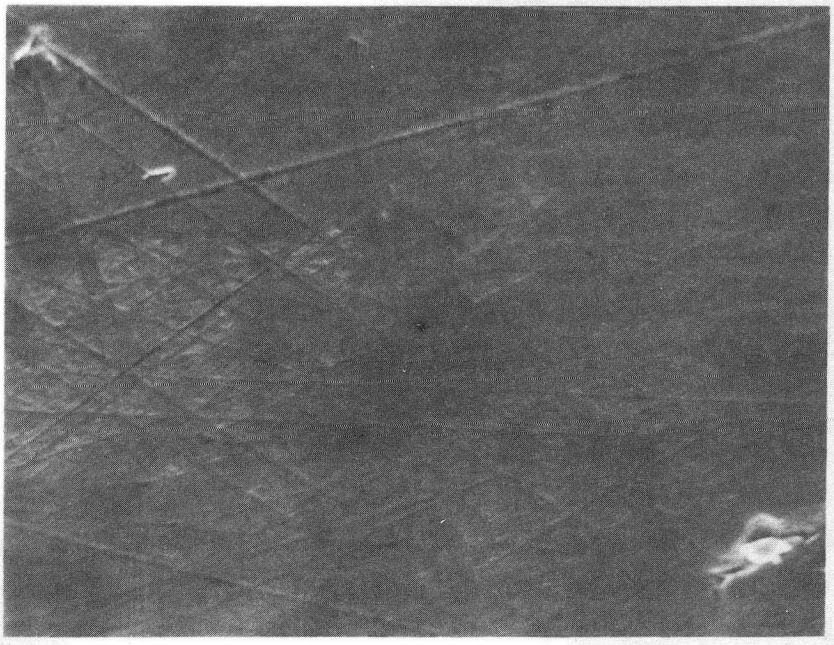

(b)

XBB 833-2070

Fig. 4-16. Scanning electromicrograph of,
(a) Laser-irradiated spot and
(b) Target surface before laser shot.

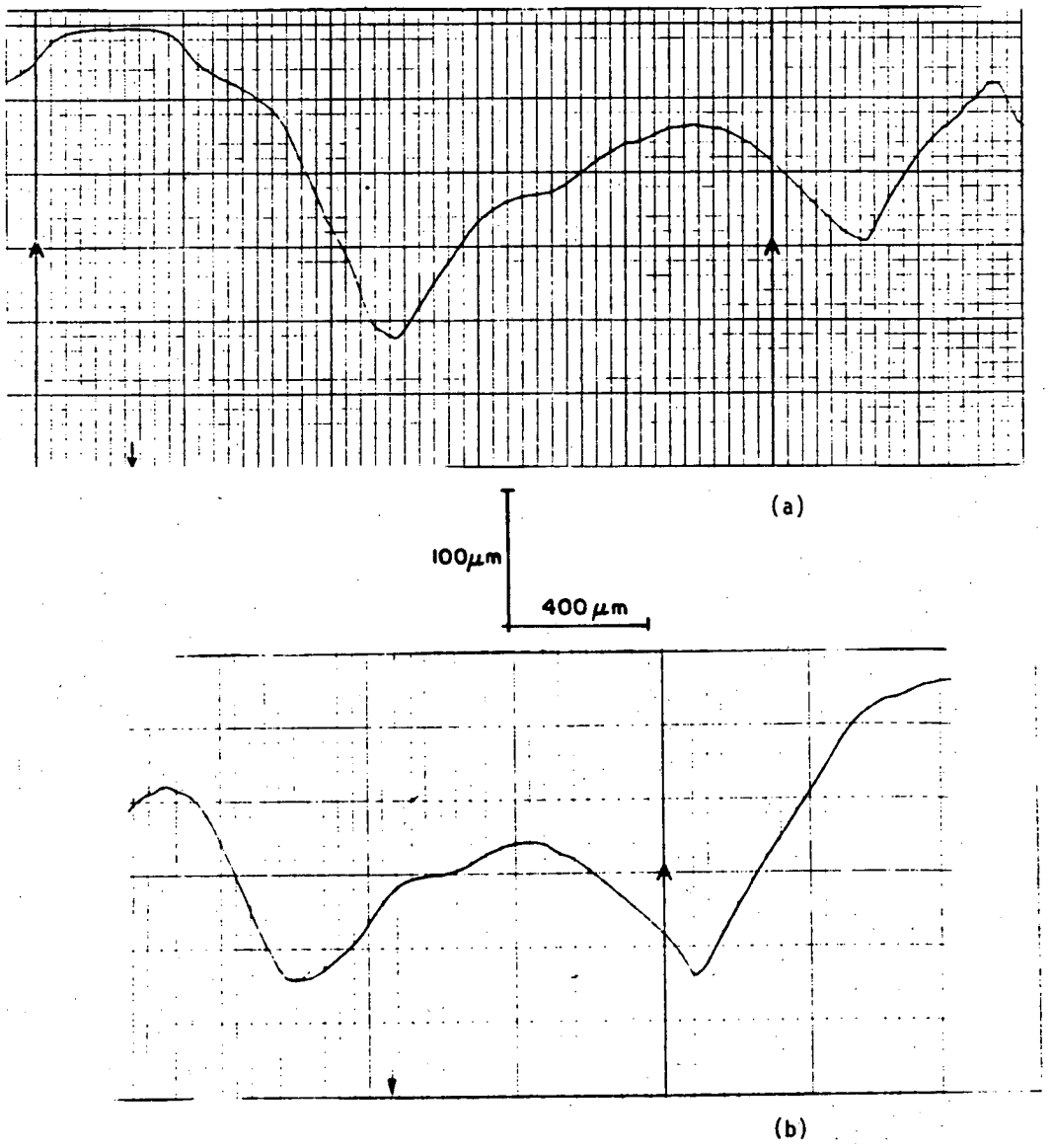

Fig. 4-17. (a) Crater depth profile along the major axis.
(b) Crater depth profile along the minor axis.

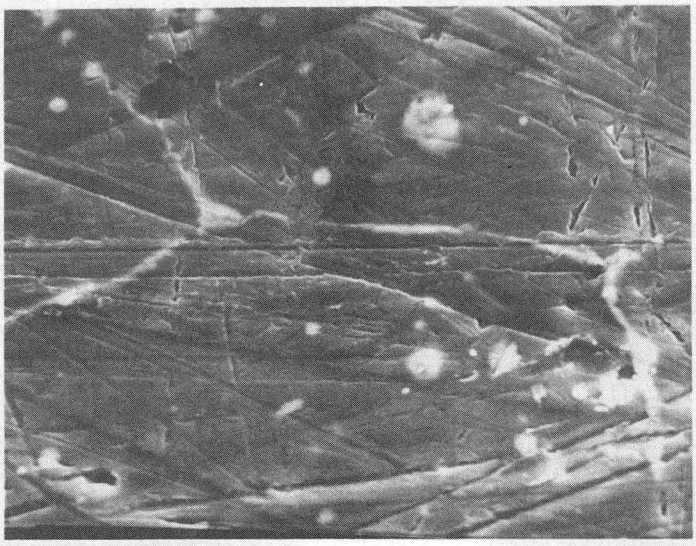

(a)

(b)

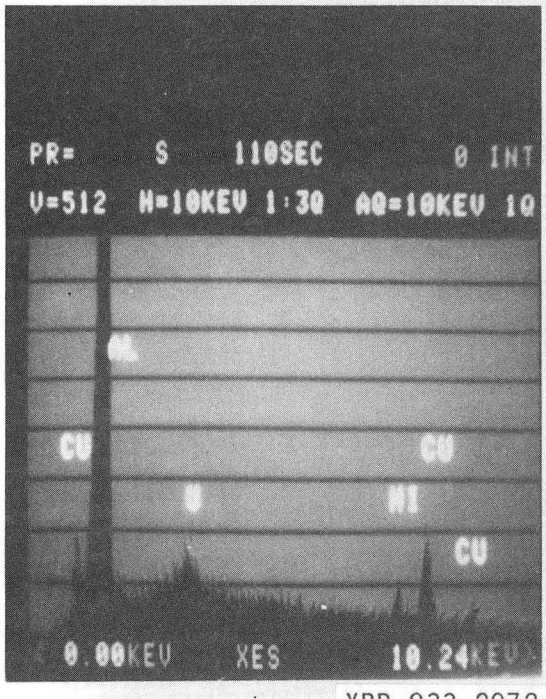

(c)

XBB 833-2072

Fig. 4-18. (a) Scanning electromicrograph of aluminum disk surface.
(b) EDAX analysis of the white spots in (a).
(c) EDAX analysis of the dark area in (a).

disk surface which show a dark area along with some white spots of different sizes. Figure 4.18.b and 4.18.c show the EDAX analysis of the white spots and the dark area on the surface. The amplitude of the U peak on the white spots and the dark area is the same. This suggests that the white spots are not previously-liquid droplets of UC. On the other hand the difference in Cu and Fe peaks shows that the white spots are simply surface impurities in the aluminum mainly copper and iron. The result of this study is contrary to the result of a similar study by Tsai [10], who observed UO_2 droplets with radii of 1μm to 15μm. The use of low-porosity UC samples (ρ = 99% of theoretical density) and the resulting lack of microexplosions beneath the surface due to the high porosity [10,52], may be the reason for the different result obtained in this study.

V. CONCLUSION

The partial pressures of different vapor species over liquid $UC_{1\pm x}$ were calculated by extrapolating the low temperature uranium and carbon activities into the liquid phase.

The heat conduction and species diffusion equations were solved numerically to obtain temperature and surface composition profiles. A sensitivity analysis was done to study the effect of uncertainties in the thermal conductivity, spectral reflectivity and effective laser spot area on the temperature profile. A variance of 10% was obtained for the surface temperature calculation due to the uncertainties. The pyrometrically measured temperatures were in the uncertainty limits of the calculated ones. The discrepency between measured and calculated temperatures is mainly due to the uncertainty in the spectral reflectivity and emissivity of the surface.

Different vapor species were identified by the mass spectrometer and their rates of evaporation were measured. Comparison of the time-of-arrival and the width of the measured mass spectrometer signals with the calculations based on free-molecule model and hydrodynamic model suggested that the former best represents the expansion process in the vacuum. At high laser energies the rates of evaporation for all the species were one to two orders of magnitude smaller than the equilibrium rates given by the Hertz-Langmuir equation. This difference is believed to be due to either lower-than-predicted-vapor pressures or evaporation coefficients considerably less than unity. The region of greatest disagreement of the

experimental and calculated number densities also exhibited very significant retardation of the uranium-bearing species compared to expectations based on thermal velocity transit times.

The degree of ionization of the vapor was measured by a Faraday cup. The fraction ionized was found to be ~0.15, independent of temperature.

APPENDIX A

THERMODYNAMIC DATA AND MATERIAL PROPERTIES OF UC

A-1 Density

The theoretical density of solid UC at room temperature is 13.5 g/cm^3. Using the average linear thermal expansion coefficient from room temperature to the melting point ($1.30 \times 10^{-5}/K$) given by Sheth [53] we find the the temperature dependence of the density for the solid UC to be

$$\rho = 13.5\ [1-3.9 \times 10^{-5}\ (T-300)]. \qquad \text{(A-1)}$$

The density of liquid UC has been given [53] as:

$$\rho = \frac{12.57}{1+9.98 \times 10^{-5} T} \qquad T > 2780K \qquad \text{(A-2)}$$

where ρ is in g/cm^3 and T is in K.

A-2 Thermal Conductivity

Based on the data obtained by Lewis and Kerrisk [54], Sheth et al. derived the following equations for the thermal conductivity of 100% theoretically dense UC below melting point.

$$k = 0.0519 - 7.266 \times 10^{-6} T + 8.628 \times 10^{-9} T^2; \quad 50 < T^{\circ}C < 700 \qquad \text{(A-3)}$$

$$k = 0.0483 + 3.537 \times 10^{-6} T \ ; \quad 700 < T^{\circ}C < 2507 \qquad \text{(A-4)}$$

where k is the cal/sec-cm-°C and T is in °C.

For the liquid UC the empirical approach of Tumbull [55] has been used [53] to obtain the thermal conductivity at the melting point as:

$$k = 0.049 \text{ cal/sec-cm-}^{\circ}C. \qquad \text{(A-5)}$$

This value is recommended [53] and used in our calculations for the whole liquid region.

A-3 Specific Heat

Based on the values for heat capacity of UC below melting point recommended by Tetenbaum et al., [56] the following equation has been derived [53] for the heat capacity of solid UC up to the melting temperature.

$$C_p = 14.727-5.3466\times10^{-4}T+9.9912\times10^{-7}T^2-\frac{2.3797\times10^5}{T^2} \quad 300K<T<2780K \quad (A-6)$$

where C_p is in cal/mole-K and T is in Kelvin.

The heat capacity of UC in the liquid region has been estimated [53] and is given by:

$$C_p = 11.9232 + 1.8629\times10^{-3}T \qquad T>2780K \qquad (A-7)$$

At the melting point there is a discontinuity in the enthalpy due to the phase change. In the thermal modeling of Section II.2 the heat of fusion is taken into consideration by defining an effective molar heat capacity in the following way:

The molar enthalpy of UC above melting point can be expressed in terms of heat of fusion and the molar heat cap capacity at constant pressure as:

$$H^\circ(T) = H^\circ_{298} + \Delta H_f + \int_{298}^{T} C_p \, dT' \qquad (A-8)$$

where H°_{298} is the standard molar enthalpy at 298K and ΔH_f is the heat of fusion. We define an effective heat capacity $C_p'(T)$:

$$C_p'(T) = C_p(T) + \Delta H_f \delta(T-T_{mp}) \qquad (A-9)$$

substituting for $C_p(T)$ in eq. (A-8) from eq. (A-9) we get:

$$H^\circ(T) = H^\circ_{298} + \int_{298}^{T} C_p' \, dT' \qquad (A-10)$$

Since discontinuities in material properties are not desirable in the numerical solution of the conduction equation, the heat capacity is approximated by a continuous function of temperature. Instead of using a delta function to account for the heat of fusion, a Gaussian function of finite width centered at the melting point is used [11].

Let $C_{pp} = \Delta H_f \, \delta(T-T_{mp})$ be approximated by a function of Gaussian form:

$$C_{pp} = \frac{\Delta H_f}{\pi \, \sigma_1} \exp \left(- \frac{(T-T_{mp})^2}{\sigma_1^2} \right) \tag{A-11}$$

where ΔH_f = 195 J/g [23]

T_{mp} = 2780K [57]

σ_1 = half width of heat of fusion peak = 50K (arbitrary)

and the apparent specific heat

$$C_p' = C_p + C_{pp}. \tag{A-12}$$

A-5 Heat of Vaporization

The heat of vaporization of solid UC, ΔH_s is 5.36×10^5 J/mole [33].

A-6 Diffusion Coefficient

The diffusion coefficient of carbon in solid $UC_{1\pm x}$ has been measured [58] for different compositions. For compositions close to stoichiometric the diffusion coefficient varies sharply with composition but levels off for compositions above $UC_{1.1}$. In our calculations the result of measurement by Chubb et al., [59] for $UC_{1.04}$ is used. The diffusion carbon coefficient in the solid is expressed by the equation

$$D_c = 0.02 \exp(-25252./T) \text{ cm}^2/\text{sec}. \tag{A-13}$$

The binary diffusion of carbon and uranium in liquid UC is not known. An estimate of the diffusion coefficient (D) at the melting point is made by using the Nernst-Einstein theory.

$$\frac{D\mu}{KT} = \frac{1}{6\pi R_c} \qquad \text{(A-14)}$$

where μ is the viscosity of the mixture and R_c is the atomic radius of the diffusing component (carbon). Using this equation for the uranium-carbon liquid mixture we obtain a value of 2.6×10^{-5} cm^2/sec for D at the melting point.

At the critical point (T = 9750K[37]) of UC there is no distinction between liquid and gas, so the diffusion coefficient at this temperature can be obtained by using kinetic gas theory. For rigid spheres of unequal mass and diameters the following equation has been derived for the diffusion ceofficient of a binary gas mixture [60].

$$D = 2/3 \left(\frac{K^3}{\pi^3}\right)^{1/2} \left(\frac{1}{2m_U} + \frac{1}{2m_C}\right)^{1/2} \frac{T^{3/2}}{p\left(\frac{d_U+d_C}{2}\right)^2} \qquad \text{(A-15)}$$

where K = Boltzmann constant, 1.38×10^{-16} erg/K

p = pressure, dyn/cm^2

T = Temperature, K

m_C, m_U = atomic diameters of the two components [61], cm.

Using this equation for UC at the critical point results in a value of 1.11×10^{-2} cm^2/sec for D at 9750K. This value of D along with the one obtained at the melting temperature are used to derive the following equation for the diffusion coefficient in the liquid

$$D = 0.114 \exp(-2.33\times10^{4}/T) \qquad \text{(A-16)}$$

A-7 Optical Emissivity

The normal spectral emissivity ($\varepsilon_{.65\ \mu m}$) as well as total normal emissivity (ε_t) of solid UC has been measured by Grossman [62] and Deconinck [63].

The values measured by Grossman have been recommended [53] and are given as follows:

$$\begin{aligned} \varepsilon_t &= 0.42 \pm 0.02 \quad ; 1250K<T<1980K \\ \varepsilon_{0.65\ \mu m} &= 0.539 - 2\times10^{-5}T; \ 1150K<T<1890K. \end{aligned} \qquad \text{(A-17)}$$

The normal spectral emissivity of UC at 0.63 has been measured by M. Bober [26] up to 4200K and the results is shown in Fig. A-1. The spectral emissivity is used in the pyrometric temperature measurements.

The spectral directional-hemispherical reflectance $R_\lambda(\theta;2\pi)$ of the sample surface is related to the directinal emissivity $\varepsilon_\lambda(\theta)$ by Kirchhoff's Law as:

$$R_\lambda(\theta;2\pi) = 1 - \varepsilon_\lambda(\theta). \qquad \text{(A-18)}$$

To know the laser energy deposited on the target the spectral reflectivity at 1.06 μm (laser wavelength) should be given. In the absence of such information the value measured at 0.63 μm is used in the calculations.

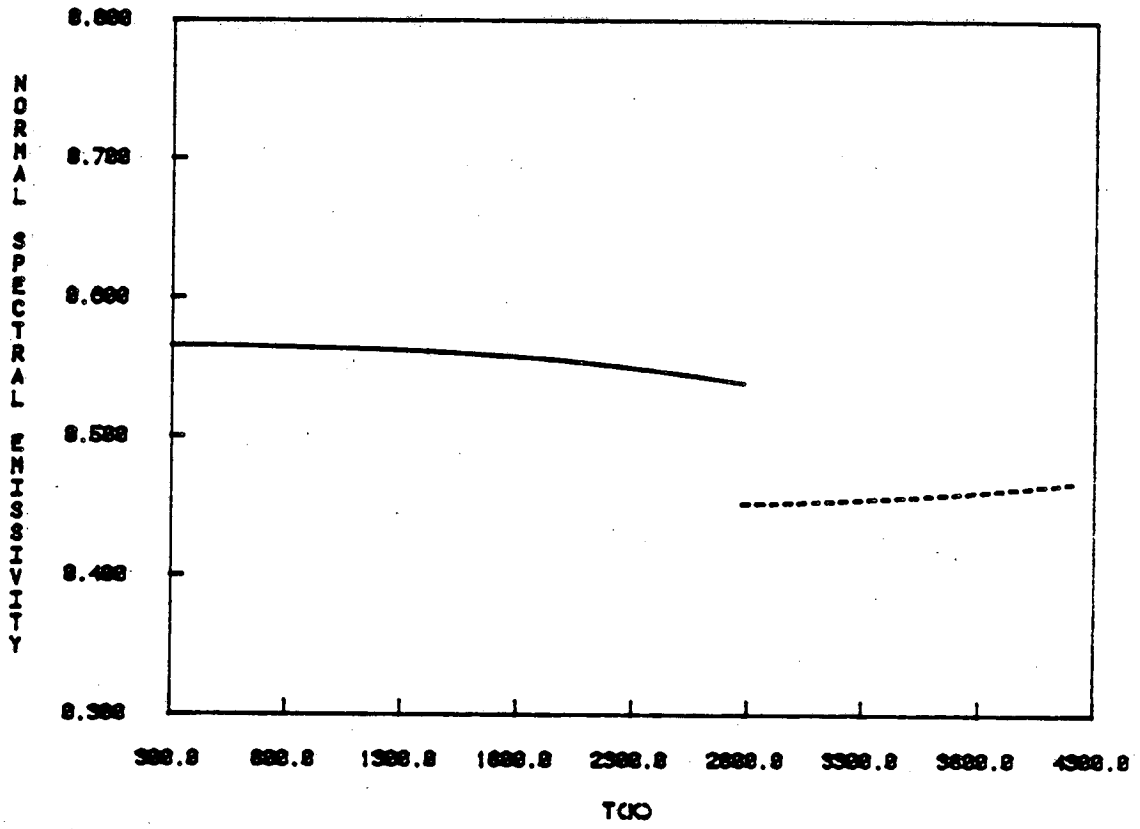

Fig. A-1. The normal spectral emissivity ($\varepsilon_{0.63}$) of uranium carbide [47].

APPENDIX B

SURFACE TEMPERATURE SENSITIVITY ANALYSIS

To study the effect of uncertainties in the material properties given in Appendix A on temperature calculations of Section II.2, The Response Surface Method (RSM) [45,46] used by C. H. Tsai [10] for UO_2 is applied to UC.

B.1 Response Surface Method

In this method, each of the outputs of the code (e.g., surface temperature or surface composition) is called a "Response". The response of each of the outputs to the input variables produces a surface called "Response Surface". The Response Surface Method is based on a systematic sampling of the true surface response which is then approximated by a polynomial equation in the input variables.

If $Y(Z_i)$ is one of the outputs of the code as a function of the input variables (Z_i, Z_2, Z_3, ...) the Taylor' series expansion of Y about any point μ_i will be

$$Y(Z_i) = Y(\mu_i) + \sum_{i=1}^{k} \frac{\partial Y(\mu_i)}{\partial Z_i} (Z_i-\mu_i) + \frac{1}{2} \sum_{i=1}^{k} \frac{\partial^2 Y(\mu_i}{\partial Z_i^2} (Zi-\mu_i)^2 + \sum_{ij>i}^{k} \frac{\partial^2 Y(\mu_i)}{\partial Z_i \partial Z_j} (Z_i-\mu_i)\,(Z_j-\mu_i) + \text{higher order terms.} \tag{B-1}$$

It has been shown that a range of plus and minus one standard deviation ($\pm 1\sigma$) in the input variable uncertainties permit construction of a sample surface small enough for approximating the response surface by a second order polynomial. Multiplying and dividing each term of Eq. (B-1) by one standard deviation, σ_i, of the respective variable and defining the following parameters:

$$C_0 = Y(\mu_i)$$

$$C_i = \frac{\partial Y(\mu_i)}{\partial Z_i}\,\sigma_i$$

$$C_{ii} = \frac{1}{2}\,\frac{\partial^2 Y(\mu_i)}{\partial Z_i^{\,2}}\,\sigma_i^{\,2}$$

$$C_{ij} = \frac{\partial^2 Y(\mu_i)}{\partial Z_i^{\,2}}\,\sigma_i\sigma_j$$

and (B-3)

$$X_i = \frac{Z_i - \mu_i}{\sigma_i}$$

reduces Eq. (B-1) to a normal form:

$$Y(X_i) = C_0 + \sum_{i=1}^{k} C_i X_i + \sum_{i=1}^{k} C_{ii} X_i^{\,2} + \sum_{ij>i}^{k} C_{ij}\, X_i X_j \qquad \text{(B-4)}$$

The following steps comprise the analysis:

1) Make a choice of the output responses to be investigated and input variables to be perturbed.

2) Design a pattern of input variable perturbation; run the code as many times as the design dictates, each time varying the input variables according to the pattern.

3) Generate the response surface equations from the results of the runs.

4) Solve the response surface equations for the response parameters C's; estimate the mean and variances of the responses (second order mean $\mu = C_0 + \sum_{i=1}^{k} C_{ii}$ and variance $\sigma_Y^{\,2} = \sum_{i=1}^{k} C_i^{\,2} + \sum_{ij>i}^{k} C_{ij}^{\,2}$).

5) Estimate the fractional contributions of the input variables to the response variance ($FC_i = C_i^2 \Big/ \sum_{i=1}^{k} C_i^2$).

B.2 Perturbation Pattern

Two Level Factorial perturbation pattern [46] is used in this study. "Two Level" means that each input variable is evaluated at two different values (e.g., plus and minus one standard deviation). "Factorial" means that the input variables will be changed simultaneously, with permutations of the original pattern used to to obtain a sufficient number of runs. Each run produces one point on the response surface Y, and if n runs are required, a set of n equations with the form of Eq. (B-4) and coefficients either +1 or -1 is constructed to solve for the C's.

B.3 Sensitivity Study for UC Vaporization

The most uncertain input variables i.e., thermal conductivity of the liquid, the reflectivity and the effective laser spot area are considered. All the other variables are relatively accurate compared to the ones singled out above. The surface temperature is the only output variable considered. The surface composition is quite insensitive to the above input variables.

The response surface equations for the perturbation pattern considering only seven computer runs will be:

$$
\begin{aligned}
Y_1 &= C_0 + C_1 + C_2 + C_3 + C_{11} + C_{22} + C_{33} + C_{12} + C_{23} + C_{13} \\
Y_2 &= C_0 - C_1 + C_2 - C_3 + C_{11} + C_{22} + C_{33} - C_{12} - C_{23} + C_{13} \\
Y_3 &= C_0 + C_1 - C_2 + C_3 + C_{11} + C_{22} + C_{33} - C_{12} - C_{23} + C_{13} \\
Y_4 &= C_0 - C_1 + C_2 + C_3 + C_{11} + C_{22} + C_{33} + C_{12} + C_{23} - C_{13} \\
Y_5 &= C_0 - C_1 - C_2 - C_3 + C_{11} + C_{22} + C_{33} + C_{12} + C_{23} + C_{13} \\
Y_6 &= C_0 - C_1 - C_2 + C_3 + C_{11} + C_{22} + C_{33} + C_{12} - C_{23} - C_{13} \\
Y_7 &= C_0 + C_1 + C_2 - C_3 + C_{11} + C_{22} + C_{33} + C_{12} - C_{23} - C_{13}
\end{aligned}
\qquad \text{(B-5)}
$$

On the right hand side of these equations, subscript 1 denotes thermal conductivity, 2 denotes surface reflectivity at 1.06μ wavelength, and 3 denotes the effective laser spot area.

Letting $\mu = C_0 + C_{11} + C_{22} + C_{33}$, which is equal to the mean of Y, eq. (B.5) can be written as:

$$
\begin{bmatrix} Y_1 \\ Y_2 \\ Y_3 \\ Y_4 \\ Y_5 \\ Y_6 \\ Y_7 \end{bmatrix} = \begin{bmatrix} 1 & 1 & 1 & 1 & 1 & 1 & 1 \\ 1 & -1 & 1 & -1 & -1 & -1 & 1 \\ 1 & 1 & -1 & 1 & -1 & -1 & 1 \\ 1 & -1 & 1 & 1 & -1 & 1 & -1 \\ 1 & -1 & -1 & -1 & 1 & 1 & 1 \\ 1 & -1 & -1 & 1 & 1 & -1 & -1 \\ 1 & 1 & 1 & -1 & 1 & -1 & -1 \end{bmatrix} \begin{bmatrix} \mu \\ C_1 \\ C_2 \\ C_3 \\ C_{12} \\ C_{23} \\ C_{13} \end{bmatrix} \qquad \text{(B-6)}
$$

Applying Gaussian elimination to Eq. (B-6) we get:

$$\begin{bmatrix} 1 & 1 & 1 & 1 & 1 & 1 & 1 \\ 0 & 1 & 0 & 1 & 1 & 1 & 0 \\ 0 & 0 & 1 & 0 & 1 & 1 & 0 \\ 0 & 0 & 0 & 1 & 0 & 1 & -1 \\ 0 & 0 & 0 & 0 & 1 & 1 & 0 \\ 0 & 0 & 0 & 0 & 0 & 1 & 0 \\ 0 & 0 & 0 & 0 & 0 & 0 & 1 \end{bmatrix} \begin{bmatrix} \mu \\ C_1 \\ C_2 \\ C_3 \\ C_{12} \\ C_{23} \\ C_{13} \end{bmatrix} = \begin{bmatrix} Y_1 \\ \frac{1}{2}(Y_1-Y_2) \\ \frac{1}{2}(Y_1-Y_3) \\ \frac{1}{2}(Y_4-Y_2) \\ \frac{1}{4}(Y_1+Y_5-Y_2-Y_3) \\ \frac{1}{4}(Y_4+Y_5-Y_2-Y_6) \\ \frac{1}{4}(Y_1+Y_2-Y_4-Y_7) \end{bmatrix} \qquad \text{(B-7)}$$

This equation can be solved for μ and C_i's:

$$\begin{aligned} C_{13} &= \tfrac{1}{4}(Y_1+Y_2-Y_4-Y_7) \\ C_{23} &= \tfrac{1}{4}(Y_4+Y_5-Y_2-Y_6) \\ C_{12} &= \tfrac{1}{4}(Y_1+Y_6-Y_3-Y_4) \end{aligned} \qquad \text{(B-8)}$$

$$\begin{aligned} C_3 &= \frac{Y_4-Y_2}{2} - C_{23}+C_{13} \\ C_2 &= \frac{Y_1-Y_3}{2} - C_{12}-C_{13} \\ C_1 &= \frac{Y_1-Y_2}{2} - C_3-C_{12}-C_{13} \end{aligned}$$

Using the computed surface temperature response for different runs in eq. (B-8), the values of the C- coefficients are calculated. Finally the mean and variance of the surface temperature and the fractional contributions of the three input variables to the variance are calculated using eqs. (B-9) - (B-11).

$$\mu = Y_1-C_1-C_2-C_3-C_{12}-C_{13}-C_{23} \qquad \text{(B-9)}$$

$$\sigma_Y^2 = C_1^2+C_2^2+C_3^2+C_{12}^2+C_{13}^2+C_{23}^2 \qquad \text{(B-10)}$$

$$FC_i = C_i^2 \Big/ \sum_{i=1}^{k} C_i^2 \qquad \text{(B-11)}$$

APPENDIX C

A GAS DYNAMIC MODEL OF RAPID EVAPORATION OF A SOLID INTO A VACUUM

C.1 INTRODUCTION

Vaporization of a solid into vacuum has several practical applications. One laboratory-scale use is the measurement of the high temperature vapor pressure of refractory solids such as uranium dioxide by laser pulsing. A larger scale application is the description of the vaporization rate when the first wall of a fusion device is heated by radiation from the contained plasma. In both cases, the heat source deposits energy at or very close to the surface of the solid. In what follows, the steady state vaporization rate from a surface at specified temperature T_0 is determined. Application to transient surface heating is considered by taking the transient to be a sequence of steady state processes driven by a time-dependent surface temperature $T_0(t)$.

The difference between the two applications mentioned above is the extent of the surface which is heated by the impinging radiation; in laser pulsing experiments, a small spot (< 5 mm in diameter) is heated, whereas in the CTR application, a much larger extent of surface is heated. This distinction does not affect the processes very close to the surface but it does affect the nature of the vapor blow-off far from the surface. In both cases, we seek to calculate the rate of vaporization (J) and the gas density (n) at a distance x from the heated surface. The latter characteristics is needed in interpreting the laser pulsing experiments, in which a detector such as a mass spectrometer measures the gas density and a model is needed

to back-calculate the vapor pressure of the solid which causes the evaporation of solid.

C.2 Langmuir Vaporization

At low surface temperatures, the density of the emitted vapor is so low that free molecule flow (i.e. Langmuir vaporization) describes the entire process. The rate of vaporization (J_o) depends solely on the surface temperature T_o by the Hertz-Langmuir equation:

$$J_o = \frac{\alpha P_o(T_o)}{\sqrt{2\pi m k T_o}} \quad \frac{\text{molecules}}{\text{cm}^2 - \text{sec}} \tag{C-1}$$

where P_o is the vapor pressure, α is the evaporation coefficient, m is the molecular mass, and T_o is the surface temperature. The molecular density at a distance x from the surface (to which the mass spectrometer responds) is:

$$n_\ell = \frac{d^2 J_o}{4x^2 \bar{v}_o} \tag{C-2}$$

where d is the diameter of the emitting surface and

$$\bar{v}_o = \left(\frac{8k\ T_o}{\pi m} \right)^{1/2}$$

is the mean speed of the Maxwellian distribution. If $n_o = \frac{P_o}{kT_o}$ is the number density of the saturated vapor, equations (C-1) and (C-2) can be combined to give

$$\frac{n_\ell}{n_o} = \frac{1}{16(x/d)^2} \tag{C-3}$$

This method of measuring the vapor pressure of refractory materials extends back to Langmuir's measurement of the vapor pressure of tungsten by free evaporation. The weight loss of a specimen held at high temperature in vacuum for a known time can be used to determine J_o and the vapor pressure calculated by Eq. (C-1) (assuming that the evaporation coefficient is known - it is close to unity for most refractory materials, particularly metals and oxide ceramics).

C.3 Gasdynamic Vaporization

At temperatures high enough to create appreciable solid vapor pressures, the assumption of free molecule flow fails. The vaporized molecules begin to collide with each other in front of the heated solid surface and a continuum flow regime develops. In addition, some of the vaporized molecules can be backscattered onto the solid surface, so that Eq. (C-1) no longer gives the vaporization rate. The conditions for transition from free molecule to hydrodynamic flow have been calculated by Tsai [10].

In the gasdynamic model, the flow of gas from the vaporized solid is divided into three regions (Fig. (2-11)). The properties in each are governed by equations characteristic of the type of flow in that region. The regions are related by matching conditions at their boundaries.

Region 1, which is called the Knudsen Layer, has a thickness of the order of a few mean free paths [37]. The molecules leaving the surface possess a Maxwellian velocity distribution in the forward hemisphere at a temperature equal to surface temperature (just as in

Langmuir vaporization). However, the distribution of molecules at the outer boundary of the Knudsen layer differs from Maxwellian due to intermolecular collisions which result in re-establishment of equilibrium at a distance of a few mean free paths from the surface (plane 1 in Fig. (2-11)). It has been shown that the limiting hydrodynamic velocity of the vapor in the Knudsen layer is the sonic velocity, which occurs at high surface heat fluxes and in high vacuum. The flow properties exhibit large changes in this region and the net evaporation rate is reduced below that given by Eq. (C-1) because of back-scattering of the molecules to the surface. The analytical results for this region are given C.3.1.

The second region is the Hydrodynamic Region which starts at the sonic plane. In the case of vaporization from a nearly-point-source (as in laser pulsing), the flow of the vapor in this region resembles that of a supersonic free expansion of a gas from a sonic orifice into a vacuum. Section C.3.2 gives the solution to hydrodynamic equations along with appropriate boundary conditions determined from the Knudsen layer analysis.

As the vapor moves away from the surface, its density decreases because of expansion. Finally a point is reached beyond which there are no more collisions between molecules. This freezing plane in Fig. (2-11) is discussed in Section C.3.3.

For application of the gasdynamic model to an extended surface source such as the heated first wall of a fusion reactor, a detailed description of Regions 2 and 3 would have to consider a one-dimensional flow rather than the axisymmetric two-dimensional flow appropriate to

the nearly-point-source character of the irradiated laser spot on the surface. Sections C.3.2 and C.3.3 of the present analysis are restricted to the latter application. However, if only the rate of vaporization is needed in the CTR case, the backscatter factor calculated in Section C.3.1 is applicable.

C.3.1 The Nonequilibrium Region (Knudsen Layer)

The first region of Figure 2-11 shows the nonequilibrium region between the two equilibrium planes 0 and 1. At plane 0, the solid surface at temperature T_0 emits vapor molecules at a rate given by equation (C-1) with a Maxwellian velocity distribution function $f_0(\underline{v})$. The outer boundary is in contact with the hydrodynamic region. Ytrehus [37] has presented a thorough study of the Knudsen layer for a wide range of background gas pressure. He has shown that the maximum net evaporation occurs when the velocity of molecules at the hydrodynamic boundary (plane 1) is sonic, and that the sound velocity is the maximum velocity the vapor can attain in Knudsen layer. Since we are interested only in the limiting case of sonic velocity at the hydrodynamic boundary (corresponding to evaporation into vacuum), the study by Anisimov [35], in which sonic veloicty is assumed as a boundary condition, will be adopted here. The properties at the sonic plane (temperature, pressure, mean speed, density and distribution function) are denoted by T_1, p_1, u_1, n_1 and f_1.

The Knudsen layer is treated as a gasdynamic discontinuity (similar to a strong shock wave). Because the layer is very narrow, the

distribution function can be approximated by a linear combination of the distribution functions at the two boundaries:

$$f(x,\underline{v}) = \frac{1+g(x)}{2} f_o(\underline{v}) + \frac{1-g(x)}{2} f_1(\underline{v}) \qquad \text{(C-4)}$$

where x is distance from the surface, $\underline{v}$ is the vector molecular velocity and the function g(x) is to be determined. The distribution function at the surface is:

$$f_o(\underline{v}) = \begin{cases} f_+(\underline{v}) & v_x > 0 \\ B\, f_-(\underline{v}) & v_x < 0 \end{cases} \qquad \text{(C-5)}$$

B is a constant to be determined. f_+ denotes a Maxwellian distribution in the forward direction and f_- the corresponding distribution function in the reverse direction.

$$f_-(\underline{v}) = n_1 \left(\frac{m}{2\pi k T_1}\right)^{3/2} \exp \frac{(v_x-u_1)^2 + v_y^2 + v_z^2}{2kT_1} \qquad \text{(C-6)}$$

$$f_+(\underline{v}) = n_o \left(\frac{m}{2kT_o}\right)^{3/2} \exp\left(-\frac{mv^2}{2kT_o}\right). \qquad \text{(C-7)}$$

The velocity distribution at the sonic plane is

$$f_1(\underline{v}) = f_-(\underline{v}) \qquad \text{all } v_x. \qquad \text{(C-8)}$$

Conservation of mass, momentum and energy in the Knudsen layer yields:

$$\int_{\text{all } \underline{v}} d\,\underline{v}\, f(x,\underline{v})\, v_x = C_1 \qquad \text{(C-9)}$$

$$\int_{\text{all } \underline{v}} d\,\underline{v}\, f(x,\underline{v})\, v_x^2 = C_2 \qquad \text{(C-10)}$$

$$\int_{\text{all } \underline{v}} d\,\underline{v}\, f(x,\underline{v})\, v_x\, v^2 = C_3\,. \qquad \text{(C-11)}$$

The condition of sonic flow at plane 1 gives:

$$u_1 = (\gamma k T_1/m)^{1/2} \qquad \text{(C-12)}$$

where γ is the ratio of the specific heats of the vapor. In addition the gas is assumed to be ideal:

$$n_1 = \frac{p_1}{kT_1} . \tag{C-13}$$

The five unknowns B, n_1, T_1, p_1 and u_1 can be determined by integration of equations (C-9) (C-11) using equation (C-4) for f(x $\underline{v}$), which yields

$$n_o \sqrt{\frac{kT_o}{2\pi m}} = n_1 \, u_1 [1 + B \, \psi_1 \, (y)] \tag{C-14}$$

$$n_o \left(\frac{kT_o}{2m} \right) = n_1 \, u_1^2 \, [8/5 - B \, \psi_2 \, (y)] \tag{C-15}$$

$$n_o \left(\frac{2kT_o}{m} \right)^{3/2} = \sqrt{\pi} \, n_1 \, u_1^3 \, [4 + B \, \psi_3 \, (y)] . \tag{C-16}$$

The functions on the right hand sides are:

$$\Psi_1(y) = 1/2 \left[\frac{e^{-y^2}}{y\sqrt{\pi}} - \text{erf}(y) \right]$$

$$\Psi_2(y) = 1/2 \left[\left(1 + \frac{1}{2y^2} \right) \text{erfc}(y) - \frac{e^{-y^2}}{y\sqrt{\pi}} \right]$$

$$\Psi_3(y) = 1/2 \left\{ \frac{[1 + (2/y^2)]}{y\sqrt{\pi}} e^{-y^2} - \left(1 + \frac{5}{2y^2}\right) \text{erfc}(y) \right\}$$

$$y = \sqrt{\gamma/2}$$

where erf and erfc are the error function and its complement, respectively.

Solving the system of equations (C-12) - (C-16) yields the values of the parameters in the downstream flow (i.e. location 1 in Figure (2-11) in terms of γ. For a monoatomic gas γ = 5/3; for polyatomic molecules, however, the value of γ depends on the number of

degrees of freedom which are actually relaxed in the vapor at location 1. If the number of degrees of relaxation is denoted by f:

$$\gamma = \frac{f+2}{f} . \tag{C-17}$$

Although in UC vaporization the gas phase is a mixture of monatomic (U,C) and polyatomic (UC_2,C_3) species, uranium is the major species. Therefore we can consider the vapor over UC to be a monatomic gas with $\gamma = 5/3$.

The ratios of the vapor properties at the sonic plane to those at the surface are given in Table (C-1) as a function of γ.

The fraction of mass flux which is backscattered because of collisions, is calculated as follows. The net flux leaving the surface is equal to that entering the hydrodynamic zone at the sonic plane.

$$J_{net} = n_1 u_1 = \frac{p_1}{KT_1} \sqrt{\frac{\gamma k T_1}{m}} = \frac{\sqrt{\gamma} p_1}{\sqrt{mkT_1}} = J_o - J_b$$

where J_b denotes the backscattered flus on the surface. Expressing J_o by Eq. (C-1), the fraction backscattered is:

$$\frac{J_b}{J_o} = 1 - \frac{\sqrt{2\pi\gamma}\, p_1/p_o}{\sqrt{T_1/T_o}} . \tag{C-18}$$

This fraction is given in the last column of Table (C-1). The study of strong evaporation for a spherical interphase boundary into vacuums by Edwards et al. [64] as well as the Monte Carlo simulation of the transient vapor motion by Murakami et al. [65] give backscattered fluxes very close to the values shown in Table (C-1).

The vapor properties at the source plane 1 given in Table 1 will be used as boundary conditions for the hydrodynamic region.

TABLE (C.1)
Vapor Properties at the Sonic Plane

γ	n_1/n_o	T_1/T_o	p_1/p_o	J_b/J_o
5/3	0.308	0.669	0.206	0.184
7/5	0.332	0.692	0.229	0.181
9/7	0.344	0.702	0.242	0.180
11/9	0.351	0.708	0.249	0.181
13/11	0.356	0.712	0.254	0.181

For computation of the net vaporization rate, only the backscattered fraction in the last column of Table (C-1) and Eq. (C-1) are needed.

To determine the size of the Knudsen layer the function g(x) must be known. This requires solving Boltzmann equation; the width of the region has been reported to be of the order of a few mean free paths [37].

C.3.2 Hydrodynamic Region

The continuum region starts at the sonic plane (plane 1). For small diameter heated spots on the surface, the flow of molecules can be modeled as a supersonic free-jet expansion of a gas from a sonic orifice [66]. As Fig. (2-11) shows, the streamlines appear to radiate from a source at a distance x_o downstream of the sonic plane. The density decreases along each streamline as the inverse square of the distance from this source. Variation of density from streamline to streamline (i.e. with polar angle at constant x) is approximately independent of x [66].

In the following analysis the conservation equations are used to calculate the properties of the flow in terms of the properties at the sonic plane and the stream Mach number M. The analysis is based on one-dimensional steady state continuum flow of an ideal gas with adiabatic exponent γ.

The energy equation gives:

$$\frac{u^2}{2} + \left(\frac{\gamma}{\gamma-1}\right) RT = \frac{u_1^2}{2} + \left(\frac{\gamma}{\gamma-1}\right) RT_1 \qquad \text{(C-19)}$$

$$u = Ma = M\sqrt{\gamma RT} \qquad \text{(C-20)}$$

where $R = k/m$, u is the stream velocity and $\underline{a}$ is the local velocity of

sound. At plane 1, $M_1 = 1$ or $u_1 = M_1 a_1 = a_1 = \sqrt{\gamma RT_1}$ and Eq. (C-19) yields:

$$\frac{T}{T_1} = \frac{1 + \frac{\gamma-1}{2}}{1 + \frac{\gamma-1}{2} M^2} = \frac{\frac{\gamma+1}{2}}{1 + \frac{\gamma-1}{2} M^2} \cdot \qquad \text{(C-21)}$$

The velocity relative to sonic velocity at plane 1 is:

$$\frac{u}{u_1} = \frac{M\sqrt{\gamma RT}}{\sqrt{\gamma RT_1}} = M \left(\frac{T}{T_1}\right)^{1/2} = M \left(\frac{\frac{\gamma+1}{2}}{1 + \frac{\gamma-1}{2} M^2} \right)^{1/2} . \qquad \text{(C-22)}$$

Assuming isentropic flow and the ideal gas law, $\left(\frac{n}{n_1}\right)^{\gamma-1} = \frac{T}{T_1}$, or with Eq. (C-21):

$$\frac{n}{n_1} = \left(\frac{\frac{\gamma+1}{2}}{1 + \frac{\gamma-1}{2} M^2} \right)^{\frac{1}{\gamma-1}} . \qquad \text{(C-23)}$$

Sherman [66] has fitted experimental data on free-jet expansion from orifices to obtain the following formula for the centerline Mach number:

$$M = A \left(\frac{x - x_o}{d} \right)^{\gamma-1} - 1/2 \left(\frac{\gamma+1}{\gamma-1}\right) \Big/ A \left(\frac{x-x_o}{d} \right)^{\gamma-1} \qquad \text{(C-24)}$$

where d is the diameter of the orifice (or the heated spot on the surface in the present application). The values of constants A and x_o (which depend on γ) are given in Table (C-2).

Equation (C-24), which gives M as a function of (x/d), permits determination of the centerline stream parameters through equations (C-21), (C-22) and (C-23). The properties at sonic plane 1 are eliminated in favor of those on the surface by use of Table (C-1), the ideal gas law, and Eq. (C-12).

TABLE (C.2)
The values of the constants in Eq. (C-24) as a Function of γ

γ	x_o/d	A
5/3	0.075	3.26
7/5	0.40	3.65
9/7	0.85	3.96

C.3.3 Transition from Continuum to Free Molecule Flow

The transition from continuum flow (zone 2) back to free molecule flow (zone 3) occurs when all degrees of freedom (vibrational, rotational and translational) are frozen.

In the "sudden freeze" model the approximate location of freezing (plane 2 in Fig. (2-11) is given by Anderson [67] as:

$$u \frac{1}{T} \left| \frac{dT}{dx} \right| = \left(\frac{8kT}{\pi m} \right)^{1/2} \sqrt{2}\, n\, S \qquad \text{(C-25)}$$

where S is the collision cross section. The derivative dT/dx, u, and n are obtained from Eqs. (C-21) - (C-24) as functions of distance from the surface (x). Transition occurs when the local values of these properties satisfy Eq. (C-25). This distance is designated x_2. Thereafter the temperature and velocity remain constant through the entire free molecule region because there are no more collisions between molecules. The density continues to decrease as the inverse square of the distance.

C.4 Sample Calculation

The equations given in Section C.3.2, along with the values of the parameters at the sonic point given in Table (C-1) have been used to calculate the vapor properties as a function of distance from a small spot on a UC surface which is heated to temperatures of 4000 K, 4500 K, and 5000 K. The UC vapor pressure above melting point given in Section II.1 is used for $P_o(T_o)$. The hard sphere model is used for the collision cross sections.

Table (C-3) gives the centerline freezing plane (plane 2 in Fig. (2-11) calculated by equation (C-25) for three different temperatures and five different hot spot diameters. γ is assumed to be 5/3 for the calculation.

Figure (C-1) shows the variation of temperature with distance from the surface for different surface temperature. The freezing planes are also shown. There is no change in temperature after the transition to free-molecule flow. Variation of the number density with distance for a surface temperature of 4500 K is shown in Fig. (C-2). Inverse square dependence on the distance is assumed beyond the freezing plane. Also shown in this figure is the number density variation obtained using free molecule flow for the whole region (Eq. (C-3)).

Although the centerline flux in the free jet flow is ~ 5% greater than that for free molecular flow, the number densities behave in the opposite sense. Figure (C-2) shows that the centerline number density in free jet is about ~ 1.40 times that of free molecule flow. However, the maximum velocity from a free jet attains supersonic values which are greater than the average thermal velocity of free molecule flow by a factor of ~ 1.3 (Table (C.3).

C.5 Application to Transient Surface Heating

In a transient surface heating such as laser heating, the temperature of the surface varies with time and so does the molecular flux from the surface. It has been shown [ ] that the flux (Φ) at any time is given by eq. (C-1) with the instantaneous value of P_o and T_o. Considering the backscattering of the molecules to the surface, the

TABLE (C.3)
Location of Freezing Plane, x_2(cm) and the Stream Velocity Relative to the Mean Thermal Velocity at the Surface (in parentheses); $\gamma = 5/3$

d,cm	T,K 4000	4500	5000
0.1	0.12(1.14)	0.31(1.28)	0.74(1.31)
0.2	0.34(1.22)	0.90(1.30)	2.20(1.32)
0.3	0.63(1.25)	1.70(1.30)	4.20(1.32)
0.4	1.00(1.26)	2.70(1.31)	6.70(1.32)
0.5	1.40(1.27)	3.80(1.31)	9.60(1.32)

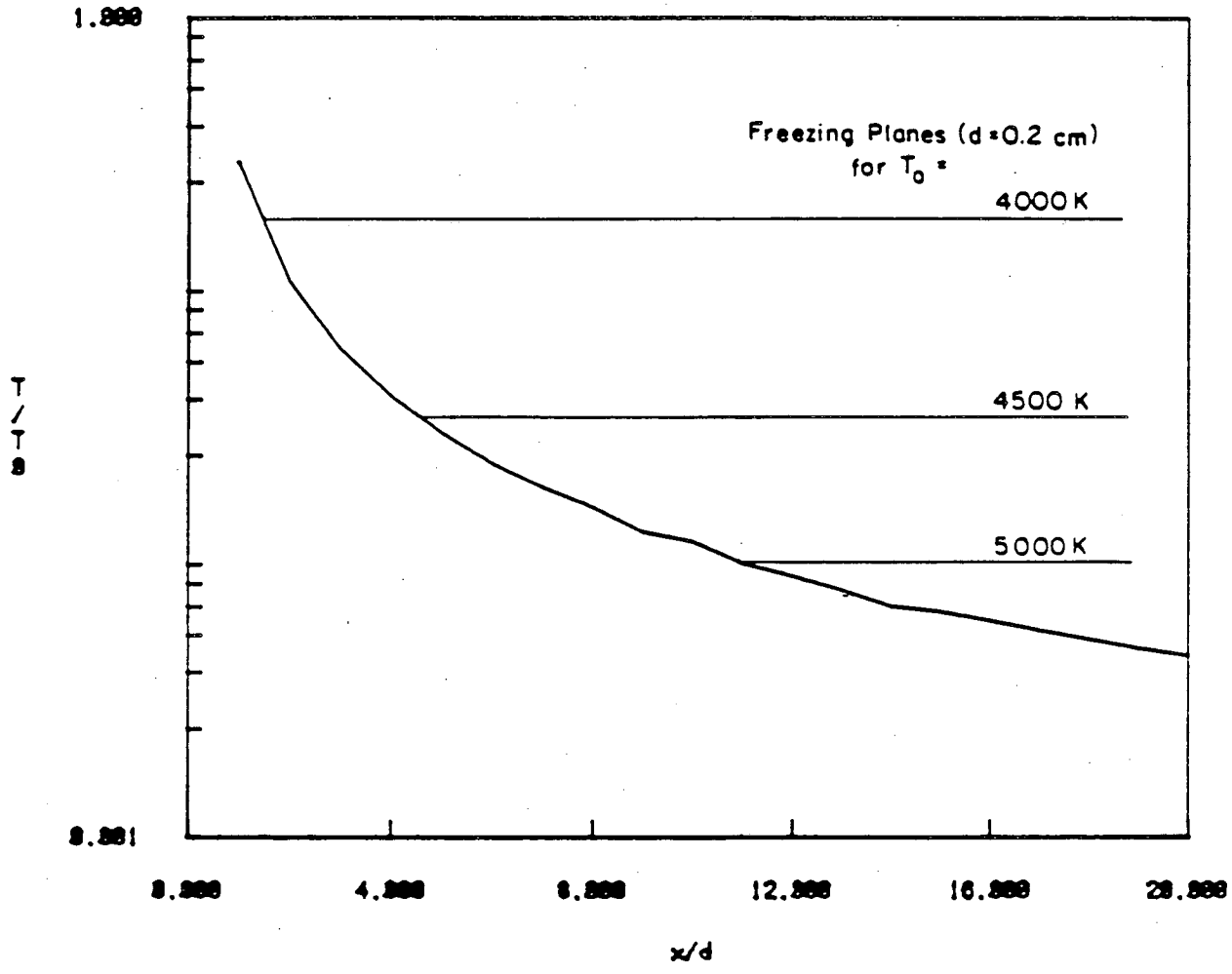

Fig. C-1 : Variation of temperature with x/d for different temperatures.

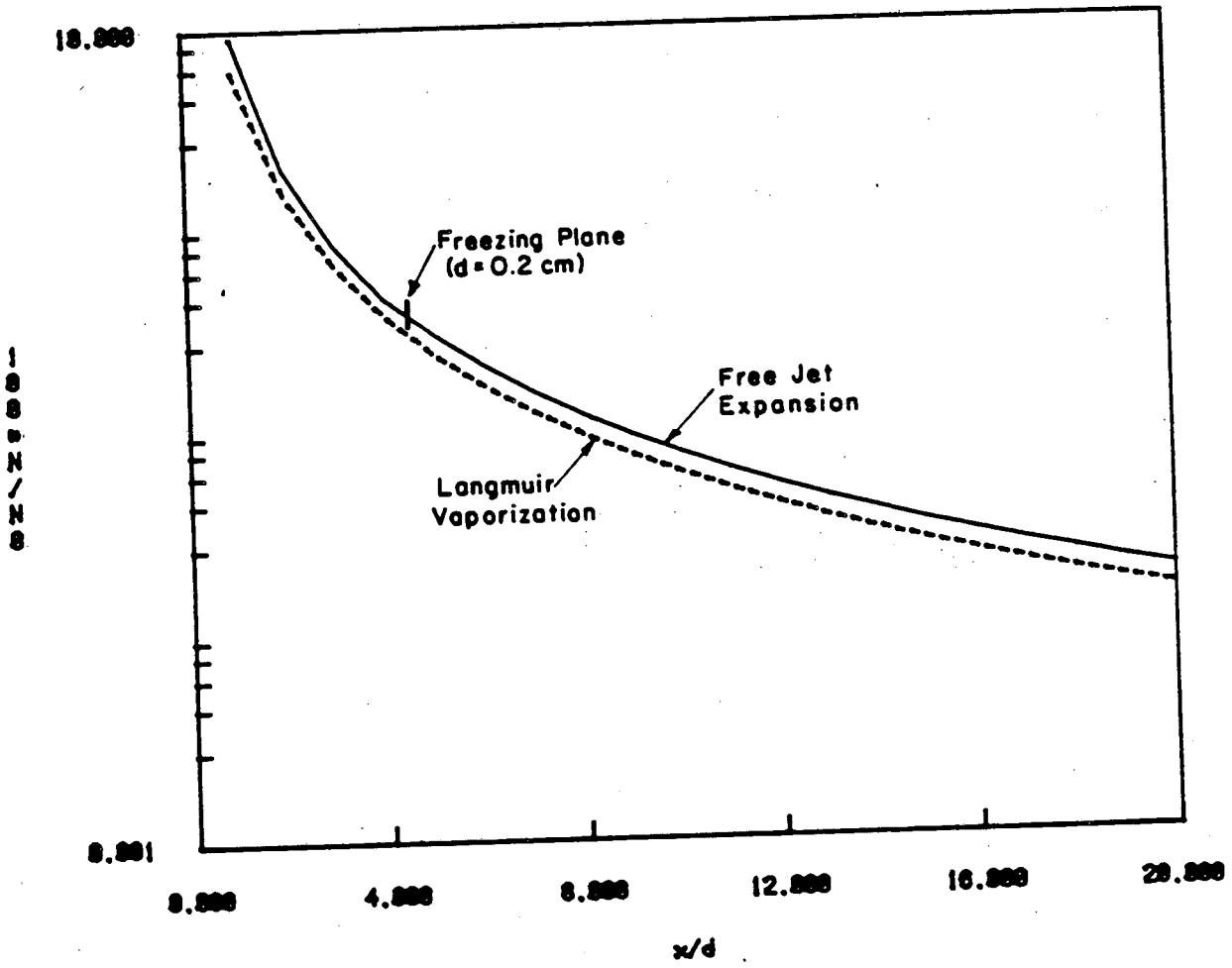

Fig. C-2: Variation of Number Density with x/d at a Temperature of 4500 K.

rate of evaporation at time τ from an area of A cm^2 will be

$$\Phi = \frac{(1-\beta)\, P_o A}{\sqrt{2\pi m k T_o}} \text{ molecules/sec} \qquad \text{(C-26)}$$

where T_o and P_o are the surface temperature and corresponding pressure at time τ. If $\phi(\theta) = f(\theta)\phi(0)$ in $\frac{\text{molecules}}{\text{sec-sr}}$, $f(\theta)$ being the empirical angular distribution and $\phi(\theta)$, the centerline flux, then Φ can be written as:

$$\Phi = 2\pi \int_0^{\pi/2} \phi(\theta) d(\cos\theta) = 2\pi\phi(0) \int_0^{\pi/2} f(\theta) d(\cos\theta)$$

or

$$\phi(0) = \frac{\Phi}{2\pi \int_0^{\pi/2} f(\theta) d(\cos\theta)} = \frac{\Phi}{F} \qquad \text{(C-27)}$$

where $F = 2\pi \int_0^{\pi/2} f(\theta) d(\cos\theta)$.

The centerline flux at distance L from the source

solid angle $= \frac{1}{L^2} = \frac{\phi(\theta)}{L^2}$. But flux $= nu_T$, n being the density of the molecules at distance L and u_T being the terminal speed of the molecules given by eq. (C-22).

so, $$n = \frac{\phi(0)}{u_T L^2} = \frac{\Phi}{u_T L^2 F} . \qquad \text{(C-28)}$$

Eq. (C-28) gives the number density of the molecules at distance L from the source which have departed the surface at time τ. The transit time (t_{tr}) of these molecules an be expressed as:

$$t_{tr} = \int_0^{x_2} \frac{dx}{u(x)} + \frac{L-x_2}{u_T} = \left[\int_0^{x_2} \frac{dx}{u(x)/u_1} + \frac{L-x_2}{u_T/u_1} \right] \Big/ u_1 . \qquad \text{(C-29)}$$

The first term on the right hand side of eq. (C-29) gives the transit time from surface up to the freezing plane and the second term is the time that molecules travel with the uniform speed (u_T) from the freezing plane to a distance of L. u_1, $\bar{u}(x)/u_1$ and x_2 which can be obtained through eqs. (C-12), (C-22) and (C-25) respectively, all are functions of surface temperature T_o which is a function of time τ.

The number density of all the molecules at distance L from the source at time t will be the sum of the number densities of the molecules whose transit times satisfy the relation:

$$t_{tr}\,[T_o(\tau)] = t - \tau. \tag{C-30}$$

Equation (C-30) is solved numerically for different values of t. The roots of the equation (τ_1, τ_2,...) are then used in eq. (C-28) to calculate the number density as:

$$n(t) = \frac{1}{L^2 F}\left[\frac{\Phi(\tau_1)}{u_T(\tau_1)} + \frac{\Phi(\tau_2)}{u_T(\tau_2)} + \cdots\right]. \tag{C-31}$$

APPENDIX D

MASS SPECTROMETER AND PYROMETER SIGNALS

The mass spectrometer signals for the species, U, UC_2, C and C_3 are given in Figs. (D-1) - (D-32). Also given in these figures are the RC corrected signals obtained through the use of equations (3-34) - (3-37). Using the corrected signals and the calibration constants obtained in Section III.2.3 in Eqs. (3-38) - (3-41), the number densities of different molecular species as a function of time can be calculated.

The corresponding surface temperature profiles for different runs are given in Figs. (D-33) - (D-40).

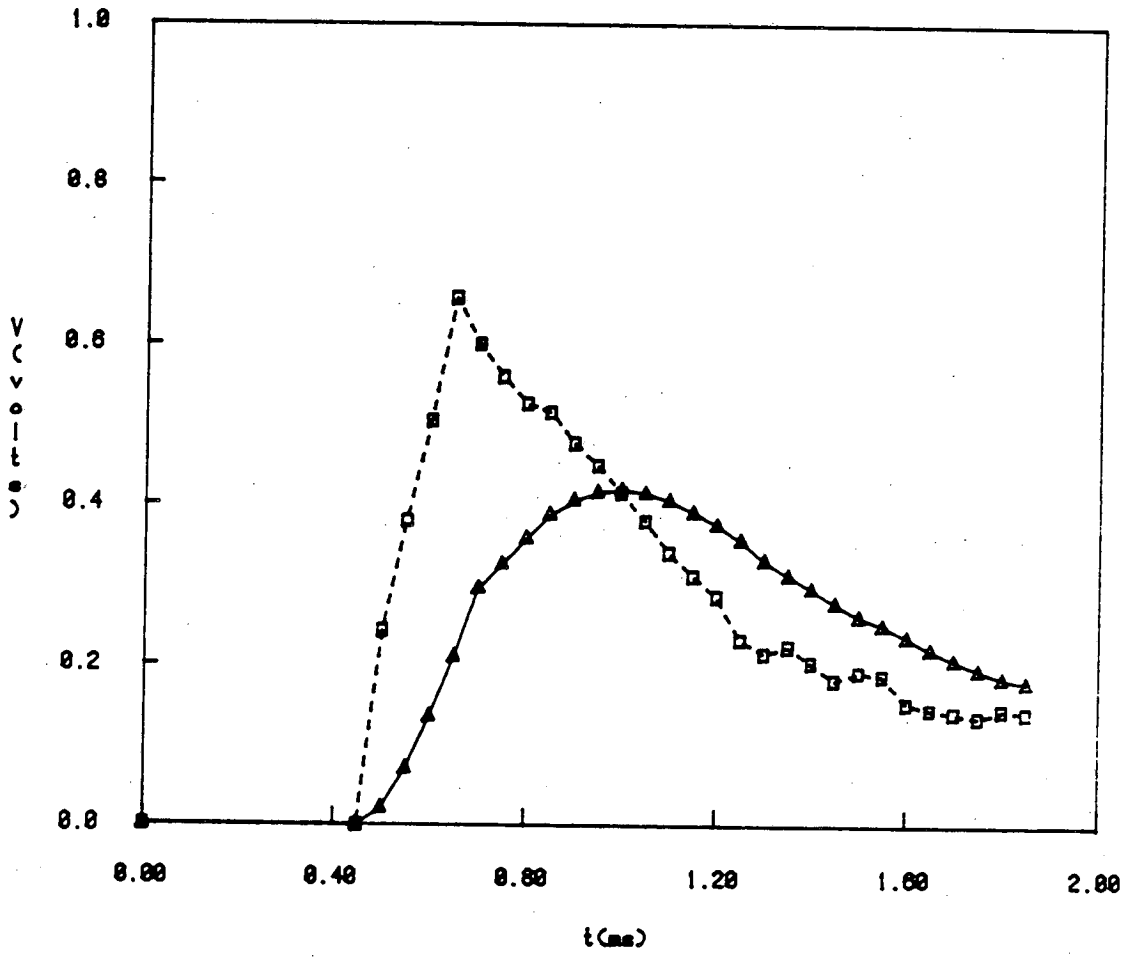

Triangle-Measured data Square-Corrected data
Fig. D-1:U Signal(Run1);E=5.9 joules

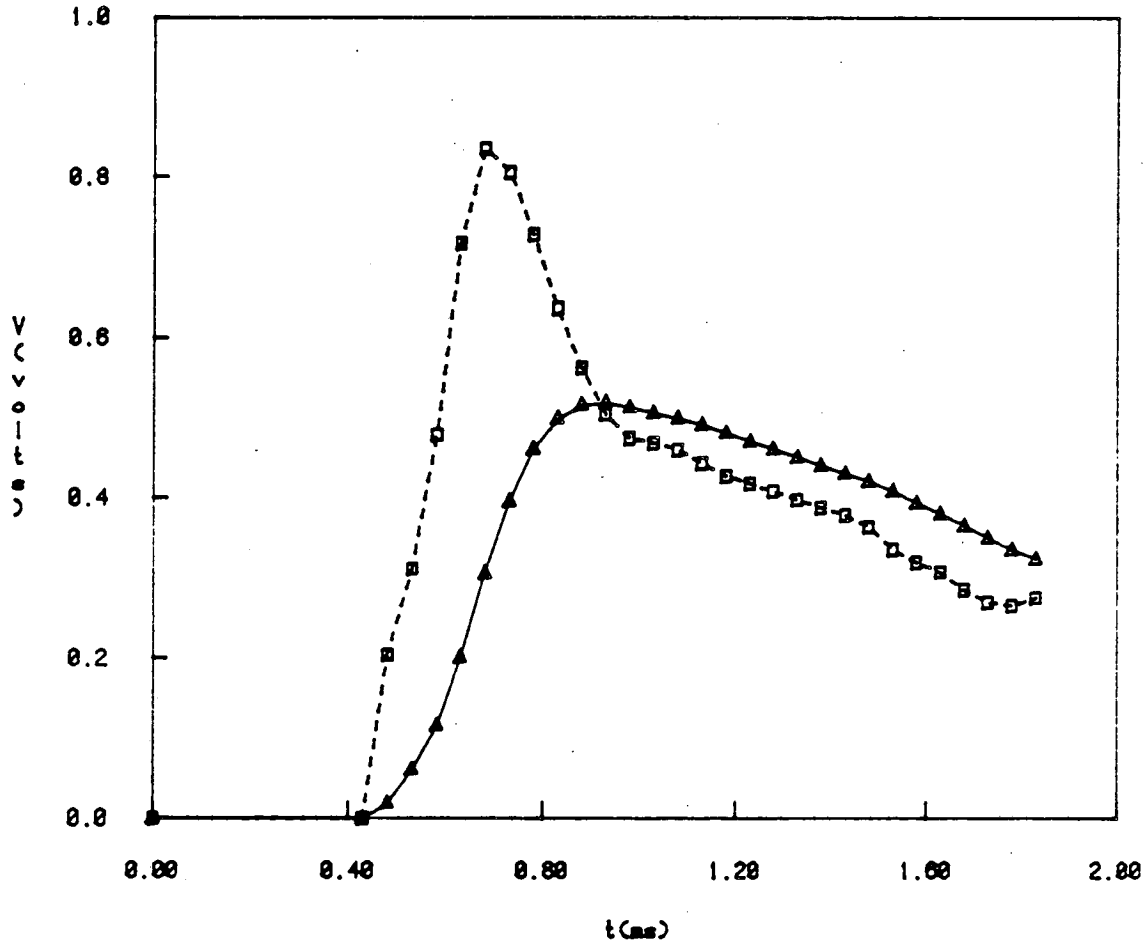

Triangle-Measured data Square-Corrected data
Fig. D-2:U Signal(Run2);E=6.7 Joules

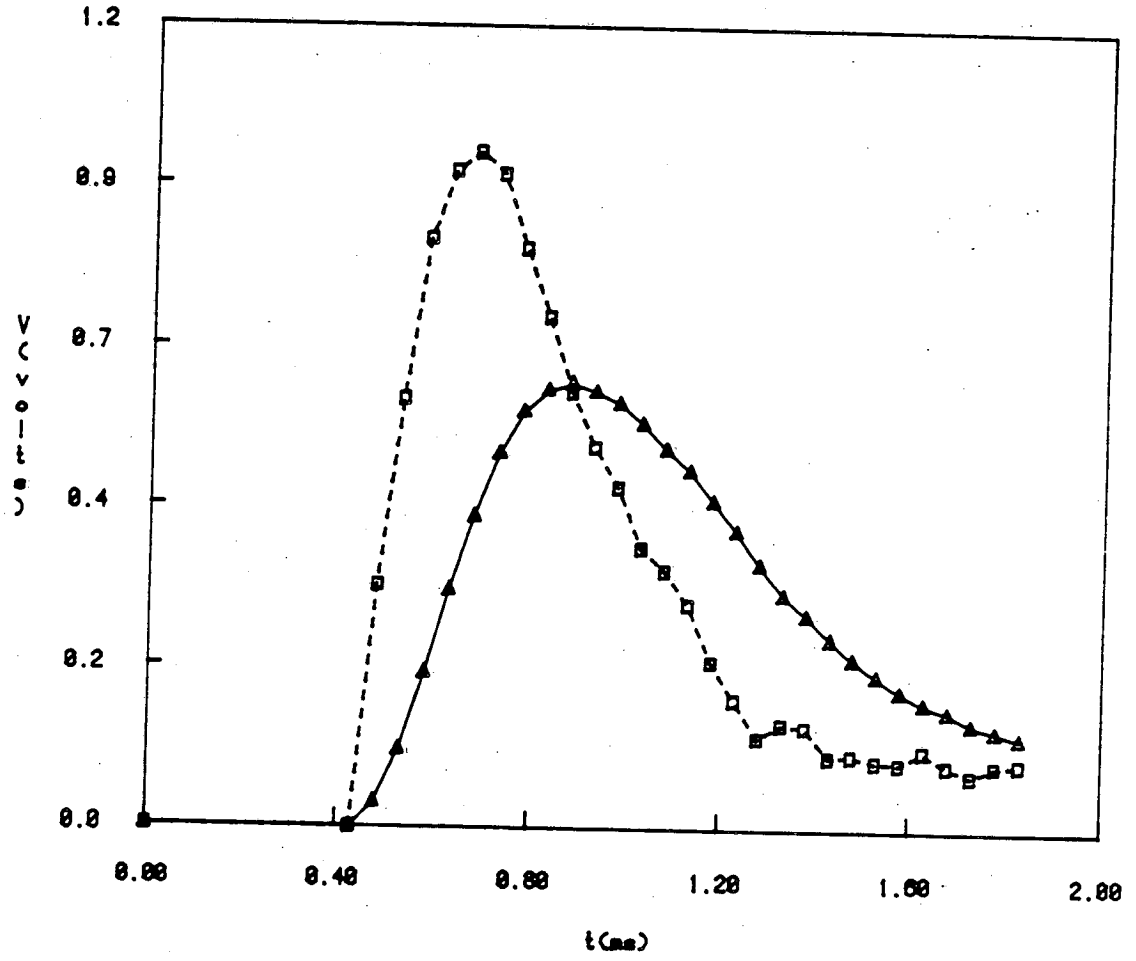

Triangle-Measured data Square-Corrected data
Fig. D-3:U Signal(Run3);E=6.7 joules

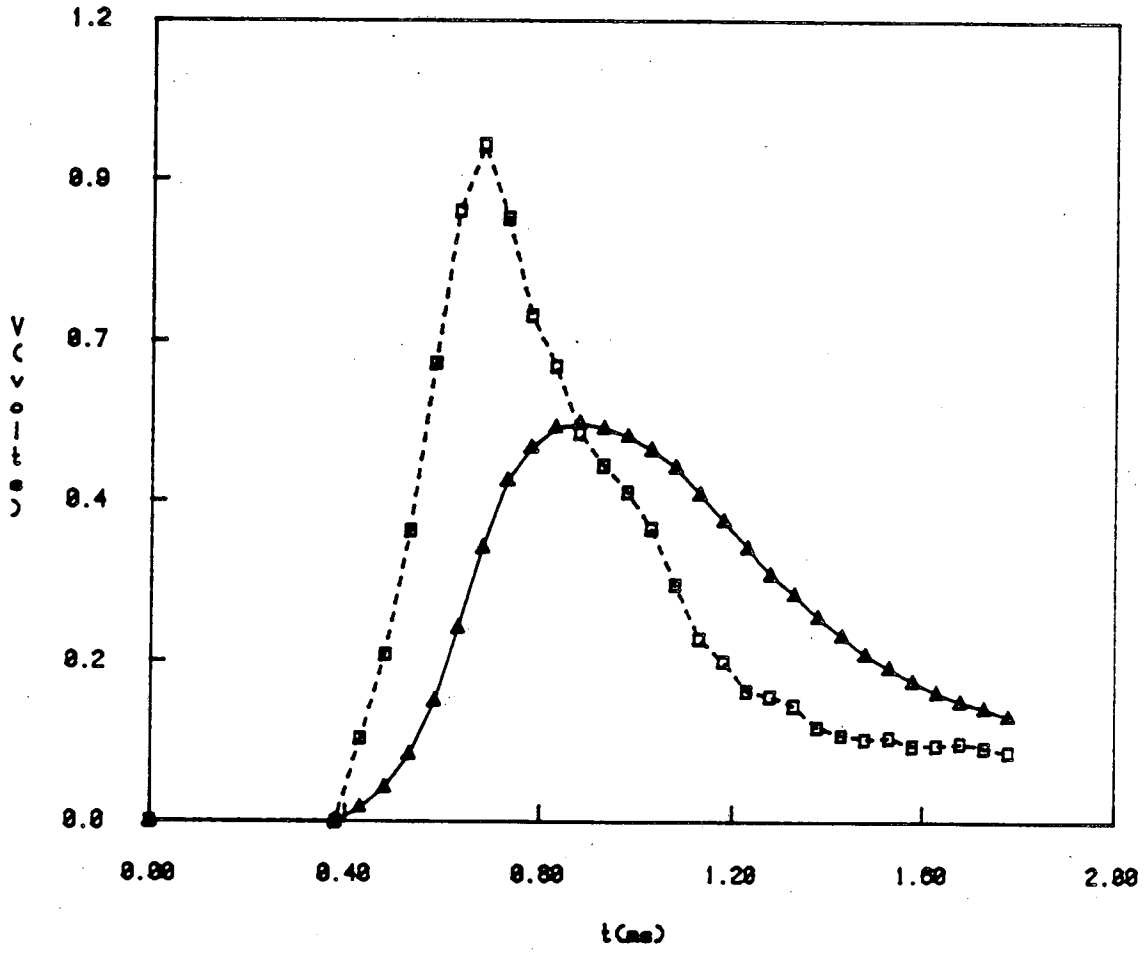

Triangle-Measured data Square-Corrected data
Fig. D-4:U Signal(Run4);E=7.4 joules

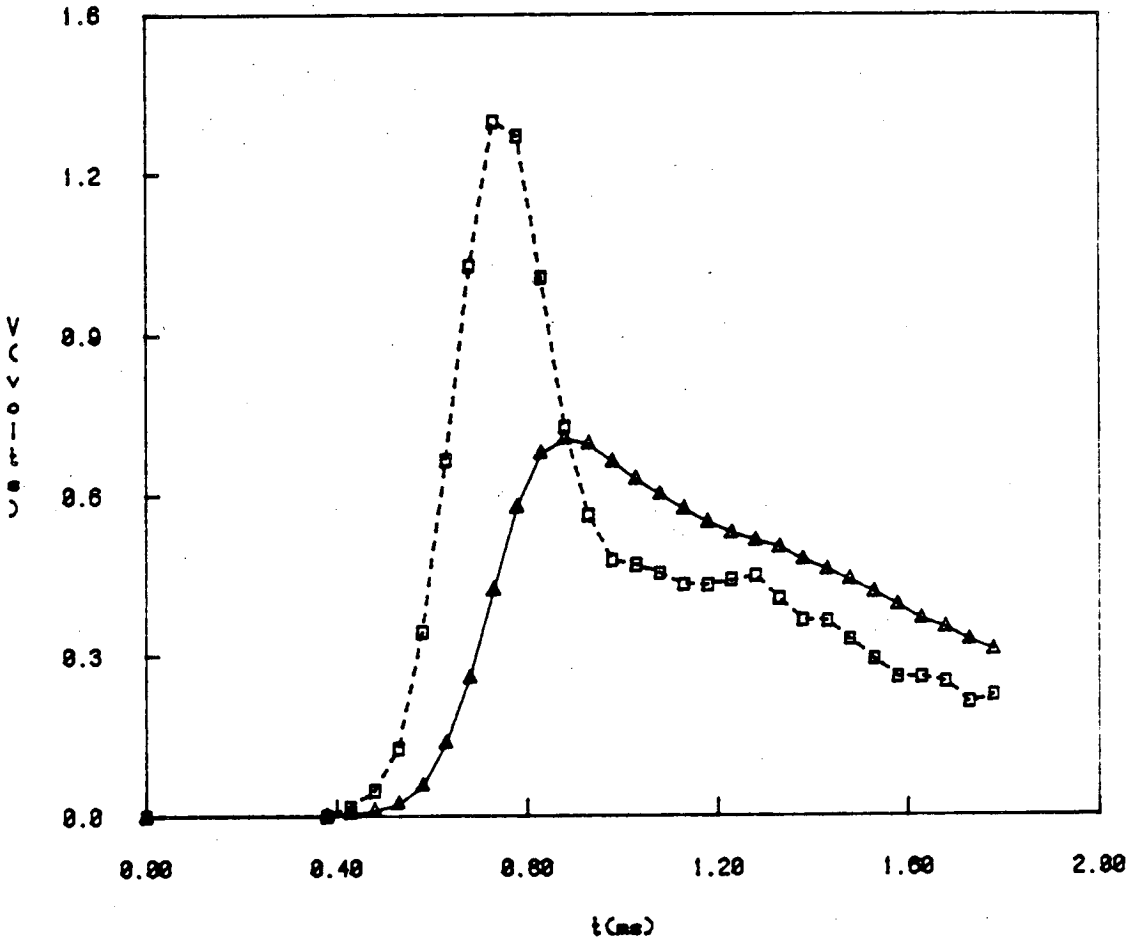

Triangle-Measured data Square-Corrected data
Fig. D-5:U Signal(Run5);E=8.6 Joules

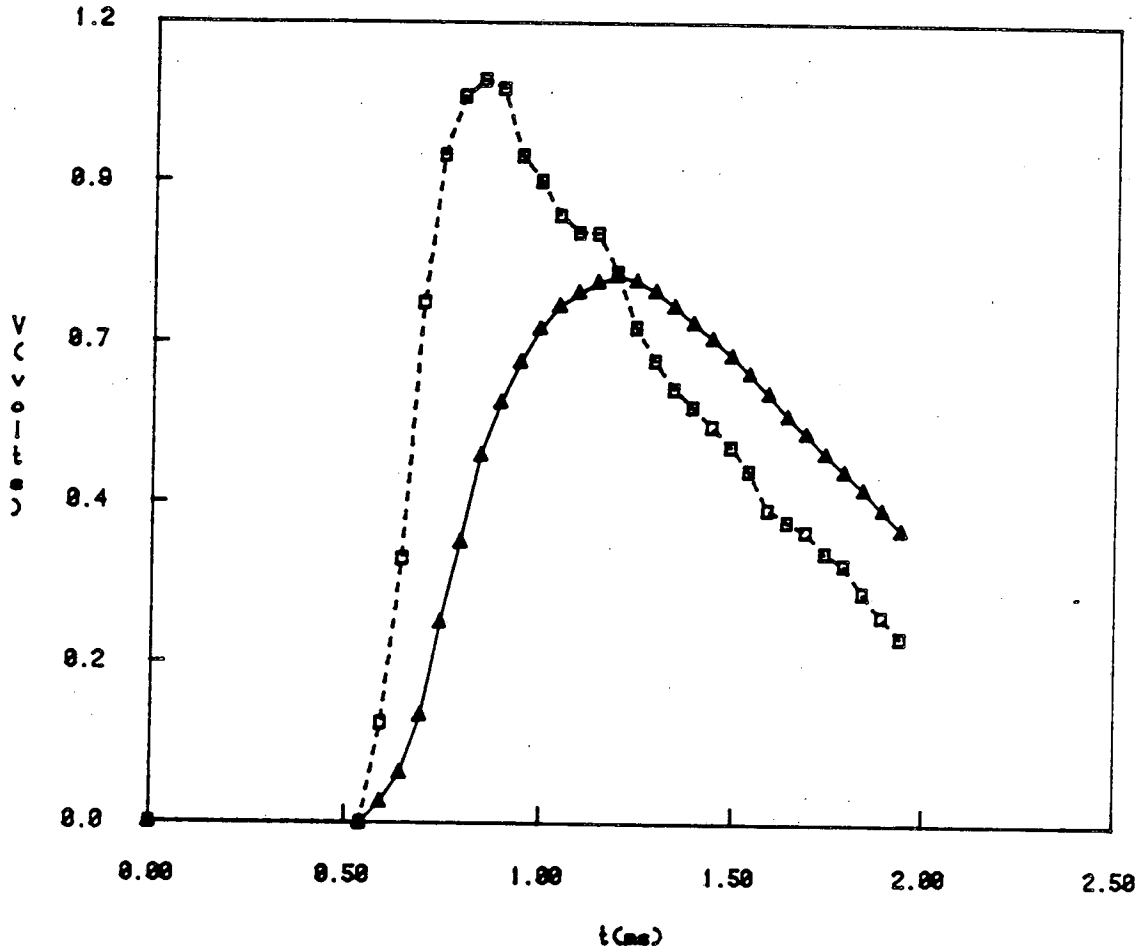

Triangle-Measured data Square-Corrected data
Fig. D-6:U Signal(Run6);E=11.5 joules

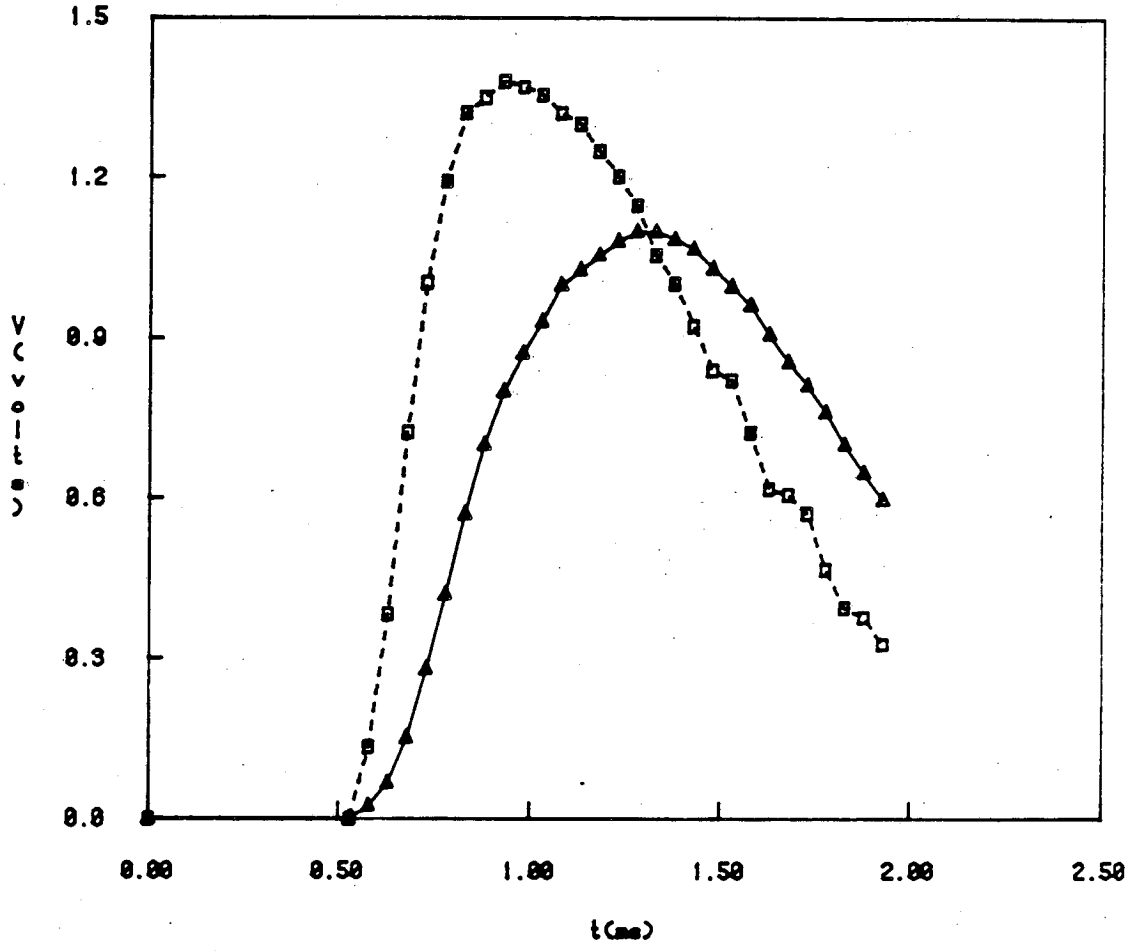

Triangle-Measured data Square-Corrected data
Fig. D-7:U Signal(Run7);E=12.8 Joules

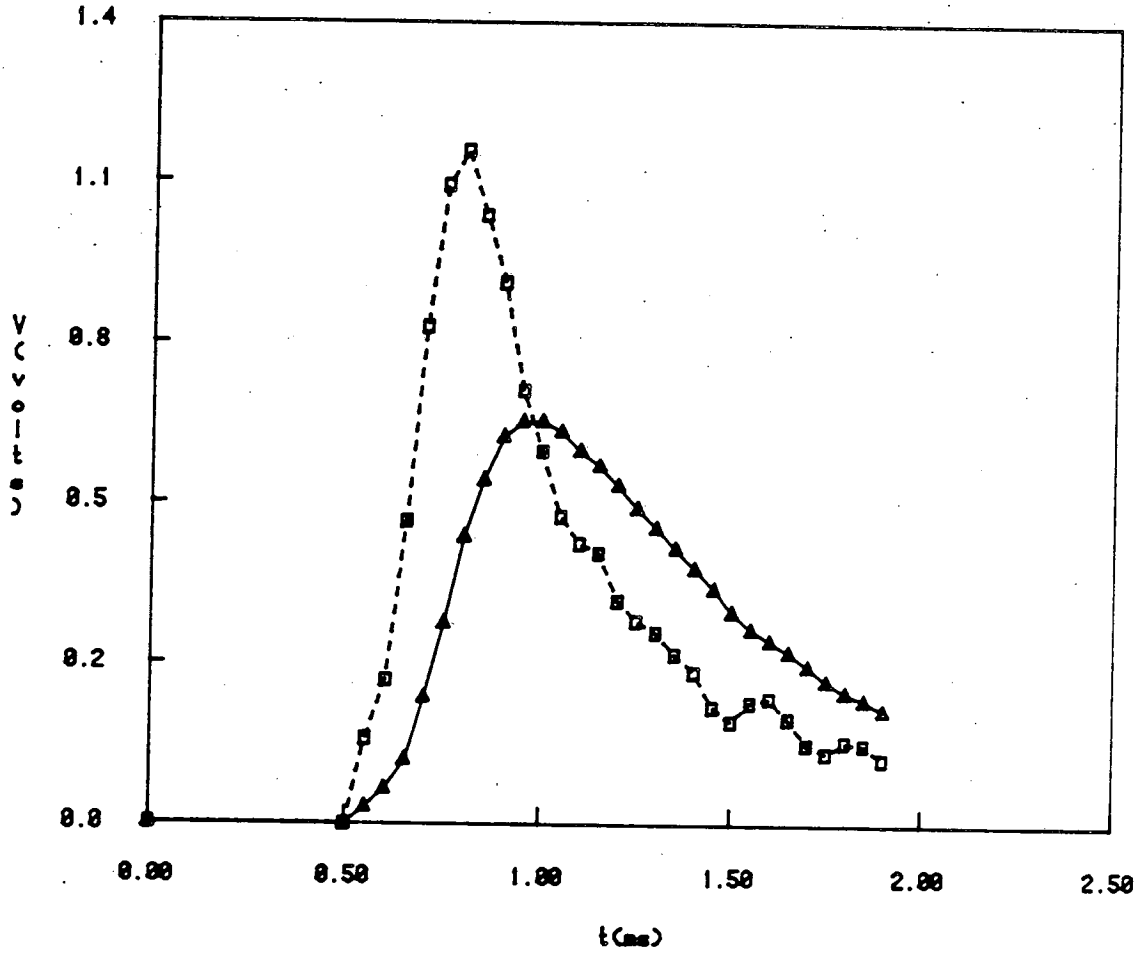

Triangle-Measured data Square-Corrected data
Fig. D-8:U Signal(Run8);E=14.5 joules

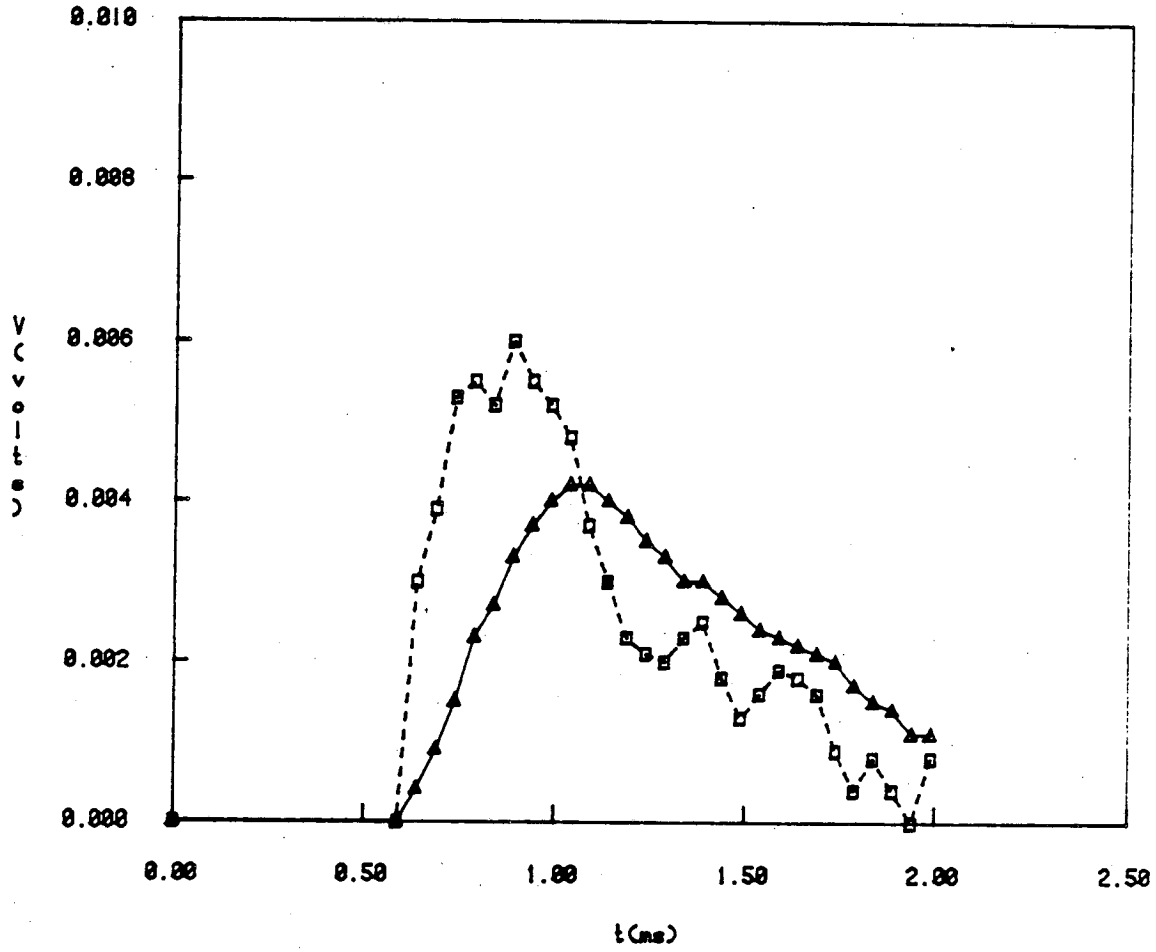

Triangle- Measured data Square-Corrected data
Fig. D-9:UC2 Signal(Run1);E=5.9 joules

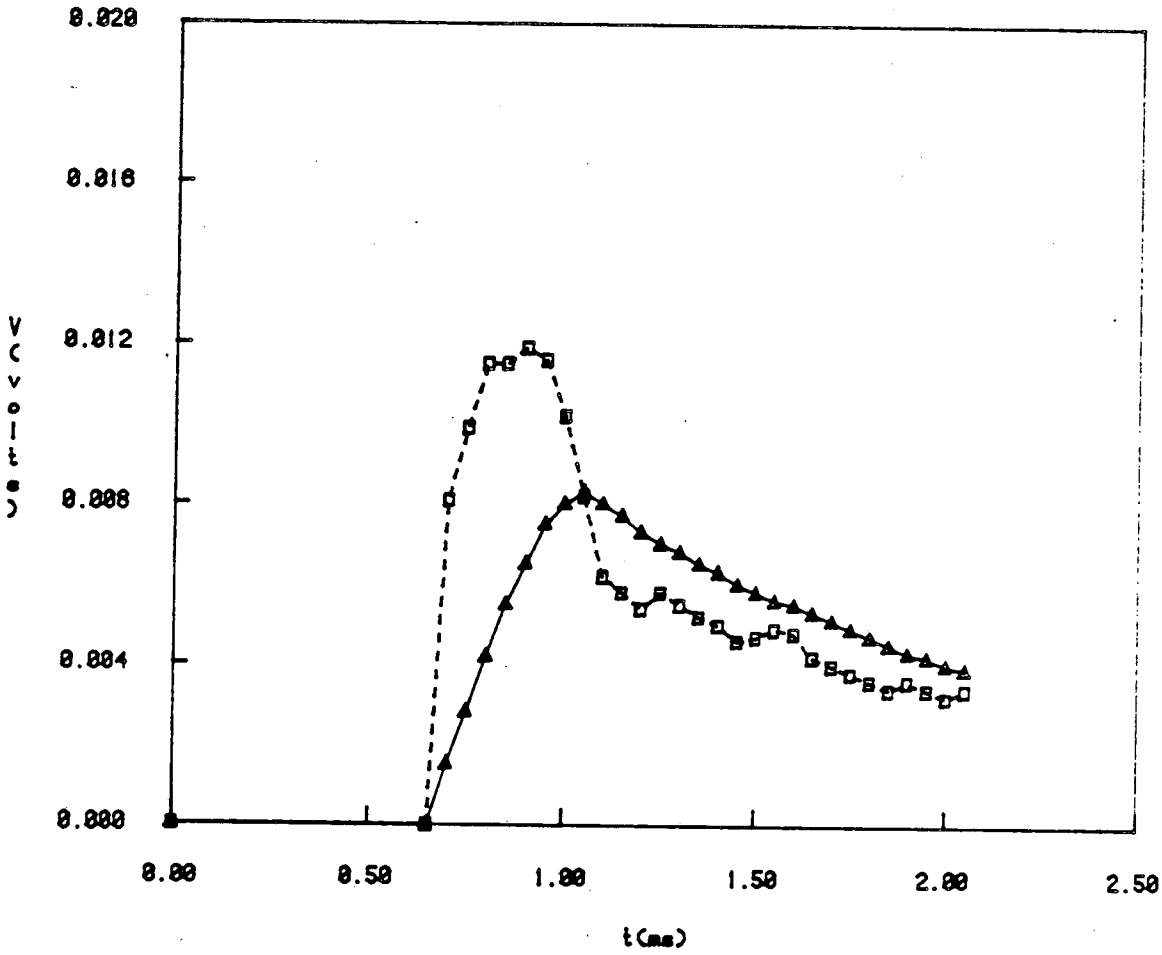

Triangle- Measured data Square-Corrected data
Fig. D-10:UC2 Signal(Run2);E=6.7 joules

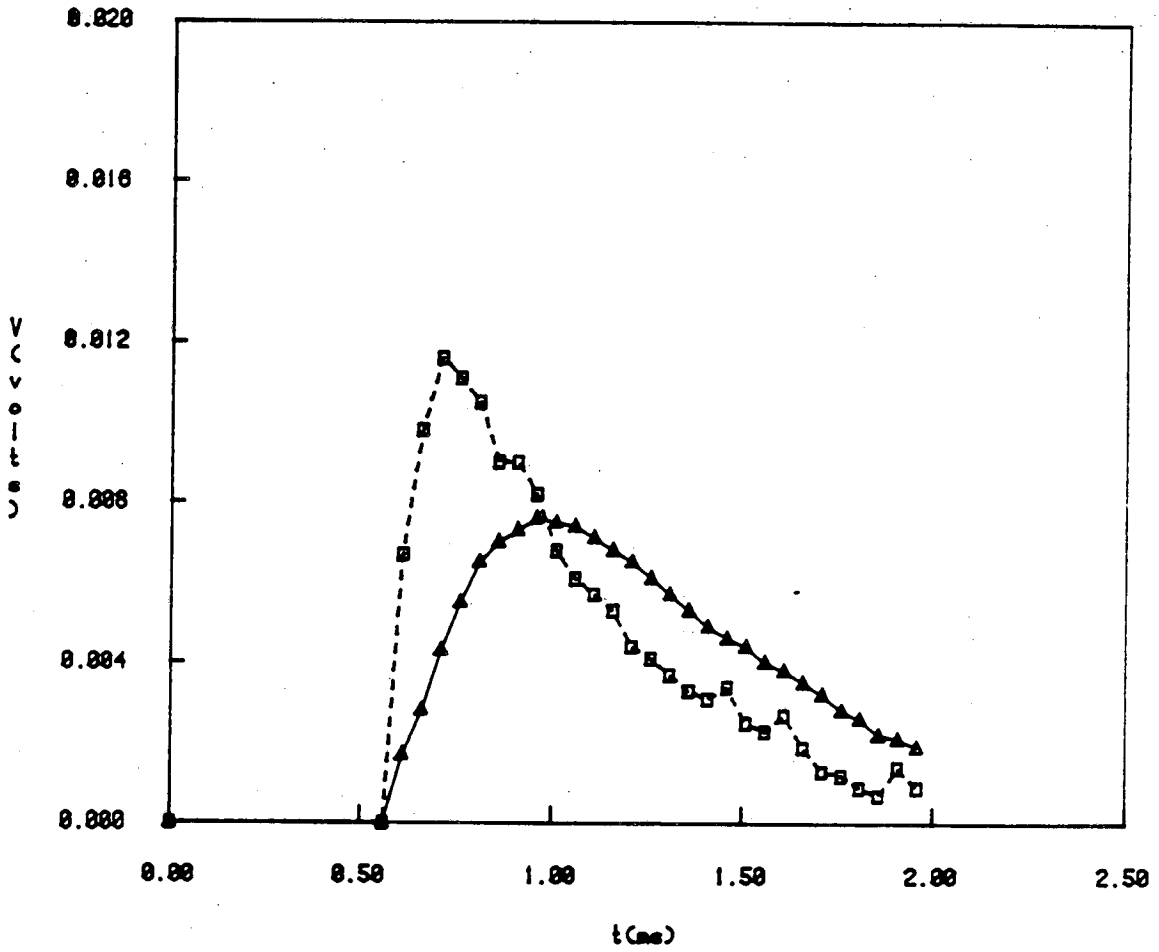

Triangle- Measured data Square-Corrected data
Fig. D-11:UC2 Signal(Run3);E=6.7 joules

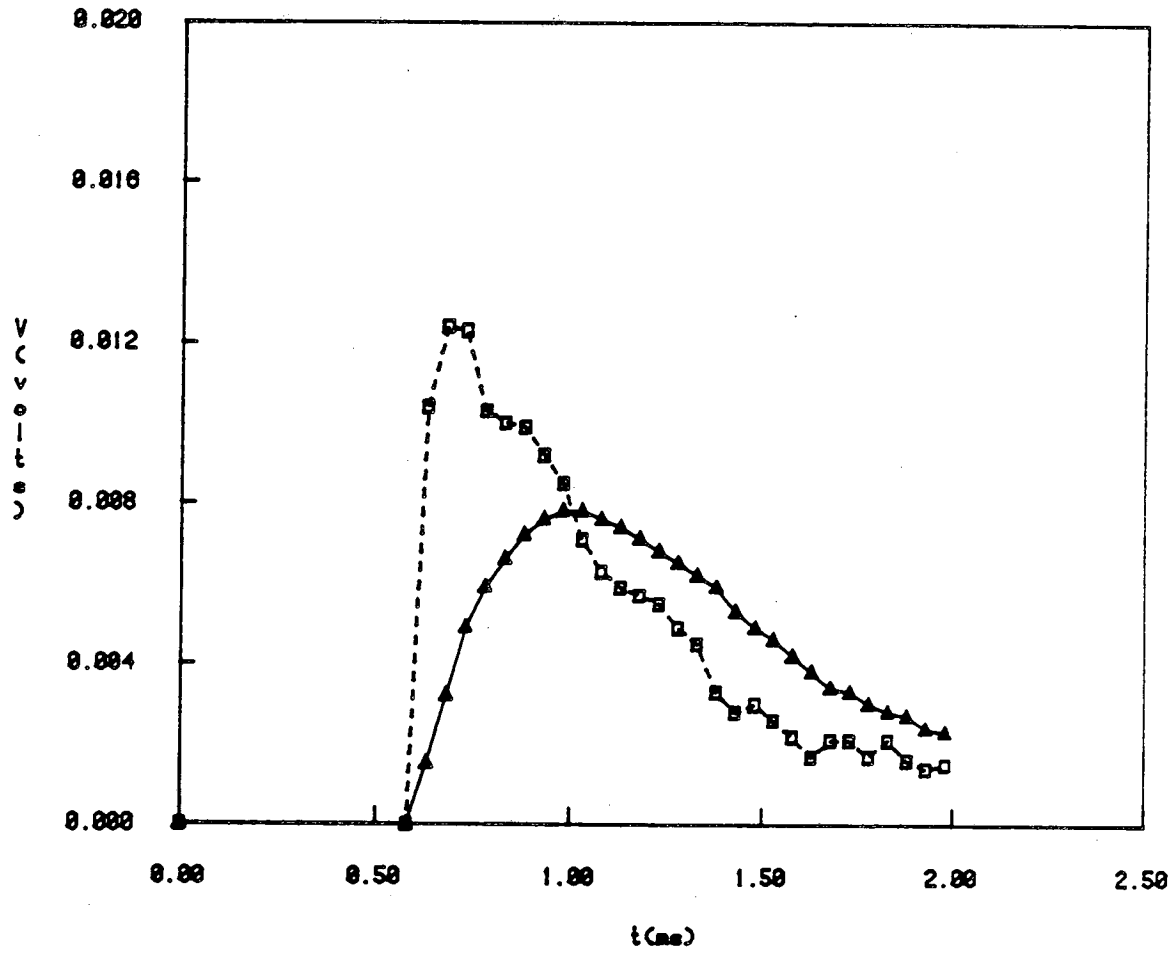

Triangle- Measured data Square-Corrected data
Fig. D-12:UC2 Signal(Run4);E=7.4 joules

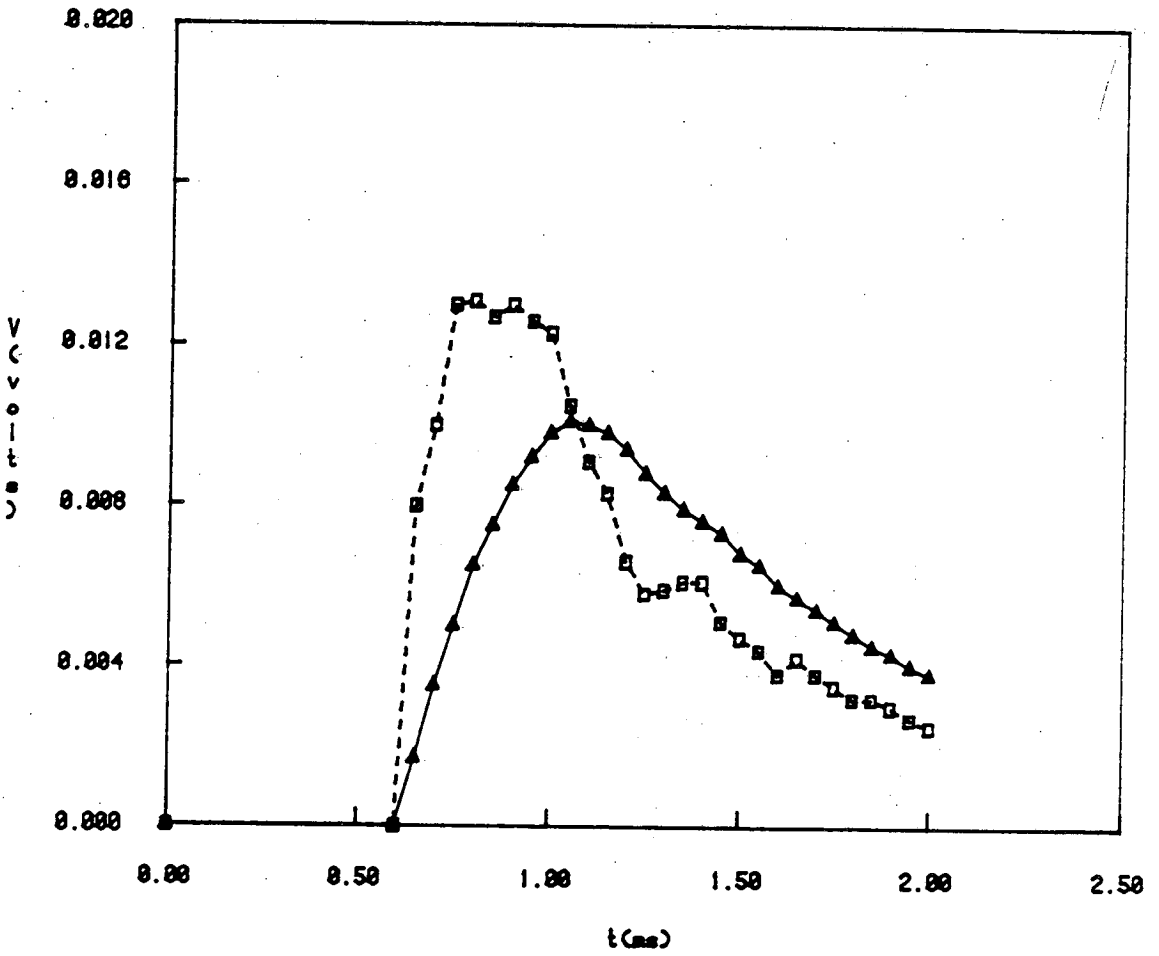

Triangle- Measured data Square-Corrected data
Fig. D-13:UC2 Signal(Run5);E=6.6 joules

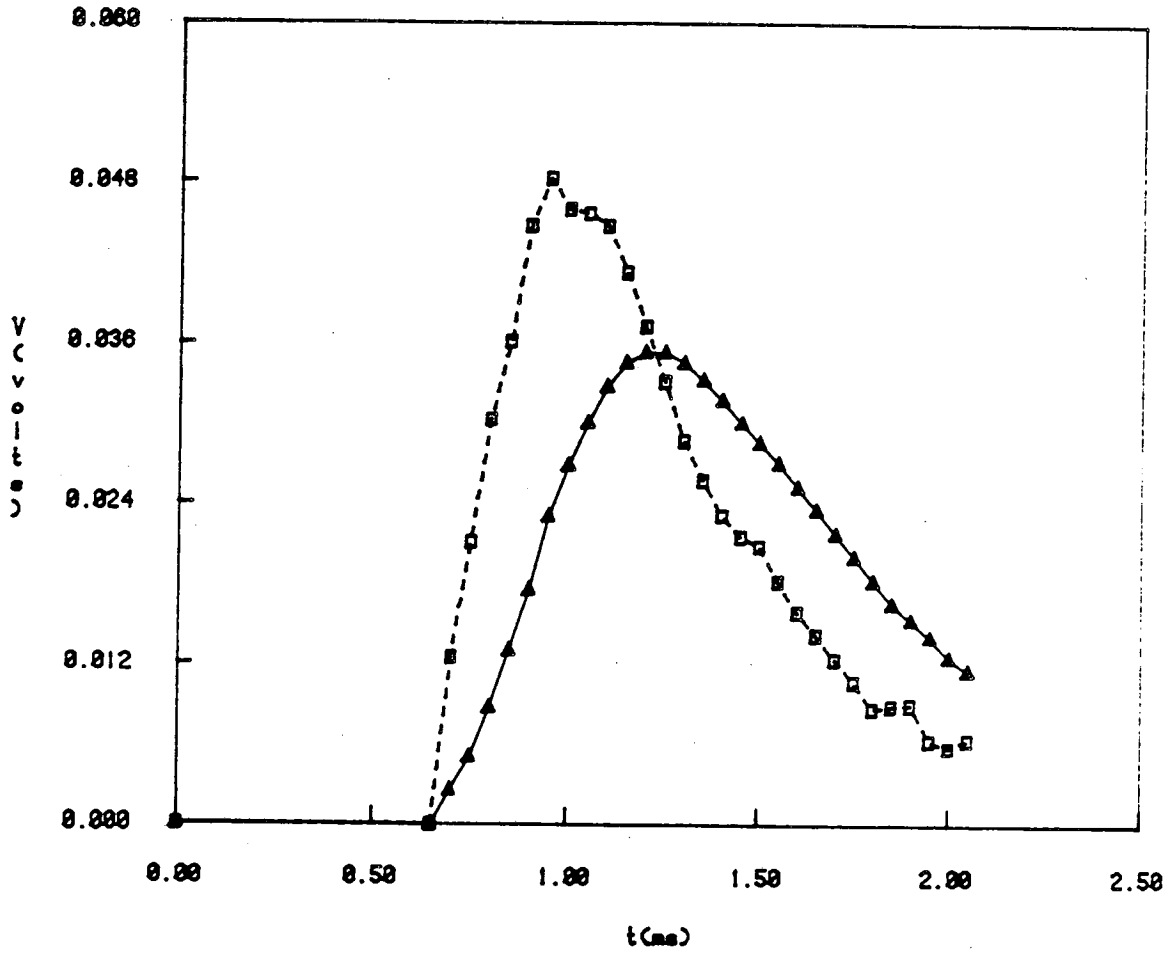

Triangle- Measured data Square-Corrected data
Fig. D-14:UC2 Signal(Run6);E=11.5 joules

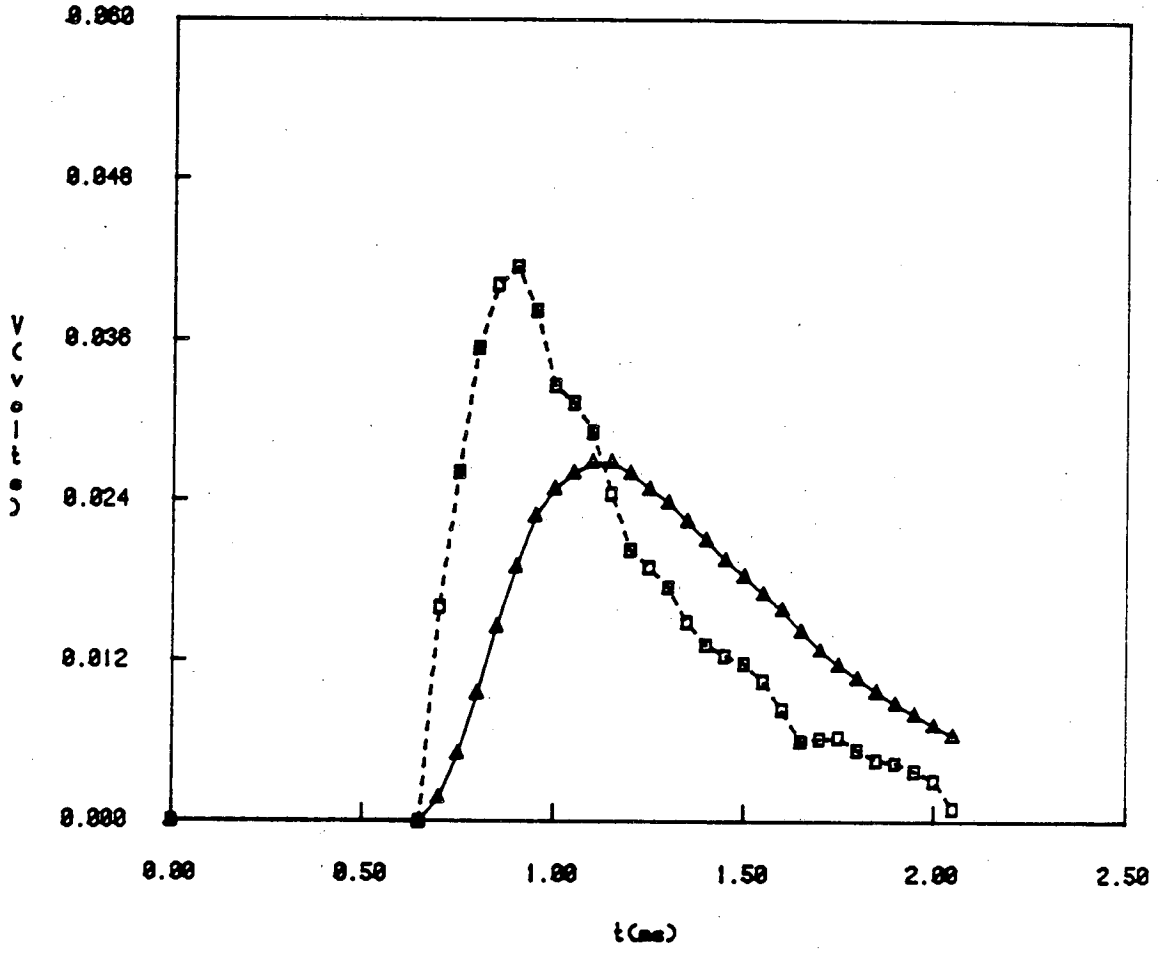

Triangle- Measured data Square-Corrected data
Fig. D-15:UC2 Signal(Run7);E=12.0 joules

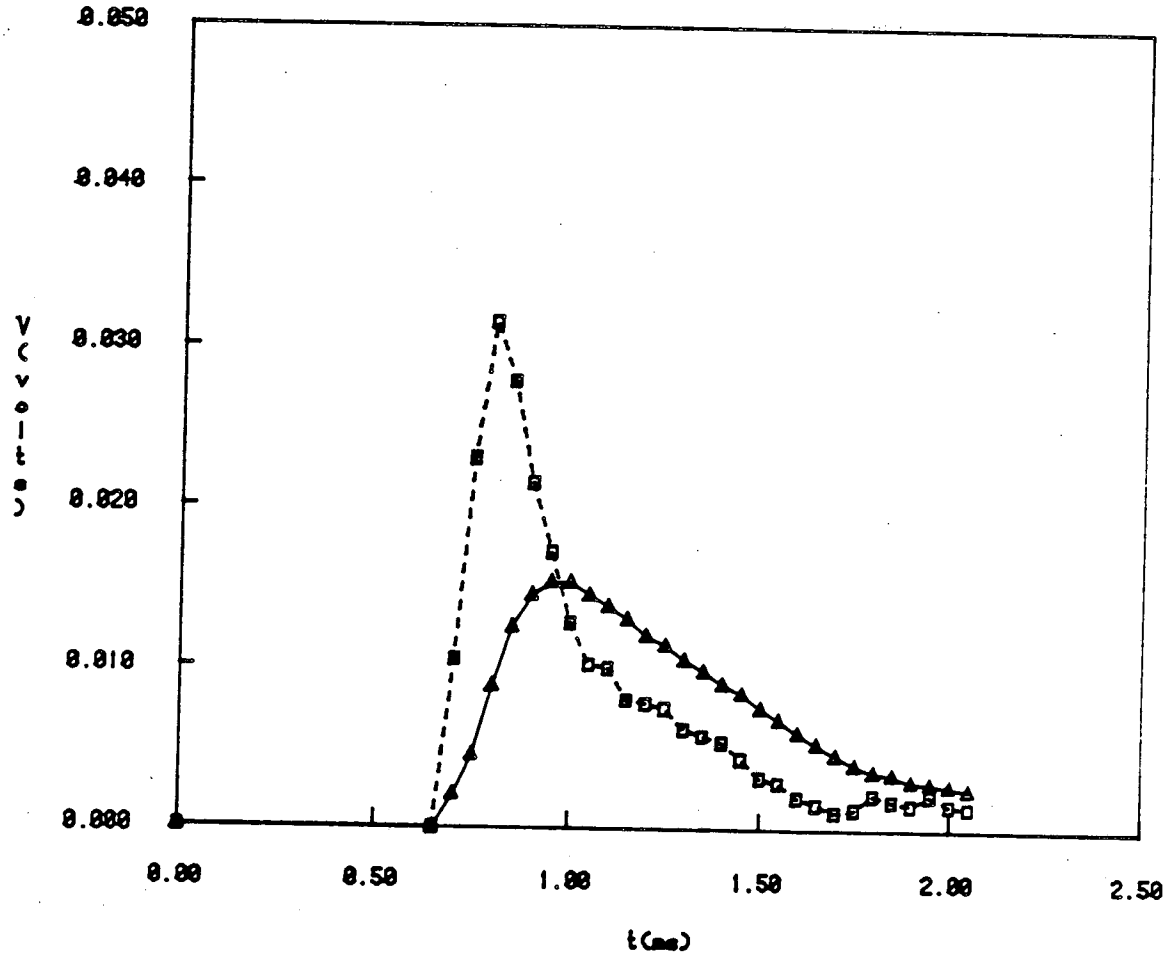

Triangle- Measured data Square-Corrected data
Fig. D-16:UC2 Signal(Run8);E=14.5 joules

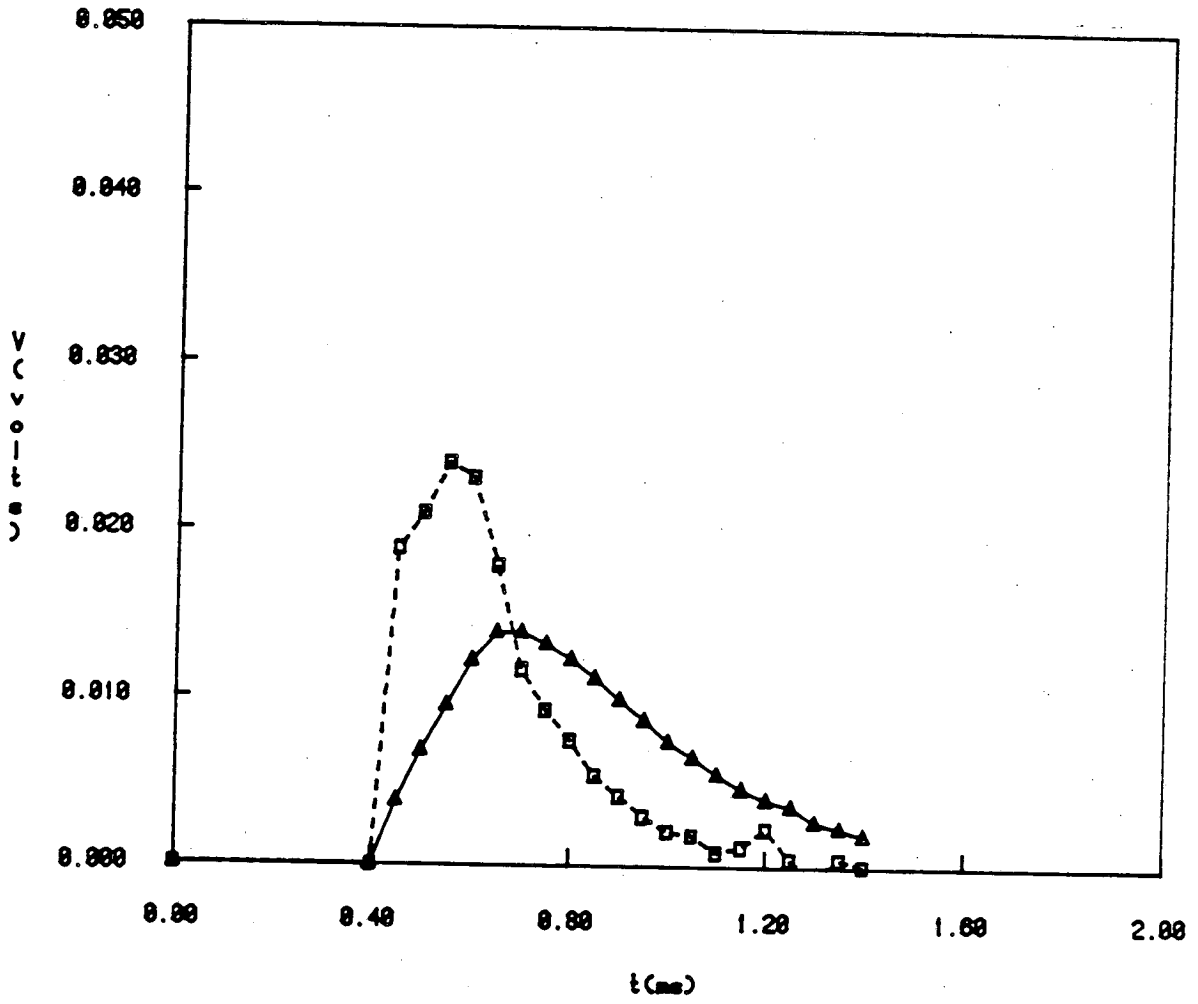

Triangle-Measured data Square-Corrected data
Fig. D-17:C3 Signal(Run1);E=5.8 joules

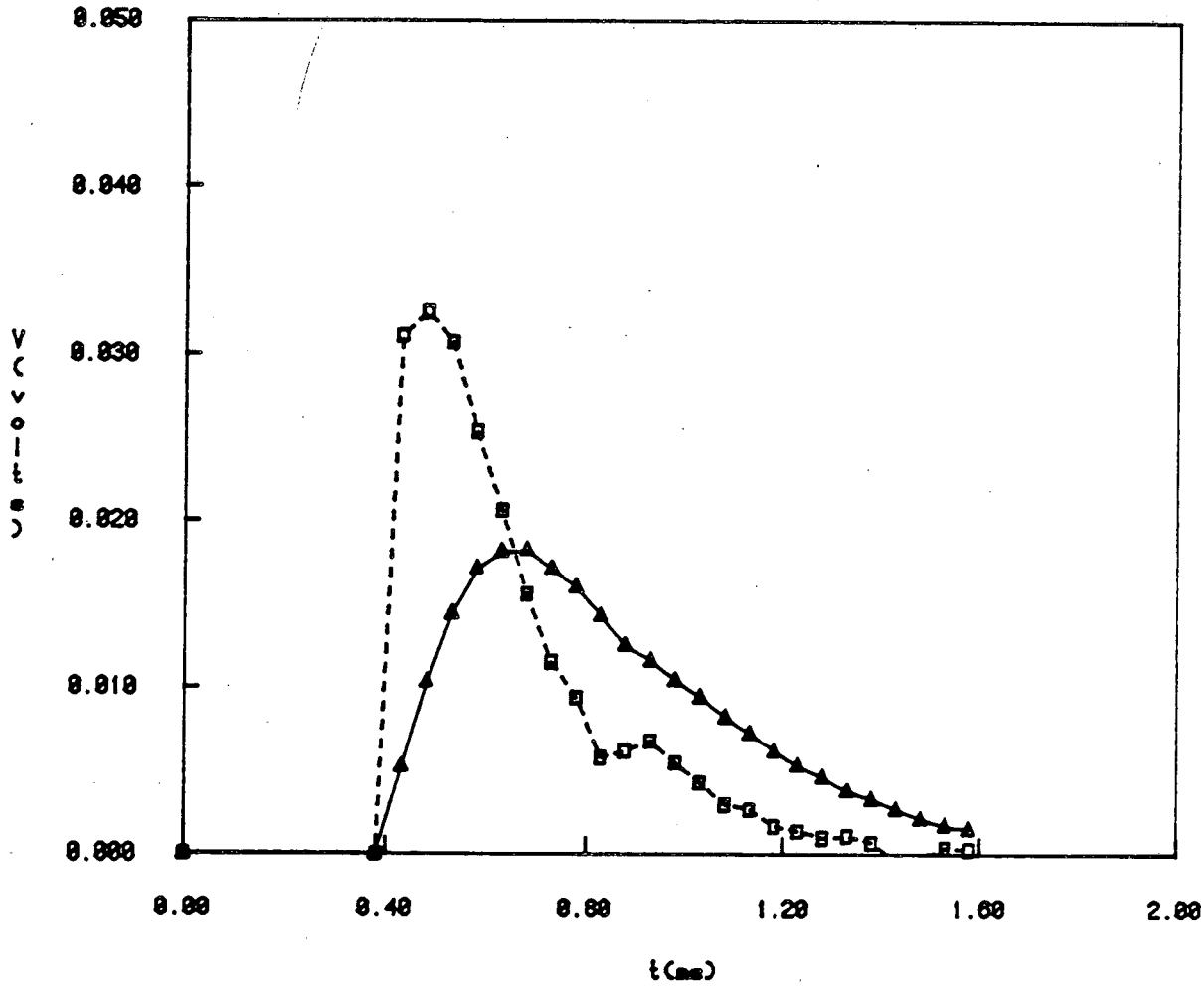

Triangle-Measured data Square-Corrected data
Fig. D-18:C3 Signal(Run2);E=6.7 joules

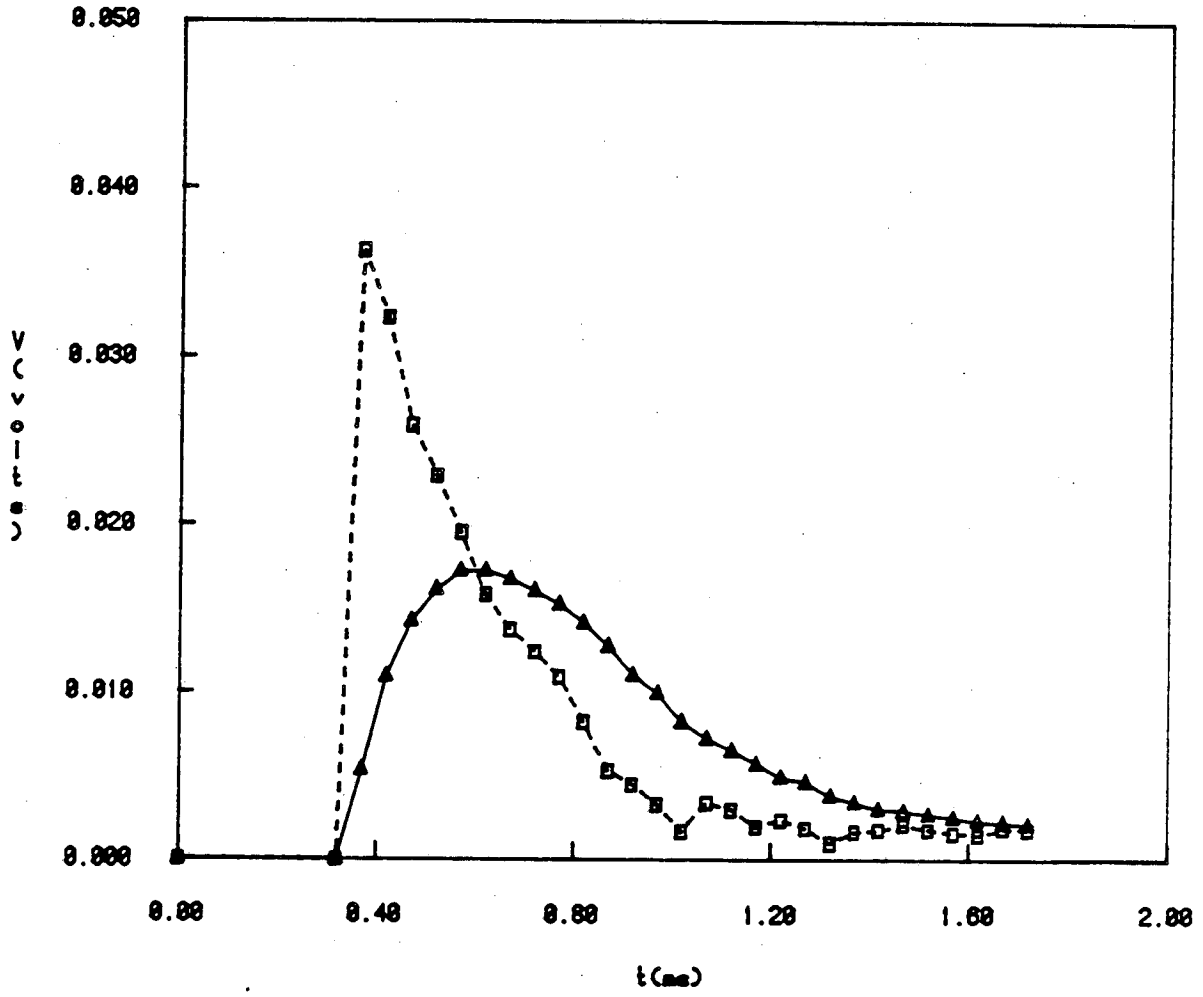

Triangle-Measured data Square-Corrected data
Fig. D-19:C3 Signal(Run3);E=6.7 joules

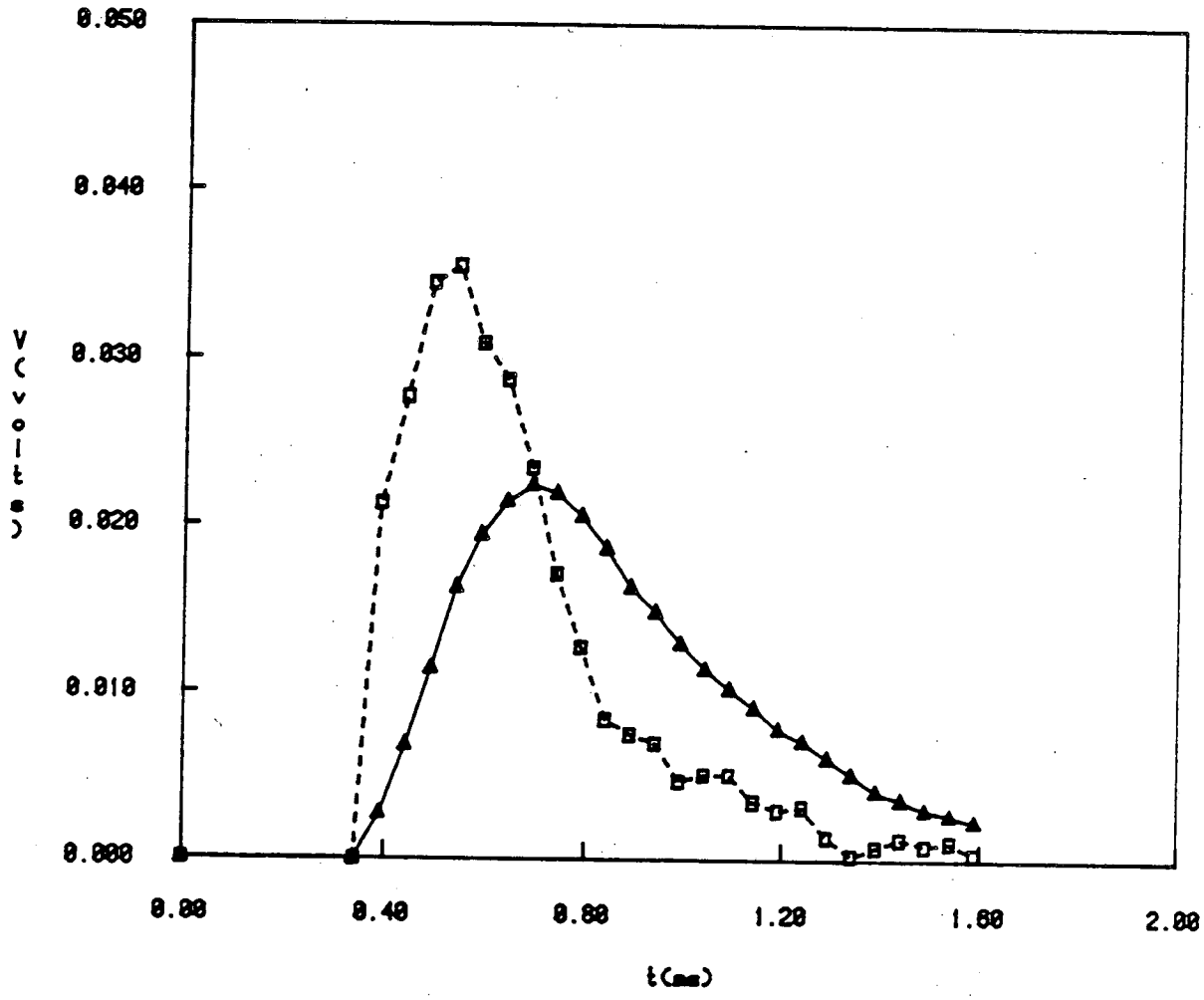

Triangle-Measured data Square-Corrected data
Fig. D-20:C3 Signal(Run4);E=7.4 joules

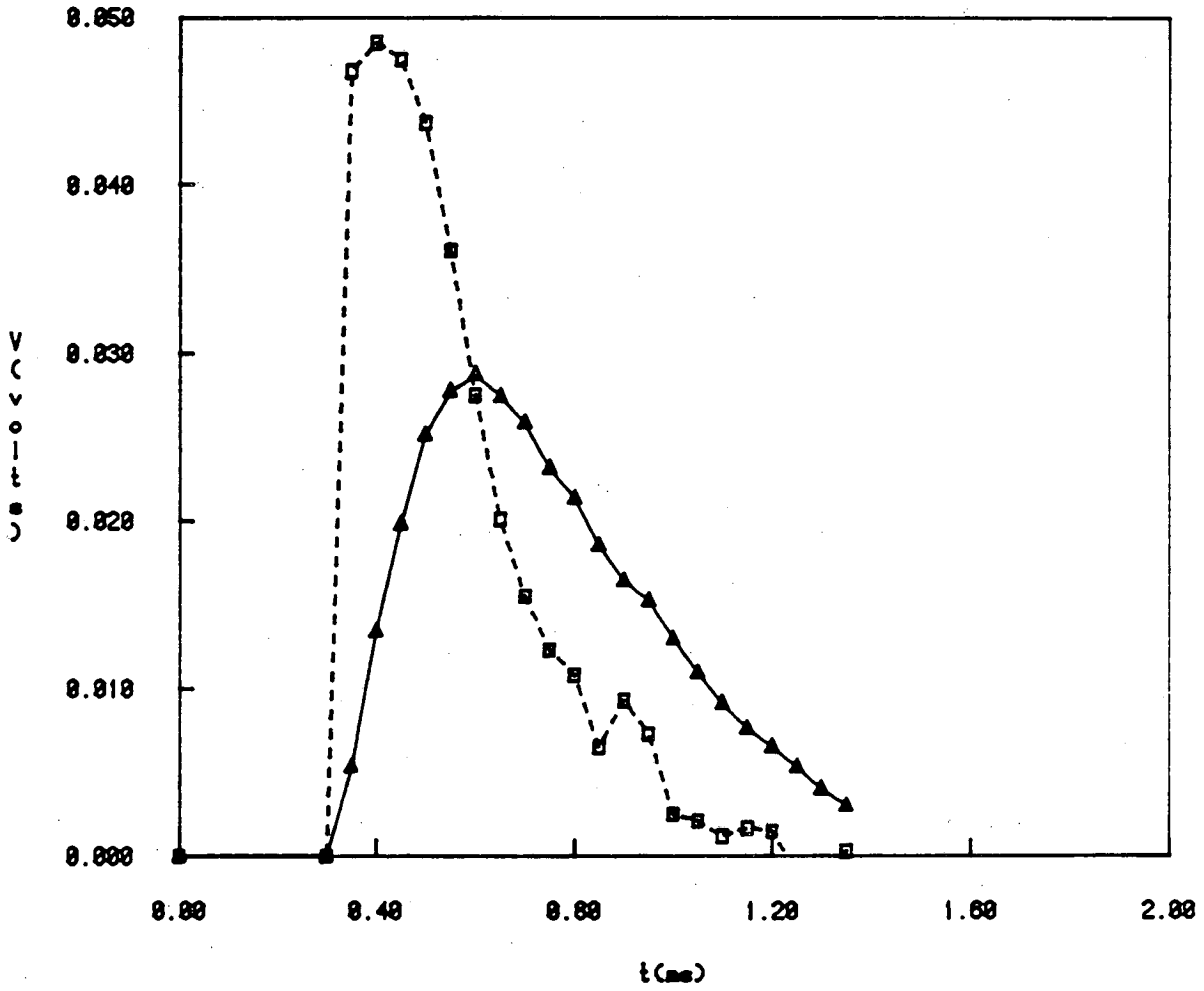

Triangle-Measured data Square-Corrected data
Fig. D-21:C3 Signal(Run5);E=8.8 Joules

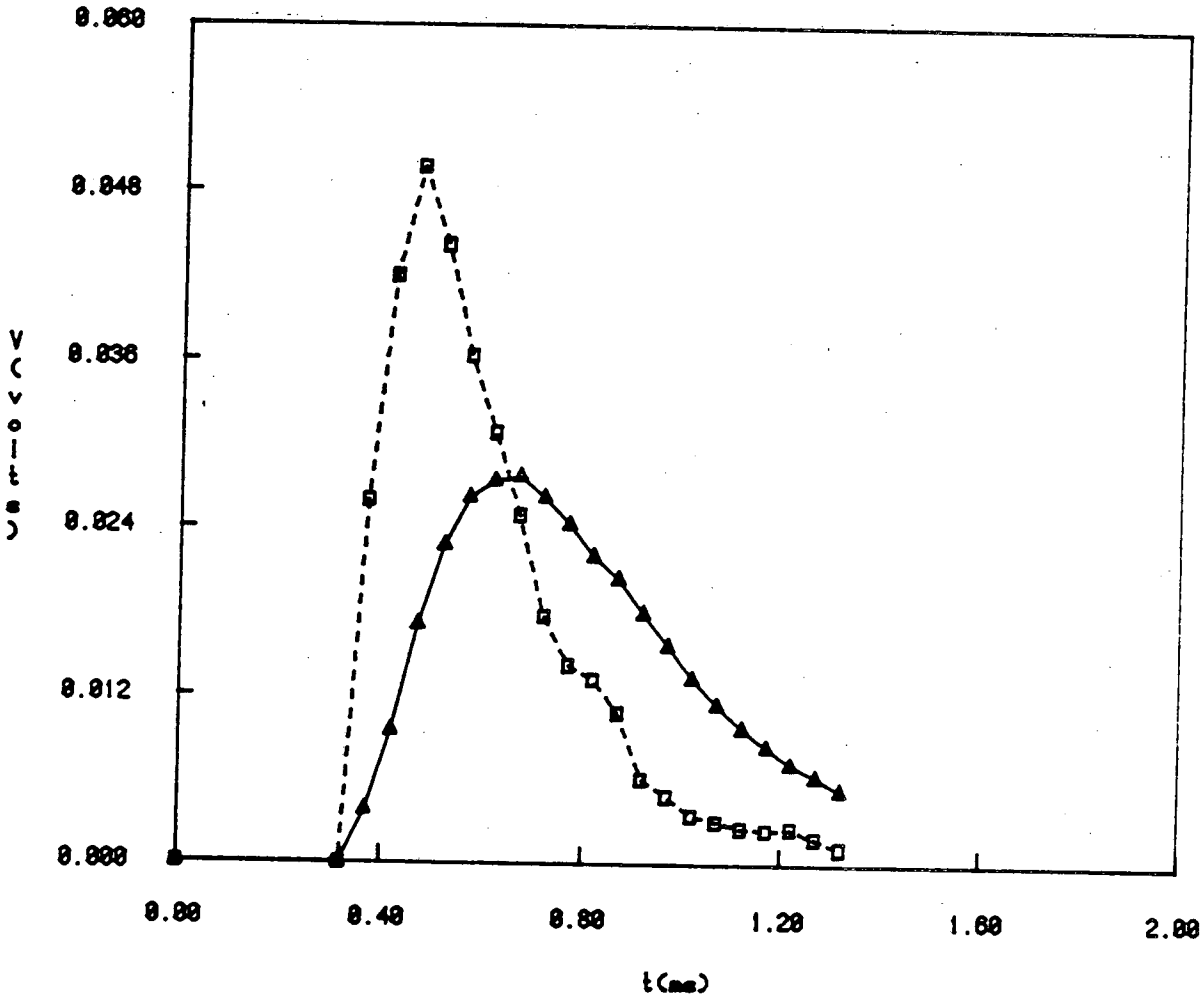

Triangle-Measured data Square-Corrected data
Fig. D-22:C3 Signal(Run6);E=11.5 joules

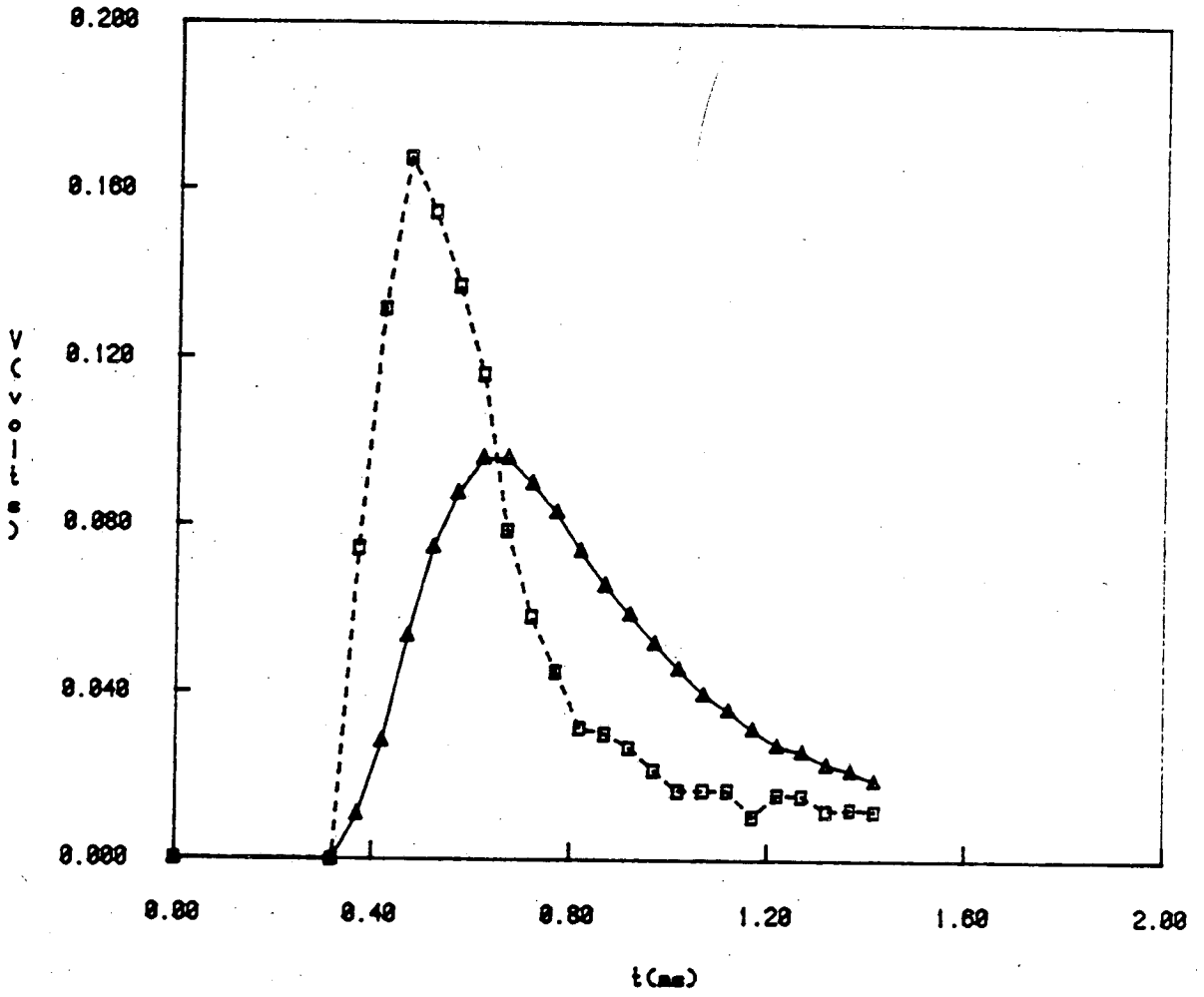

Triangle-Measured data Square-Corrected data
Fig. D-23:C3 Signal(Run7);E=12.0 joules

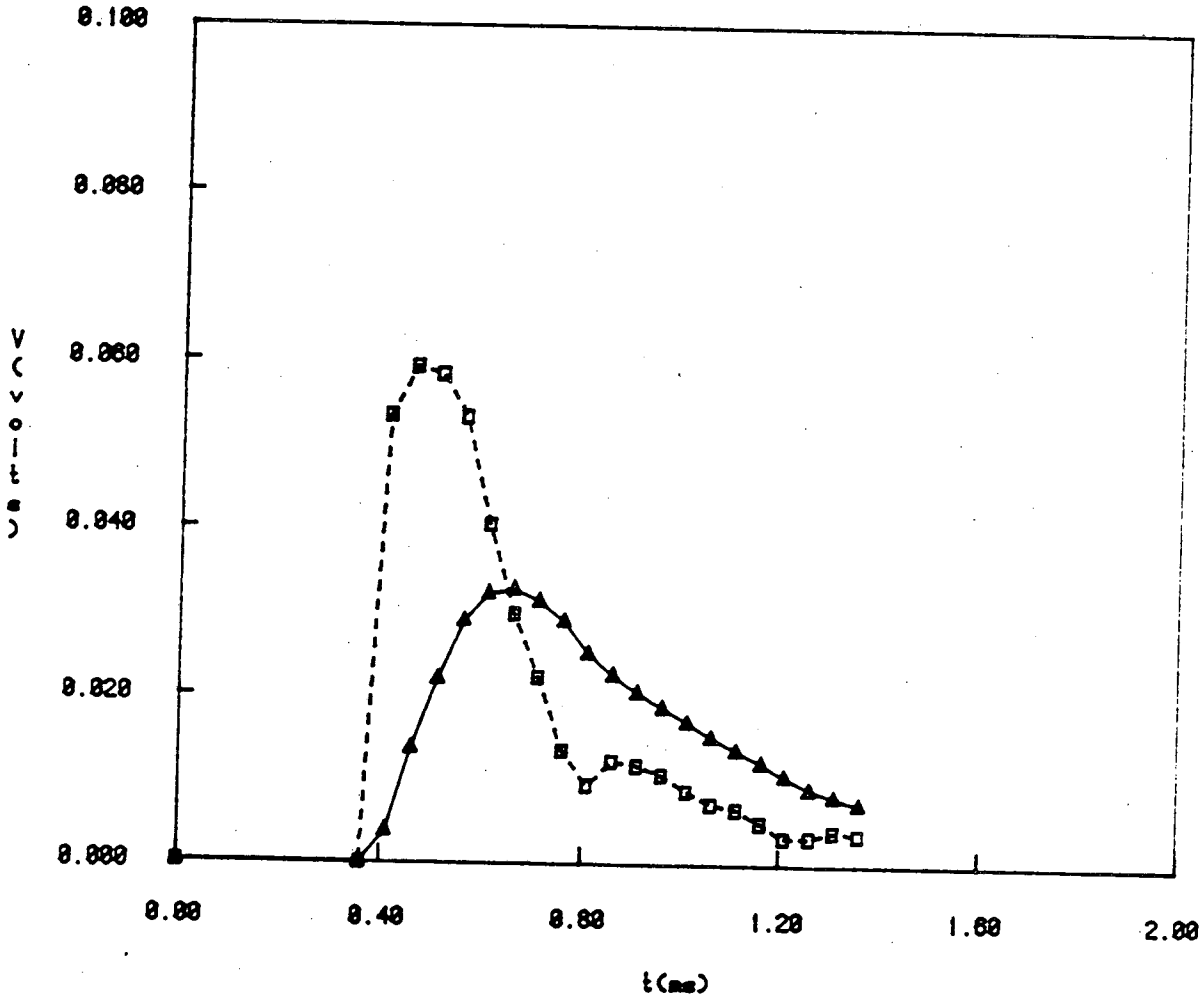

Triangle-Measured data Square-Corrected data
Fig. D-24:C3 Signal(Run8);E=14.5 joules

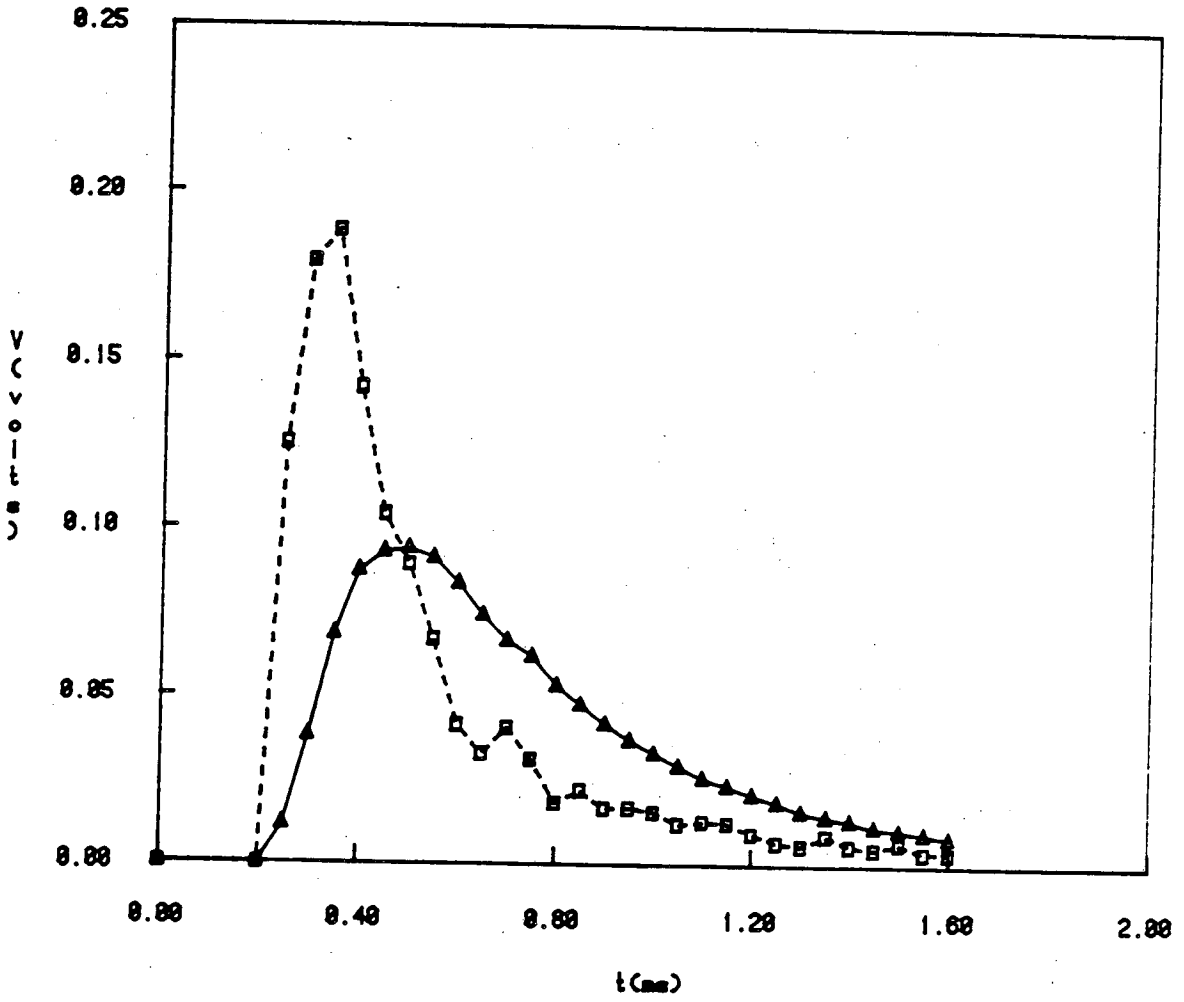

Triangle- Measured data Square- Corrected data
Fig. D-25:Cl Signal(Run1);E=5.9 Joules

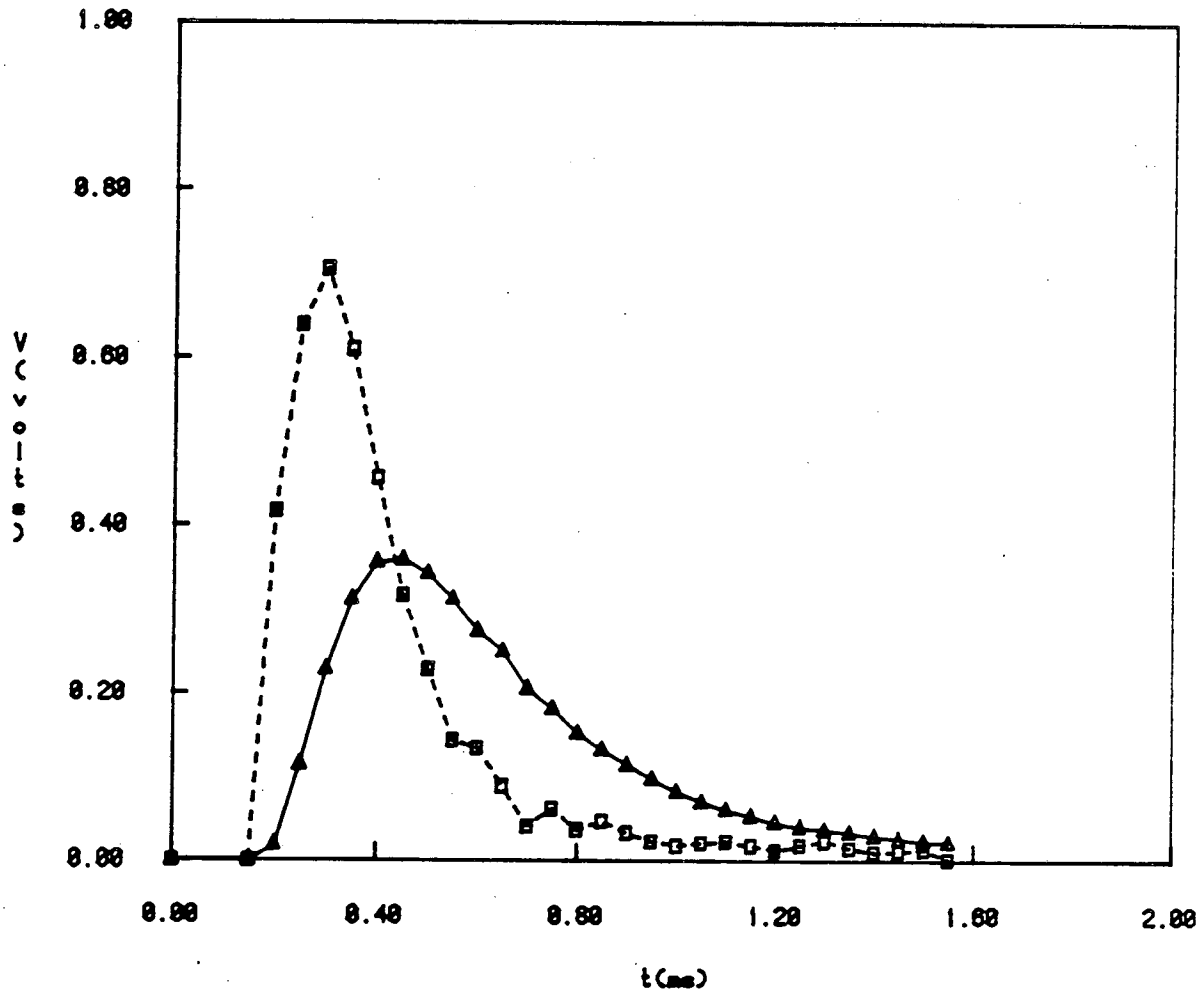

Triangle- Measured data Square- Corrected data
Fig. D-26:C1 Signal(Run2);E=6.7 joules

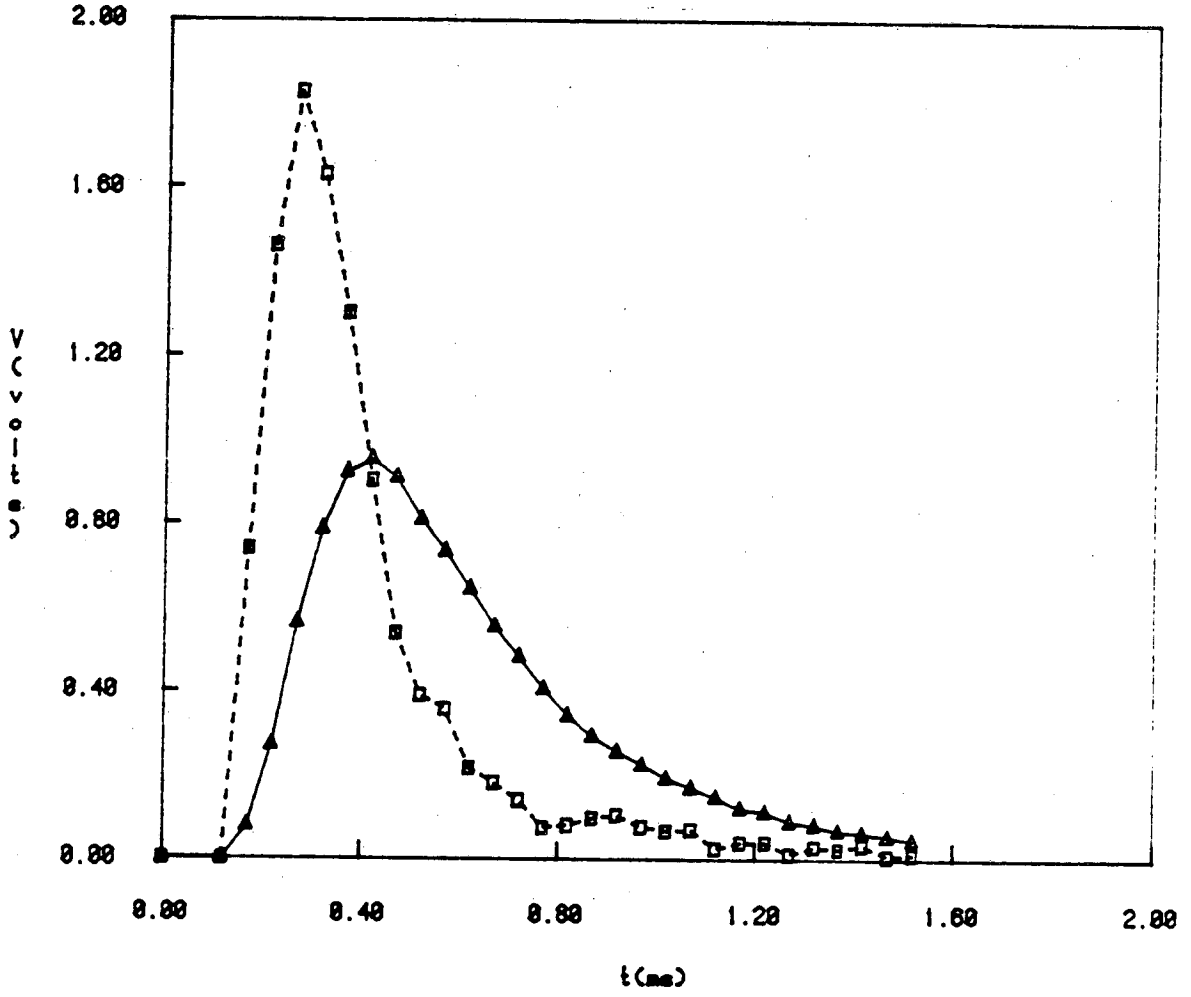

Triangle- Measured data Square- Corrected data
Fig. D-27:C1 Signal(Run3);E=6.7 joules

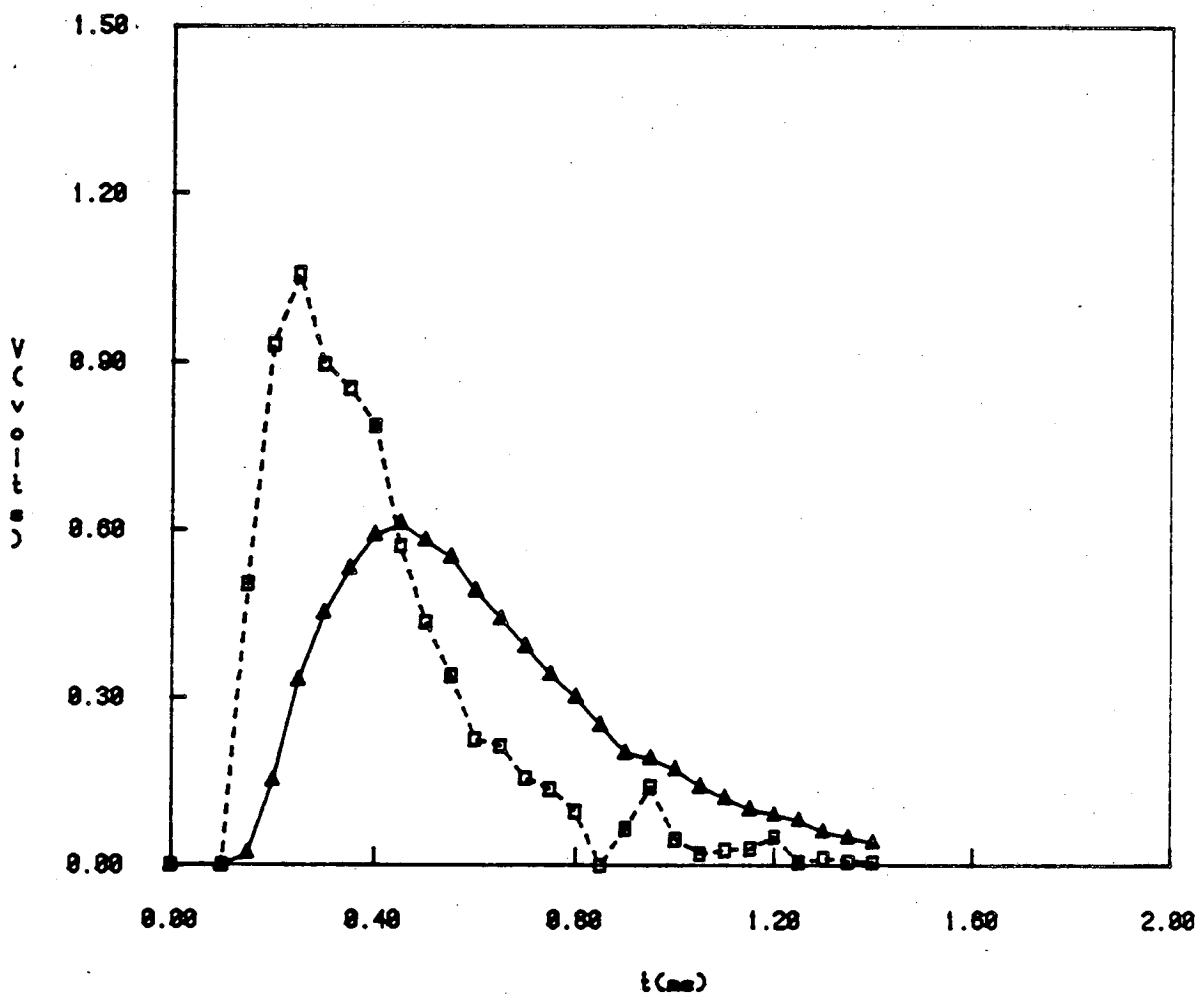

Triangle- Measured data Square- Corrected data
Fig. D-28:Cl Signal(Run4);E=7.4 joules

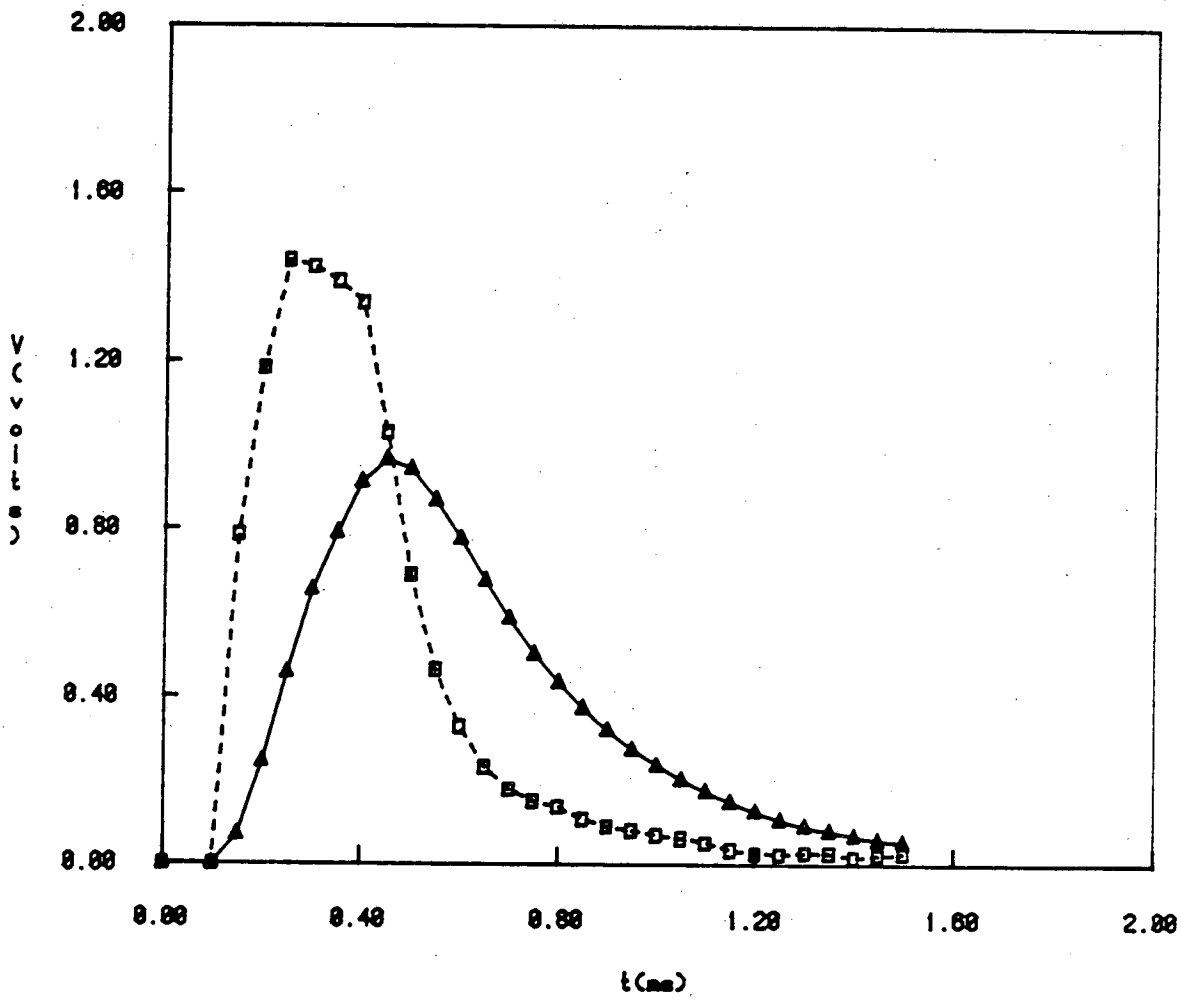

Triangle- Measured data Square- Corrected data
Fig. D-29:C1 Signal(Run5);E=8.6 joules

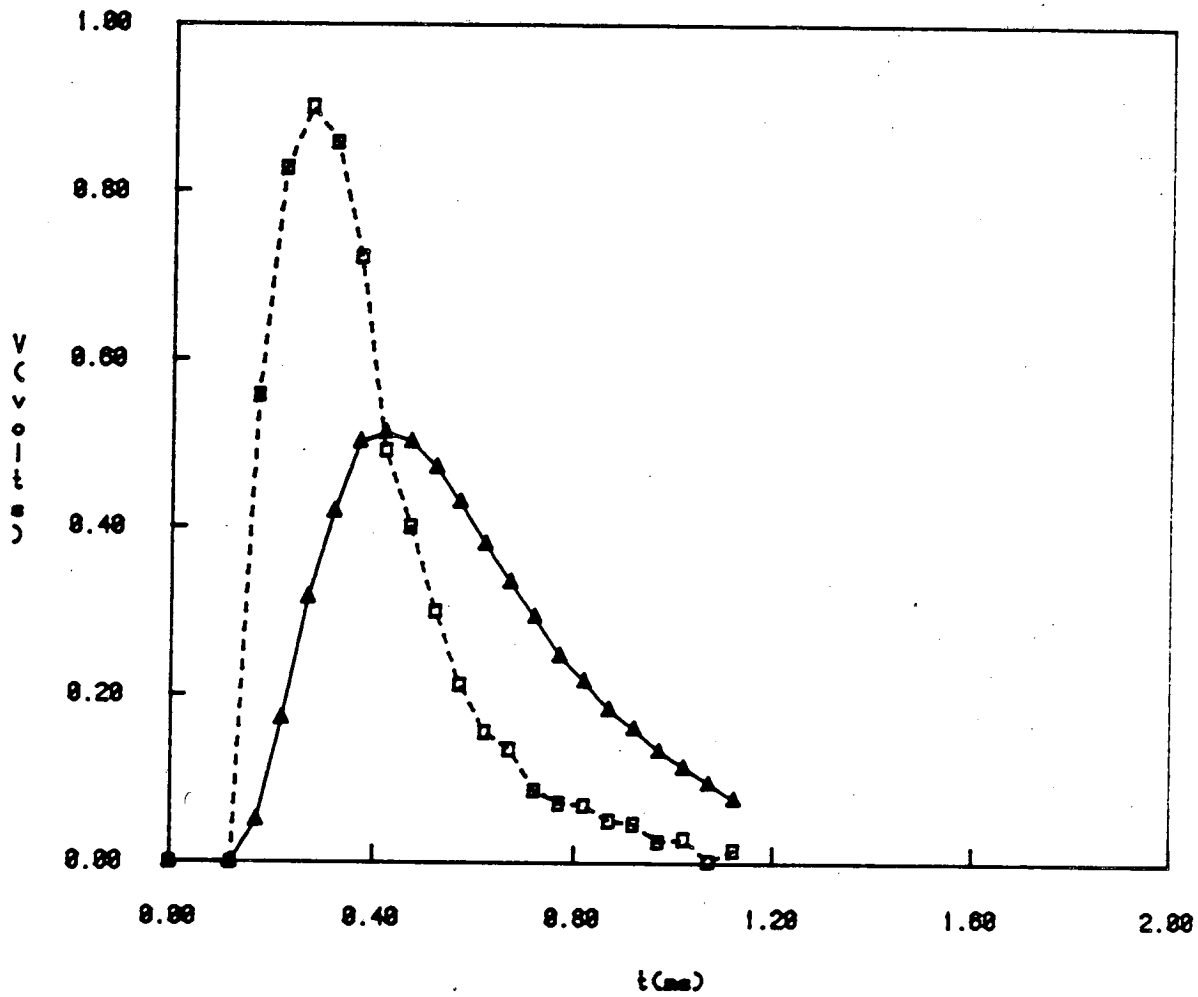

Triangle- Measured data Square- Corrected data
Fig. D-30:C1 Signal(Run6);E=11.5 joules

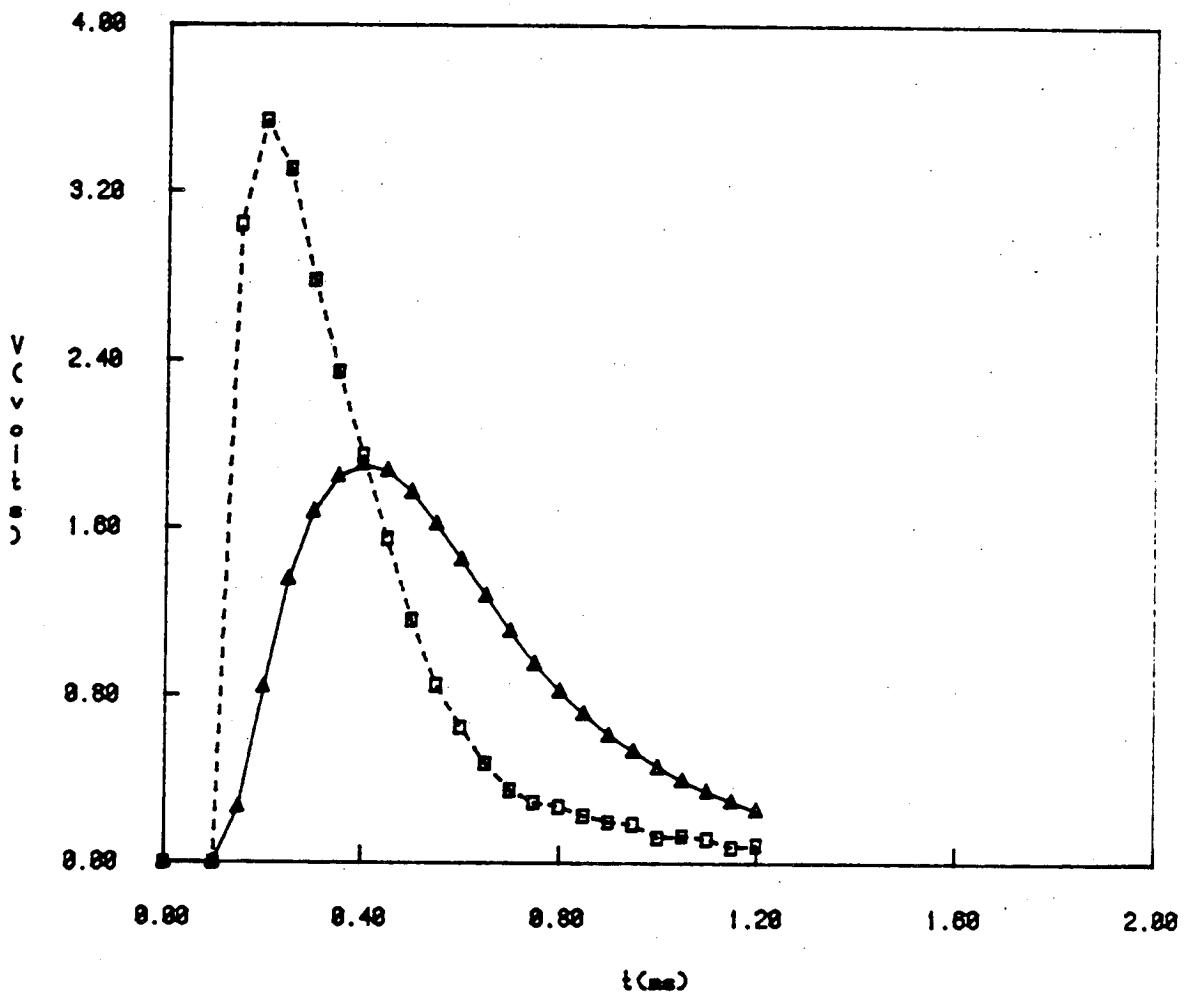

Triangle- Measured data Square- Corrected data
Fig. D-31:Cl Signal(Run7);E=12.8 Joules

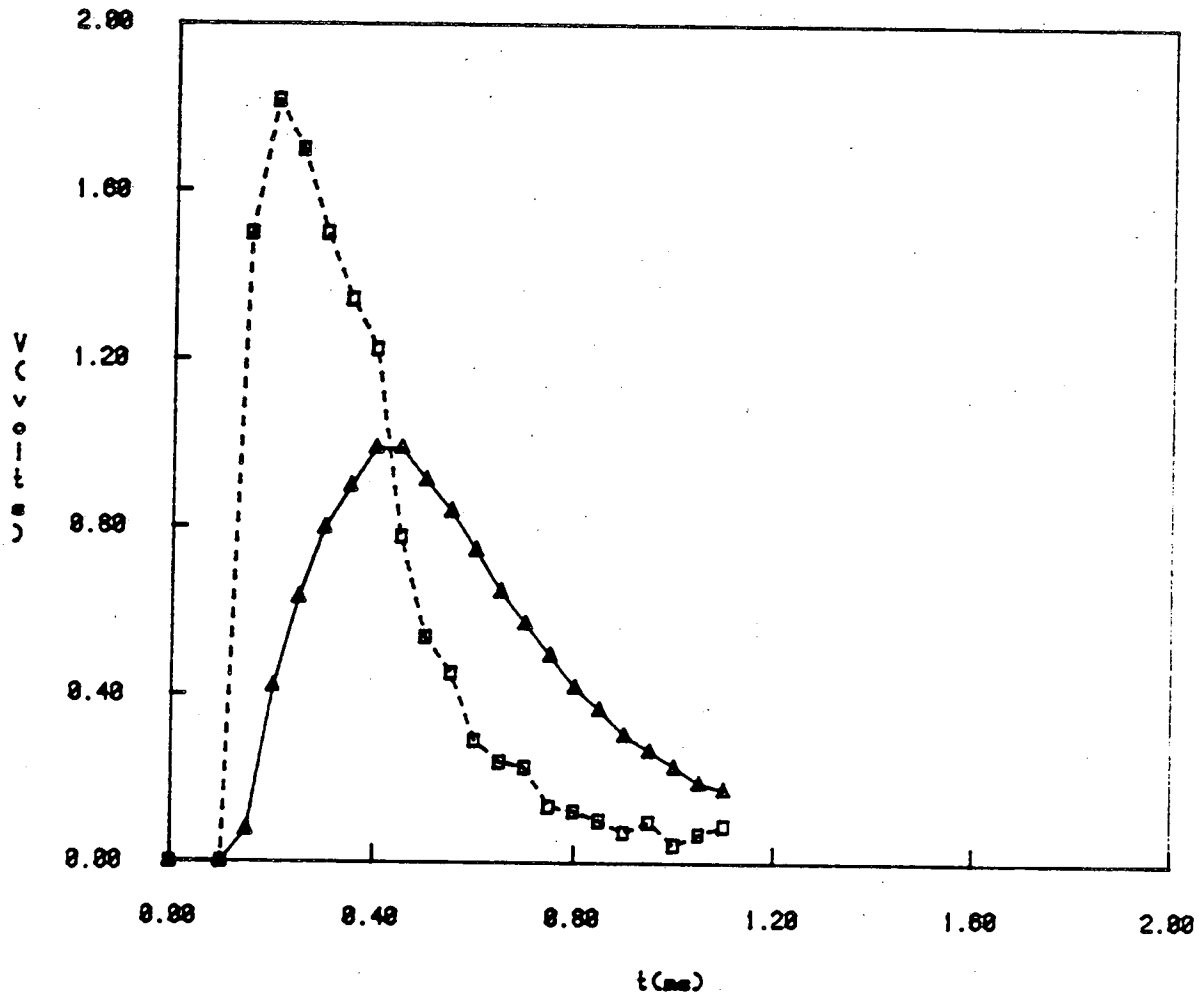

Triangle- Measured data Square- Corrected data
Fig. D-32:Cl Signal(Run8);E=14.5 Joules

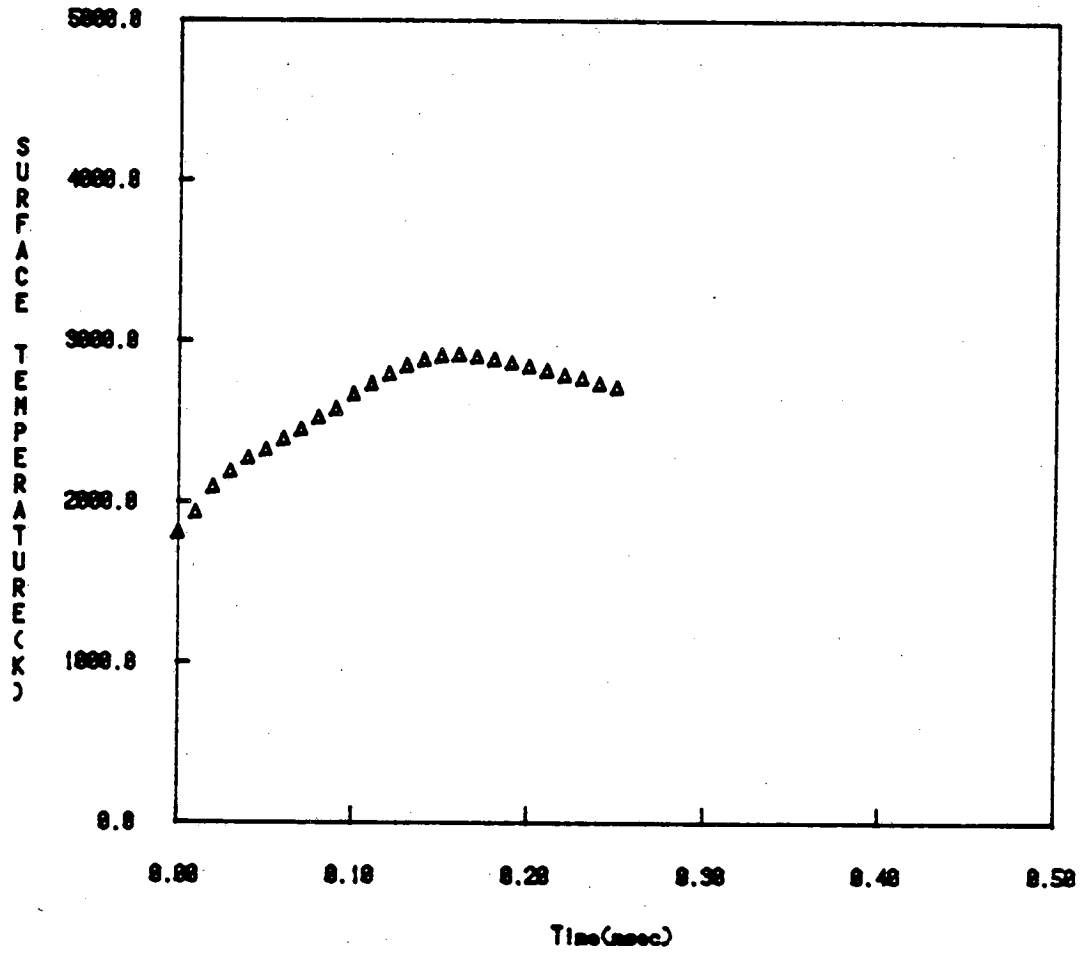

Fig. D-33:Measured Surface Temperature (Run1);E=5.9 Joules
T0=1000.K

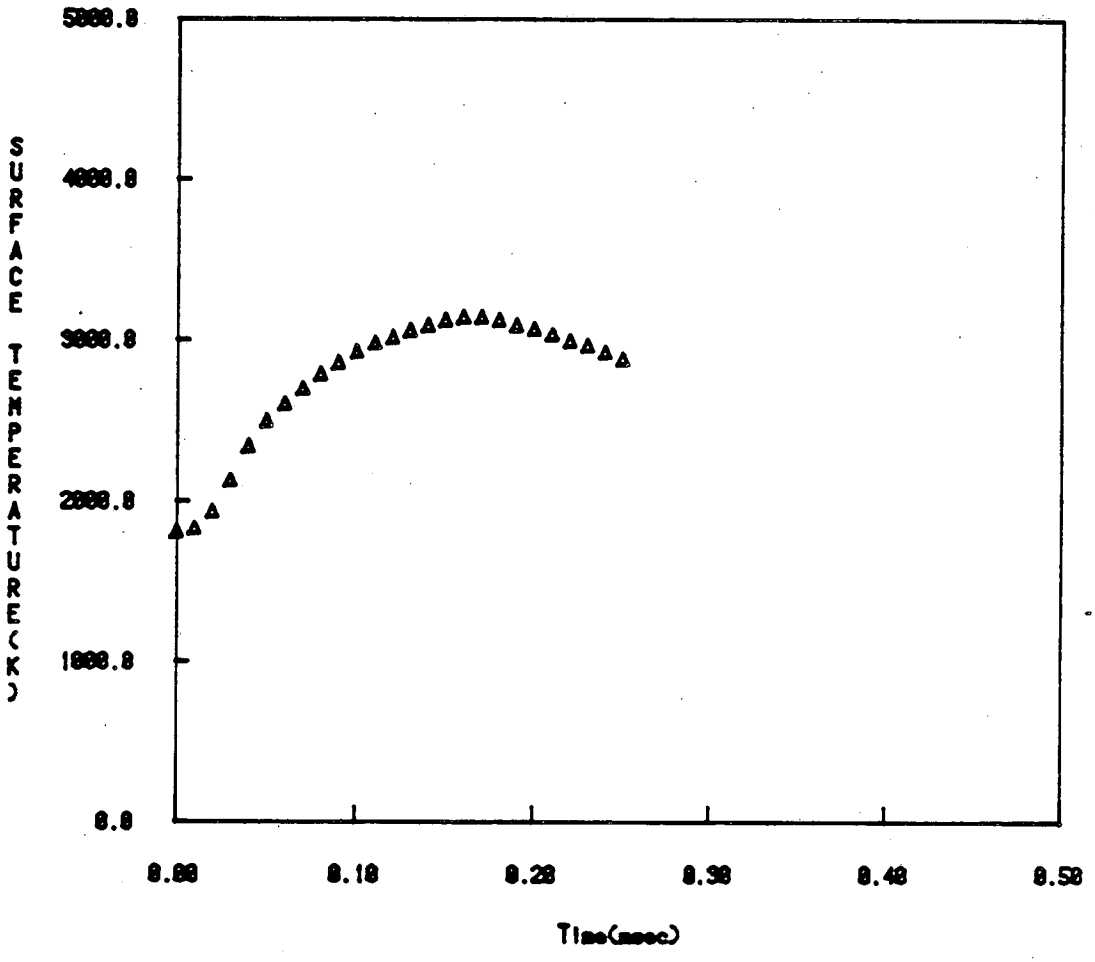

Fig. D-34:Measured Surface Temperature (Run2);E=6.7 joules
T0=1000.K

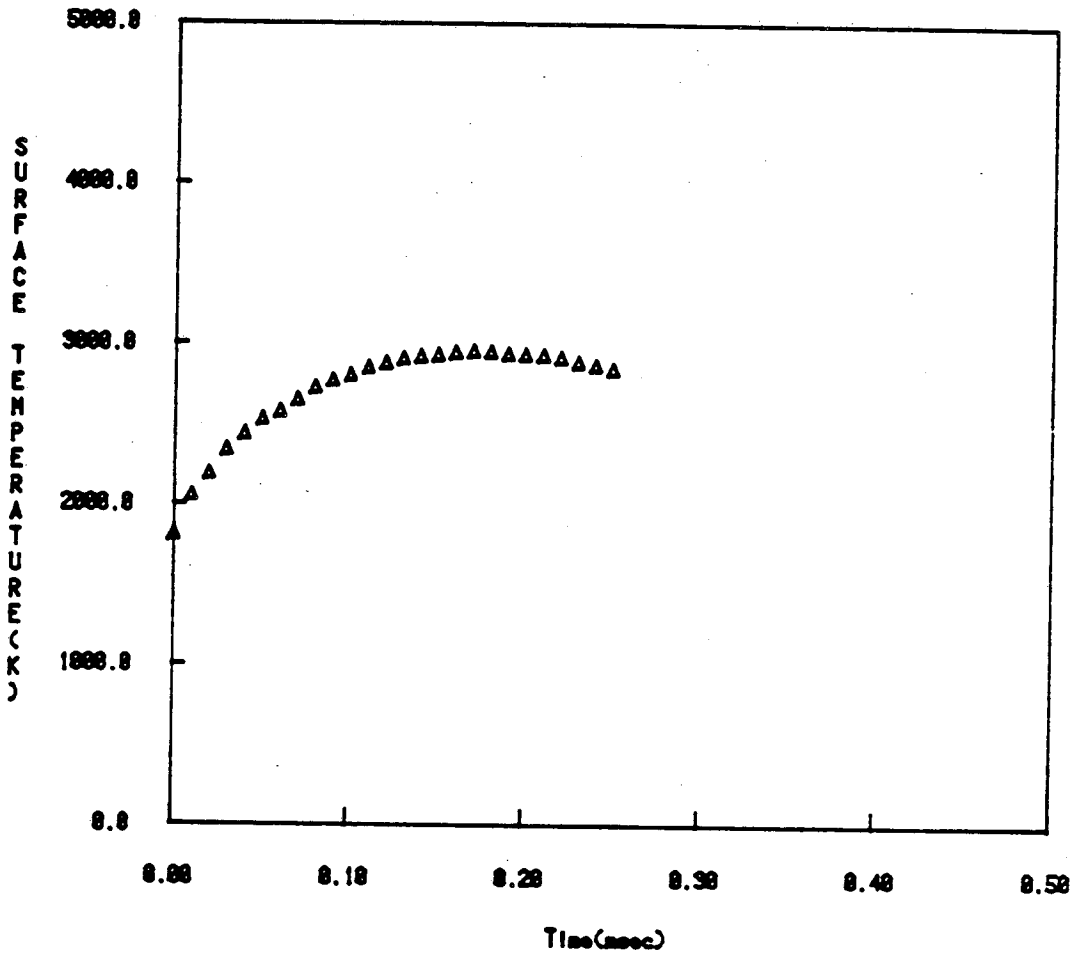

Fig. D-35:Measured Surface Temperature (Run3);E=6.7 Joules
T0=1000.K

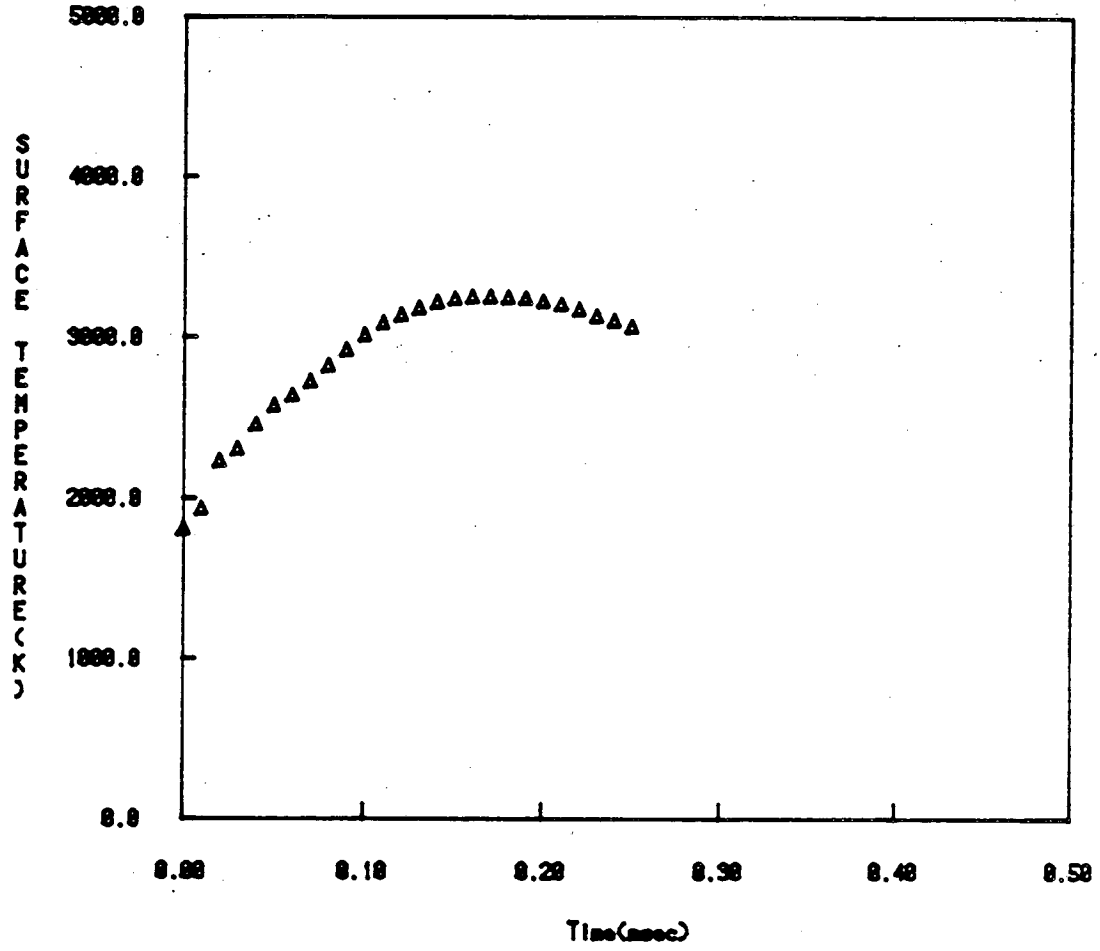

Fig. D-98:Measured Surface Temperature (Run4),E=7.4 joules
T0=1000.K

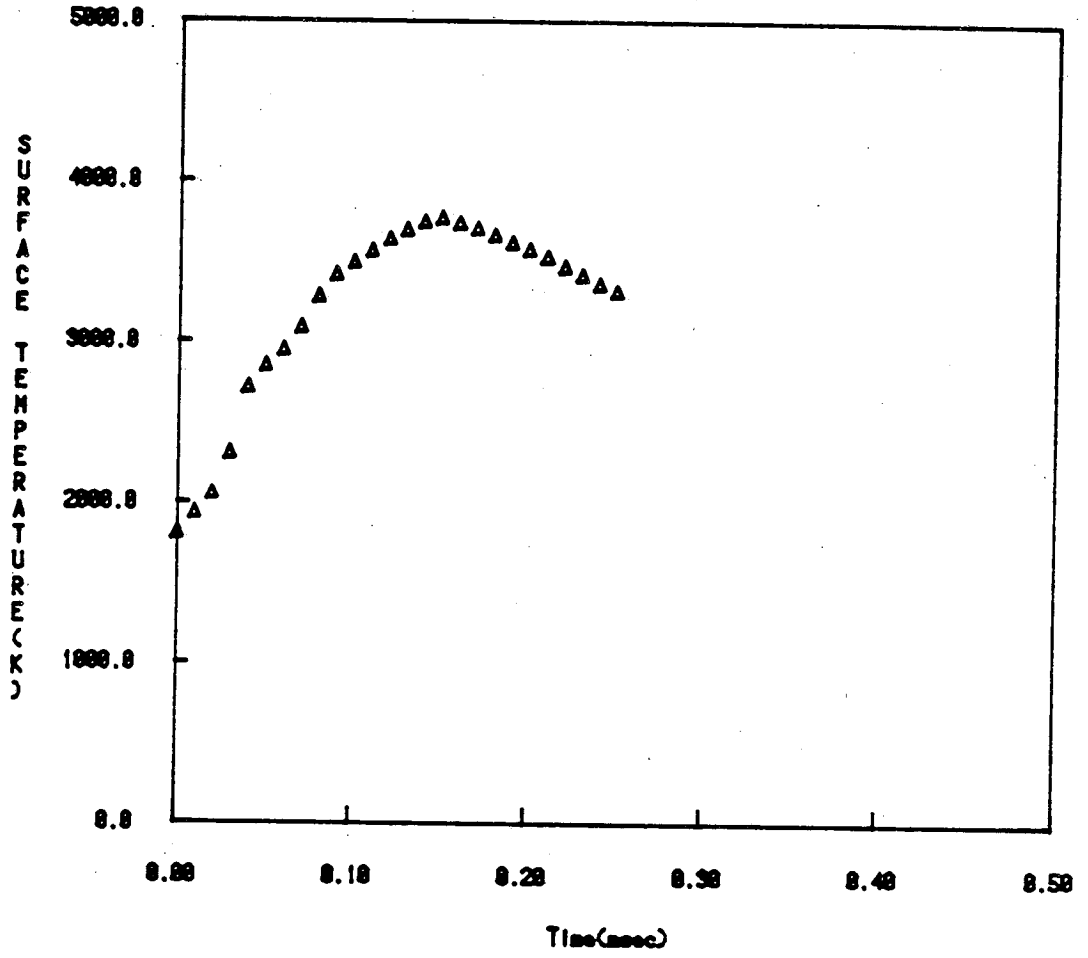

Fig. D-37:Measured Surface Temperature (Run5);E=0.0 Joules
T0=1000.K

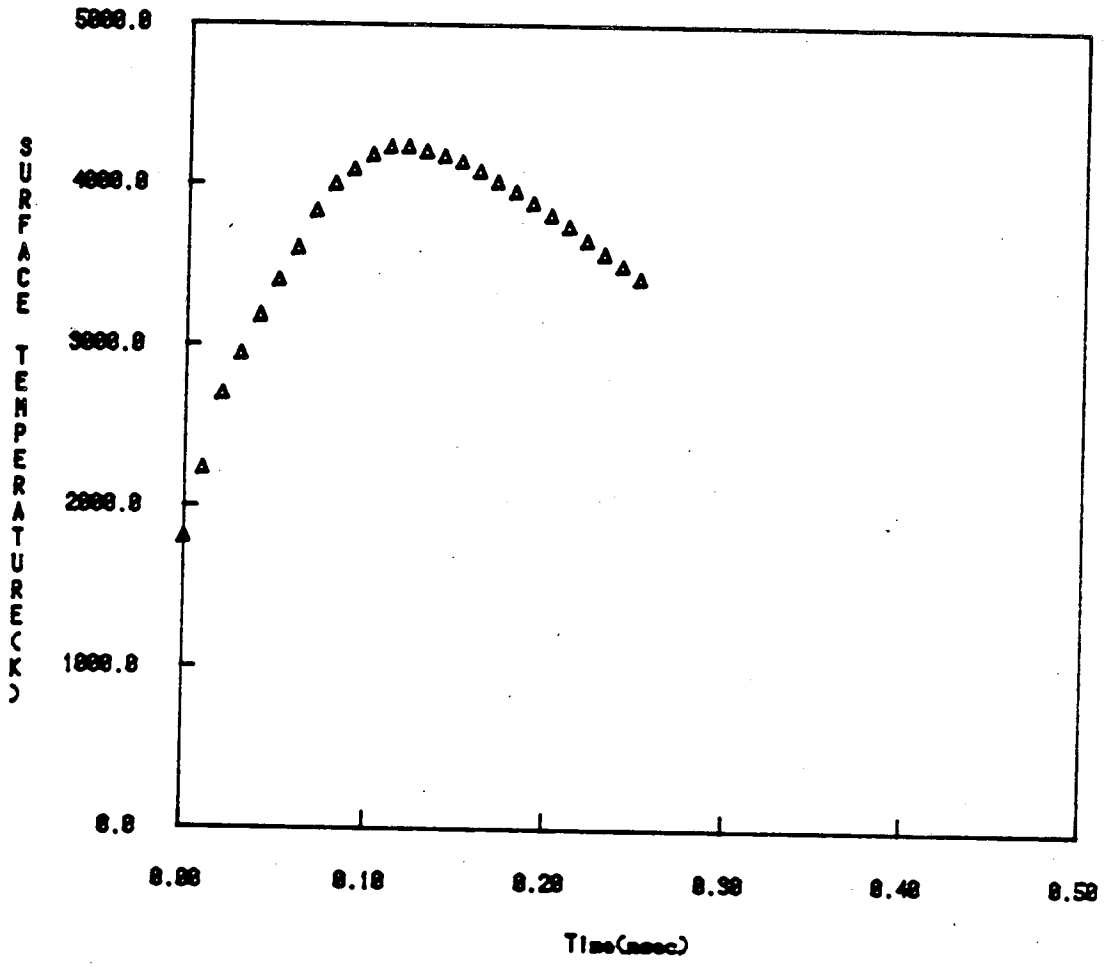

Fig. D-38:Measured Surface Temperature (Run8);E=11.5 joules
T0=1000.K

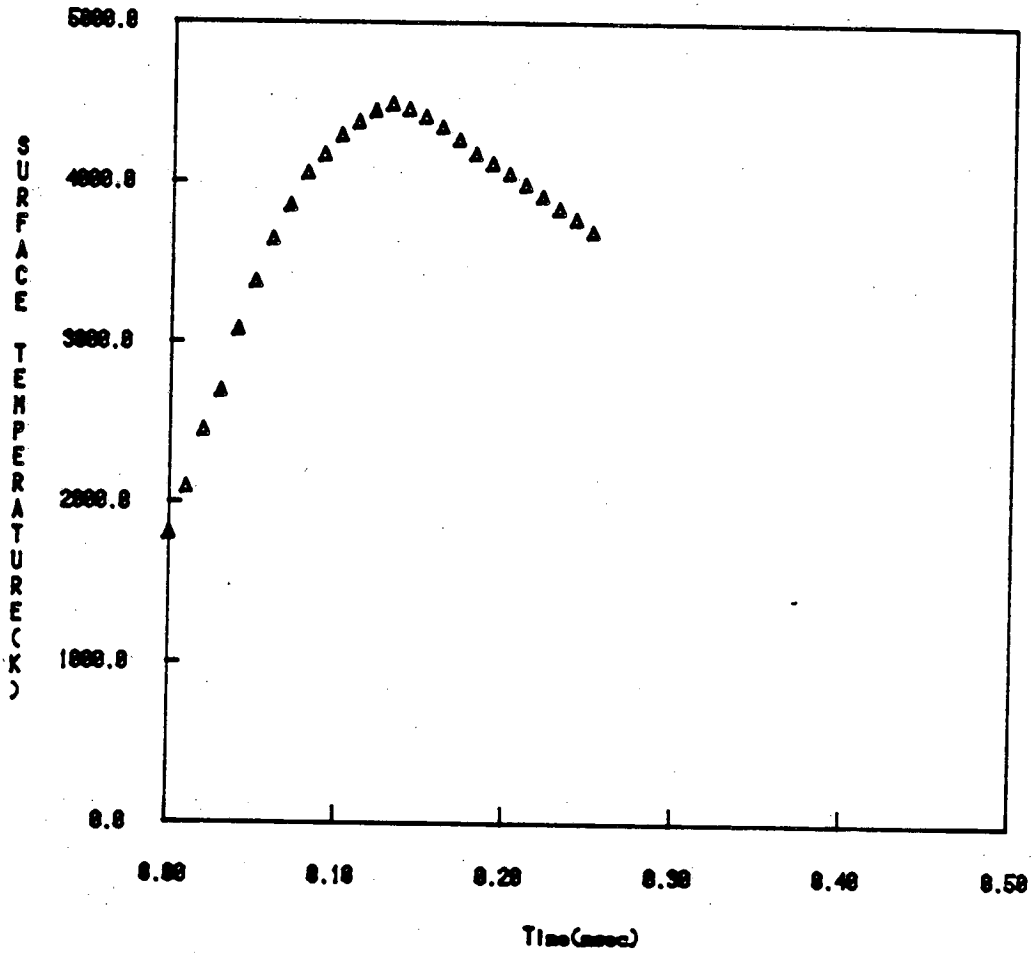

Fig. D-39:Measured Surface Temperature (Run7);E=12.8 Joules
T0=1000.K

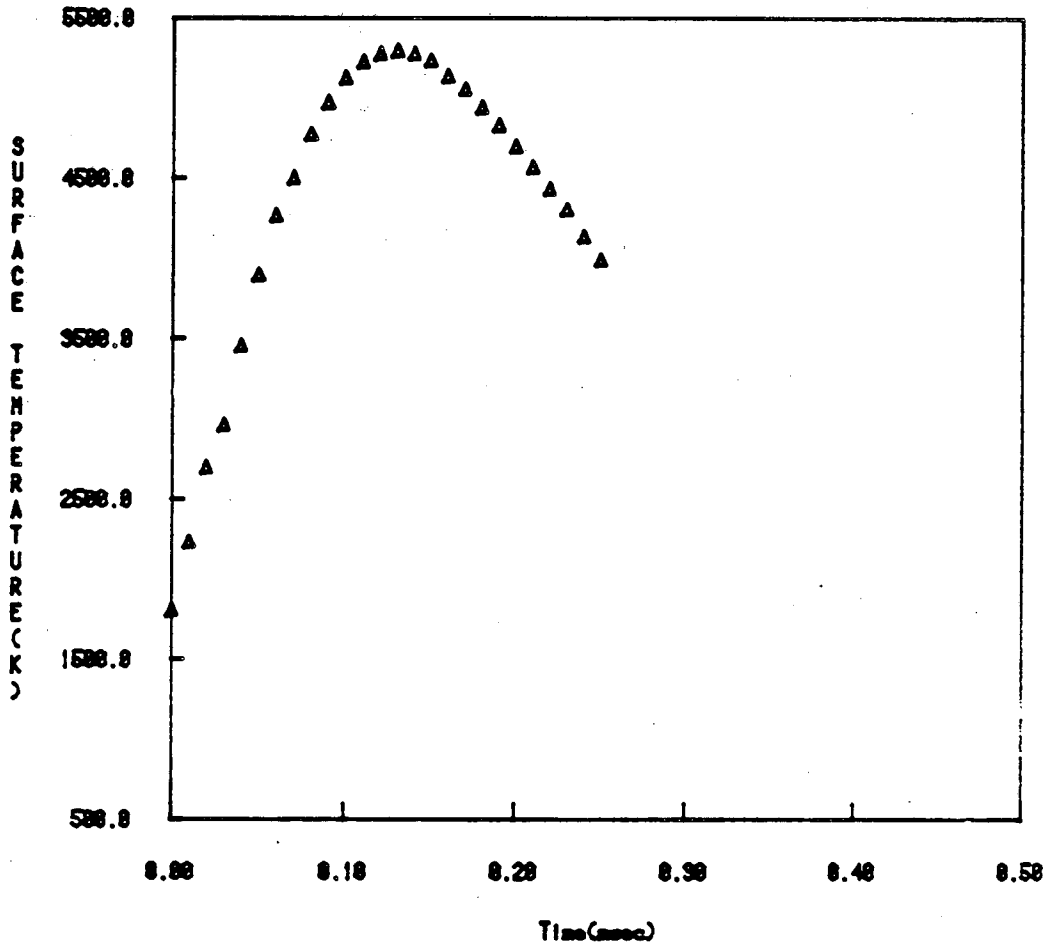

Fig. D-48:Measured Surface Temperature (Run8),E=14.5 Joules
T0=1000.K

ACKNOWLEDGEMENTS

I would like to thank Professor Donald R. Olander of the Department of Nuclear Engineering, University of California at Berkeley for always being accessible for guidance and providing many fruitful suggestions for the experiment and analyzing the data.

I would also like to thank Dan Winterbauer in the machine shop and Jack Harrell in the electronic shop for promptly fabricating needed parts.

The supervision, accurate typing and drafting by Jean Wolslegel, June DeLaVergne and Gloria Pelatowski are very much appreciated.

This work has been supported by the Director, Office of Energy Research, Office of Basic Energy Science, Materials Science Division of the U.S. Department of Energy under Contract No. DE-AC03-76SF00098.

REFERENCES

1. Gathers, G. R., Shaner, J. W., and Brier, R. L., Rev. Sci. Instrum. 47 (1970) 65.

2. Cezairliyan, A., Morse, M. S., Berman, H. A., and Beckett, C. W., J. Res. NBS 74A (1970) 65.

3. Seydel, U., and Fucke, W., Z. Naturforsch 32a (1977) 994.

4. Reil, K. O., Cronenberg, A. W., Trans. Am. Nucl. Soc. 27 (1977) 576.

5. Benson, D. A., Application of Pulsed Electron Beam Vaporization to Studies of UO_2, Sand-77-0429, Sandia Laboratories, Albuquerque, New Mexico, 1977.

6. Asami, N., Nischikawa, M., and Taguchi, M., Thermodynamics of Nuclear Materials 1974, Vol. 1, p. 287, IAEA, Vienna, 1975.

7. Ohse, R. W., Berrie, P. G., Bogensberger, H. G., and Fischer, E. A., Thermodynamics of Nuclear Materials 1974, Vol. 1, 307, IAEA, Vienna, 1975.

8. Bober, M., Karow, H. U., and Schretzmann, K., Thermodynamics of Nuclear Materials 1974, Vol. 1, 295, IAEA, Vienna, 1975.

9. Ohse, R. W., V. Tippelskrich, H., The Critical Constants of the Element of Some Refractory Materials with High Critical Temperature, 29th IUPAC General Assembly, Warsaw, Aug. 1977, High Temperatures-High Press.

10. C. H. Tsai, Ph. D. Thesis, University of California at Berkeley, November 1981.

11. R. W. Ohse, J. F. Babelot, K. A. Long, J. Magill," Vapor Pressure Measurements of Uranium Carbides up to 7000 K using Laser Pulse Heating", International Symposium on Thermodynamics of Nuclear Materials, IAEA, (1979).

12. Hertz, H., Ann. Physik 17 (1882) 117.

13. Knudsen, M., Ann. Physik 28 (1909) 75, 28 (1909) 999, 29 (1909) 179.

14. Ivanov, V. E., Kruglich, A. A., Pavlov, V. S. Kovtun, G. P., and Amonerko, V. M., Thermodynamics of Nuclear Materials 1962, p. 735, IAEA, Vienna, 1962.

15. Alexander, C. A., Ward, J. J., Ogden, J. S., and Cunningham, G. W., Carbides in Nuclear Energy, Proceedings of a Symposium held at Harwell, 1963, Vol. ___, p. 192, Ed. by Russel, L. E., Bradbury, B. T., Harrison, J. D. L., Hedger, H. J., and Mardon, P. G., Macmillan and Co. Ltd., London, 1964.

16. Vozzella, P. A., and Decrescente, M. A., Thermodynamic Properties of Uranium Monocarbide, Report PWAC-478, Pratt and Whitney Aircraft, Middletown, Connecticut, 1965.

17. Khromonozhkin, V. V., and Andrievskii, R. A., Thermodynamics 1965, Vol. 1,p. 35, IAEA, Vienna, 1966

18. Storms, E. K., Thermodynamics 1965, Vol. 1, p. 309, IAEA, Vienna, 1966.

19. Krupka, M. C., given in Ref. [55].

20. Anselin, F., and Poitreau, J., Measure de la Pression de Dissociation du Moncarbure d'Uranium entre 2250 et 2500 K par la Methods d'Effusion de Knudsen, Report CEA-R 2961, 1966, Commissariat a l'Energie Atomique, Centre d'Etudes Nucleaires de Fontenay-au Roses, France.

21. Garbanyu, A., Paulinov, L. V., and Bykov, V. N., Energie Atomique 23 (1967) 7.

22. Pattoret, A., Drowart, J., and Smoes, S., Bull. Soc. France Ceram. 77 (1967).

23. Vozzella, P. A., Miller, A. D., and Decrescente, M. A., J. Chem. Phys. 49 (1968) 876.

24. Andrievskii, R. A., Khromonozhkin, V. V., Galkin, E. A., and Mitrifanov, V. I., Atomnaya Energiya 26 (1969) 494.

25. Solovev, G. I., given in Report ANL/CEN/AF-100 by Sheth, A., Gabelnick, S. D., Foster, M. S., Chasanov, M. G., and Johnson, C. E., Argonne National Laboratory, Argonne, Illinois, 1974.

26. H. V. Karow, M. Bober, "Experimental Investigation into the Spectral Reflectivity and Emissivity of Liquid UO_2, UC, ThO_2, and Nd_2O_3", Symposium on Thermodynamics of Nuclear Materials, IAEA (1979).

27. W. Breitung, KFK-2091 (1975).

28. P. E. Blackburn, J. Nucl. Mater., 46:244 (1973), Argonne National Laboratory, private communication.

29. S. S. Nikol'skii, Teplofiz.vys.Temp. 7, 873 (1969).

30. S. S. Nikol'skii and I. N. Levina op. cit p. 1014.

31. E. K. Storms, Thermodynamics, 1, IAEA, Vienna (1966), p. 309.

32. F. L. Oetting, M. Rad, R. J. Achermann, "The Chemical Thermodynamics of the Actinide Elements and Compounds," Part 1, IAEA (1976).

33. P. A. Finn, A. Sheth, G. Windlow and L. Leibowitz, "Advanced LMFBR Fuels," p. 189, Topical Meeting Proceedings, Tucson, Arizona, October 10-13, 1977. Edited by Leary, J., and Kittle, H.

34. L. Leibowitz, Argonne National Laboratory, private communication (1981).

35. S. J. Anisimov, Soviet Physics JETP, vol. 27, No. 1, July 1968, pp. 182,183.

36. Masahide Murakami and Koichi Oshima, 9th Int. Symp. on Rarefied Gas Dynamics, 1974, vol. II, pp. F.6.1-F.6.9.

37. Tor Ytrehus, 10th Int. Symp. on Rarefied Gas Dynamics, paper 88, July 1976.

38. R. A. Olstad and D. R. Olander, J. Appl. Phys. vol. 46, No. 4, April 1975, pp. 1499-1508.

39. R. A. Olstad and D. R. Olander, J. Appl. Phys. vol. 46, No. 4, April 1975, pp. 1509-1518.

40. Instructional Manual for American Optical Model 30 Nd-Glass Laser System, Southbridge, Massachusetts, 1968.

41. C. G. Young, Laser Focus, Laser Technology Section, July 1968, p. 72.

42. R. W. Ohse, J. F. Bobelot, K. A. Long, J. Magil, International Symposium on Thermodynamics of Nuclear Materials, 29 January, 2 February 1979, IAEA-SM-236/4.

43. Instructional Manual for PHTO I. Automatic Pyrometer Serial No. A-164, The Pyrometer Instrument Co., Inc. 1973.

44. R. A. Olstad, Ph. D. Thesis, University of California at Berkeley, December 1972.

45. N. D. Cox, "A Report on a Sensitivity Study of the Response Surface Method of Uncertainty Analysis of a PWR Model," EGaG Idaho, Inc. Report No. Re-S-77-7, January 1977.

46. S. O. Peak, "Code Development and Analysis Program," EGaG Idaho, Inc. Report No. CDAP-TR-78-024, July 1978.

47. John Corcoran, Ampex Corp., Laser Focus, June 1973, p. 61.

48. J. F. Ready, Private communication.

49. J. F. Ready, "Effects of High-Power Laser Radiation," Academic press, New York--London (1971), pp. 115-116.

50. J. Magill and R. W. Ohse, J. Nucl. Mater. 71 (1977) 191-193.

51. J. F. Ready, J. Apply-Phys. 36 (1965) 462.

52. R. W. Ohse, P. G. Berrie, H. G. Bogensberger and E. A. Fishe, IAEA Symposium on Thermodynamics of Nuclear Materials, Paper IAEA-SM-19018, Vienna, October 1974.

53. A. Sheth and L. Leibowitz, Equation of State and Transport Properties of Uranium and Plutonium Carbides in the Liquid Region, ANL-AFP-11 (Septemter 1975).

54. H. D. Lewis, et al., A. Review of the Literature on the Electrical and Thermal Transport Properties of the Carbides of Uranium and Plutonium, Los Alamos Scientific Laboratory report (to be published).

55. A. G. Tunbull, The Thermal Conductivity of Molten Salts, II: Theory and Results for Pure Salts, Aust. J. Applied Sci. 12, 324 (1961).

56. M. Tetenbaum, et al., A Review of the Thermodynamics of the U.C., PU-C and U-PU-C Systems. ANL-AFP-8 (June 1975).

57. D. Fee and C. B. Johnson, Phase Equilibria and Melting Point Data for Advanced Fuel Systems, ANL-AFP-10 (June 1975).

58. J. L. Routbort and R. N. Singh, Elastic, Diffusional, and Mechanical Properties of Carbide and Nitride Nuclear Fuels. A Review, J. Nucl. Mater. 58 (October 1975), pp. 78-114.

59. W. Chubb, V. W. Getz and C. W. Towley, J. Nucl. Mater. 13 (1964) 63.

60. Bird

61. Nucl. Engr. Handbook

62. L. N. Grossman, High-Temperature Thermophysical Properties of Uranium Monocarbide, J. Am. Ceram. Soc. 46, 264 (1963).

63. R. Deconinck, Physical Properties of Uranium Carbides, Annual Scientific Report, 1973, BLG495/74, ed. R. Billian, K. Bober, G. Michiels, and J. Proost.

64. R. H. Edwards, and R. L. Collins, Evaporation from a Spherical Source into a Vacuum in "Rarefied Gas Dynamics," L. Trilling and H. Y. Wachmann, eds., Academic Press, New York--London, p. 1489.

65. M. Murakami and K. Oshima, "Kinetic Approach to the Evaporation and Condensation Problem," ISAS, Tokyo, Report No. 518, 1974, p. 261.

66. F. S. Sherman, and H. Ashkenas, "Rarefied Gas Dynamics," 2, 84, 1966.

67. J. B. Anderson, and J. B. Fenn, Phys. Fluids 8, 780, 1965.

68. L. P. Smith, Phys. Rev. 35, 381 (1930).

69. J. Magill, J. Bloem, and R. W. Ohse, "The Mechanism and Kinetics of Evaporation from Laser Irradiated UO_2 Surfaces", J. Chem. Phys. 76 (12), 15 June 1982.

This report was done with support from the Department of Energy. Any conclusions or opinions expressed in this report represent solely those of the author(s) and not necessarily those of The Regents of the University of California, the Lawrence Berkeley Laboratory or the Department of Energy.

Reference to a company or product name does not imply approval or recommendation of the product by the University of California or the U.S. Department of Energy to the exclusion of others that may be suitable.

TECHNICAL INFORMATION DEPARTMENT
LAWRENCE BERKELEY LABORATORY
UNIVERSITY OF CALIFORNIA
BERKELEY, CALIFORNIA 94720